# On the Mesospheric Removal of Very Long-lived Greenhouse Gases

## Anna Elizabeth MacKinlay Totterdill

**Submitted in accordance with the requirements for the**

**degree of Doctor of Philosophy.**

**The University of Leeds**

**School of Chemistry**

**December 2015**

# Published Work

The candidate confirms that the work submitted is her own, except where work which has formed part of jointly-authored publications has been included. The contribution of the candidate and the other authors to this work has been explicitly indicated below. The candidate confirms that appropriate credit has been given within the thesis where reference has been made to the work of others.

Chapters 3 – 5 contain work that has been published in jointly-authored journal articles. Chapter 3 describes kinetic measurements and Lyman-α cross-sections of the very long-lived greenhouse species: $SF_6$, $NF_3$ and CFC-115. This work has been published in:

Totterdill, A; J. C. Gomez-Martín, T. Kovács, W. H. Feng and J. M. C. Plane. Experimental Study of the Mesospheric Removal of $NF_3$ by Neutral Meteoric Metals and Lyman-α Radiation. *J. Phys. Chem.*, 2014, **118**(23), pp.4120-4129.

Totterdill, A., T. Kovács, J. C. Gomez-Martín, W. H. Feng and J. M. C. Plane. Mesospheric Removal of Very Long-Lived Greenhouse Gases $SF_6$ and CFC-115 by Metal Reactions, Lyman-alpha Photolysis, and Electron Attachment. *J. Phys. Chem.*, 2015, **119**(10), pp.2016-2025.

The candidate carried out the experiments and analysis described in these papers. The theoretical work described in these publications was carried out by J. M. C. Plane. The work relating to Lyman- α cross-sections, electron attachment and loss rates was carried out by T. Kovács in conjunction with W. H. Feng.

Chapters 4 and 5 describe the calculation of global warming potentials and their atmospheric implications. This work will be submitted for publication in:

Totterdill, A., T. Kovács, W. H. Feng, S. Dhormse, C. Smith, J. C. Gomez-Martín, M. Chipperfield, P. Forster and J. Plane. *Atmospheric Lifetimes, Infrared Absorption Spectra, Radiative Forcings and Global Warming Potentials of $NF_3$ and CFC-115*. Unpublished, 2016.

Kovács, T., A. Totterdill, W. H. Feng, S. Dhormse, C. Smith, J. C. Gomez-Martín, M. Chipperfield, P. Forster and J. Plane. *Atmospheric Lifetimes, Infrared Spectra, Radiative Forcings and Global Warming Potentials of $SF_6$*. Unpublished, 2016.

The candidate carried out the experiments, modelling and analysis described in these papers. Modelling relating to atmospheric lifetimes was carried out by T. Kovács with W. H. Feng.

# Acknowledgements

Firstly, I would like to thank my supervisor John Plane for introducing me to such a fascinating area of research. His guidance, patience and support has been invaluable.

I must also give thanks to the people who have helped me with my work over the past few years. Mark Blitz for initially helping me with the lasers, Tamás Kovács for his contribution to the project, Wuhu Feng for his constant willingness to help and especially Juan Carlos Gomez-Martín for his proof-reading and his guidance in all experimental matters.

Special thanks goes to my friend Danny for his emotional support and always being willing to drop what he's doing for a coffee and some mutual complaining. Thanks also go to my friends Daniel and Rob for their help and advice in handling many various modelling disasters! To the other members of the Plane group: thank you for your company, your friendship, support and encouragement.

My gratitude also goes out to my friends, in particular: Laura, Adam and Louise but also Hirra, Dave, Nadia, Vikki and Naomi. I'll always appreciate you for putting up with me and always being understanding through the cancelled plans and bad moods. Your encouragement and the laughs have meant a lot to me.

Finally, my love and thanks go to my family, in particular my Dad, without whom this thesis would not have been possible. Thank you for believing in me and always being at the other end of the phone.

# Abstract

The fluorinated gases $SF_6$, $NF_3$ and CFC-115 are chemically inert with atmospheric lifetimes of many centuries which, combined with their strong absorption of infrared radiation, results in unusually high global warming potentials. Very long lifetimes imply that potential mesospheric sinks could make important contributions to their atmospheric removal. In order to investigate this, the reactions of each species with the neutral metal atoms Na, K, Mg and Fe, which are produced by meteoric ablation in the upper mesosphere, were therefore studied. The observed non-Arrhenius temperature dependences of the reactions are interpreted using quantum chemistry calculations of the relevant potential energy surfaces. The absorption cross-section at the prominent solar Lyman-α solar emission line (121.6 nm) was also determined.

In the second part of this study updated values for the infrared absorption cross-sections of $SF_6$, $NF_3$ and CFC-115 were experimentally determined and used in two radiative transfer models in order to determine radiative forcing and efficiency values. These were carried out with thorough sensitivity analysis and included the effect of clouds and stratospheric adjustment. A three-dimensional chemistry-climate model was used separately to determine updated atmospheric lifetimes of each species. Finally, we combined our results to determine updated global warming potentials over a 20, 100 and 500 year time period.

# Table of Contents

# List of Figures

## Chapter 1

## Chapter 2

## Chapter 3

## Chapter 5

# List of Tables

## Chapter 4

## Chapter 5

# Chapter 1: Introduction

Atmospheric chemistry concerns the reactions and transport of various gases and aerosols, primarily across the troposphere, stratosphere and mesosphere. From understanding these reactions the atmospheric lifetimes and consequently, global warming potentials of any chemical species can be evaluated.

The aim of this work is to revaluate the global warming potentials of the very long lived greenhouse gases $SF_6$, $NF_3$ and CFC-115 ($C_2F_5Cl$). This will be done through consideration of their radiative forcings and their atmospheric lifetimes. For species with long lifetimes such as these, removal processes in the mesosphere can become rate determining. Consequently the relevance of different mesospheric removal processes is central to this research. Some discussion of these processes relative to $SF_5CF_3$ is also provided.

This chapter will outline the basic structure of the atmosphere followed by a description of the origin and role of meteoric metals in the upper atmosphere. Discussion of atmospheric lifetimes, radiative forcings and global warming potentials will then be described, along with a discussion of the specific species studied here.

## 1.1   Atmospheric Composition and the Greenhouse Effect

Atmospheric chemistry concerns the reactions and transport of various gases and aerosols, primarily across the troposphere, stratosphere and mesosphere. Heat radiation is provided by the sun and is subject to fluctuations including diurnal, seasonal and longer term variations in which different locations experience a significant variation in radiation input. This not only changes the total energy but affects the rate of some reaction cycles, shifting equilibria so that alternative

gaseous species become energetically favourable, altering the atmospheric composition and consequently, the greenhouse effect (1).

The composition of various planetary atmospheres can be identified via their transmitted infrared (IR) emission patterns through space. Earth's atmosphere is composed of several strongly IR absorbing gases such as $CO_2$ and $H_2O$. As a result there is a significant 'greenhouse effect' when compared with other planets within our solar system, specifically those more lacking in atmosphere such as Mercury and Mars. Mars, like Mercury, experiences almost no greenhouse effect and possesses a surface temperature of approximately 220 K. Nights on Mercury can reach as low as 100 K despite it being significantly closer to the Sun than Earth (1, 2). Conversely, planets such as Venus or, Saturn's moon Titan, exhibit a significant greenhouse effect. The surface temperature on Venus can reach as high as 750 K due to a high density atmosphere consisting 95 % of the infrared absorbing gas $CO_2$. The surface temperature on Titan is approximately 94 K, which is significant considering that Titan's solar input is only 1 % of the Earth. The relatively high temperature on Titan is caused almost solely by the presence of 1.6 % methane in its atmosphere (2).

The greenhouse effect can be quantified to some extent by applying the Stefan-Boltzmann law:

$$T_{eq} = \left(\left(\frac{r_E}{r}\right)^2 \frac{F_E(1-A)}{4\varepsilon\sigma}\right)^{\frac{1}{4}} \qquad (E1.1)$$

where $T_{eq}$ is the predicted average planetary surface temperature, $A$ is the albedo, $F_E$ the solar flux at Earth's surface, $r_E$ is distance of Earth to Sun, $r$ is distance of planet to Sun, $\varepsilon$ is emissivity and $\sigma$ is Stefan's constant ($5.67 \times 10^{-8}$ $Wm^{-2}K^{-4}$).

E1.1 predicts $T_{eq}$ for Mars, Venus and Earth as 212, 220 and 255 K where the actual observed temperatures are 218, 733 and 288 K. This provides discrepancies of 6 K for Mars, 33 K for Earth and over 500 K for Venus (3). Atmospheric composition and therefore global warming effects, are not accounted for in the equation. The huge difference in predicted and observed temperatures for Venus are consequently

attributed to global warming, an effect observed to a lesser degree for the Earth's temperature.

The Stefan-Boltzmann law gives a very accurate prediction for the temperature on Mars where almost no greenhouse effect is observed (1, 2). Conversely, the predicted temperature for Venus is hugely underestimated. This is because the planet exhibits a significant greenhouse effect despite it having the same atmospheric composition as Mars. The atmospheres of both planets are comprised of 95 % $CO_2$, however the surface pressure of Venus is over 90 bar, 150 times that of Mars. This effect is summarised below in Table 1.1.

| Planet | Surface $Temp_{predicted}$ /K | Surface $Temp_{observed}$ /K | Surface Pressure /bar | Atmospheric Composition |
|---|---|---|---|---|
| Mercury | 437 | 440 | $\sim 10^{-14}$ | Trace amounts of $H_2$, He and $O_2$ |
| Venus | 220 | 733 | > 90 | 95% $CO_2$<br>4% $N_2$ |
| Earth | 255 | 288 | 1 | 78% $N_2$<br>21% $O_2$ |
| Mars | 212 | 218 | $6 \times 10^{-3}$ | 95% $CO_2$<br>3% $N_2$<br>2% Ar |

**Table 1.1** Stefan-Boltzmann predicted surface temperatures of the terrestrial planets compared against their observed surface temperatures, surface pressures and atmospheric compositions (1).

## 1.2 Structure of the Atmosphere

The atmosphere is separated into several layers defined by alternating positive and negative temperature gradients. These layers are depicted in Figure 1.1 and, are termed in order of increasing altitude, the troposphere, stratosphere, mesosphere and thermosphere. The mesosphere, occurring between ~ 50 – 85 km, is the predominant region of interest for this study.
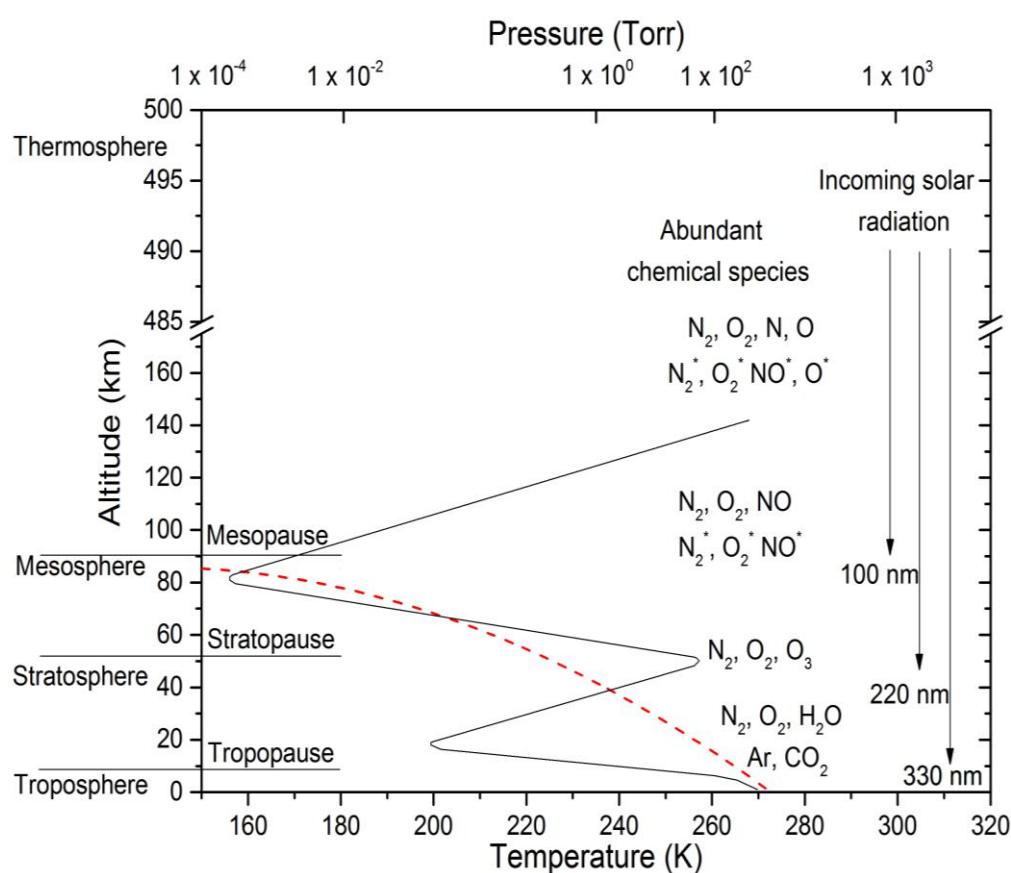


**Figure 1.1.** The vertical structure of the atmosphere as characterized by temperature/ pressure change with increasing altitude. Where in the above figure, temperature is represented by the solid line and pressure by the dashed line. Also defined are the most abundant chemical species at each atmospheric layer and approximate wavelength range of penetrating solar radiation. Reproduced from Christian Baresel (4).

The major constituents of the Earth's atmosphere are $N_2$ (~ 78 %), $O_2$ (~ 21 %) and ~ 1 % various trace species (including water vapour, $CO_2$ and Ar). Due to turbulent mixing, the atmospheric composition of unreactive species is fairly uniform below 95 km. Below this altitude, gravitational effects are responsible for the greater density of gas closer to Earth's surface. Atmospheric pressure decreases approximately exponentially with altitude so that almost half the total mass of the atmosphere exists below 5.5 km and 99 % below 30 km.

The boundaries, termed by the suffix "pause" of each atmospheric layer are not constant and are subject to variation according to changes in season and, at different latitudes. The troposphere is the oxygen-rich region in which all living organisms exist. With pressure being highest in the troposphere, the abundance of many key greenhouse gases is also greatest. This means radiative trapping effects are larger here due to the repeated absorption and re-emission of longwave radiation which causes local heating, falling with altitude as density decreases. The troposphere is consequently characterised by a steady decline of approximately 80 K in temperature with altitude, reaching around 200 K between 10 and 12 km at the tropopause (5).

In the stratosphere, the exothermic recombination of $O_2$ and O to form ozone dominates the region. Recombination occurs at such a rate that, along with the absorption of UV radiation by ozone, causes local heating resulting in a temperature profile which is related to the ozone concentration profile. Convection causes lighter, warmer gases to rise above the heavier, cooler gases, initiating temperature increase and the suppression of vertical mixing leading to a local temperature maximum of around 270 K at the stratopause (1).

The mesosphere exists between approximately 50 and 80 km. Due to pressures in this region reaching as low as falling as low as $10^{-5}$ bar at around 80 km, the region experiences decreased solar heating and increased radiative emission. The pressure dependant recombination of ozone is very slow in this area. Temperatures in the mesosphere fall as low as 100 K, making it the coldest region on the planet (6). As altitude increases, mesospheric temperature falls due to the absorption of high energy radiation in the thermosphere above and in conjunction with the

increased infrared radiative effect of greenhouse gases present (7). This is discussed in greater detail in Section 1.2.2.

The thermosphere is a layer of extremely low pressure and high temperature. The high temperature is caused by the absorption of extreme UV and x-ray (<200 nm) radiation by residual levels of $O_2$. As most of this high energy radiation is absorbed in the thermosphere, it does not penetrate to lower levels. The low pressure means that the mean free path is such that gaseous collisions become so infrequent that molecules are unable to achieve local thermodynamic equilibrium and lose energy through radiative transfer. In particular, translational temperatures may become much higher than vibrational or rotational temperatures leading to inefficient cooling through infrared emission. A significant temperature increase with altitude is observed where temperatures become extremely high, culminating at around 2000 K during extreme solar events (5). Again, this is discussed in greater detail in Section 1.2.2.

### 1.2.1 Ozone

As discussed in the preceding section, the temperature profile of the stratosphere is largely dictated by the local concentration of ozone. In the stratosphere (and mesosphere), solar energy is primarily absorbed by $O_3$ and consequently liberated as heat. The decreasing efficiency of ozone formation with altitude largely accounts for simultaneously declining temperature.

Daily global ozone production results in the generation of around 400 million metric tons, mainly produced around the tropical upper stratosphere and mesosphere. The photochemical mechanism of ozone production was first proposed by Chapman *et al.* (8) who hypothesised that atomic oxygen was formed through the dissociation of $O_2$ by UV photons above around 20 km through the reaction:

$$O_2 + h\nu \rightarrow O + O \qquad\qquad\text{(R1.1)}$$

where $h$ is Planck's constant ($6.626 \times 10^{-34}$ Js) and $\nu$ is the frequency of the photon in $s^{-1}$. The lifetime of the atomic oxygen formed in R1.1 is less than one second. This indicates that the following reaction occurs very quickly:

$$O + O_2 + M \rightarrow O_3 + M \qquad\qquad\text{(R1.2)}$$

where atmospherically, M is likely to be either $N_2$ or $O_2$ which comprise 99 % of the atmosphere. An approximation to the potential energy curve along the O + $O_2$ reaction coordinate is given below in Figure 1.2.
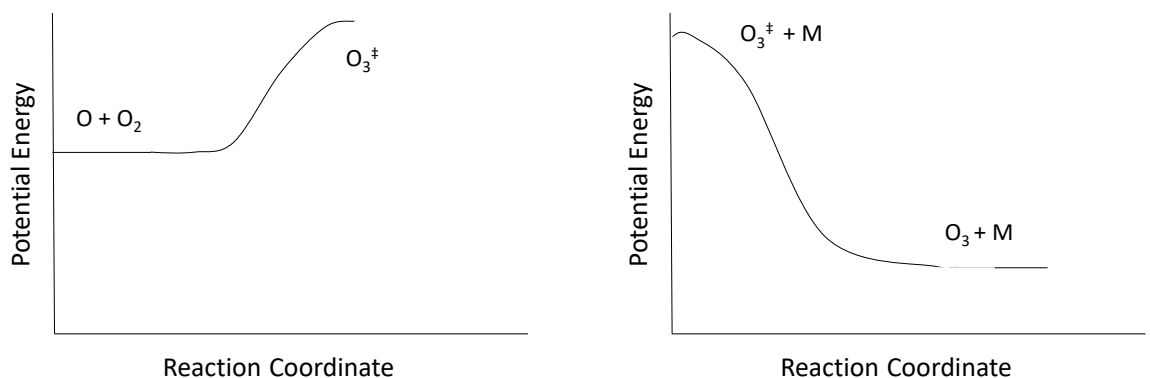


**Figure 1.2.** Potential energy curves for the formation of ozone.

Without the third body M, R1.2 would be unlikely to occur. Because a bond is being formed, the reaction is exothermic. In order to obey the law of conservation of energy, the total kinetic energy possessed by the $O_3$ product must equal the sum of the reaction exothermicity and the kinetic energies of the reactants. Conservation of momentum requires the molecule to be stationary and so this excess kinetic energy is translated into vibrational motion of the $O_3$ molecule. Highly excited species such as this are extremely unstable and can decompose very rapidly. For the ozone molecule to survive, it transfers this excess energy through collision with a

third body, M. This is either translated into internal excitation of the M body or into kinetic energy causing the two molecules to fly away from each other (1).

Cycling between R1.1 and R2.2 causes local heating and above 60 km the pressure becomes too low for R1.2 to compete with R1.1 and atomic oxygen becomes the dominant form of oxygen.

Ozone has a large absorption cross section at 253.6 nm of $1.15 \times 10^{-17}$ cm$^2$ molecule$^{-1}$. This means that nearly all photons at this wavelength are absorbed by ozone and consequently never reach Earth's surface. This absorption leads to its dissociation by the reaction:

$$O_3 + hv \rightarrow O_2 + O \qquad \text{(R1.3)}$$

and the consequent rapid recombination by R1.2, converting the energy of the photons at these wavelengths to thermal energy through the third body, M.

However, the effect of these reactions alone would result in concentrations of ozone far greater than those observed. Consequently, it was deduced that ozone must be lost through reaction with odd oxygen:

$$O_3 + O \rightarrow O_2 + O_2 \qquad \text{(R1.4)}$$

Above 60 km as pressure decreases, R1.2 becomes significantly slower. Odd oxygen in the mesosphere/ lower thermosphere (MLT) is removed by the following sequence of reactions:

$$H + O_3 \rightarrow OH + O_2 \qquad \text{(R1.5)}$$

$$O + OH \rightarrow H + O_2 \qquad \text{(R1.6)}$$

$$O_2 + H (+ M) \rightarrow HO_2 (+M) \qquad \text{(R1.7)}$$

$$HO_2 + O \rightarrow OH + O_2 \qquad \text{(R1.8)}$$

In the MLT lifetimes of atomic O and H reach in excess of 12 hours. This is because low pressures reduce the rates of R1.2 and R1.7 significantly. This reduction in $k_{1.2}$ and $k_{1.7}$ results in high concentrations of atomic O and H, even during night-time. A sharp increase in atomic oxygen observed between 75 and 85 km is known as the atomic oxygen shelf. Odd hydrogen species ($HO_x$) involved in R1.5 – R1.8 result from the transport and photolysis of $CH_4$, $H_2O$ vapour and $H_2$ from the lower atmosphere.

## 1.2.2  The Mesosphere/ Lower Thermosphere

The MLT occurs between approximately 75 and 110 km. As well as chemical and radiative processes, a number of physical and dynamic processes govern the unusual energy balance and temperature profile of the MLT.

The mesosphere begins at around 50 km and has a negative temperature gradient leading to a minimum at the mesopause at approximately 80 km. Cooling in the mesosphere occurs as heating by absorption of UV by ozone drops off with decreased $O_3$ concentration with altitude. A further cooling process is the infrared emission by $CO_2$. In the troposphere infrared radiation is absorbed by the Earth and reradiated as heat. In the mesosphere infrared radiation is radiated back into space (9).

Atmospheric heating processes include the continuous absorption and emission of infrared radiation by greenhouse gases. This results in these greenhouse gases retaining  an excess of kinetic energy which leads to energy exchange through collisions, heating the gases. However, infrared absorption does not make a significant contribution to temperature in the mesosphere because pressures are so low (~ $10^{-5}$ - $10^{-6}$ bar at the mesopause) (6). Above the mesosphere, the thermosphere experiences a steeply positive temperature gradient, opposite to that of the mesosphere (9).

Gravity waves are vertical oscillations with relatively short horizontal wavelengths (10 – 1000 km) produced by orographic forcing (air flow over mountains), thunderstorms or frontal systems (9). As gravity waves propagate upwards through

the atmosphere, they become unstable and break. These breaking waves deposit energy and momentum, providing a major source of dynamical variability in the mesosphere. Propagation of gravity waves through the atmosphere varies with season and is dependent on thermal structure and wind distribution. As waves propagate upwards, their amplitude grows exponentially with increasing altitude, due to decreased atmospheric density. At a critical altitude the wave becomes unstable and breaks, creating a drive of residual circulation from the summer to the winter hemisphere (2).

The meridional wind travels from the summer to the winter pole as shown in Figure 1.3. This circulation gives rise to very low temperatures in the summer pole due to cooling by adiabatic expansion of upwelling air.
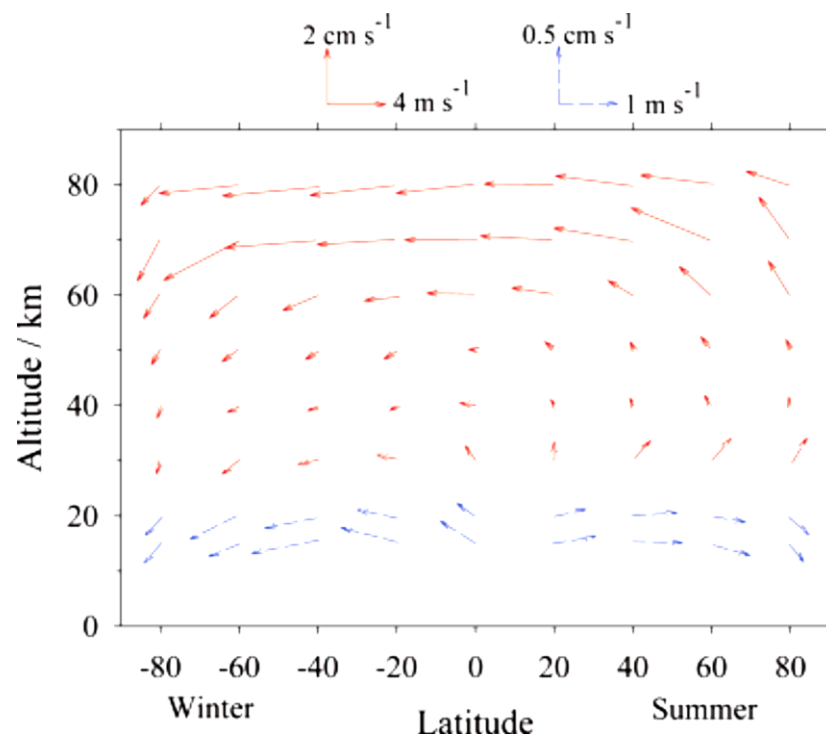


**Figure 1.3.** Meridonal wind vectors as a function of altitude and latitude. Reproduced from Plane (2003).

Chemical species are transported throughout the atmosphere on several scales. Advection is a large scale process which occurs as the movement of molecules in response to a concentration gradient. Eddy diffusion, where species are mixed as a result of turbulence, takes place on a smaller temporal and spatial scale (1). At approximately 105 km in the turbopause, the pressure is too low for bulk motion of air to occur and there is a steady state between gravitational sedimentation and molecular diffusion. This means that above this height, air is not well mixed and molecules are separated by mass so that only H, $H_2$ and He are present in the highest regions (1).

### 1.2.3 The Ionosphere

The ionosphere begins at approximately 60 km, overlapping with the MLT. It describes a layer of the atmosphere in which a large concentration of ions exist. In this region absorbing species become ionised through the absorption of high energy solar radiation (< 200 nm) and (potentially) interaction with cosmic rays or precipitating energetic particles. Furthermore, in some cases, the energy absorbed may be sufficient to cause both dissociation and ionisation of the dissociation products.
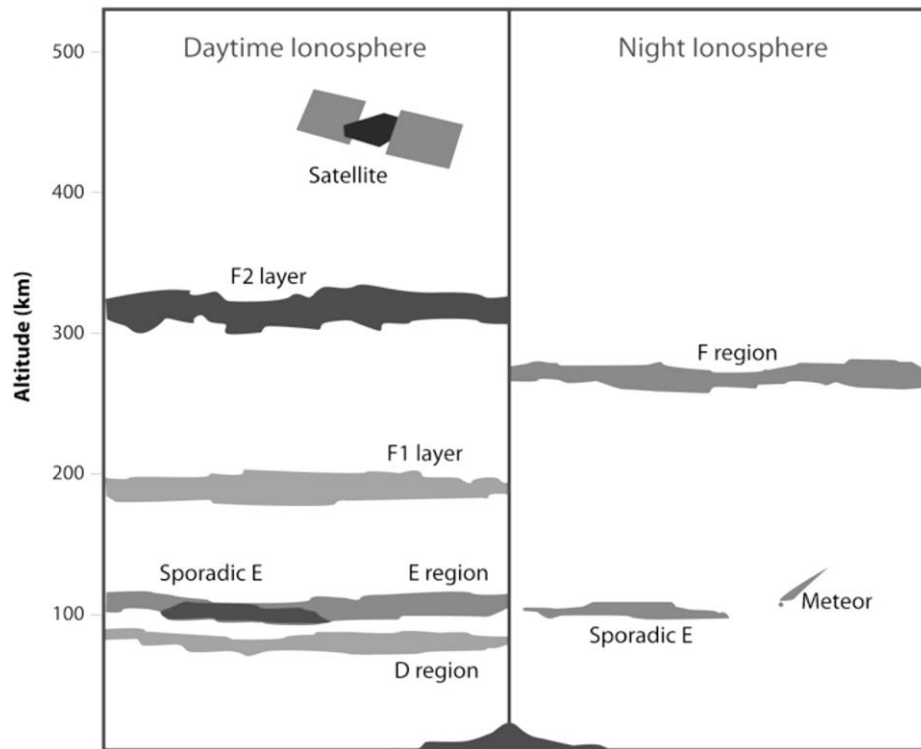
**Figure 1.4.** The day and night structures of the terrestrial ionosphere.

As shown on Figure 1.4, the ionosphere is divided into three regions, D, E and F. These boundaries are dictated by the dominant species present and relative electron density. The lowest region between 70 – 95 km is the D region. This experiences the most complicated chemistry in the ionosphere due to the relatively high pressures ($\sim$5 x $10^{-5}$ – 3 x $10^{-7}$ bar) and large quantities of trace species, primarily proton hydrates (i.e. $H^+(H_2O)_n$ where n $\geq$ 1) and other smaller quantities of cluster ions such as $O_4^+$, $NO^+(H_2O)$ and $NO^+(CO_2)$ . Ionisation in the D region is caused primarily through the absorption of Lyman-$\alpha$ radiation ($\lambda$ = 121.6 nm) (1).

Between 70 – 80 km negative ions exist produced initially through electron attachment to $O_2$:

$$O_2 + e^- (+M) \rightarrow O_2^- (+M) \qquad \text{(R1.9)}$$
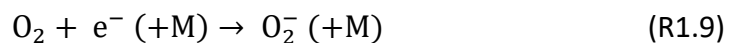
which then undergoes reaction with other species leading to the generation of negative ions such as $NO_3^-$ and $CO_3^-$. At higher altitudes these negative species are rapidly destroyed through photo-detachment:

$$O_2^- + h\nu \rightarrow \ O_2 + e^- \qquad\qquad (R1.10)$$

and through associative attachment with O:

$$O_2^- + O \rightarrow \ O_3 + e^- \qquad\qquad (R1.11)$$

$O_2^+$ and $N_2^+$ are major ions in the E-region which exists between $95 - 170$ km. $O_2^+$ and $N_2^+$ are formed by photoionisation of $O_2$ and $N_2$ by Lyman-$\beta$ radiation ($\lambda = 102.6$ nm) and x-rays. However $NO^+$, along with $O_2^+$, are the dominant ions in the E-region and are formed through the following sequence of reactions:

$$N_2^+ + O \rightarrow N^* + NO \qquad\qquad (R1.12)$$

$$N_2^+ + O_2 \rightarrow N_2 + O_2^+ \qquad\qquad (R1.13)$$

$$O_2^+ + NO \rightarrow O_2 + NO^+ \qquad\qquad (R1.14)$$

The F-region then lies between $170 - 500$ km. In this region $N^+$ and $O^+$ are the dominant ions and are formed from the absorption of EUV radiation by O and $N_2$. The F-region can be further divided into the $F_1$ and $F_2$ sub-regions (Figure 1.4), so characterised as two peaks in electron density may sometimes be observed. The maximum electron density reaches a concentration of around $10^6$ cm$^{-3}$ in this region and decreases rapidly beyond this maximum. Above 500km $He^+$ and $H_2^+$ become the dominant ions (10).

## 1.3   Meteoric Metals

Metallic layers exist in the atmosphere between 75 and 110 km in the MLT (7). The source of these metals is ablation from the influx of particles of extra-terrestrial dust, known as meteoroids. These particles originate from the asteroid belt beyond Mars and from the dust trails of comets. Meteor showers occur as Earth passes through these dust trails (11). Meteoric ablation is considered to be the major source of metals in the MLT due to the correlation between the elemental abundances and direct observations of metals in meteor trails (12).

### 1.3.1 Observations and Instruments

#### 1.3.1.1 Meteoric Input

Early efforts to quantify the average daily input of interplanetary dust into Earth's atmosphere were conducted in 1978 by Hughes [13]. Data were gathered from ground based meteor radar and optical observations and in-situ satellite measurements resulting in an estimated value of 44 t $d^{-1}$ [13]. This value is widely used, although it has been subject to criticism as the estimate was derived by disregarding radar data which disagreed with the satellite data [14].

#### 1.3.1.2 Metal Layers

Rocket-borne mass spectrometry, lidars, large aperture radars and satellite remote sensing are used to estimate the presence and densities of metallic layers which exist in the atmosphere between 75 and 110 km in the MLT [7]. Such techniques are employed in this region as an alternative to aircraft or balloon measurements whose operating ranges are up to approximately 20 and 40 km respectively.

The first observations of metal atoms in the MLT were made in the early 1950s using ground based photometers. These instruments measured the resonance fluorescence of spectroscopic transitions caused by the excitation of atmospheric metals (such as Na, K, Fe and Ca) by solar radiation [15].

Tuneable lasers were invented some twenty years later in the 1970s, and with them ground based laser radar (lidar). Lidar is a hugely significant technique and is still used for taking measurements in the MLT [7, 16]. The technique involves the transmission of a pulsed beam tuned to a strongly allowed spectroscopic transition wavelength through the atmosphere. The pulse is then resonantly scattered by metal atoms in the mesosphere. A fraction of this scattered light returns to the ground where it collected by a telescope. It can then be analysed by time-resolved photon counting to establish the height of the scattering layer where the metal

density is determined from comparison with a Rayleigh-scattered signal at a lower altitude of known atmospheric temperature and density (7).  Lidar has been used to successfully observe K, Li, Na, Fe and Ca. Ions are not usually observable by lidar as their resonance transitions are usually in the UV and therefore absorbed by stratospheric ozone, $Ca^+$ however is the only ion observable by this method. The lidar technique has been developed and has advanced to the stage where layers can be so accurately defined that they are now used as tracers for dynamical processes (17). Lidars have also been employed to make more general measurements in the MLT. For example, temperature measurements have been made with Na, K and Fe lidars (18) and Na lidars used to measure wind profiles (19).

Metallic ion concentrations have also been observed *in-situ* by rocket-borne mass spectrometry. Istomin (20) made the first measurements of metal ions in a layer near 95 km. A database of published sounding rocket ion density altitude profiles has been compiled by Grebowsky and Aikin (21) who have made a comprehensive review of *in situ* measurements of meteoric ions.

Satellite-borne limb-scanning spectrometers which detect resonant scattering of sunlight, have also been used to observe neutral metal atoms and determine their vertical profiles. Several different satellite programs have been used to obtain column densities of various metals (22). These satellites include Odin which incorporates the Optical Spectrograph and Infra-Red Imager System (OSIRIS) spectrometer which measures Na (23) and K (24) and Envisat with the Scanning Imaging  Absorption Spectrometer for Atmospheric Chartography (SCIAMACHY) for Mg and $Mg^+$ (25) and the Global Ozone Measurement by Occultation of Stars (GOMOS) spectrometer for Na (26). Unlike ground-based lidars which only operate locally, satellites are capable of obtaining global coverage. Both OSIRIS and SCIAMACHY are in sun-synchronous polar orbits which have therefore provided near-global coverage (82° S to 82° N and 82° S to 78° N respectively).  The disadvantage with a sun-synchronous orbit however,  is a limited ability to study diurnal variation.

Initial theories of the origin of metallic layers in the atmosphere speculated that a dust layer originating from volcanoes and oceanic aerosols existed at 90 km, from which metallic species would evaporate throughout the day (7). It is now widely accepted that these layers result from the ablation of 20 – 100 tonnes (27) of cosmic dust from meteor shower trails and meteoroids originating in the asteroid belt, both entering the atmosphere daily (17, 28). Currently, it is not possible to obtain accurate projections of the mass of material entering from space because instrumentation capabilities are insufficient (27).

The most abundant atmospheric metals are Fe, Na and Mg with peak concentrations of approximately 10,000, 5000 and 3000 $cm^{-3}$ respectively (29). The most abundant species in meteors is Si, accounting for approximately 20 % of their mass on average. Mg is the most abundant metal accounting for 12.5 % by mass (16). The Mg concentration in the MLT is lower than that of Na, despite the latter having a relative abundance of 0.6 % by mass in meteoroids. This observation is explained by the relatively higher volatility of Na (17). Unlike the other metals, the ratio of concentration of the neutral and ionised species $Mg^+$ and Mg is rather large, between 1.5 and 10 compared to ~ 0.2 – 2 for other metals. The reasons for this are unclear.

Accurate determination of the ratios of metals present in both meteorites and the atmosphere is amongst the best evidence for meteoric ablation (17) and these theories are wholly supported by CABMOD, the meteor ablation model designed by Vondrak *et al*. (30). The model not only supports the theory but explains anomalies such as the low relative atmospheric abundance of Ca in terms of Ca ablation's heavy dependence on meteor entrance velocity (30). Si, Mg and Fe ablated from meteors react quickly with atmospheric species, particularly $O_3$, $H_2O$ and $CO_2$. They are then likely to recondense to form meteoric smoke particles (MSPs), nanometre sized particles which probably act as ice nuclei in the formation of noctilucent clouds in the summer polar mesosphere or condensation nuclei for sulphate particles in the lower stratosphere (31).

Observations show significant seasonal variation in the concentration and thickness of these metallic layers (Figure 1.5) (7, 17, 32). Lidar and satellite observations have

been made for periods greater than a year, and the layers have been found to exhibit seasonal variation (33, 34). The Fe and Na layers show an early winter maximum and a mid-summer minimum in concentration whereas the K and Ca layers show a semi-annual variation with a second maximum in mid-summer. Reservoir species (such as $NaHCO_3$, $FeOH$ and $FeO_3$) account for the summertime minima of the Na and Fe layers through recycling back to their atomic metal by reactions with a positive temperature dependence. Consequently, they are recycled less efficiently during summer (7).
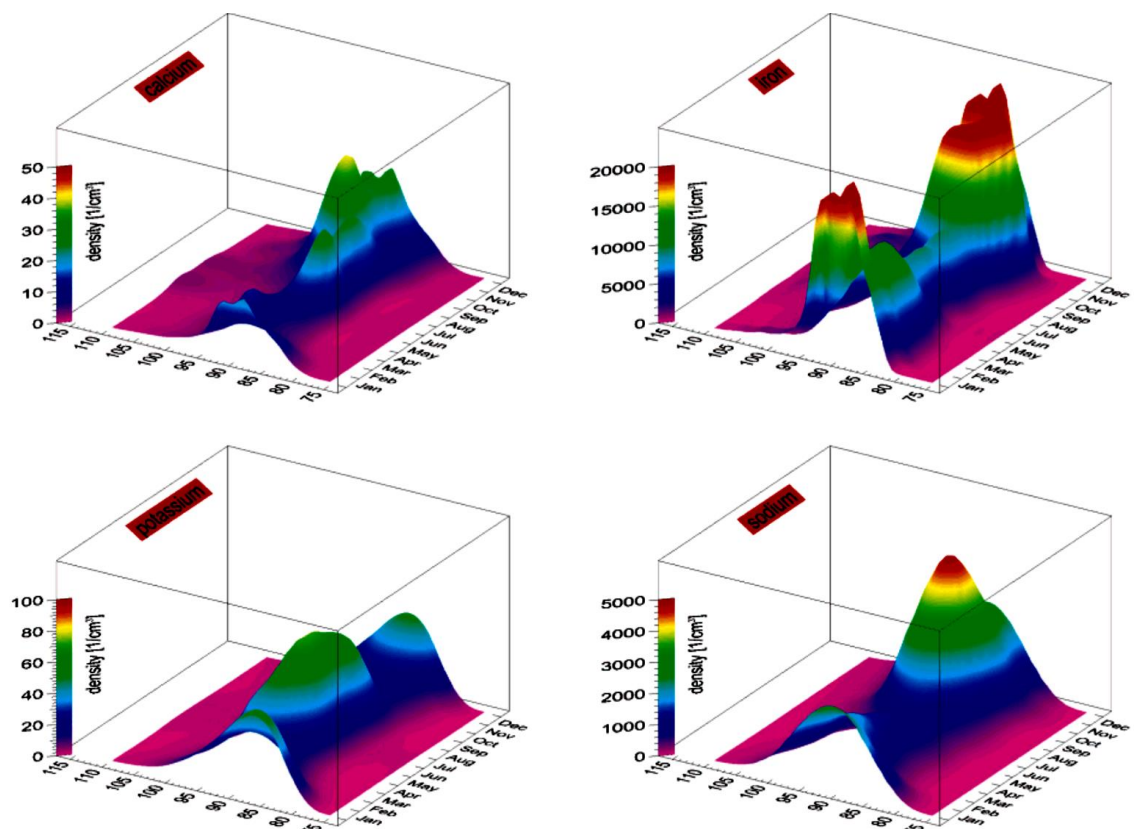


**Figure 1.5.** Three-dimensional mesh plots of the seasonal variation of the Fe, Ca, K and Na layers as measured by lidar at mid-latitudes. Reproduced from Plane (2003).

### 1.3.2  Ablation Theory and Modelling

The major metallic constituents of cosmic dust particles by elemental atomic abundance are: Mg (14.4 %), Si (13.6 %), Fe (12.1 %), Al (1.2 %), Ca (0.82 %) and Na (0.80 %) (35). These cosmic dust particles typically have a mass between 5 and 50 μg (density of 2000 kg m$^{-3}$) (27) however, the total range of meteoric mass spans over 30 orders of magnitude. No instrument currently exists which is capable of observing particles over the entire mass range (12). This contributes to the significant uncertainty in the range of the average daily input of cosmic dust into Earth's atmosphere.

Ablation theory describes the process through which particles entering the atmosphere at high velocity are subject to frictional heating resulting in the sublimation of metallic species from that species surface. Upon entering the MLT at high velocity, meteoric species consisting of micron-sized particles undergo rapid frictional heating upon collision with air molecules  (36). This raises their temperatures to over 1800 K, at which point they melt. This causes ablation and the constituent elements are deposited in the MLT. The unablated particles fall to the ground as micrometeorites (7, 16, 30).

Meteoroids have a mean entry velocity of about 20 km s$^{-1}$. Entry velocities range from 11.5 to 72 km s$^{-1}$ for particles in prograde and retrograde Earth orbits, respectively (37).

Meteoroids are currently assumed to have the same composition as ordinary chondrites, although it may be the case that meteoroids which ablate in the upper atmosphere are of different composition to those which survive transit to the Earth's surface (38). Differential ablation infers that different metals are released at different times along the meteor's path through the atmosphere and also accounts for the different abundances of metals in the atmosphere compared with their abundances in meteorites.

Differential ablation occurs because different metals have varying volatilities (7). More volatile metals such as Na and K are more likely to ablate sooner in the meteor's flight than the less volatile Mg, Fe and particularly Ca (30). The correlation

between the abundances of metallic species in meteors and those observed in the atmosphere and during meteor showers largely supports this theory. In the atmosphere Ca is depleted in comparison with Na, despite the two metals having a similar abundance in meteorites (16, 17). A differential ablation model based on fractation has been reasonably able to explain the depletion of Ca to Na observed in meteor trails (30). The Chemical Ablation Model (CABMOD) developed by Vondrak *et al*. (27) describes: sputtering by inelastic collisions with air molecules before the meteoroid melts; evaporation of atoms and oxides from the molten particle (assuming thermodynamic equilibrium between the molten meteoroid and the vapour phase); diffusion controlled migration of volatile constituents; and impact ionisation of ablated fragments by hyperthermal collisions with air molecules (27).

### 1.3.3 Atmospheric Phenomena Involving Meteoric Metals

### 1.3.3.1 Sporadic Layers

Some metallic ions, primarily $Mg^+$ and $Fe^+$, form sporadic E layers which are thin layers of concentrated plasma between 1 and 3 km thick occurring at altitudes between 85 and 140 km (17), in the ionosphere. Metal ions have long lifetimes at these altitudes as they are monoatomic and hence dielectric recombination is slow. This allows sustained $E_s$ layers to form which are noted as being responsible for phenomena such as severe interference to short wave radio waves, obscuring space to ground communication (17).

Sporadic neutral metal ($N_s$) layers are highly concentrated thin layers of neutral metal atoms. $N_s$ layers have been observed in Na, Fe and Ca and are usually < 2km thick, most commonly occurring at altitudes between 90 and 100 km. $N_s$ layers are roughly Gaussian in shape and are superimposed over a background layer of the same metal at a concentration 2 – 20 times greater (39). One proposed theory on the formation mechanism of these layers suggests they are formed by the neutralisation of metallic ions in descending $E_s$ layers (40). The rate of

neutralisation of these ions is very slow; however, they can also undergo dissociative electron recombination with cluster and molecular ions which is a much faster process.

### 1.3.3.2 Airglow and Aurorae

The airglow is an atmospheric phenomenon in which a faint continuous glow consisting of atomic and molecular emission lines and bands from species above 80 km observable at all latitudes. Aurorae are a similar phenomena occurring at similar altitudes. Unlike the airglow however, aurorae can be very bright and predominantly only occur at high altitudes (41).

Airglow is generated through a chain of events which begins with the dissociation of molecules by daytime solar UV radiation (41) followed by chemical reactions that produce excited states of atmospheric species (usually oxygen) resulting in the emission of a photon. Spectrally, airglow gives a weak continuum in the blue and the green from the $O_2$ Herzberg bands and $NO_2$ emissions respectively. Additional stronger emissions arise predominantly from neutral atomic oxygen and hydroxyl radicals (42). The sodium $D$-line of the airglow is of particular interest due to the unexpected $D_2/D_1$ ratio which has also been observed in persistent meteor trains (7).

Auroral excitation however, results from molecular collisions with energetic particles (predominantly electrons) which originate from the solar wind and have been directed along the Earth's magnetic field lines. Like airglow, these collisions result in a host of emission lines. Emission in the blue region results from collisions with molecular nitrogen molecules, exciting them to $N_2^+$. While in the green region, the brightest emission originates from atomic oxygen. This occurs from the transition from the $O(^1S)$ state to $O(^1D)$. Finally, the red line is occasionally visible in the upper border of strong auroral arcs. Again, this is emitted by atomic oxygen although this time from the transition from $O(^1D)$ to $O(^3P_2)$ (42).

### 1.3.3.3 Meteoric Smoke

It is estimated that approximately 70 % of incoming meteoric material ablates between 70 and 110 km. This ablation produces vapour which condenses to form meteoric smoke particles (MSPs). MSPs generally have a radius between ~0.2 and 1.0 nm and are likely to consist of metallic species polymerised with silicon oxides. Following their formation the particles settle downwards in the atmosphere, residing in the stratosphere and mesosphere (43). MSPs have been directly observed in the atmosphere above 70 km using rocket-borne particle detectors (44).

Whole atmosphere circulation models predict that below 80 km, MSPs get caught in the mean meridonal circulation in the mesosphere and are transported to the winter pole before travelling to the polar vortex and being transported downwards to the lower stratosphere (45). This causes a strong seasonal pattern in MSP concentration where no particles are observed at the summer pole. Recent airborne measurements have revealed a 3-fold increase of the meteoritic content of stratospheric sulphate aerosol inside the winter Arctic vortex (46). During the months which MSPs spend in the mesosphere and upper stratosphere, the particles are likely to grow by agglomerative coagulation. This can be very rapid because of the long-range magnetic dipole forces between the Fe-containing particles (45). Furthermore, model predictions suggest that that the particles could grow to around 40 nm in radius by the time they reach the middle stratosphere around 30 km (46).

A laboratory study conducted by Saunders *et al.* (45) showed that amorphous Fe-Mg-silicate particles dissolve in concentrated $H_2SO_4$ solutions at temperatures around 230 K (typical lower stratospheric temperatures) on a time scale of less than a week. Consequently, an observed decrease in the concentration of $H_2SO_4$ in the upper stratosphere could potentially be attributed to removal by reaction with metal rich MSPs. Solid particles such as MSPs act as efficient heterogeneous nuclei. Additionally, the surface recombination of $H_2$ and O on MSPs is thought to be responsible for an enhanced $H_2O$ vapour layer at around 70 km (47).

### 1.3.3.4 Noctilucent Clouds

MSPs that have a radius > 1 nm may act as ice nucleation species (47). This process of the nucleation of ice particles results in the formation of noctilucent clouds (NLCs). NLCs are ice clouds which exit in the mesosphere between ~80 – 86 km. This is a relatively recently discovered phenomenon having first been reported in 1885. Because NLCs are relatively thin clouds they are usually only observable at high latitudes during twilight hours where the observer is in darkness but the clouds are sunlit. NLCs resemble high cirrus clouds and are commonly observed as pale blue, because of absorption by ozone in the path of sunlight forward scattered from the cloud.

Infrared measurements show the main component of NLCs to be water ice. Understanding the nature of the ice nuclei is an important uncertainty when studying NLCs. This is because changes to the dominant meridional circulation in the mesosphere may affect the concentration of these nuclei, which in turn could affect the frequency and brightness of the clouds (45). NLCs require a stringent set of conditions to facilitate their formation. The nucleation species must be present at very cold temperatures and then fall into contact with water vapour (which is only present in a few ppm in the region). NLCs most commonly form in the summer months when the mesosphere is coldest in the polar regions (47). Because the mesosphere is dry, very low temperatures are required for the water frost point to be reached. The mesospheric meridional circulation results in upwelling air during the summer, which cools adiabatically leading to low temperatures. This transport effect also results in an increase in water vapour concentration (45).

Electronic structure calculations have been used to demonstrate that the smallest MSPs which should act as ice nuclei are the metal silicate molecules $FeSiO_3$ and $MgSiO_3$. This is because $MgSiO_3$ and $FeSiO_3$ have extremely large electric dipole moments so that $H_2O$ molecules bind to them with large negative free energies. The hydration thermodynamics indicate that ice nucleation should occur at a

temperature around 140 K for a $H_2O$ mixing ratio of 4 ppm, typical of the polar summer mesosphere where NLCs form (48).

NLCs are thought to be indicative of climate change.  Since their initial observation the clouds have been observed to be increasing in brightness and spreading to lower latitudes. Occurrences of NLCs have recently been shown to be increasing in frequency (49), something which had previously been contested (50). Increased greenhouse emissions lead to mesospheric cooling, which may be a cause of this (49). It has also been suggested that increased sightings of NLCs suggest a higher presence of water in the upper atmosphere. This may be due to methane being driven higher into the mesosphere where it is photolysed and reacts to form water (50).

## 1.4  Long-Lived Fluorinated Gases in the Atmosphere

The Pauling periodic scale of electronegativity places fluorine as the most electronegative element in existence with a score of 3.98. Because of this, it is not commonly found in its pure, gaseous form and when it is broken down it reacts very quickly to form new, very stable compounds (51).

Fluorine accounts for 0.65 % of the Earth's crust making it the 12th most abundant element. In the atmosphere it is found in the form of natural or man-made, organic and inorganic compounds. Prior to the 1960s, fluorinated gases were only known to be organic and originate from natural sources. These gases are broken down in the atmosphere into fluoride radicals which then react to form inorganic fluorides. (51).

### 1.4.1  Introduction of $SF_6$, $NF_3$, CFC-115 and $SF_5CF_3$

Species which are released into the atmosphere naturally undergo processes which remove or convert them into other products. This typically occurs by oxidation or photolysis reactions (52). The potentially devastating effect of species such as hydrofluorocarbons (HFCs), chlorofluorocarbons (CFCs) and perfluorocarbons

(PFCs) in the atmosphere has long been documented, leading to many species being inventoried through acts such as the Kyoto and Montreal Protocols (53). The Kyoto Protocol to the United Nations Framework Convention on Climate Change (UNFCCC) outlined an international agreement on emission reductions based on scientific research conducted by the Intergovernmental Panel on Climate Change (IPCC). Plans to reduce known natural greenhouse gases were introduced and, for the first time, several synthetic halogenated gases including CFCs and PFCs were acknowledged and prohibited (53, 54). Not included in the list was $NF_3$ and as such it has experienced an increased usage. This being due to it being implemented in several of the processes previously requiring the banned gases (54). The species outlined here provide a major environmental concern not only due to their greenhouse effect but, in the case of CFCs, their powerful effect on stratospheric ozone.

Although these gases are usually considered to be entirely anthropogenic in origin, research has suggested that there may be natural, primarily volcanic sources of several halogenated greenhouse gases (55). Experimentation carried out by Jordan *et. al* (55) has indicated that the upper limit for the atmospheric concentration of such fluorinated gases from volcanic sources is negligible when compared to a typical ambient air concentrations (55, 56).

Table 1.2 below summarises some of the fundamental physical properties of $SF_6$, $NF_3$ and CFC-115. Understanding these properties can in some cases provide clues to likely and relative behaviour in the atmosphere. For example, the $NF_2$-F bond in nitrogen trifluoride is relatively weak at approximately 139 kJ mol$^{-1}$ (57). This is significantly lower than other similar fluorine compounds, including $SF_6$ which has a bond energy of 389 kJ mol$^{-1}$ (57). This may consequently indicate that $NF_3$ may be potentially more reactive and prone to dissociation or photolysis.

| Molecule | Melting point /K | Boiling point /K | Liquid density / g mL$^{-1}$ | Heat of Formation / kJ mol$^{-1}$ | Dipole moment / Debye | Bond energy / XF$_a$-F kJ mol$^{-1}$ |
|---|---|---|---|---|---|---|
| SF$_6$ | 222 | 480 | 1.33 | -1220 | 0 | 387 |
| NF$_3$ | 66 | 143 | 1.53 | -131 | 0.23 | 139 |
| CFC-115 | 174 | 233 | 1.22 | -1114 | 0.52 | 109[a] |
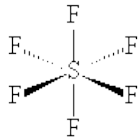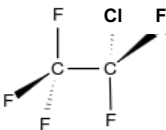
[a] XF$_a$-Cl bond energy

**Table 1.2** comparison of the physiochemical properties of SF$_6$, NF$_3$ and CFC-115 (57).

Industrial deposition processes such as chemical vapour deposition (CVD) and physical vapour deposition (PVD) have become increasingly common over the last few decades due to the rise of the semi-conductor and photovoltaic industries. This rise is attributed to an increased demand for integrated circuits and thin film transistor displays (82). The manufacturing process of these items require cleaning of their reactor chambers so that the purity of the deposited product can be maintained. Previously, this was done through manual scrubbing and dry etching by use of PFCs. F radicals resulting from thermal decomposition of the PFCs would react with deposited Si residues left by the processes to form gaseous SiF$_4$ which can then be vented:

$$Si_{(s)} + 4F^{\cdot}{}_{(g)} \rightarrow SiF_{4\,(g)} \qquad\qquad (R1.15)$$

With increasing demand from industry and the implementation of the Kyoto Protocol, principal etchers were switched from PFCs (including $SF_6$), to $NF_3$ which dissociates more easily and thus makes for a more efficient etchant with lower emissions. $NF_3$, despite being a significant global warming agent itself, has consequently become the principal chemical cleaner in the last 15 years (58-60).

There are several reasons why the atmospheric impact of $NF_3$ may have been overlooked in making these decisions: a lack of research specific to $NF_3$; and the industrial convenience of the species outweighing the likely problems, leading to a consequent reluctance to research into them.

CFC-115 was the first species studied here to be banned. It was controlled under the 1997 Montreal protocol due to its ozone depleting potential. Prior to this, it had been used as a commercial refrigerant and foam blower (61).

Since 2007, $SF_6$ has been banned as a chemical etchant and in all other applications with the exception of high-voltage switchgears under the 2007 Montreal protocol. Attempts to control emissions in such industrial processes include means such as process gas recycling. Employment of remote plasma sources to dissociate gases prior to entering the reaction chamber have also reportedly contributed to the decline as well as smaller scale efforts such as cylinder refill leakage and venting capture (59). General efforts to repair leaks at the Princeton Plasma Physics Laboratory where $SF_6$ is used as a high voltage insulator, have reportedly achieved a reduction in total annual emissions of approximately 65 % (62).

85 % of industrial processes using $NF_3$ release < 2 % of their emissions into the atmosphere. The remaining 15 % of processes release 30 %, where this latter value largely represents processes being phased out (63). Although production of $NF_3$ is rising by a dramatic 41 % per year, its emissions have only increased by around 11 % (64). Consequently, expressing $NF_3$ concentration in the atmosphere as a function of global production shows a decline in emission factor. Following reports of a decline in emissions from major manufacturers it has been suggested that this

decrease is due to the increased efficiency of $NF_3$ destruction in industrial processes, and the phasing out of higher emission applications (59).

## 1.4.2  Observations in the Atmosphere

The method by which a trace gas can be detected and measured in the atmosphere is somewhat dependent on its atmospheric burden and the sensitivity of potential instruments. The measurement of trace gases requires direct measuring by either in-situ or remote sensing methods. Many of these species, including the PFCs studied here, have strong absorption in the near to mid infrared (IR) region. This means that changes in their concentration affects the absorption and re-radiation of long wave terrestrial radiation: a feature which could potentially lead to significant climatological problems, but can also be used to detect their presence in the atmosphere (65).

The majority of passive trace gas remote sensing uses moderate to high spectral resolution (< 0.1 - ~ 1 nm) instruments such as SCIAMACHY described in Section 1.3.1.2 (25, 66). This allows gas identification via their spectral fingerprints, minimising water vapour and aerosol interference  compared to lower resolution instruments.

The IR absorption lines of the PFCs in this study can be probed by narrow spectral laser radiation using light detection and ranging (lidar) instrumentation. This allows for accurate remote measurements of concentrations within ranges of several meters to tens of kilometres (67). The primary type of lidar employed for making atmospheric measurements is inelastic scattering Raman lidar although elastic scattering differential absorption lidar is often employed.  Raman lidar involves detecting transmitted laser radiation which has been shifted in wavelength due to interaction with scattering molecule. This is known as the Stokes shift and is equal in energy to a vibrational-rotational or rotational transition.  This shifted signal has backscattered power proportional to the concentration of the scattering molecule. This means that an advantage of the technique is that it offers a direct measurement of the species concentration however, the Raman backscattering

signal is relatively weak and elastic backscattering signal may be as much as three orders of magnitude stronger .

Additional methods of detection may involve either obtaining air samples at various locations and analysing them later, or analysing stored historic samples in a lab. Techniques used to test for the presence of these gases in samples include infrared spectroscopy as described in Chapter 2, and gas chromatography where gases can be identified by a specific peak or residence time. Gas chromatography techniques can incorporate various detection methods such as mass spectrometry (GC-MS) (65).

Atmospheric $SF_6$ measurements have been obtained by Krieg *et al.* at three Northern hemisphere locations: Ålesund in Norway at 79° N; the Jungfraujoch observatory in Switzerland at 47° N and the Kitt Peak observatory in Arizona at 32° N: between 1993 and 2002 (31). The infrared solar absorption spectra from all three stations were recorded with similar Michelson-type FTIR spectrometers. The averaged measurements from the three locations indicated a 2002 global mean tropospheric mixing ratio in the region of 2.80 ppt, increasing by approximately 0.22 ppt $yr^{-1}$ (31).

As discussed in the previous section, global production of $NF_3$ is thought to have grown by an average of 41% a year since 1995, reaching 2,300 tonnes in 2006 and 7,200 tons in 2008 (63). For the period 1953 – 1994, estimates of these values were based on annual industrial production and release estimates which were converted to concentrations by scaling cumulative release quantities for each year to modern measurements. The atmospheric concentration prior to 1953 was assumed to be zero (55). Measurements conducted by Ehhalt *et al.* in 2001 found the estimated concentration of $NF_3$ in the troposphere to be 0.45 pptv (65).  Field measurements of $NF_3$ have also been obtained at two NH locations,  between 1998 and 2008 at Trinidad Head in Northern California (41° N), and between 1978 and 1991 at La Jolla in Southern California (33° N). The locations were chosen due to the high integrity of previous measurement of similar gases modelled against known trends and were measured by gas chromatograph/ mass spectrometer. The data showed a quasi-exponential growth over the measured time period and yielded a July 1 2008

mean global tropospheric concentration of 0.45 ppt (5,380 tons) increasing at a rate of 0.053 ppt $yr^{-1}$ or, 11% annually (31, 63).

CFC-115 measurements were gathered by Reimann *et al.* (68) at the Jungfraujoch observatory in Switzerland. Measurements were obtained quasi-continuously by GC-MS since early 2000. The background concentration of CFC-115 was determined to be 8.0 ppt with no observable change in concentration over the measured period. Since CFC-115 was banned in January 1996, its emissions have fallen drastically, although no downward trend in concentration has yet been observed. This is due to the very long atmospheric lifetime of CFC-115, estimated to be 1,700 years (68).

An often over-looked consideration is the fate of the by-products from the decomposition of halogenated species in industrial processes. It is speculated that such reactive radicals may react again to form new species such as $SF_5CF_3$. Increasing parallel trends with the suspected source gases are the strongest indicator of such secondary reactions (69). The trends of $SF_6$ and $SF_5CF_3$ have tracked each other very closely between the late 1960s until around the year 2000. This is demonstrated in Figure 1.6. $SF_5CF_3$ is not present in pure samples of $SF_6$ and consequently it has been speculated to originate as a by-product of $SF_6$ manufacture (70). Another theory is that electrical breakdown in the high-voltage equipment where $SF_6$ and fluoropolymers are used forms $SF_5$ and $CF_3$ radicals which recombine via the following reaction:

$$SF_5 \; + \; CF_3 \; \rightarrow \; SF_5CF_3 \tag{R1.16}$$

The estimated ratio of $SF_5CF_3$ to $SF_6$ is 1:32, indicating a low overall atmospheric concentration (70).
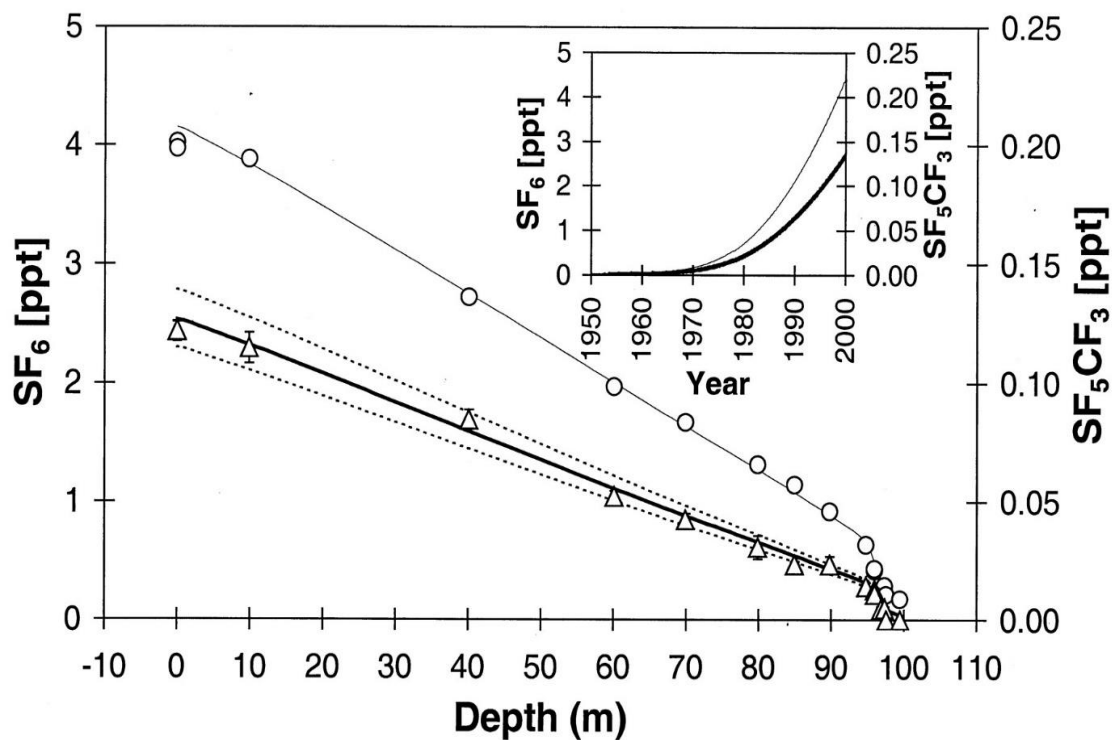
**Figure 1.6:** Graph representing growth trends of both SF$_6$ (circles) and SF$_5$CF$_3$ (triangles) where measurements in air were extracted from firn at Dome Concordia, Antarctica, in January 1999 and firn modelling (SF$_5$CF$_3$, thick solid line; SF$_6$, thin solid line) of expected depth profiles based on the atmospheric scenarios shown in the inset. The dotted lines shown for SF$_5$CF$_3$ denote concentrations that are ± 10 % of the modelled line. Reproduced from Sturges *et al.* (70).

Despite the rate of increasing background concentration of both SF$_6$ and SF$_5$CF$_3$ being almost identical until around the year 2000, more recent measurements have shown that whilst the trend in increasing mixing ratio of SF$_5$CF$_3$ has halted, SF$_6$ continues to rise. The mixing ratio of ~ 0.14 ppt obtained in 2012 falls short of the model projected 2012 value based on the rate of increase measured in 2000 of ~ 0.16 ppt (71). Instead, SF$_5$CF$_3$ was determined to be generated as a by-product of fluoro surfactant manufacture. Model runs determined that in order to reach the rapid decline in atmospheric growth rate observed, emissions would have had to halted abruptly between 2000 and 2003, which coincides with the phase out of this industry (71).

## 1.5  Atmospheric Lifetimes

A complex series of reactions occur throughout the atmosphere. These are defined by the surrounding physical and chemical conditions which govern each layer. An accurate quantification of the lifetime of long-lived ($\tau$ > ~5 years) anthropogenic gases emitted into the atmosphere is essential for assessing their ozone depletion and climate impacts. Lifetimes are also necessary prior knowledge for quantifying top-down emission estimates. In calculating the projected lifetime of an atmospheric species we consider its sources and sinks. A source is defined as a species' method of input into the atmosphere either by natural or man-made ground sources or, secondarily as a by-product of another reaction. A sink is defined as a permanent removal mechanism.

The atmospheric lifetime ($\tau$) of a long-lived trace gas can be defined as the ratio of its global atmospheric burden to its annually averaged global loss rate. Loss processes vary at each level of the atmosphere but usually include reactions with various oxygen-bearing gases, hydrogen, electrons, thermolysis and photolysis, primarily by Lyman-$\alpha$ radiation. Some fractions are also removed by other processes such as high temperature combustors at ground level, lightning, and by uptake by plants, soil and oceans (52).

The various sinks dominating species in each region of the atmosphere are summarised below in Figure 1.7.
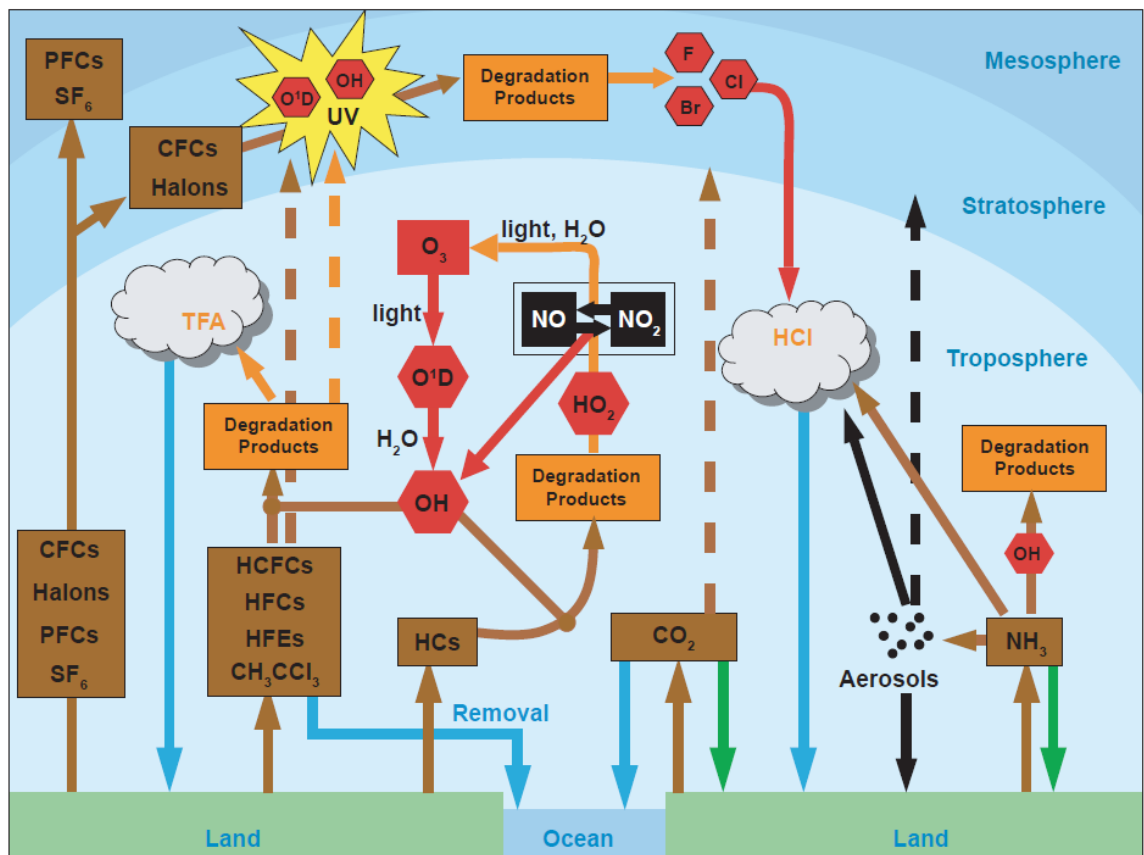
**Figure 1.7.** Summary of the rate determining loss processes affecting major greenhouse gases at each level of the atmosphere. Reproduced from IPCC 4th Assessment (72).

The concentration of a greenhouse gas in the atmosphere depends on the rates of the emission of that gas into the atmosphere, and the rates of its sink processes. For example, the sources and sinks affecting carbon dioxide are well understood. $CO_2$ is exchanged between the atmosphere, the ocean and the land through systems such as atmosphere-ocean gas transfer as well as chemical (e.g., weathering) and biological (e.g. photosynthesis) processes. Currently, about 57 % of human-emitted $CO_2$ is removed from the atmosphere within a century while around 20 % remains in the atmosphere for several millennia (73). Because the rates of its relative sinks are comparatively slow, atmospheric $CO_2$ will continue to increase in the long term even if its emission is substantially reduced from present levels. The adjustment of species concentrations in the atmosphere to reductions

in emissions depends on the chemical and physical processes that remove each gas from the atmosphere.

Atmospheric methane is removed by chemical reactions, primarily reaction with hydroxyl radicals in the troposphere and stratosphere (74). Atmospheric nitrous oxide and some chemically stable halogenated compounds like CFC-115 or $NF_3$ are assumed to be destroyed in the mesosphere/ upper atmosphere by energetic solar radiation. These processes operate at different timescales ranging from years to millennia.

The calculated lifetime of a gas can vary significantly depending on the identification of the dominant removal process. For example, in the case of $SF_6$, photo-dissociation by UV radiation at $\lambda < 240$ nm, was assumed to be the species' dominant removal process in the mesosphere. This gives a calculated atmospheric lifetime between 1000 and 13,500 years. However, when electron attachment reactions were considered as the dominant removal process, this lifetime range fell to between 800 and 4200 years (75).

### 1.5.1  Mesospheric Sinks

Most chemicals released into the atmosphere react with oxidants or are photolysed by radiation at wavelengths ($\lambda > 190$ nm) in the troposphere and stratosphere. However, due to the high stability and consequent long-lifetimes of PFCs, their chemistry in the lower atmosphere is assumed to be insignificant (52).

When lifetimes of species approach ~ 300 years  loss processes in the mesosphere and thermosphere start to become rate determining, with their concentrations becoming increasingly sparse with altitude as chemical destruction through mesospheric sinks increases (52). This is the case for the PFCs studied here. For example, age-of-air studies of $SF_6$ in the winter polar vortex show that it experiences significant removal in the mesosphere (56). However, because the mass of the mesosphere is a small fraction ($< 10^{-3}$) of the whole atmosphere, the efficiency of mesospheric removal depends on the turnover time of air in the mesosphere through residual circulation along with turbulent vertical diffusion of

the trace species. A 1D model designed by Plane (7) describing the effects of vertical transport characterised by an eddy diffusion coefficient (ranging from 4000 $cm^2 s^{-1}$ in the lower stratosphere to $2 \times 10^5$ $cm^2 s^{-1}$ at 85 km) indicates that a compound which is removed rapidly above ~70 km will have a lifetime approaching 400 years.

The major sinks in the MLT include photolysis by solar Lyman-α radiation at λ = 121.6 nm, reactions with $O(^1D)$, OH and H or destruction by electron attachment (52, 76). Where mesospheric sinks dominate, atmospheric lifetime is dependent on photochemistry and transport processes because these control the transfer rate to the mesospheric loss region. Atmospheric models have found the net reduction in the mixing ratios of several long lived gases to be < 5% when accounting for major reactions and loss routes across the stratosphere, mesosphere and lower thermosphere (52). Additionally, in the case of $SF_6$, mesospheric loss processes when unaccounted for can lead to an overestimation of lifetime by as much as 65% at subarctic latitudes (77).

Photolysis by solar Lyman-α radiation is a dominant loss process in the mesosphere. Radiation penetrates below 80 km due to a "hole" in the absorption spectrum of the Schumann-Runge continuum of $O_2$, whereas other wavelengths ≤ 180 nm are severely attenuated (53).
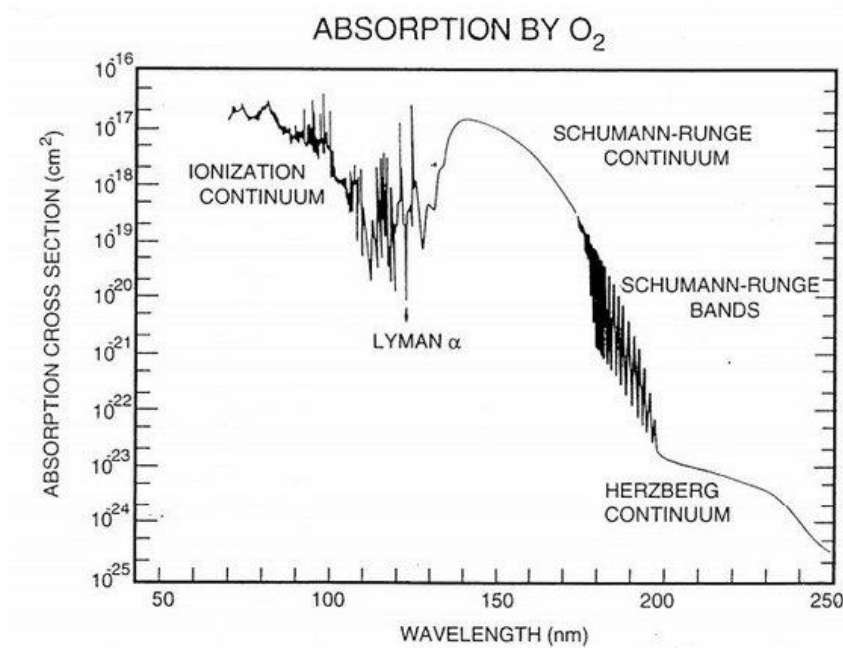
**Figure 1.8.** Absorption spectrum of molecular oxygen. The Lyman- α line is visible at 121 nm over the hole in the spectrum. Reproduced from Brasseur and Solomon (9).

Electron attachment plays a significant role on the lifetime of $SF_6$. This involves the attachment of an electron to $SF_6$, leaving it in the excited state, $(SF_6^-)^*$. This process, along with the other sinks of $SF_6$ as summated by Reddmann *et al.* (82) are shown in the scheme below:

$$SF_6 \quad \overset{e^-}{\longleftrightarrow} \quad (SF_6^-)^* \quad \rightarrow \quad SF_6^- \quad \overset{H,HCl}{\longrightarrow} \quad HF + SF_5^-$$

$$hv \downarrow \qquad \searrow e^- \qquad\qquad\qquad\qquad \downarrow hv, \text{charge transfer}$$

$$SF_5 + F \quad SF_5^- + F \qquad\qquad SF_6 + e^-$$
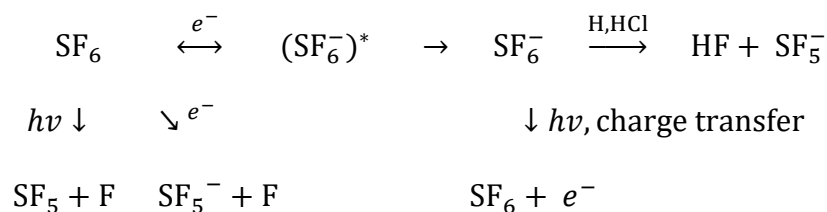
As the electron density in the upper mesosphere is significant, electron attachment to $SF_6$ is thought to dominate and has been considered rate-determining. However, removal by other species may dominate in the lower mesosphere where the electron density is less (75). This makes accurate determination of atmospheric electron density measurements a further consideration when calculating

atmospheric lifetime. In contrast, this sink is insignificant for $NF_3$ and its rate is slow, approximately $4.10 \times 10^{-13}$ $cm^3$ molecule$^{-1}$ s$^{-1}$ (78).

One mesospheric process which does not appear to have been considered previously is removal by the metallic atoms deposited by meteoric ablation (7). The three most abundant metals are Fe, Na and Mg, which occur in layers between ~75 and 105 km. The peak concentrations of Fe, Na and Mg are ~10,000, 5,000 and 3,000 $cm^{-3}$, respectively, and the layers exhibit little diurnal variation. However, in order to compete with Lyman-$\alpha$ photolysis (a daytime only process), the rate coefficients would need to be greater than ~$5 \times 10^{-12}$ $cm^3$ molecule$^{-1}$ s$^{-1}$.

## 1.6 Radiative Forcing and Global Warming Potentials

The long atmospheric lifetimes of fluorinated gases means that it is important to assess the potential impact of accumulative and future emissions which are calculated by radiative forcing (RF), a measure of externally imposed perturbations to the radiation budget within the atmosphere induced by changes in concentrations of greenhouse gases and aerosols, solar energy and the albedo (60, 79). In this study, radiative forcing refers to a perturbation of modern day concentration of the PFC against its pre-industrial concentration and is given in units of Wm$^{-2}$. Radiative efficiency refers to a perturbation of $0 - 1$ ppb and is given in units of Wm$^{-2}$ ppbv$^{-1}$.

The understanding of anthropogenic warming and cooling influences on climate has improved in recent years and the IPCC report that the effect of human activities since 1750 has resulted in a net positive forcing between +0.6 and +2.4 Wm$^{-2}$ (72). The effect on this range of individual forcing agents is shown below in Figure 1.9. Of this, very long-lived greenhouse gases, such as those explored in this study, account for a positive net forcing range of +2.63 ± 0.26 Wm$^{-2}$, which is the dominant radiative forcing term and has the highest level of scientific understanding. In contrast, the total direct aerosol, cloud albedo and surface albedo effects that contribute negative forcings are less well understood and have

larger uncertainties. The range in the net estimate is increased by the negative forcing terms, which have larger uncertainties than the positive terms.
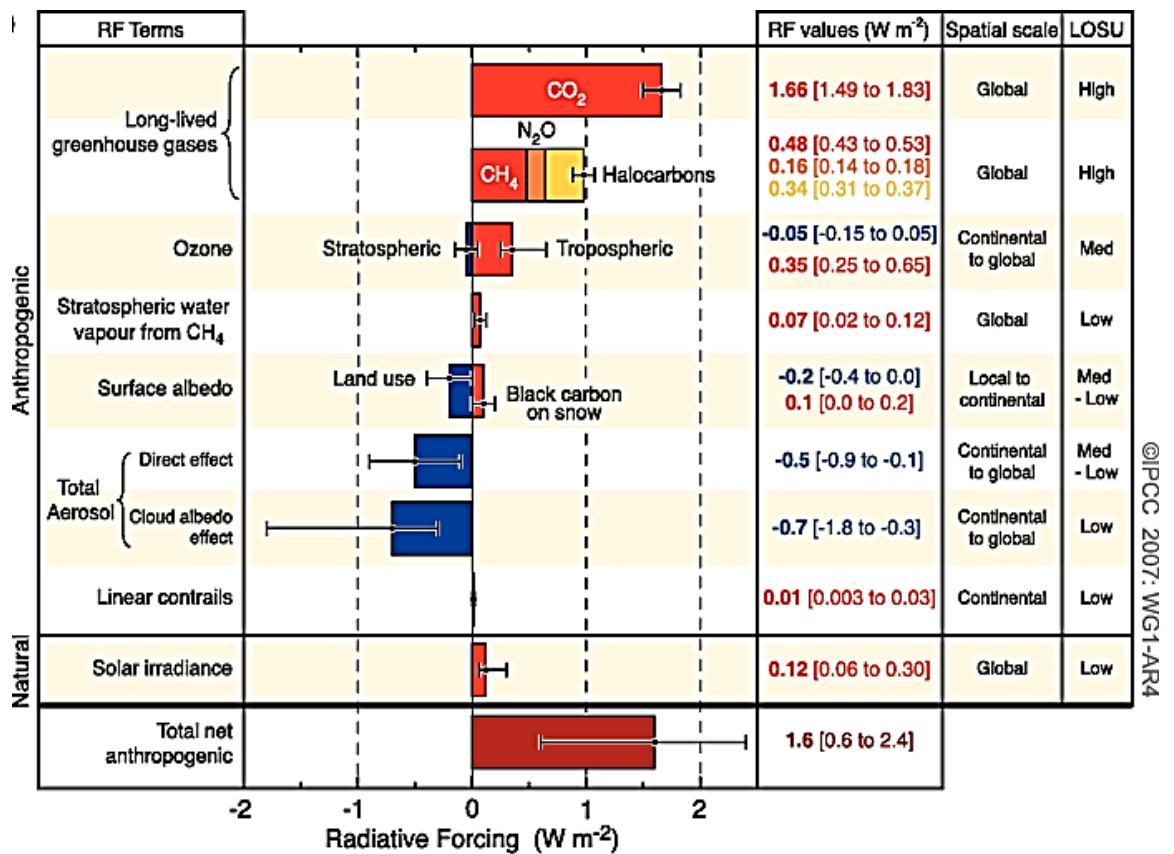


**Figure 1.9.** Global mean RFs and their 90% confidence intervals in 2005 for various agents and mechanisms. The net anthropogenic radiative forcing and its range are also shown. Volcanic aerosols contribute an additional form of natural forcing but are not included due to their episodic nature. Reproduced from the IPCC (72).

International agreements on greenhouse gases such as the Kyoto protocol employ metrics to compare different gases and place them on an equivalent footing. The 100-year Global Warming Potential (GWP) is generally used as the primary metric, although 20 and 500 year GWPs are also commonly used. GWP is a useful metric for comparing the potential climate impact of the emissions of different long-lived greenhouse gases. GWPs compare the integrated radiative forcing over the specified period from a unit mass pulse emission and are a way of comparing the potential climate change associated with emissions of different greenhouse gases.

There are well-documented shortcomings of the GWP concept, particularly in using it to assess the impact of short-lived species. Further definition and detail for RFs and GWPs are discussed in Chapter 4.

## 1.7     Motivations for Research

The long lived PFCs discussed in this chapter are all potent greenhouse gases. For these gases mesospheric loss processes, which are usually ignored or treated very crudely, could significantly reduce their atmospheric lifetimes, thereby decreasing their estimated climate impact. The reactions of these gases with metallic atoms (Fe, Na, K and Mg) in the upper mesosphere could be an important additional sink. In order to ascertain whether these reactions compete with Lyman-$\alpha$ photolysis, these cross-sections are also measured here.

In summary, the main questions addressed in this study are:

- What are the current best estimates of atmospheric lifetimes and GWPs for $SF_6$, $NF_3$ and CFC-115?

- For these very long lived species, will the newly determined rates of mesospheric sinks decrease their lifetimes and hence GWPs?

## 1.8     Thesis Structure

Chapter 2 describes the experimental techniques used to study the reactions of the metal species: Na, K, Fe and Mg with the perfluorinated species $SF_6$, $NF_3$ and CFC-115.  The specific reactions are described within the chapter.

Chapter 2 also describes the methods used to measure the Lyman-$\alpha$ and infrared absorption cross-sections of the greenhouse gases $SF_6$, $NF_3$ and CFC-115.

The kinetics of each of the reactions measured are explored through electronic structure calculations and are presented alongside their experimental results in

Chapter 3. These results are also discussed in terms of their relevance to the mesosphere.

Chapter 4 outlines the various models and methods used to determine atmospheric lifetimes, radiative forcings and global warming potentials from the experimental results discussed in the previous chapter. The atmospheric implications of these findings are discussed in Chapter 5.

Finally, conclusions, a brief summation and discussion of future work are given in Chapter 6.

# List of References

1.      Wayne, R.P. *Chemistry of Atmospheres* Third ed. Oxford: University Press, 2006.

2.      Chamberlain, J.W. *Theory of Planetary Atmospheres: an Introduction to their Physics and Chemistry* [online].  London: Academic Press Inc., 1978.

3.      Sander, S.P., J. Abbatt, J.R. Barker, J.B. Burkholder, R.R. Friedl, D.M. Golden, R.E. Huie, C.E. Kolb, M.J. Kurylo, G.K. Moortgat, V.L. Orkin and P.H. Wine. *Chemical Kinetics and Photochemical Data for Use in Atmospheric Studies; Evaluation No. 17, JPL Publication 10 - 6.* Pasadena, CA: Jet Propulsion Laboratory, 2011.

4.      Cvetkovic, V., P. Martinet, C. Baresel, G. Lindgren, A. Nikolic, S. Molin and C. Carstens. *Environmental Dynamics: An Introduction to Modeling Anthropogenic Impact on Natural Systems: Chapter 6 (Climate change).* Water Resources Engineering (Vattenvårdsteknik, KTH), 2008.

5.      Hewitt, C.N. and A.V. Jackson eds. *Atmospheric Science for Environmental Scientists.*  West Sussex: Wiley, 2009.

6.      Rees, M.H. *Physics and Chemistry of the Upper Atmosphere.* Cambridge: University Press, 1989.

7.      Plane, J.M.C. Atmospheric Chemistry of Meteoric Metals. *Chem. Rev.*, 2003, **103**, pp.4963 - 4984.

8.      Chapman, S. A Theory of Upper - Atmospheric Ozone. *Roy. Meteorol. Soc. Mem.*, 1930, **3**(26), pp.103 - 125.

9.      Brasseur, G.P. and S. Solomon. *Aeronomy of the Middle Atmosphere.* Atmospheric and Oceanographic Sciences Library.  Springer, 2005.

10.     Danilov, A. *Chemistry of the Ionosphere.*  Springer US, 2012.

11.     Ceplecha, Z., J. Borovička, W.G. Elford, D.O. ReVelle, R.L. Hawkes, V. Porubčan and M. Šimek. Meteor Phenomena and Bodies. *Space Sci. Rev.*, 1998, **84**(3-4), pp.327-471.

12.     Berger, U. and U.v. Zahn. The Two-Level Structure of the Mesopause: A Model Study. *J.  Geophys. Res.*, 1999, **104**(D18), pp.22083-22093.

13.     Hughes, D.W. Meteors. *In:* J.A.M. McDonnell, ed. *Cosmic dust*.  Chichester, New York: John Wiley & Sons Ltd, 1978, pp.123-185.

14.     Plane, J.M.C. Cosmic Dust in the Earth's Atmosphere. *Chem. Soc. Rev.*, 2012, **41**(19), pp.6507-6518.

15.     Plane, J.M.C., W. Feng and E.C.M. Dawkins. The Mesosphere and Metals: Chemistry and Changes. *Chem. Rev.*, 2015, **115**(10), pp.4497-4541.

16.     Plane, J.M.C. *Magnesium Chemistry in the Upper Atmosphere.* Leeds: University of Leeds, 2010.

17.     Plane, J.M.C. and M. Helmer. Laboratory Study of the Reactions $Mg + O_3$ and $MgO + O_3$ Implications for the Chemistry of Magnesium in the Upper Atmosphere. *Faraday Discuss.*, 1995, **100**, pp.411 - 430.

18.     Tepley, C.A., S. Raizada, Q. Zhou and J.S. Friedman. First Simultaneous Observations of $Ca^+$, K, and Electron Density Using Lidar and Incoherent Scatter Radar at Arecibo. *Geophysical Research Letters*, 2003, **30**(1), pp.9-1-9-4.

19. She, C.Y., J. Sherman, T. Yuan, B.P. Williams, K. Arnold, T.D. Kawahara, T. T. Li, L.F. Xu, J.D. Vance, P. Acott and D.A. Krueger. The First 80-hour Continuous Lidar Campaign for Simultaneous Observation of Mesopause Region Temperature and Wind. *Geophys. Res. Lett.*, 2003, **30**(6), pp.n/a-n/a.

20. Istomin, V.G. Absolute Concentrations of Ion Components of the Earth's Atmosphere at Altitudes Between 100 and 200 km. *Planet. Space Sci.*, 1963, **11**(2), pp.169-172.

21. Grebowsky, J.M. and D. Bilitza. Sounding Rocket Database of E- and D-region Ion Composition. *Adv. Space Res.*, 2000, **25**(1), pp.183-192.

22. Bhattacharyya, A., M.A. Abdu and D. Pancheva. *Aeronomy of the Earth's Atmosphere and Ionosphere.* Springer Netherlands, 2011.

23. Fan, Z.Y., J.M.C. Plane, J. Gumbel, J. Stegman and E.J. Llewellyn. Satellite Measurements of the Global Mesospheric Sodium Layer. *Atmos. Chem. Phys.*, 2007, **7**(15), pp.4107-4115.

24. Dawkins, E.C.M., J.M.C. Plane, M.P. Chipperfield and W. Feng. The Near-global Mesospheric Potassium Layer: Observations and Modeling. *J. Geophys. Res.*, 2015, **120**(15), pp.7975-7987.

25. Langowski, M.P., C. VonSavigny, J.P. Burrows, W. Feng, J.M.C. Plane, D.R. Marsh, D. Janches, M. Sinnhuber, A.C. Aikin and P. Liebing. Global Investigation of the Mg Atom and Ion Layers Using SCIAMACHY/Envisat Observations Between 70 and 150 km Altitude and WACCM-Mg Model Results. *Atmos. Chem. Phys.*, 2015, **15**(1), pp.273-295.

26. Fussen, D., F. Vanhellemont, C. Tétard, N. Mateshvili, E. Dekemper, N. Loodts, C. Bingen, E. Kyrölä, J. Tamminen, V. Sofieva, A. Hauchecorne, F.

Dalaudier, J.L. Bertaux, G. Barrot, L. Blanot, O.F. d'Andon, T. Fehr, L. Saavedra, T. Yuan and C.Y. She. A Global Climatology of the Mesospheric Sodium Layer from GOMOS Data During the 2002–2008 Period. *Atmos. Chem. Phys.*, 2010, **10**(19), pp.9225-9236.

27.    Vondrak, T., J.M.C. Plane, S. Broadley and D. Janches. A Chemical Model for Meteoric Ablation. *Atmos. Chem. Phys.*, 2008, **8**, pp.7015–7031.

28.    Plane, J.M.C., T. Vondrak and S. Broadley. Kinetic Study of the Reaction $Ca^+$ + $N_2O$ from 188 to 1207 K. *J. Phys. Chem.*, 2006, **110**, pp.7874 - 7882.

29.    Chipperfield, M., J.M.C. Plane, P. Forster and P. Braesicke. *NERC Funding Proposal*, 2011.

30.    Vondrak, T., J.M.C. Plane, S. Broadley and D. Janches. A Chemical Model for Meteoric Ablation *Atmos. Chem. Phys.*, 2008, **8**, pp.7015 – 7032.

31.    Krieg, J., J. Nothholt, E. Mahieu, C.P. Rinsland and R. Zander. Sulphur Hexafluoride ($SF_6$): Comparison of FTIR Measurements at Three Sites and Determination of its Trend in the Northern Hemisphere. *J. Quant. Spectrosc. Radiat. Transfer*, 2004, **92**, pp.383 - 392.

32.    Plane, J.M.C., R.M. Cox and R.J. Rollason. Metallic Layers in the Mesopause and Lower Thermosphere Region. *J. Adv. Space*, 1999, **74**(11), pp.I W-1 S70.

33.    Eska, V., U.v. Zahn and J.M.C. Plane. The Terrestrial Potassium Layer (75–110 km) Between 71°S and 54°N: Observations and modeling. *J. Geophys. Res.*, 1999, **104**(A8), pp.17173-17186.

34.    Gerding, M., M. Alpers, U.v. Zahn, R.J. Rollason and J.M.C. Plane. Atmospheric Ca and Ca+ layers: Midlatitude Observations and Modeling. *J. Geophys. Res.*, 2000, **105**(A12), pp.27131-27146.

35.     Murad, E. and I.P. Williams. *Meteors in the Earth's Atmosphere: Meteoroids and Cosmic Dust and Their Interactions with the Earth's Upper Atmosphere.* Cambridge University Press, 2002.

36.     Martin, J.C.G., M.A. Blitz and J.M.C. Plane. Kinetic Studies of Atmospherically Relevant Silicon Chemistry Part I: Silicon Atom Reactions. *Phys. chem. chem. phys.*, 2008, **11**, pp.671 - 678.

37.     Janches, D. and D.O. ReVelle. Initial Altitude of the Micrometeor Phenomenon: Comparison Between Arecibo Radar Observations and Theory. *J. Geophys. Res.*, 2005, **110**(A8).

38.     Plane, J.M.C. The Chemistry of Meteoric Metals in the Earths Upper - Atmosphere. *Int. Rev. Phys. Chem.*, 1991, **10**(1), pp.55-106.

39.     Clemesha, B.R. Sporadic Neutral Metal Layers in the Mesosphere and Lower Thermosphere. *J. Atmos. Terr. Phys.*, 1995, **57**(7), pp.725-736.

40.     Cox, R.M. and J.M.C. Plane. An Ion-molecule Mechanism for the Formation of Neutral Sporadic Na Layers. *J. Geophys. Res.*, 1998, **103**(D6), pp.6349-6359.

41.     Craig, R.A. *The Upper Atmosphere: Meteorology and Physics.* Academic Press, 1965.

42.     Sims, G., M.C.B. Ashley, A.M. Moore, R. Riddle, Z. Shang, J.W.V. Storey, N. Tothill, T. Travouillon, L. Wang, H. Yang, J. Yang, X. Zhou, X. Cui, Z. Zhu, J.R. Everett, L. Feng, X. Gong, S. Hengst, Z. Hu, J.S. Lawrence and D.M. Luong-Van. Airglow and Aurorae from Dome A, Antarctica. *Ast. Soc. Pac.*, 2012, **124**(916), pp.637-649.

43. Hervig, M.E., L.L. Gordley, L.E. Deaver, D.E. Siskind, M.H. Stevens, J.M. Russell, S.M. Bailey, L. Megner and C.G. Bardeen. First Satellite Observations of Meteoric Smoke in the Middle Atmosphere. *Geophys. Res. Lett.*, 2009, **36**(18), pp.n/a-n/a.

44. Lynch, K.A., L.J. Gelinas, M.C. Kelley, R.L. Collins, M. Widholm, D. Rau, E. MacDonald, Y. Liu, J. Ulwick and P. Mace. Multiple Sounding Rocket Observations of Charged Dust in the Polar Winter Mesosphere. *J. Geophys. Res.*, 2005, **110**(A3), pp.n/a-n/a.

45. Saunders, R.W., S. Dhomse, W.S. Tian, M.P. Chipperfield and J.M.C. Plane. Interactions of Meteoric Smoke Particles with Sulphuric Acid in the Earth's Stratosphere. *Atmos. Chem. Phys.*, 2012, **12**(10), pp.4387-4398.

46. Megner, L., D.E. Siskind, M. Rapp and J. Gumbel. Global and Temporal Distribution of Meteoric Smoke: A Two-dimensional Simulation Study. *J. Geophys. Res.*, 2008, **113**(D3), pp.n/a-n/a.

47. Summers, M.E. and D.E. Siskind. Surface Recombination of O and $H_2$ on Meteoric Dust as a Source of Mesospheric Water Vapor. *Geophys. Res. Lett.*, 1999, **26**(13), pp.1837-1840.

48. Plane, J.M.C. On the Role of Metal Silicate Molecules as Ice Nuclei. *J. Atmos. Terr. Phys.*, 2011, **73**(14–15), pp.2192-2200.

49. Warren, S.G., G.E. Thomas, G. Hernandez and R.W. Smith. Noctilucent Cloud Observed in Late April at South Pole Station: Temperature Anomaly or Meteoritic Debris? *J. Geophys. Res.*, 1997, **102**(D2), pp.1991-2000.

50. Thomas, G.E. Are Noctilucent Clouds Harbingers of Global Change in the Middle Atmosphere? *Adv. Space Res.*, 2003, **32**(9), pp.1737-1746.

51.     Tressaud, A. ed. *Fluorine and the Environment Atmospheric Chemistry*.

        Oxford: Elsevier, 2006.

52.     Ravishankara, A.R., S. Solomon, A.A. Turnipseed and R.F. Warren.

        Atmospheric Lifetimes of Long-Lived Halogenated Species. *Science*, 1993,

        **259**, pp.194 - 199.

53.     *Kyoto Protocol to the United Nations Framework Convention on Climate

        Change.*  United Nations, 1998.

54.     Prather, M.J. and J. Hsu. $NF_3$, the Greenhouse Gas Missing from Kyoto.

        *Geophys. Res. Lett.*, 2008, **35**(12).

55.     Jordan, A., J. Harnisch, R. Borchers, F.L. Guern and H. Shinohara.

        Volcanogenic Halocarbons. *Environ. Sci. Technol.*, 2000, **34**(6), pp.1122 -

        1124.

56.     Engel, T. and P.J. Reid. *Physical Chemistry.*  Pearson Benjamin Cummings,

        2006.

57.     Lide, D.R. *Handbook of Physics and Chemistry.* Boca Raton, FL: CRC Press,

        2006.

58.     Tasaka, A. Electrochemical Synthesis and Application of $NF_3$. *J. Fluor. Chem.*,

        2007, **128**, pp.296 - 310.

59.     Fthenakis, V., D.O. Clark, M. Moalem, P. Chandler, R.G. Ridgeway, F.E.

        Hulbert, D.B. Cooper and P.J. Maroulis. Life-Cycle Nitrogen Trifluoride

        Emissions from Photovoltaics. *Environmental Science and Technology*, 2010,

        **44**, pp.8750 - 8757.

60.     Feng, W., M.P. Chipperfield, S. Davies, B. Sen, G. Toon, J.F. Blavier, C.R.

        Webster, C.M. Volk, A. Ulanovsky, F. Ravegnani, P.v.d. Gathen, H. Jost, E.C.

Richard and H. Claude. Three-dimensional Model Study of the Arctic Ozone Loss in 2002/2003 and Comparison with 1999/2000 and 2003/2004. *Atmos. Chem. Phys.*, 2005, **5**, pp.139-152.

61. *Emissions of Greenhouse Gases in the United States 1998.* DIANE Publishing.

62. Wines, M. Department of Energy's Crusade Against Leaks of a Potent Greenhouse Gas Yields Results. *The New York Times*, 2013.

63. Weiss, R.F., J. Muhle, P.K. Salameh and C.M. Harth. Nitrogen Trifluoride in the Global Atmosphere. *Geophys. Res. Letts*, 2008, **35**.

64. Arnold, T., C.M. Harth, J. Mühle, A.J. Manning, P.K. Salameh, J. Kim, D.J. Ivy, L.P. Steele, V.V. Petrenko, J.P. Severinghaus, D. Baggenstos and R.F. Weiss. Nitrogen Trifluoride Global Emissions Estimated From Updated Atmospheric Measurements. *Proc. Nat. Acad. Sci.*, 2012, **110**(6), pp.2029-2034.

65. Ehhalt, D. and M. Prather. *Atmospheric Chemistry and Greenhouse Gases*. Climate Change 2001: The Scientific Basis, IPCC, 2001.

66. Burrows, J.P., E. Hölzle, A.P.H. Goede, H. Visser and W. Fricke. SCIAMACHY—Scanning Imaging Absorption Spectrometer for Atmospheric Chartography. *Act. Astr.*, 1995, **35**(7), pp.445-451.

67. Weitkamp, C. *Lidar: Range-Resolved Optical Remote Sensing of the Atmosphere.* Springer, 2005.

68. Reimann, S., M.K. Vollmer, D. Folini, M. Steinbacher, M. Hill, B. Buchmann, R. Zander and E. Mahieu. Observations of Long-lived Anthropogenic Halocarbons at the High-Alpine Site of Jungfraujoch (Switzerland) for

Assessment of Trends and European Sources. *Sci. Total Environ.*, 2008, **391**(2–3), pp.224-231.

69. Tsai, W.-T. The Prediction of Environmental Fate for Trifluoromethyl Sulfur Pentafluoride (SF$_5$CF$_3$), a Potent Greenhouse Gas. *J. Haz. Mat.*, 2007, **149**, pp.747-751.

70. Sturges, W.T., T.J. Wallington, M.D. Hurley, K.P. Shine, K. Sihra, A. Engel, D.E. Oram, S.A. Penkett, R. Mulvaney and C.A.M. Brenninkmeijer6. A Potent Greenhouse Gas Identified in the Atmosphere: SF$_5$CF$_3$. *Atmos. Chem. Phys.*, 2000, **289**(5479), pp.611-613

71. Sturges, W.T., D.E. Oram, J.C. Laube, C.E. Reeves, M.J. Newland, C. Hogan, P. Martinerie, E. Witrant, C.A.M. Brenninkmeijer, T.J. Schuck and P.J. Fraser. Emissions Halted of the Potent Greenhouse Gas SF$_5$CF$_3$. *Atmos. Chem. Phys.*, 2012, **12**(8), pp.3653-3658.

72. Solomon, S., D. Qin, M. Manning, Z. Chen, M. Marquis, K.B. Averyt, M. Tignor and H.L. Miller. *Contribution of Working Group I to the Fourth Assessment Report of the Intergovernmental Panel on Climate Change.* Climate Change 2007: The Physical Science Basis. Cambridge: Cambridge University Press, 2007.

73. Canadell, J.G., C.L. Quéré, M.R. Raupach, C.B. Field, E.T. Buitenhuis, P. Ciais, T.J. Conway, N.P. Gillett, R.A. Houghton and G. Marland. Contributions to Accelerating Atmospheric CO2 Growth from Economic Activity, Carbon Intensity, and Efficiency of Natural Sinks. *Proc. Natl. Acad. Sci.*, 2007, **104**(47), pp.18866-18870.

74.     Brasseur, G.P., R.G. Prinn and A.A.P. Pszenny. *Atmospheric Chemistry in a Changing World: An Integration and Synthesis of a Decade of Tropospheric Chemistry Research.*  Springer Berlin Heidelberg, 2012.

75.     Reddmann, T., R. Ruhnke and W. Kouker. Three-dimensional Model Simulations of $SF_6$ with Mesospheric Chemistry. *J. Geophys. Res.*, 2001, **106**, pp.14525-14537.

76.     Dougherty, M. and L. Esposito. *Saturn from Cassini - Huygens* [online]. Springer, 2009.

77.     Hall, T.M. and D.W. Waugh. Influence of Nonlocal Chemistry on Tracer Distributions: Inferring the Mean Age of Air from $SF_6$. *J. Geophys. Res.*, 1998, **110**(D11), pp.13,327-13,33.

78.     Baulch, D.L., J. Duxbury, S.J. Grant and D.C. Montague. Evaluated Kinetic Data for High Temperature Reactions. Volume 4 Homogeneous Gas Phase Reactions of Halogen and Cyanide-containing Species. *J. Phys. Chem. Ref. Data*, 1981, **10**.

79.     Robson, J.L., L.K. Gohar, M.D. Hurley, K.P. Shine and T.J. Wallington. Revised IR Spectrum, Radiative Efficiency and Global Warming Potential of Nitrogen Trifluoride. *Geophys. Res. Lett.*, 2006, **33**(10), p.L10817.

# Chapter 2: Experimental

The first section of this chapter aims to introduce the experimental techniques used for studying the kinetics of gas-phase reactions between a neutral metal atom and a perfluorinated compound (PFC). Several examples relating to similar reactions are explored. Background and principles as well as the advantages and disadvantages of these techniques will be discussed, and a description of the experimental systems used in this study will also be provided. The final section will provide a brief discussion on the techniques used to obtain infrared and Lyman–α cross sections. The preparation of gas mixtures and the gas handling vacuum systems are also described.

## 2.1 Experimental Techniques for Kinetic Studies of Gas–phase Metal Reactions

An early method of measuring rate coefficients is the crossed molecular beam technique developed in the 1950s. The apparatus consists of a collimated beam of gas phase reactant atoms or molecules which travel through an evacuated chamber where it intersects a second stream of atoms/molecules. The direction and velocity of the resulting scattered product molecules are measured and typically coupled with mass spectrometric data. This allows information on the distribution of energy among the translational, rotational and vibrational modes of the product species to be obtained (1). Molecular beam systems have been employed by Duren *et al.* and Riley *et al.* to obtain cross sections for the reactions of $SF_6$ with Na and K, respectively (2, 3).

Shock tubes are an example of a homogeneous reactor. The apparatus comprises of a tube several meters in length partitioned by a diaphragm. The first section of the tube contains a low-pressure mixture of reactant gas species and the second section contains a non-reacting gas. The pressure within the latter section is increased until the diaphragm bursts, forming a shock wave which propagates

down the tube causing the rapid compression and temperature increase of the reactant gas mixture. This results in the dissociation of reactants and subsequent generation of highly reactive species. The changing composition within the second section of the tube is usually monitored *in situ* using a spectroscopic technique (4). Shock tube experiments are generally performed at temperatures > 800 K which means extrapolation to temperatures relevant to atmospheric temperatures results in significant uncertainties.

Similarly, rate coefficients determined through flame studies are restricted to higher temperatures (> 1500 K). In these experiments measurements are obtained through modelling the change in chemistry of a flame following the injection of a trace amount of metal (1). A further limitation of flame studies arises from the potential heterogeneous chemistry which can occur on soot particles.

The flow tube and flash photolysis systems are the most prolific experimental techniques used in the study of gas phase reactions (5, 6). Both techniques have been used in previous studies to examine the neutral and ion-molecule reactions of various gas–phase metals (7).

Flow tube experiments involve the addition of a flow of gaseous reactants at one end of a tube which become mixed and travel downstream. Where flow velocity is known, the position along the tube corresponds to a relative concentration of reactant at different times following the initiation of the reaction. A sliding injector can be incorporated in the system to allow reactants to be introduced at various points relative to the detector (5, 6). The stopped flow technique is a variation of this system and can be used when large quantities of reactant are not available. This involves injecting a fixed volume of reactant into a reaction chamber and monitoring the change in composition using a time-resolved optical technique (1).

Flash photolysis experiments are initiated by a pulse of light which dissociate a reactant-containing precursor resulting in the generation of the reactive species. The rate coefficient is determined by monitoring the concentration of this reactive species as a function of time. The time scale of photolysis systems is in part determined by the duration of the initiating light pulse. Where early systems

incorporated a discharge lamp to produce a pulse with a duration in the microsecond range, modern systems may incorporate lasers capable of generating significantly shorter pulses ($10^{-12}$ – $10^{-9}$ s), allowing much faster reactions to be measured (8).

## 2.1.1  Detection methods

Reaction kinetics may be ascertained through the determination of the decay rate of a reactive species over time.  The relative concentration of the metal can be monitored by a time–resolved optical technique such as resonance absorption, chemiluminescence or laser induced fluorescence (LIF).

Chemiluminescence occurs when a reaction is exothermic enough to generate a product in its excited state. This excited state undergoes radiative decay to its ground state, emitting a photon. Resonance absorption uses a monochromatic light source, usually a tuneable laser, which corresponds to a specific transition within a species, to pass through a reaction mixture; the relative change in transmitted light is observed over time. This is related to concentration of a species through the Beer–Lambert law (1).

A species electronically excited by the absorption of a photon may decay to its ground state either through the emission of a photon of light (fluorescence) or non-radiatively through collisions with other molecules (quenching). In order to generate photons at a specific wavelength for this kind of analysis, a laser excitation source is required along with a detection method, typically incorporating a photomultiplier tube (PMT). This is a type of vacuum tube containing a photocathode which converts emitted photons into electrons. These are multiplied by an electron multiplier and detected as an electric signal, the magnitude of which is proportional to the concentration of fluorescing material.

The types of resonance generally used when detecting species by fluorescence are resonant and off–resonant detection. The former results from the absorption of a photon of a specific wavelength corresponding to that of an electronic transition, promoting an electron into a higher energy level. This results in the formation of an electronically excited species, which then relaxes back to its former state through

the emission of another photon with the same wavelength as the exciting photon. Off–resonance occurs where the excited electron relaxes to a different level than that of its initial state by the emission of a photon at a different wavelength to the exciting photon (9, 10). Both fluorescence schemes are illustrated in Figure 2.1. Because an excited species is generally more likely to relax to its initial state, non-resonant fluorescence is expected to be weaker and potentially more difficult to observe than resonant. It is consequently preferential in most cases to devise a resonant scheme for monitoring metals, although there may be cases where off - resonance is advantageous, such as where saturation or 'blinding' of a PMT from strong signal is an issue (11, 12).
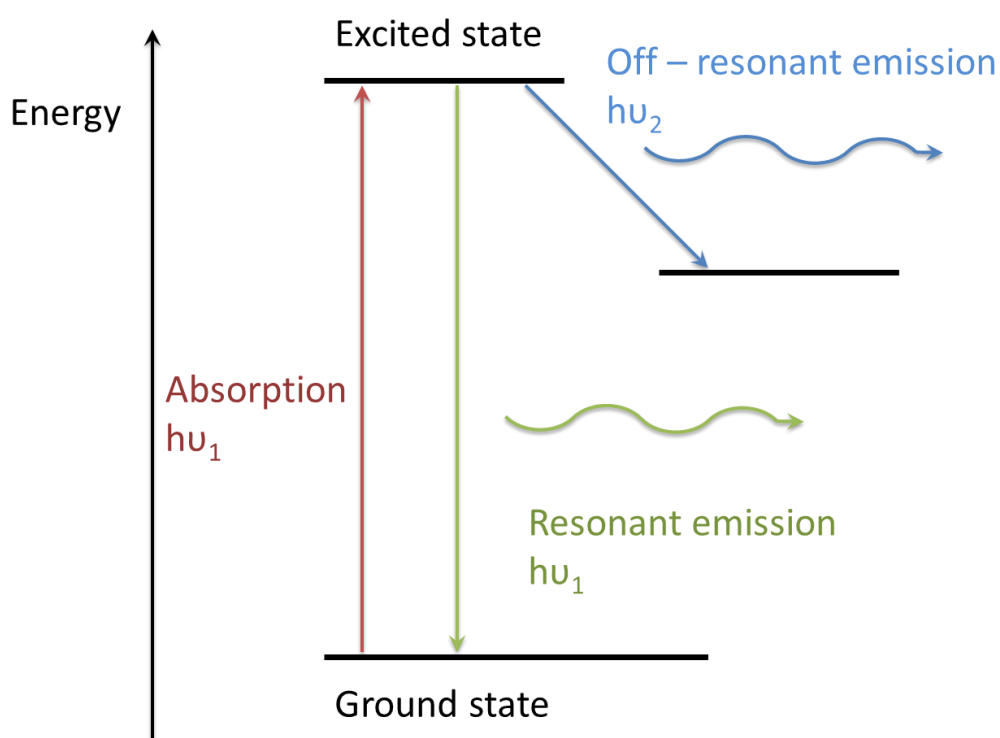


**Figure 2.1.** Schematic representation of an energy diagram showing the difference in resonant and off – resonant florescence of a hypothetical species.

The laser induced fluorescence (LIF) technique is a highly sensitive electronic spectroscopy method with several applications. LIF can be used to produce strong

resonant and non-resonant signals variable with temperature or concentration but is limited to single species detection due to the specificity of electronic transitions (13).

In order for a laser to generate light, the species examined must be capable of achieving a population inversion. This is achieved by exciting the species, typically using an additional laser through a process known as pumping, into a metastable excited state with a lifetime sufficient to enable stimulated emission to occur. The population of this excited state must be greater than the ground state so that when the transition terminates, a net emission of radiation occurs.

In selecting a transition to monitor, it has to be ascertained that the photon emitted is within a reasonable detection range for LIF. For example, the sodium spectrum gives rise to a doublet known as the sodium D lines which occur at 589.0 and 589.6 nm: $^2S_{\frac{1}{2}} \begin{smallmatrix} \nearrow\ ^2P_{\frac{3}{2}} \\ \searrow\ ^2P_{\frac{1}{2}} \end{smallmatrix}$, the resonant 3p $\rightarrow$3s transition. Furthermore, one of the secondary emission photons from excitation to the 3p level, back to the ground state (3 $^2P_{3/2} \rightarrow$ $3^2$s) occurs at 589.2 nm. This is within the resonant doublet range with the two absorptions where each is known to be easily detectable (14).

The pulse-probe technique incorporates LIF and is used within flash photolysis systems to monitor the decay rate of a reactant generated *in situ* within the reaction chamber using flash photolysis. This photolysis product, in these experiments a metal atom, is probed and the fluorescence decay monitored using a dye laser, intersecting the photolysis beam at an increasing time delay (15). Gated detection is often implemented when using LIF in order to improve sensitivity by eliminating background noise, or to avoid temporary blinding of the PMT by intense laser scattered light. This is achieved by specifying a set timespan over which observation can occur, e.g. the duration of the laser pulse.

Further detection methods such as mass spectrometry and ultra-violet or infrared spectrometers can be employed to monitor gas exiting the reacting system in order to observe the presence and relative concentrations of additional products and excess reagents (15).

## 2.1.2   Flash Photolysis and the Fast Flow Tube

The flash photolysis and fast flow tube systems were selected for use in this study. The majority of measurements are taken using the photolysis system due to its efficiency, suitability over a large temperature range and ease of use. Results were corroborated using the flow tube system.

In the flash photolysis technique, the reactive species (in this case the neutral metal atom) is generated by exposing a photolytic metal-containing precursor to a short ($10^{-6} - 10^{-8}$ s) pulse of light. This would typically be generated using a discharge lamp or laser (16). Photolysis occurs within a flow of an inert bath gas such as $N_2$ or He. This serves the dual purpose of maintaining thermal stability and entraining and transporting the precursor into a central chamber where it can be mixed with other reactants. The photolytic pulse generated initiates the reaction allowing the subsequent decay in concentration of the reactive species to be monitored by means of a time–resolved optical technique.

In fast flow tube (FFT) experiments, the reactive species may be generated continuously throughout the reaction, often by thermolysis, or, by photolysis methods similar to those described above. The species are then entrained within a high velocity flow (> 5 m s$^{-1}$) of an inert bath gas. The gas enters the tube upstream of the precursor, carrying the vapour downstream, where the reactant gases enter through side ports and mix. The reaction time can be altered by changing the concentration of the reactant gas or by varying the distance species have to travel, for example by means of a sliding injector. One or more of the reactants or products are observed further downstream.

### 2.1.2.1  Advantages and Disadvantages of the Flash Photolysis and Flow Tube Techniques

The techniques described above are complementary and are both used to obtain rate constants in this study. Each has various advantages and disadvantages which have been discussed in detail previously (5, 8).

**Table 2.1** Major factors to be considered when evaluating kinetic techniques
(adapted from Howard (1978) (5)).

| | Flash photolysis | Fast flow tube |
|---|---|---|
| Temperature range | 100 – 1100 K | 200 – 1000 K |
| Pressure range | 1 Torr – several atmospheres | 1 – 10 Torr |
| Rate constant range | $(10^{-10} – 10^{-18})$ cm$^3$ molecule$^{-1}$ s$^{-1}$ | $(10^{-10} – 10^{-16})$ cm$^3$ molecule$^{-1}$ s$^{-1}$ |
| Detection versatility | Requires fast detector | Excellent |
| Reactant versatility | Limited | Excellent |
| Heterogeneous reactions | None | Can be serious |
| Expense | Moderate | Low |

The useable temperature range of the two techniques is similar. The upper limit of
temperature range is dictated by factors such as the thermal stability of the
reactants and the materials from which the equipment is made. The higher
probability of heterogeneous chemistry occurring in the flow tube is potentially
limiting at lower temperatures, meaning the photolysis technique may be
preferable for low temperature reactions (5). This possibility of heterogeneous
chemistry is a major disadvantage of flow tube systems; however, the effect can be
limited somewhat through use of non-reactive coatings on the inside of the tube.
Heterogeneous chemistry does not occur with flash photolysis because the
reaction can only occur within the volume defined by the intersection of the
photolysis and probe beams. Therefore, diffusion to the walls does not occur on
the timescale of the reaction. Furthermore the reactor surface typically possesses a

high deactivation efficiency which is potentially problematic when studying excited species (5).

The flow tube is generally limited to use as a low-pressure technique and is more suitable for measuring larger rate coefficients due to lower reactant concentrations. The photolysis technique is generally capable of operating under higher pressures with the upper limit being dictated by the method available for detection of reactants or fluorescence quenching by the bath gas at high pressures. The lower limit may be determined by reactant concentrations below the limit of detection at low pressures (10). This means that photolysis systems are generally superior in studying slow and termolecular reactions as higher pressures allow for larger concentrations of reactants to be used and much smaller rate coefficients to be measured. A large useable pressure range is further advantageous as it allows a greater range for pressure dependant studies to be carried out (5, 17). Flow tubes however, require correction for transport effects and surface effects. These include axial diffusion which is the diffusion of the reactant downstream, and radial diffusion, where the reactant species is lost to the walls resulting in signal loss. Where flow within the tube is laminar, the radial flow profile within the flow tube is described as parabolic. This is where the gas in the centre of the tube travels at a greater velocity than that at the sides. The treatment of these effects is discussed in greater deal in Chapter 3. At higher flow rates, flow becomes turbulent and is no longer parabolic.

A major advantage of the flash photolysis technique is that it allows reactions to be measured in real time with a resolution in the femtosecond range. Where photolysis systems are restricted to fast detection methods, flow tubes allow a large range of compatible detection and precursor generation techniques to be implemented. This is because a steady-state environment exists within the flow tube so that along any given point of the tube, a different stage in the reaction is represented (5, 18). Because concentrations are essentially frozen at this point, there are no constraints on detector speed (5). This also allows further reactants to be added at any stage via side ports so that complex molecules may be formed, making the flow tube more versatile for reactants (7). Furthermore, where LIF is

used, the species for detection in photolysis systems must possess a discrete spectrum so that a laser can be tuned to a specific wavelength range to probe. Photolysis systems are more restrictive for compatible reactants as reactive species formed via photolysis are highly excited and far more likely to react. This is potentially problematic because the likelihood of secondary chemistry is greatly increased (6, 21). It is also difficult to identify potential photolytic precursors which will undergo photolysis without producing unwanted by-products, potentially resulting in secondary chemistry.

### 2.1.3  Apparatus and Methodology

**2.1.3.1 Pulsed Laser Photolysis – Laser Induced Fluorescence**

The pulsed laser photolysis – laser induced fluorescence system apparatus employed for this study was first used by Plane (19) to study reactions between lithium and $N_2O$. For this study, it has been modified in the way described below in order to examine the reactions of the meteoric metals Na, K, Fe and Mg with the long-lived greenhouse gases $SF_6$, $NF_3$, CFC-115 and $SF_5CF_3$.

The apparatus, shown in Figure 2.2, consisted of a cylindrical stainless-steel reaction cell, designed to facilitate high temperatures and act as an inert surface. The chamber has four orthogonal horizontal arms and a fifth vertical side arm (radius=3 cm, length=8 cm). Different metal-atom precursors were placed in a temperature-controlled stainless-steel boat located in one of the horizontal side arms and heated. The resulting vapour was entrained into a carrier gas flow ($N_2$) passing over the boat and transported into the reaction chamber where it was mixed with larger flows of the perfluorinated compound (PFC) of interest in $N_2$. Brewster-angled quartz windows were fitted to the ends of the other three horizontal arms in order to admit the laser beams into the centre of the chamber for photolysis and optical detection. The vertical side arm provided coupling to the PMT monitoring the LIF signal.

The reactor of the photolysis system was placed within a thermally insulated container surrounded by a furnace which could heat the chamber to 1100 K. A permanently inserted chromel-alumel thermocouple monitored the temperature ~ 1 cm away from photolysis region attached to a temperature controller (Omega Eng. Model 670). Space surrounding the reactor could be packed with dry ice chips for low temperature measurements (~ 190 K). Temperatures lower than that of the equilibrium sublimation temperature of $CO_2$ were achievable (195 K at 1 atm) as an increased rate of evaporation of $CO_2$ was attained through exposure to a continuous source of compressed air.

The reactor pressure was maintained between 5 and 15 Torr and measured with calibrated capacitance manometers (MKS Baratron, Model 226A, 10 and 1000 Torr) and controlled by a valve on the exit line to the pump, with fine control given through a needle valve as part of the main valve. The total gas flow rates were varied between 250 and 350 sccm, where the reactant mix was kept at ~100 sccm. The flow rate was controlled by electronic mass flow controllers (MKS Instruments, Models 1259C and 1179A).

Reactions were initiated by multi-photon photolysis of the corresponding metal-atom precursor at 193 nm using a loosely focused excimer laser beam (Lambda-Physik, Model Compex 102, pulse energy 28 – 60 mJ, pulse width 15 ns, repetition rate 5 Hz, ~ 3 – 6 x $10^{16}$ photons) passing through a quartz window (f = 45 cm). For the study of sodium reactions, sodium iodide (NaI) was placed in the side arm and heated independently using cartridge heaters to a temperature of 560 ± 5 K. A flow of $N_2$ (150- 250 sccm) carried the vapour into the cell. For reactions of potassium, potassium iodide (KI) was heated in the side arm to 530 ± 2 K, and for reactions of magnesium acetylacetonate (Mg($C_5H_7O_2$)$_2$ or MgAcAc) was heated to between 403 and 453 K and maintained to within 5 K throughout the experiment. These temperatures were monitored using a permanently inserted chromel –alumel thermocouple and a temperature controller (Omega, Model 6100).

For reactions of these metals, counter-propagating excimer and dye laser beams were employed, as shown in Figure 2.2 below.
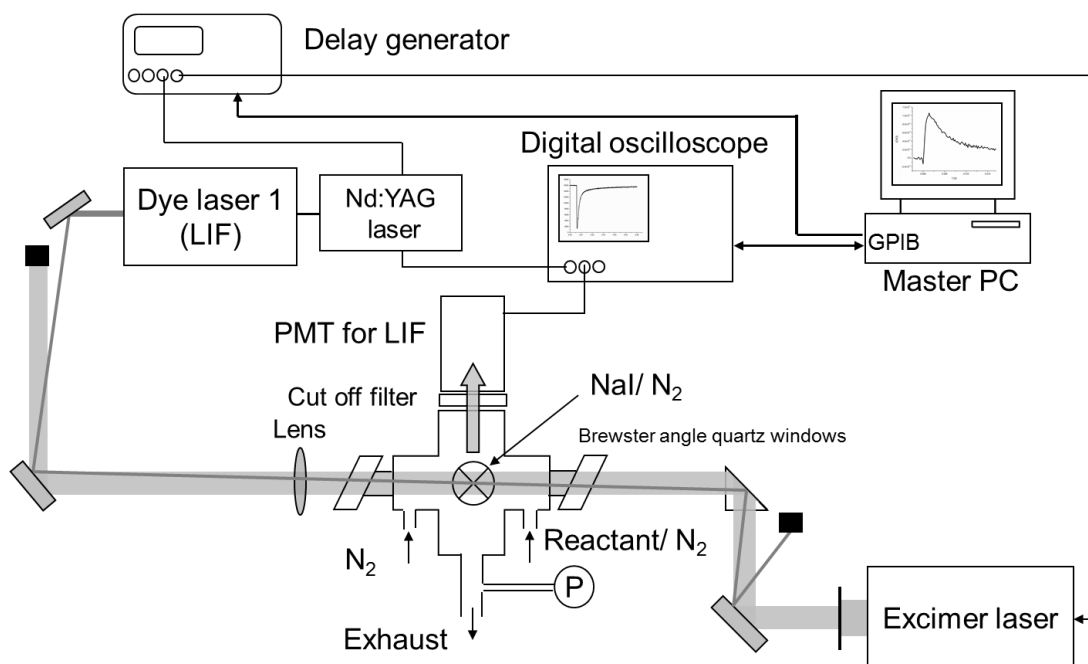
**Figure 2.2**. Schematic diagram of the pulsed laser photolysis-laser induced fluorescence apparatus employed to study the reactions of Na, K and Mg with $SF_6$, $NF_3$, $SF_5CF_3$ and CFC-115. Details of the LIF scheme are given in Table 2.2, where the wavelength of light generated from the excimer laser is 193 nm.

In contrast, for reactions involving Fe, the dye and excimer laser beams were arranged orthogonally. Powdered ferrocene (Fe $(C_5H_5)_2$) was placed in a sealed round bottomed flask kept at 295 K giving an equilibrium vapour pressure of 0.006 Torr. A small $N_2$ flow (50 – 150 sccm) passed through the flask, carrying the ferrocene vapour into the stainless-steel reaction chamber. The schematic for this set-up is shown below in Figure 2.3.
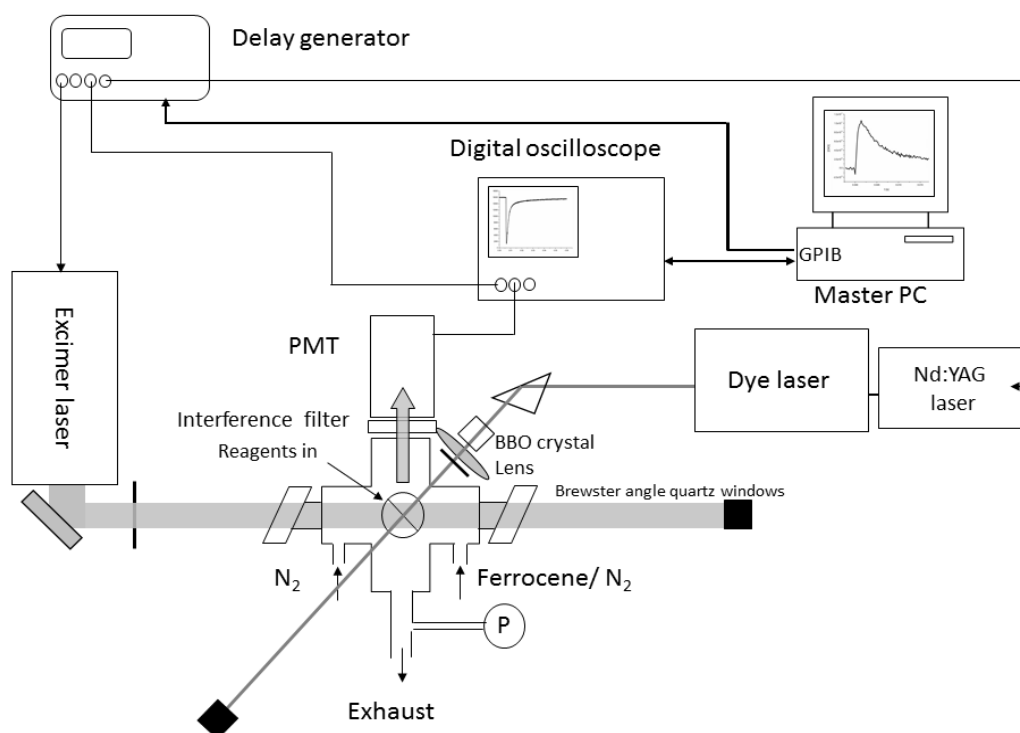
**Figure 2.3.** Schematic diagram of the pulsed laser photolysis-laser induced fluorescence apparatus employed to study the reactions of Fe with $SF_6$, $NF_3$, $SF_5CF_3$ and CFC-115. Details of the LIF scheme are given in Table 2.2, where the wavelength of light generated from the excimer laser is 193 nm.

The metal atoms were probed by the dye laser beam (Continuum Minilite II Nd:YAG pumped Sirah CBR-G-30 dye laser) using the LIF detection schemes in Table 2.2. Nd: YAG (neodymium-doped yttrium aluminium garnet; $Nd:Y_3Al_5O_{12}$) is a crystal used as a lasing medium for solid state lasers emitting light with a wavelength of 1064 nm, in the infrared. This was frequency doubled or tripled to generate light in the second and third harmonics at 532 or 355 nm. The aperture of the Nd: YAG laser was aligned with the aperture of the dye laser so that the generated radiation pulse travelled into the dye laser, initiating fluorescence of the dye. The dye laser beam then travels through the reactor, and in turn induces fluorescence from the target atomic species. The resulting LIF signal was measured by a photomultiplier tube (Hamamatsu, Model HC120-OS) after passing through an interference filter

centred at the wavelength indicated in Table 2.2, and recorded using a digital oscilloscope (LeCroy, LT262).

The transient LIF signal from the metal atom was monitored as a function of time by varying the delay between the excimer and the probing laser pulse. This was achieved using a delay generator (BNC, Model 555) controlled by a customisable LabView program. The excimer laser was triggered by a pulse from the delay generator at 50 µs and a second trigger to the Nd: YAG laser and Q switch at 50.15 µs. A typical time-resolved LIF profile consisted of 100 delay steps and resulted from the average of 5 individual delay scans, in all of which the signal for a particular delay was the average of 3 laser shots.

**Table 2.2** LIF schemes used for the detection of Na, K, Fe and Mg.

| Metal atom | $\lambda$ Nd:YAG /nm [a] | Laser dye | $\lambda_{peak}$ filter /nm [b] | $\lambda$ transition /nm | Transition |
|---|---|---|---|---|---|
| Na | 532 | Rhodamine 610 | 589 (5) | 589.0 | $3^2P_{3/2}$ - $3^2S_{1/2}$ |
| K | 355 | Exalite 404 | 765 (6) | 766.5 | $4^2P_{3/2}$ - $4^2S_{1/2}$[c] |
| Mg | 532 | Rhodamine 610 | 285 (5) | 285.2 [d] | $3^1P_1$ - $3^1S_0$ |
| Fe | 355 | Coumarin 503 | 250 (5) | 248.3 [d] | $x^5F^0_5$ - $a^5D_4$ |

[a]Dye laser pump wavelength.

[b]Interference filter peak transmission; fwhm is in parentheses.

[c] K($5^2P_{3/2}$ - $4^2S_{1/2}$) transition pumped at 404.4 nm and observed non-resonantly at 766.5 nm.

[d] Frequency–doubling crystal employed.
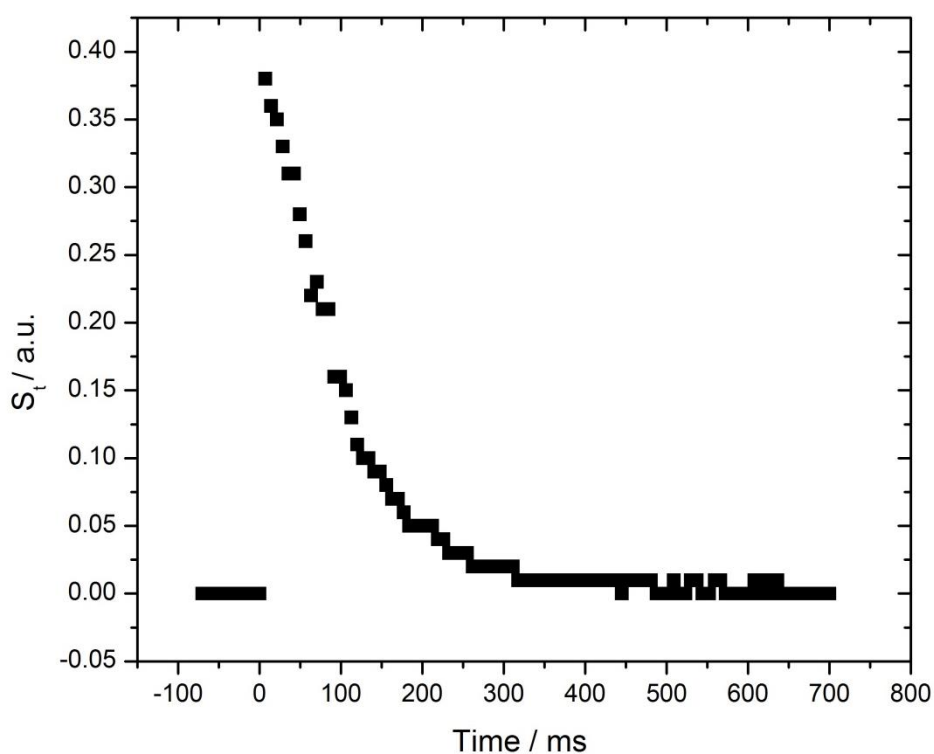
**Figure 2.4** Decay profile of sodium at ~ 770 K without the presence of reactant.

A typical time-resolved LIF profile such as that in Figure 2.4 displays the relative intensity of the reactant metal (Na) from accumulation of data. This was generated from 100 delay steps resulting from the average of three laser shots and averaged for five scans. This allowed a good signal to noise ratio, obtained within a suitable time frame.

Data points before time zero correspond to negative delays where the Nd:YAG laser has fired prior to the excimer and so represent the background noise level, providing a baseline to check for convergence of the decay (Figure 2.4). The first point is measured 150 ns after the excimer and subsequent measurements at a 150 ns delay. The decay rate, in the absence of reactant and assuming no secondary chemistry, is consequently a representation of the rate of diffusion of the metal species out of the field of view of the PMT. Further detail and full treatment of results is provided in Chapter 3.

**2.1.3.2 Fast Flow Tube**

The FFT apparatus used to study the reactions of sodium with $NF_3$ and $SF_6$. The apparatus consisted of a 37.5 mm internal diameter (ID), 1 m long stainless steel tube made up of cross-pieces and nipple sections connected by ConFlat flanges and sealed with copper gaskets. The tube also contained optical windows which allowed the LIF technique to be used as a detection method. Figure 2.5 provides a schematic diagram of the flow tube set up used to study these reactions.

Flow tube measurements were predominantly carried out at room temperature; low temperatures were achieved by surrounding the walls of the tube with solid $CO_2$ chips. These were housed within a polystyrene box encompassing the reaction zone. Temperature was measured using a removable chromel-alumel thermocouple inserted through a side port of the tube, ~ 5 cm downstream of the reactant entry point, taking care not to touch the sides. This was attached to a temperature controller (Omega Eng. Model 670).

The pressure of the flow tube was controlled by a throttle valve before the rotary-backed booster pump. Manometers were positioned near mid-point along the tube (Figure, 2.4). The total gas flow rates were varied between 2500 and 3500 sccm, controlled by electronic mass flow controllers (MKS Instruments, Models 1259C and 1179A) at total pressures between 1.2 and 4.0 Torr which were measured using a capacitance manometer (MKS Baratron, Model 226A) and controlled by a throttle valve attached to a booster pump (Edwards, Model EH500A) backed by a rotary pump (Edwards, Model E2M80).

An aluminium oxide crucible housed within a tungsten basket heater containing pure sodium chips was located within the flow tube, downstream of the bath gas inlet, and was heated to approximately 500 K. The resulting Na vapour was then entrained in the flow of carrier gas $N_2$ and carried downstream where it mixed with varying ratios of the fluorinated gas and $N_2$. Flow velocities were maintained between 0.7 and 31 m s$^{-1}$ and Reynold's numbers < 2000, ensuring laminar flow conditions.  The Reynold's number was calculated according to the formula:

$$Re = \frac{\gamma d \rho}{\mu}$$

(E2.1)

where $\gamma$ is the velocity of the bath gas (m s⁻¹), $d$ is the diameter of the flow tube (m), $\rho$ is the density of the bath gas (kg m⁻³) and $\mu$ is the dynamic viscosity of the bath gas (kg m⁻¹ s⁻¹), calculated according to the formula:

$$\mu = \sqrt{\frac{k_B T m_\mu}{\pi^3 d^4}}$$  (E2.2)

where $k_B$ is the Boltzmann constant (m² kg s⁻² K⁻¹), $T$ is the temperature, $m_\mu$ is the molecular mass and $d$ is the average collision diameter of the molecule in air (m). Flow is said to be laminar when $Re < 2000$ (15).

The sodium atoms were then probed by a Nd:YAG pumped dye laser (Sirah CBR-G-30 pulse energy 5 – 10 mJ, pulse length 25 ns, repetition rate 5 Hz) at 589.0 nm (see Table 2.2). The subsequent fluorescence was measured at right angles by a photomultiplier tube (Hamamatsu, Model HC120-OS) after passing through an interference filter centred at 589 nm, and collected and averaged with a gated integrator (Stanford Research Systems, SR250). A photodiode placed near the dye laser beam, detected when the pulse had been fired and relayed to the boxcar integrator which allowed the gate delay to be set accordingly (~ 20 ns). The pulse and gate were displayed on the oscilloscope.
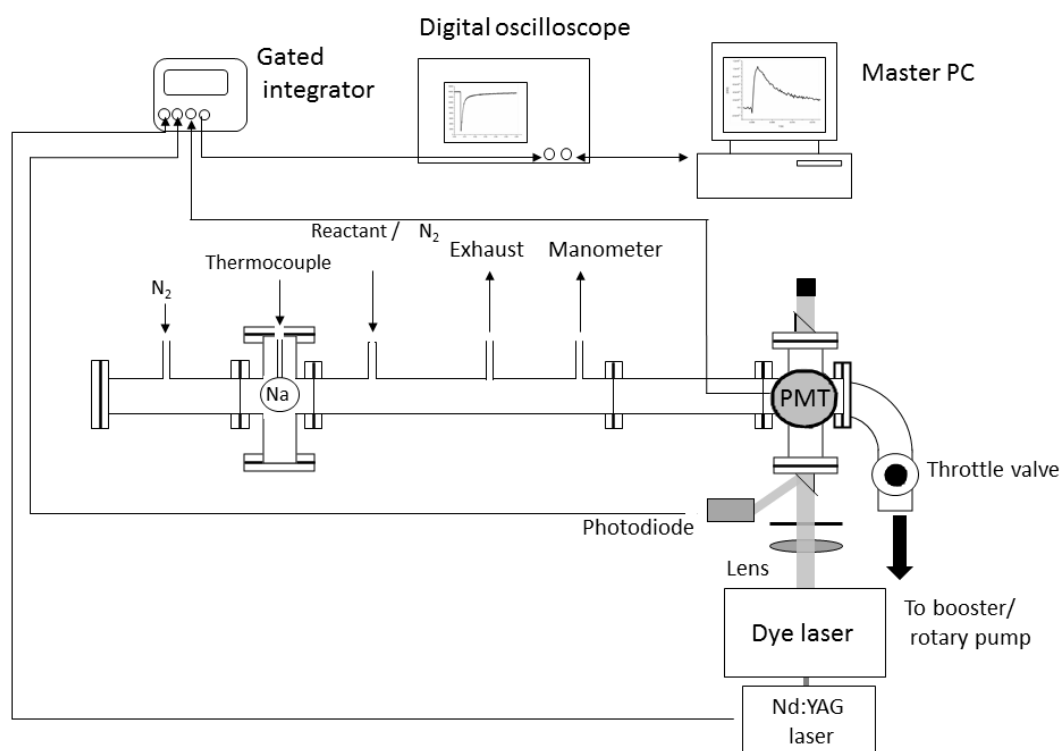
**Figure 2.5**. Schematic diagram of the fast flow tube apparatus employed to study the reactions of Na with $SF_6$ and $NF_3$.

Sodium atoms travelling down the flow tube are subject to parabolic flow and undergo significant axial and radial diffusion which, if left unaccounted for, could result in a significant overestimation of rate coefficient. A full treatment of these effects, the kinetics and calculation of rate coefficients is discussed in Chapter 3.
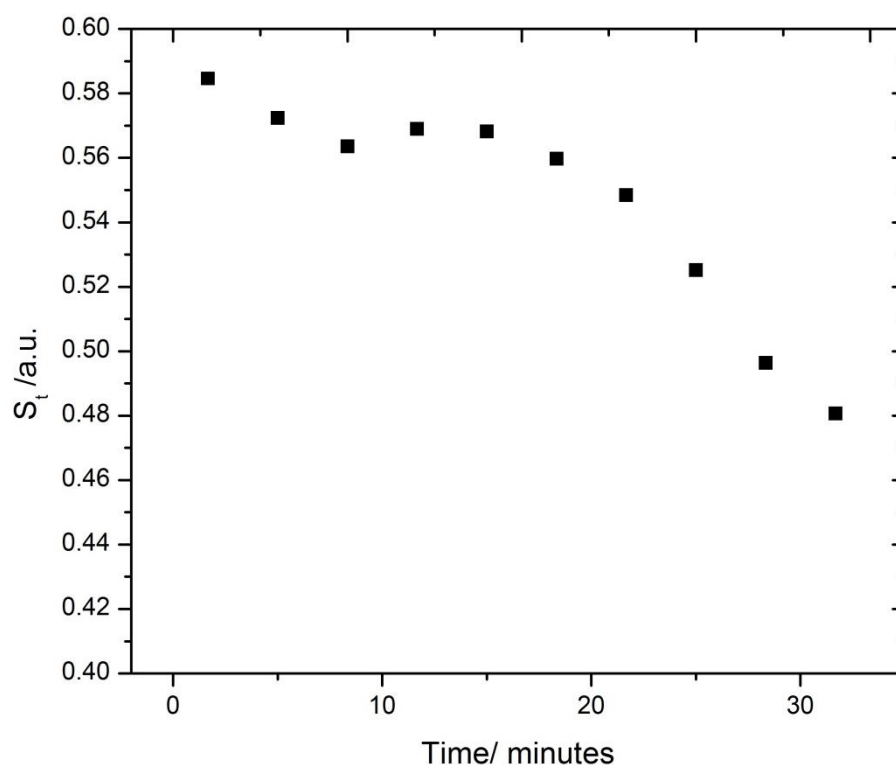
**Figure 2.6**. Room temperature sodium profile over the course of a flow tube experiment at 2 Torr.

Figure 2.6 represents the relative intensity of sodium measured over a fast flow tube experiment. Sodium was produced continuously from a thermal source. Each recorded point is the average of 100 measurements recorded one second apart. The signal at the beginning of the experiment is significantly greater than that towards the end. This is primarily due to depletion of the metal source over time. To account for this, reference measurements without reactant gas present were taken before and after each point. These were used to correct for changes in intensity. Taking reference measurements in this way also eliminates the need to account for diffusion effects. Full treatment of results is discussed in Chapter 3.

## 2.2 Measurement of the Lyman–α Absorption Cross Section

### 2.2.1 Apparatus and Methodology

A schematic of the apparatus used by Dr Tamás Kovács (University of Leeds) and employed for measuring the PFC absorption cross section at Lyman-α (121.6 nm) is shown in Figure 2.7. The apparatus consists of a radio discharge lamp connected to a 7 cm long cell containing $O_2$, in turn connected to the sample gas absorption cell (optical path length = 12.4 cm). The $O_2$ cell was separated from the discharge lamp and the absorption cell by $MgF_2$ windows (1 mm thickness). Lyman-α radiation was generated by radio-frequency discharge of a flowing $H_2$:He mixture (1:20) at a pressure of 7 Torr. Other VUV wavelengths emitted by the plasma were filtered out by the $O_2$ filter, created by flowing an $O_2$:$N_2$ mixture (1:9) through the $O_2$ cell at a pressure of 760 Torr (20). Different mixtures of the fluorinated species in He were admitted to the absorption cell to sample a range of concentrations with the Lyman-α radiation passing through it. Care was taken to remain in the low absorption regime (optical density well below 1), ensuring validity of the Beer-Lambert law, equation E2.3. The attenuated radiation was measured by a solar blind photomultiplier *via* an interference filter with peak transmission at 121.6 nm and 20 nm FWHM (Princeton Research, type 122-N). Experiments were carried out at room temperature (295 ± 2 K).

The intensity (*I*) of the filtered 121.6 nm radiation emitted by the radio-frequency discharge and transmitted through the absorption cell in the presence of varying amounts of PFC was recorded and averaged. The signal for zero absorption in the absence of PFC ($I_0$) was recorded before and after each concentration of the PFC was admitted to the absorption cell. The noise relative to the absolute signal was in the order of 1:100. Experiments for concentration were repeated four times and the individual absorbance values averaged. The Lyman-α absorption cross section of the PFC, σ, was determined by applying the Beer-Lambert equation:

$$\ln\left(\frac{I_0}{I}\right) = \sigma(121.6\ nm)\ L\ [PFC] \tag{E2.3}$$

where $I_0$ and $I$ are respectively the light intensity transmitted through the absorption cell in the absence and presence of PFC, and $L$ is the optical path length.
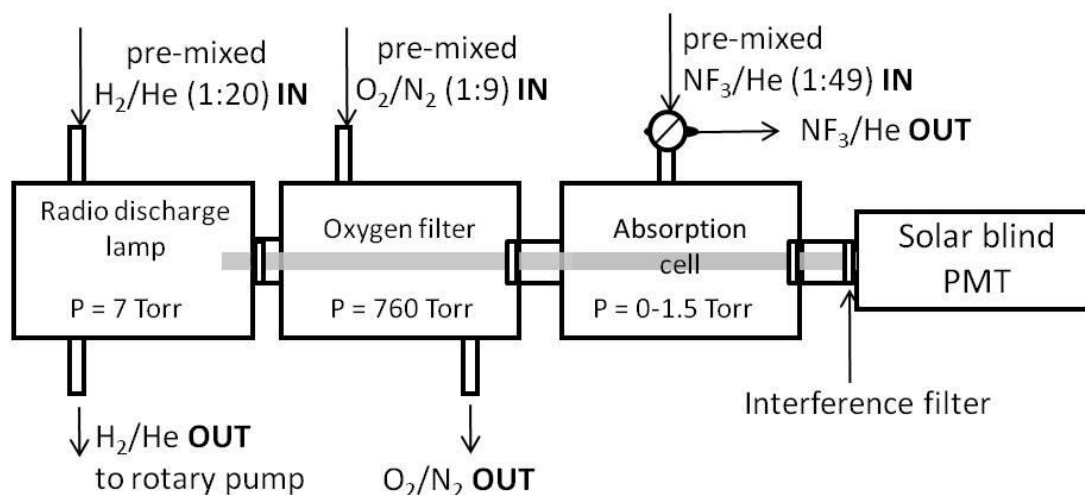


**Figure 2.7.** Schematic diagram of the experimental set-up for Lyman-α absorption measurements for NF$_3$, adapted for other PFCs.

## 2.3 Infrared Spectroscopy

Fourier transform infrared spectroscopy (FTIR) has a number of applications in analysis, namely the study of inorganic and organic chemical species, incorporating practical applications such as polymer degradation and blood alcohol analysis in forensic science. FTIR was introduced as a replacement for traditional dispersive IR spectroscopy, making the overall process significantly faster, but also improving wavelength precision and decreasing sensitivity to scattered light. The key differences and benefits are summarised in Table 2.3. These improvements have meant that new applications such as gas-chromatography-infrared spectrometry; thermogravity-infrared spectrometry and emission spectra have also evolved (21).

**Table 2.3** Summarised comparison between the traditional dispersive infrared technique and modern Fourier transform infrared technique (22).

| | Dispersive IR | FTIR |
|---|---|---|
| Speed | Slow, intensities measured at each frequency - spectrum obtainable in order of minutes. | Very fast, measurements at each frequency taken simultaneously (Felgett Advantage) - spectrum obtainable in seconds |
| Sensitivity | Restricted due to slits in aperture. | Higher optical throughput (Jacquinot Advantage) and sensitivity on detectors combined with increased speed allows signal averaging to occur resulting in significantly better signal to noise ratio. |
| Accuracy and Precision | Requires external calibration standards, instrumental unknowns can affect reliability of data and reproducibility between scans. | Self – calibrating (Connes Advantage). A helium neon (He Ne) laser is used for precision timing and to control the velocity of the moving mirror as well as internal wavelength calibration. |

FTIR operates as light from an infrared source is collimated and directed through a beam-splitter which divides the incoming radiation into two beams, one of which is directed towards a fixed mirror and the other towards a mirror attached to a mechanism which allows it to move away from, or towards, the beam splitter. The beams are then reflected and recombine at the beam splitter before being focused and passing through the sample and onto the detector. The difference in path

length and relative intensities of the two signals is measured and recorded as an interferogram (23) to which a Fourier transform is applied to convert the interferogram into a spectrum.
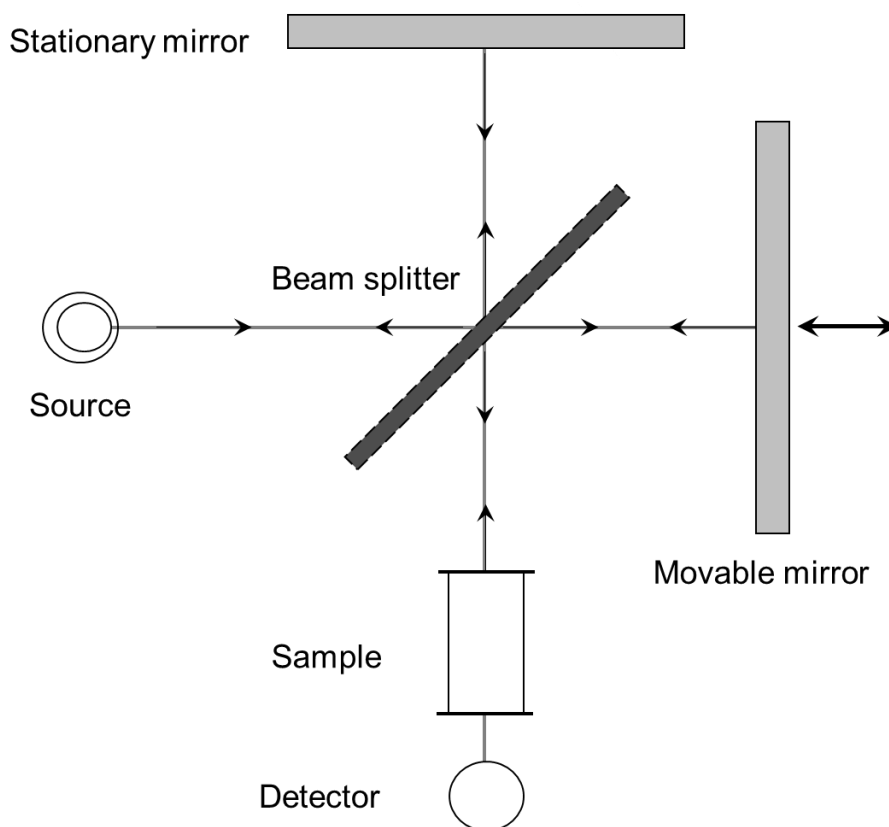


**Figure 2.8.** Schematic diagram depicting the layout of a typical Fourier transform infrared spectrometer.

### 2.3.1 Apparatus and Methodology

The infrared range used for experiments was selected based on the known positions of the main bands of interest which were known to occur within the atmospheric infrared window. This is a dynamic property of the Earth's

atmosphere, describing gaps which exist within its overall infrared spectrum where main constituents do not absorb. Species which absorb strongly in this region have a pronounced radiative effect as they absorb blackbody radiation emitted from the earth's surface which would otherwise escape to space. This effect is summarised in Figure 2.9 and discussed in greater detail in Chapter 4.
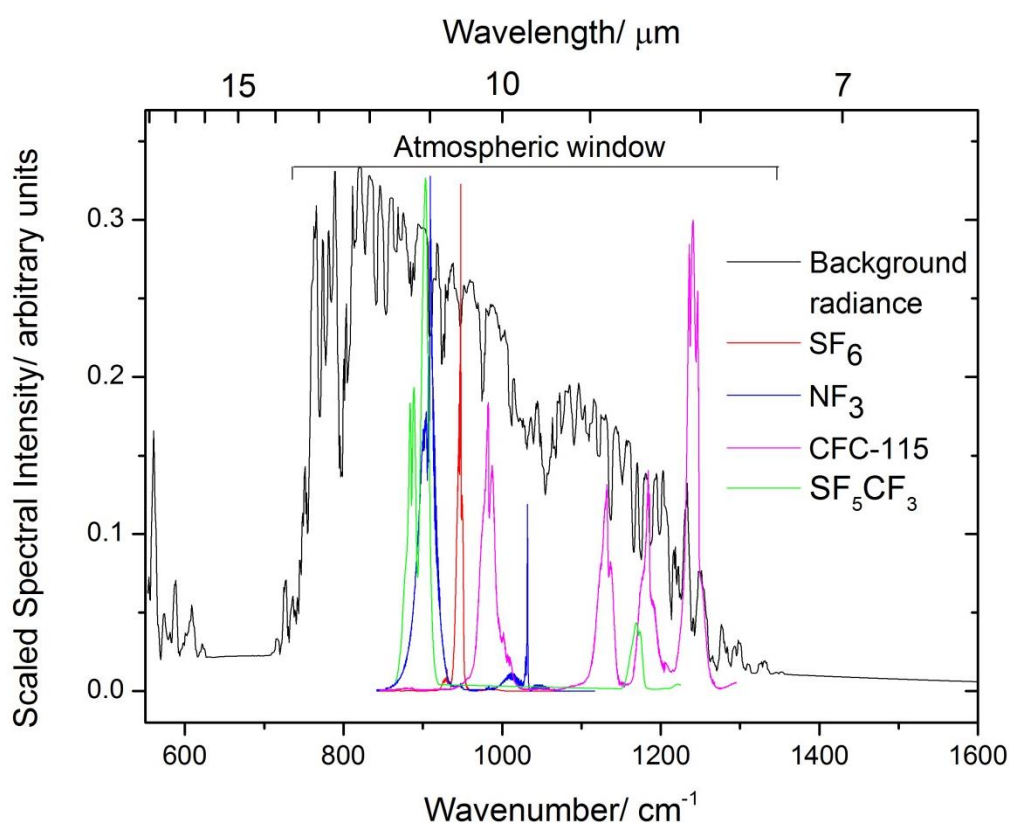


**Figure 2.9.** A representation of the position of the main bands of $SF_6$, $NF_3$, $SF_5CF_3$ and CFC-115 relative to the atmospheric window. Background radiance is comprised of the primary absorbing constituents of the atmosphere, namely $CO_2$, $H_2O$, $O_3$ and $CH_4$. Spectral data for the fluorinated species was obtained through the GEISA online database (24).

Measurements were taken using an experimental configuration consisting of a Bruker spectrometer (Model IFS/ 66) which was fitted with a mid-infrared (MIR) source used to generate radiation which passed through a removable, evacuable 15.9 cm gas cell. The cell was fitted with KBr windows which allow excellent transmission between 400 and 40000 cm$^{-1}$. The choice of source and window were

selected so as to admit radiation across the mid IR range where bands of interest were known to occur. Room temperature (296 ± 2 K) measurements were carried out between 400 and 2000 cm$^{-1}$ at a spectral resolution of 0.1 cm$^{-1}$ and compiled from the averaged total of 128 scans to 32 background scans at a scanner velocity of 1.6 kHz.

Gas mixtures were made using between 12 and 307 Torr of NF$_3$, 8 and 675 Torr of SF$_6$, 6 and 77 Torr of CFC-115 and 2 and 460 Torr diluted up to an atmosphere using nitrogen. Multiple mixtures were made up so that cross sections could be obtained at selected wavelengths by taking the slope of the linear regression of the corresponding peak absorbances against concentration according to the Beer – Lambert equation as adapted from E2.3:

$$A = \sigma l c \qquad\qquad (E2.4)$$

where A is the absorbance, σ is absorption cross section in cm$^{-2}$, c is concentration in molecule cm$^{-3}$ and l is path length in cm. The expression is accurate for values of A < 1. Concentrations were determined using the peak cross sections of each species and the Beer - Lambert law. Saturation of peaks, (occurring where A > 1) was monitored according to the expression E2.4 as deviation from linearity.

## 2.4 Vacuum System and Gas-Handling

The gas–handling set-up consisted of a system of glass tubing maintained to < 10$^{-3}$ Torr by a diffusion pump (Edwards, Model Diffstack MK2 63) backed by a rotary pump (Edwards, Model E2M80). High vacuum 'O' ring taps connected to the system allowed for the passage of pure gases and mixtures in and out of the system.

The gas mixtures required for each experiment were made up using such a vacuum line and stored in 10 litre glass bulbs attached to the system. Where further purification was required, freeze pump thaw was performed on gas samples stored in additional, smaller bulbs on the lower tier of the line.

## 2.5    Materials

For all experiments reactant gas mixtures were prepared on the all-glass vacuum lines: the gases $N_2$ (99.9999 %, BOC), $NF_3$ (99.99 %, BOC), $SF_6$ (99.99 %, BOC) and He (99.9999 %, BOC) were used without further purification. Samples of CFC-115 and $SF_5CF_3$ were provided by Professor William Sturges (University of East Anglia). These were purified by freeze–thaw distillation on a glass vacuum line and the purity confirmed by IR spectroscopy.

The metal-atom precursors used sodium (98% Sigma-Aldrich), sodium iodide (Sigma-Aldrich 98%), potassium iodide (Sigma-Aldrich 99%), magnesium acetyl acetonate (Sigma- Aldrich 98%) and ferrocene (Sigma-Aldrich 98 %), were purified under vacuum (heating where appropriate) for at least an hour before kinetic experiments commenced.

## List of References

1.      Mortimer, R.G. 12 - The Rates of Chemical Reactions. *In:* R.G. Mortimer, ed. *Physical Chemistry (Second Edition).* Burlington: Academic Press, 2000, pp.401-434.

2.      Riley, S.J. and D.R. Herschbach. Molecular Beam Kinetics: Long-Lived Collision Complexes in Reactions of K, Rb, and Cs with $SnCl_4$ and $SF_6$. *J. Chem. Phys.*, 1973, **58**(1), pp.27-43.

3.      Duren, R., M. Knepper, A. Linskens, S. Milosevic, S. Mohr and H.J. Waldapfel. Differential Cross Sections for Reactive Scattering of Na from $SF_6$. *J. Chem. Phys. A.*, 1993, **97**(10), pp.2059-2062.

4.      Sarathy, S.M., P. Osswald, N. Hansen and K. Kohse-Hoinghaus. Alcohol Combustion Chemistry. *Prog. Energ. Combust.*, 2014, **44**, pp.40-102.

5.      Howard, C.J. Kinetic Measurements Using Flow Tubes. *J. Phys. Chem.*, 1978, **83**(1), pp.3 - 9.

6.      Plane, J.M.C. and M. Helmer. Laboratory Study of the Reactions $Mg + O_3$ and $MgO + O_3$ Implications for the Chemistry of Magnesium in the Upper Atmosphere. *Faraday Discuss.*, 1995, **100**, pp.411 - 430.

7.      Plane, J.M.C. *Magnesium Chemistry in the Upper Atmosphere.* Leeds: University of Leeds, 2010.

8.      Kaufman, F. Rates of Elementary Reactions - Measurement and Application. *Science*, 1985, **230**(4724), pp.393-399.

9.      Whinnery, J.R., J. Ausubel and H.D. Langford. *Lasers: Invention to Application.* Washington: National Academy Press, 1988.

10. Chowdhury, A.M.S. and M. Kawasaki. Laser-induced Fluorescence Studies on the Physical Quenching of Superthermal $O(D^{-1})$. *Laser Physics*, 1996, **6**(6), pp.1175-1179.

11. Biennier, L., F. Salama, L.J. Allamandola and J.J. Schererb. Pulsed Discharge Nozzle Cavity Ringdown Spectroscopy of Cold Polycyclic Aromatic Hydrocarbon Ions. *J. Chem. Phys.*, 2003, **118**(17), pp.8763-8772.

12. Morris, R.A., A.A. Viggiano, S.T. Arnold and J.F. Paulson. Chemistry of Atmospheric Ions Reacting with Fully Fluorinated Compounds. *Int. J. Mass Spectrom. Ion Processes*, 1995, **149–150**, pp.287-298.

13. Sorokin, V.I., N.P. Gritsan and A.I. Chichinin. Collisions of $O(^1D)$ with HF, $F_2$, $XeF_2$, $NF_3$, and $CF_4$: Deactivation and Reaction. *J. Chem. Phys.*, 1998, **108**(21), pp.8995-9003.

14. Lakowicz, J.R. *Principals of Fluoresence Spectroscopy.* Baltimore: Springer, 2010.

15. Whalley, C.L., J.C.G. Martın, T.G. Wright and J.M.C. Plane. A Kinetic Study of $Mg^+$ and $Mg^-$ Containing Ions Reacting with $O_3$, $O_2$, $N_2$, $CO_2$, $N_2O$ and $H_2O$: Implications for Magnesium Ion Chemistry in the Upper Atmosphere. *Chem. Phys. Phys. Chem.*, 2011, **13**, pp.6352–6364.

16. Plane, J.M.C., T. Vondrak and S. Broadley. Kinetic Study of the Reaction $Ca^+$ + $N_2O$ from 188 to 1207 K. *J. Phys. Chem.*, 2006, **110**, pp.7874 - 7882.

17. Plane, J.M.C., R.M. Cox and R.J. Rollason. Metallic Layers in the Mesopause and Lower Thermosphere Region. *In:* A. Burns, T. Killeen and D. Rees, eds. *Ionospheric/Thermospheric/Mesospheric Coupling*. Oxford: Pergamon Press Ltd, 1999, pp.1559-1570.

18. Fthenakis, V., D.O. Clark, M. Moalem, P. Chandler, R.G. Ridgeway, F.E. Hulbert, D.B. Cooper and P.J. Maroulis. Life-Cycle Nitrogen Trifluoride Emissions from Photovoltaics. *Environ. Sci. Technol.*, 2010, **44**, pp.8750 - 8757.

19. Plane, J.M.C. A Kinetic Study of the Reaction Li + $N_2O$: Non-Arrhenius Behavior over the Temperature Range 363-900 K. *J. Phys. Chem.*, 1987, **91**, pp.6552 - 6557

20. Lu, H.C., H.K. Chen, H.F. Chen, B.M. Cheng and J.F. Ogilvie. Absorption Cross Section of Molecular Oxygen in the Transition E $3\Sigma u$- v = 0 – X $3\Sigma g$- v = 0 at 38 K. *Astron. Astrophys.*, 2010, **520**, p.A19.

21. Lagemann, R.T. and E.A. Jones. The Infrared Spectrum of Sulfur Hexafluoride. *J. Chem. Phys.*, 1951, **19**(5).

22. Sawant, S.D., R. Baravkar and R.N. Kale. FT-IR Spectroscopy: Principle, Technique and Mathematics *Int. J. Pharm. Biol. Sci.*, 2011, **2**(1), pp.513 - 519.

23. Chu, P.M., F.R. Guenther, G.C. Rhoderick and W.J. Lafferty. *Qunatitative Infrared Database*. 2000.

24. *GEISA : Spectroscopic Database*. [Accessed 10/2014]. Available from: http://www.pole-ether.fr/ether/pubipsl/GEISA/geisa_crossIR_frame_2011_uk.jsp. 2011.

# Chapter 3: Chemistry of SF₆, NF₃, SF₅CF₃ and CFC-115 in the Mesosphere

The perfluorinated compounds (PFCS), $SF_6$, $NF_3$, $SF_5CF_3$ and CFC-115 ($CF_3CF_2Cl$) are characterised by extremely long atmospheric lifetimes ($\tau$). This is primarily due to their chemical inertness, meaning they do not undergo destructive processes in the lower atmosphere and that loss processes in the mesosphere become rate determining. The processes studied in this chapter are presented as potential sinks affecting the studied PFCs ($SF_6$, $NF_3$, $SF_5CF_3$ and $CF_3CF_2Cl$) in the mesosphere.

## 3.1 Previous Measurements

The chemical and photochemical processes discussed in this chapter were studied with the purpose of refining the atmospheric lifetimes ($\tau$) and consequent global warming impact of $NF_3$, $SF_6$, $SF_5CF_3$ and CFC-115. $\tau$ is derived from inputting experimentally determined unknowns into a chemical transport model using the methods described in Chapter 4.

For the aforementioned PFCs, photolysis by UV radiation, reactions with O($^1$D) and electron attachment are currently acknowledged to be effective processes of destruction in the upper atmosphere (1, 2). In this study, we firstly consider the potential removal of PFCs through reaction with metal atoms which exist in significant quantities in the upper atmosphere as a result of the ablation of incoming cosmic dust (3), a process which is discussed in greater detail in Chapter 1. Secondly some discussion on removal photolysis by Lyman-$\alpha$ photons (121.6 nm) is provided.

Atmospheric removal of very long lived species by reaction with meteoric metals has never previously been considered. Determination of the relative importance of such processes should consequently be established as their omission could

potentially result in an overestimation of atmospheric lifetimes. The atmospheric implications of this chapter's findings will be discussed in Chapter 5.

Each reaction listed in Table 3.1 has been explored experimentally in this chapter and the atmospheric implications of these results discussed in Chapter 5. Previous measurements, where they exist, are presented in Table 3.1 along with reaction enthalpies calculated from tabulated bond strengths obtained from the Computational Chemistry Comparison and Benchmark Database (4).

**Table 3.1** A list of the PFC – metal reactions to be studied in this chapter. Where available, previously published measurements are stated, including reaction enthalpies which have been calculated from tabulated bond strengths (5).

| No. | Reaction | $k/$ cm$^3$ molecule$^{-1}$ s$^{-1}$ | $\Delta H_r$ (298 K)/ kJ mol$^{-1}$ |
|---|---|---|---|
| R3.1 | $Na + NF_3 \rightarrow NaF + NF_2$ | | -223 |
| R3.2 | $K + NF_3 \rightarrow KF + NF_2$ | | -235 |
| R3.3 | $Fe + NF_3 \rightarrow FeF + NF_2$ | | -209 |
| R3.4 | $Mg + NF_3 \rightarrow MgF + NF_2$ | | -193 |
| R3.5 | $Na + SF_6 \rightarrow NaF + SF_5$ | $k_{(280\ K)} = 1.2$ x $10^{-12\ a}$ $k_{(610\text{-}870\ K)} = (1.3 - 71.2)$ x $10^{-11\ b}$ | -80.4 |
| R3.6 | $K + SF_6 \rightarrow KF + SF_5$ | $k_{(691\text{-}810\ K)} =$ $(9.9 - 13.5)$ x $10^{-11\ c}$ | -74.9 |
| R3.7 | $Fe + SF_6 \rightarrow FeF + SF_5$ | | -202.7 |
| R3.8 | $Mg + SF_6 \rightarrow MgF + SF_5$ | | -198.2 |
| R3.9 | $Na + SF_5CF_3 \rightarrow NaF + SF_4CF_3$ | | -75.9 |
| R3.10 | $Na + CF_3CF_2Cl \rightarrow NaCl + CF_3CF_2$ | | -25.0 |

| No. | | $\Delta_r H(298\,K)$ |
|---|---|---|
| R3.11 | K + CF₃CF₂Cl → KCl + CF₃CF₂ | -46.0 |

| No. | PFC + Lyman-$\alpha$ (121.6 nm) | $\sigma$/ cm$^2$ |
|---|---|---|
| R3.11 | $K + CF_3CF_2Cl \rightarrow KCl + CF_3CF_2$ | -46.0 |
| R3.12 | $NF_3$ | |
| R3.13 | $SF_6$ | $1.8 \times 10^{-18}$ [d] <br> $1.2 \times 10^{-18}$ (121 nm) [e] |
| R3.14 | CFC-115 | $4.6 \times 10^{-18}$ [d] |

[a] Talcott *et al.*, 1986 (6)      [b] Husain and Marshall, 1985 (7)

[c] Husain and Lee, 1987 (8)      [d] Ravishankara *et al.*, 1993 (9)

[e] Zetzsch, 1989 (10)


## 3.2 *Ab. initio* Quantum Calculations

In order to ascertain the viability of the PFC + metal reactions and fully interpret their kinetics, a new set of quantum calculations were performed by J. M. C. Plane (Per. Comm., University of Leeds) (11). These were obtained with the Gaussian 09 suite of programs (12) using the very accurate CBS–QB3 level of theory.

$\Delta_r H$(298 K) was calculated to be -217,-234,-199 and-214 kJ mol$^{-1}$ for the reactions of Mg, Fe, Na and K with $NF_3$, respectively. Comparison with the experimental values listed in Table 3.1 shows satisfactory agreement (within 9 kJ mol$^{-1}$) for R3.1, R3.2 and R3.4. The experimental $\Delta H_r$(298 K) for R3.3 is 21 kJ mol$^{-1}$ larger, which implies that the FeF bond strength is closer to approximately $D^o$(298 K) = 460 kJ mol$^{-1}$, compared with the tabulated value of 477 kJ mol$^{-1}$ (5).

Theoretical enthalpies were obtained as the sum of vibrational zero point and electronic energies obtained from frequency and single point energy calculations respectively. Molecular geometries were first optimised and checked for wave function stability before their respective vibrational frequencies were calculated. For reactions of $NF_3$ and $SF_6$, the potential energy surfaces (PES) were also obtained supplied by J. M. C. Plane (Per. Comm., University of Leeds), to gain a deeper

understanding of the reaction kinetics of R3.1 – R3.8. The PESs for R3.1 –R3.8 were calculated at the MP2/6-311+g(2d,p) level of theory, where the Møller-Plesset correlation energy correction is used to take account for the switch from the covalent nature of the surface in the entrance channel to the ionic exit channel when the metal fluoride has formed. At this level of theory, the calculated reaction enthalpy changes (including a counterpoise correction for basis set superposition error) agree well with the literature values for R3.5, R3.6 and R3.8 (5); $\Delta_r H^{\ominus}$(Na + $SF_6$) =-90 (-85); $\Delta_r H^{\ominus}$(K + $SF_6$) =-98 (-97); $\Delta_r H^{\ominus}$(Mg + $SF_6$) =-74 (-71) kJ mol$^{-1}$.  At each point on the PES a new initial guess for the Hartree-Fock wave function was generated.  The geometry of the $SF_5$/ $NF_2$ moiety on the x axis was kept frozen for simplicity. The potential energy surfaces are illustrated later in the chapter.

## 3.3  Kinetics of Reactions of PFCs with Meteoric Metals

A full description of both systems and the experimental schemes used for each reaction is given in Chapter 2.

Reactions R3.1 – R3.11 were studied using a pulsed laser photolysis – laser induced fluorescence (PLP – LIF) system.  This technique measures rate coefficients by monitoring the decay of a metal species generated through the photolysis of an organometallic precursor by an excimer laser. The metal species was then probed using a dye laser and the resulting fluorescence measured by a photomultiplier tube (PMT).

Reactions R3.1 and R3.5 were also studied using a fast flow tube (FFT) system in which sodium atoms are generated through the thermolysis of a solid sodium sample, contained within an aluminium oxide crucible, in a side arm of the flow tube. The atoms are entrained in a flow of $N_2$ bath gas and transported down the tube where they mix with reactant gases added downstream via side-ports. As with the PLP-LIF system, the sodium atoms are detected using laser induced fluorescence (LIF).

### 3.3.1  Analysis of Experimental Results

**3.3.1.1 Pulsed Laser Photolysis – Laser Induced Fluorescence**

In order to extrapolate rate coefficients down to mesospheric temperatures (~ 140 – 280 K), the temperature dependencies of the reactions must be known. In this study, the PLP-LIF system was used to study the reactions R3.1 – R3.11 because this technique enables rate coefficients to be measured over a suitably large temperature range.

The metal species of interest was monitored using the set–up and LIF conditions described in the previous chapter. The loss of this metal through reaction with the PFC can be described by a pseudo first – order decay rate $k'$, as the concentration of the PFC was kept in excess of that of the metal. Decay profiles were generated by increasing the delay between the excimer and dye lasers, resulting in the LIF signal decaying exponentially with time giving:

$$\frac{[X]_t}{[X]_0} = \frac{S_t}{S_0} = \exp(-k' t) \qquad\qquad (E3.1)$$

where $[X]_t$ and $[X]_0$ are the concentrations of metal atom X (X=Na, K, Mg or Fe), with corresponding LIF signals $S_t$ and $S_0$, at the delays $t$ and 0 respectively.
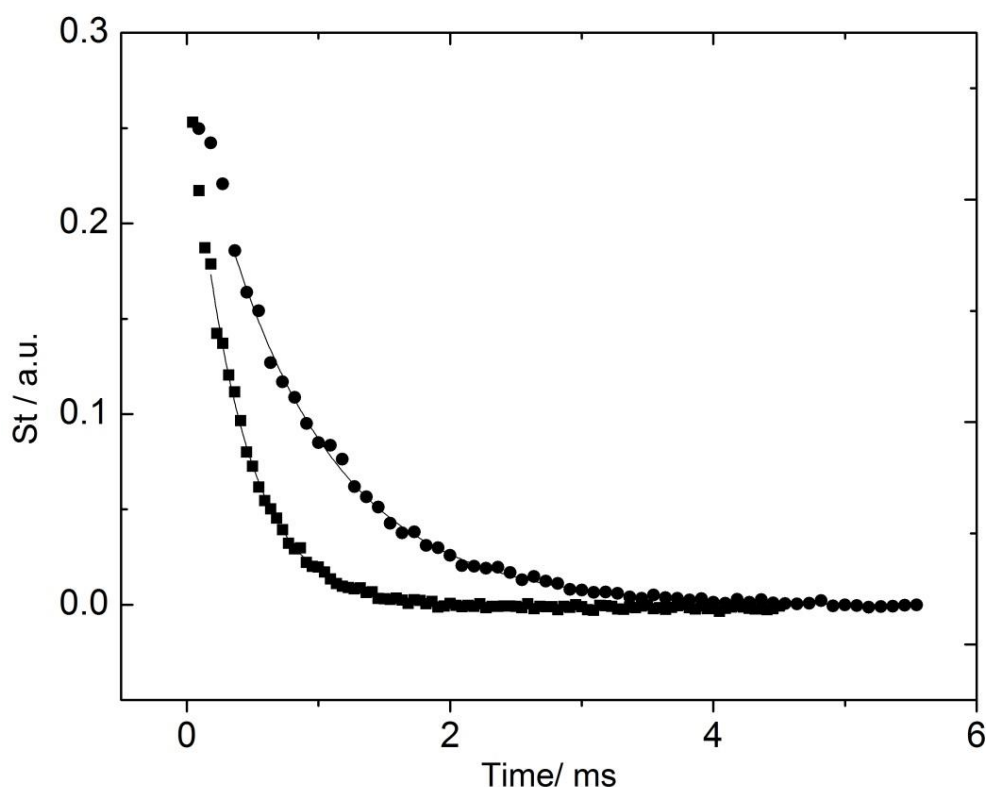
**Figure 3.1** Time-resolved LIF signals corresponding to the decay of K probed non –
resonantly at 404.4 nm K($5^2P_{3/2}$-$4^2S_{1/2}$) in the presence of $3.9 \times 10^{13}$ molecule
cm$^{-3}$ (circles) and $1.2 \times 10^{14}$ molecule cm$^{-3}$ (squares) of $NF_3$ at 400 K. The solid
lines show the fits to the exponential form Ae$^{-k't}$ and the different timescales
of the reaction are apparent.

Figure 3.1 shows typical examples of the exponentially decaying time-resolved LIF

signals representing loss of the studied metal through removal by a reaction with a

PFC. Because the reaction was carried out under pseudo first order conditions, the

second order rate coefficient $k$, can be obtained using the expression:

$$k' = k'_{\text{diff,M}} + k[\text{PFC}] \tag{E3.2}$$

where the decay rates $k'$ are previously obtained by fitting the decays of the LIF

signals such as those shown in Figure 3.1 to the simple exponential form Ae$^{-k't}$.

Some jitter in the initial few points of the decay was occasionally observed. This can

be caused by error within the delay system of the experimental set – up, where the

initial timings between the excimer and dye lasers firing are not properly

controlled. It may also be due to temporary 'blinding' of the PMT caused by the

formation of electronically excited Na, potentially resulting in a short lived flash of light. The effect of the latter is more apparent on the shorter lived decays. Consequently, excluding the initial LIF decay points from the fittings meant this jitter did not contribute to the uncertainty.

$k'_{\text{diff,M}}$ describes the rate of diffusion of the metal atom, M, out of the volume defined by the intersection of the dye and excimer beams and within the field of view of the PMT (13). The measured $k'_{\text{diff,M}}$ term for the PLP – LIF reactions studied here typically fell within the range ~ 400-15000 s$^{-1}$. The different experimental conditions used accounts for some of this variation; however, loss of the metal due to reactions with the precursor or its photolysis products makes a more significant contribution. As a result we include the term, $k'_{\text{loss}}$. This indicates that Na is being removed by a process independent of R3.1, occurring at a rate faster than that of diffusion. Larger values of $k'_{\text{diff,M}} + k'_{\text{loss}}$ are obtained at lower temperatures where formation of a smoke through polymerisation of the NaI precursor is known to occur readily (14). This NaI smoke is potentially reactive with Na.
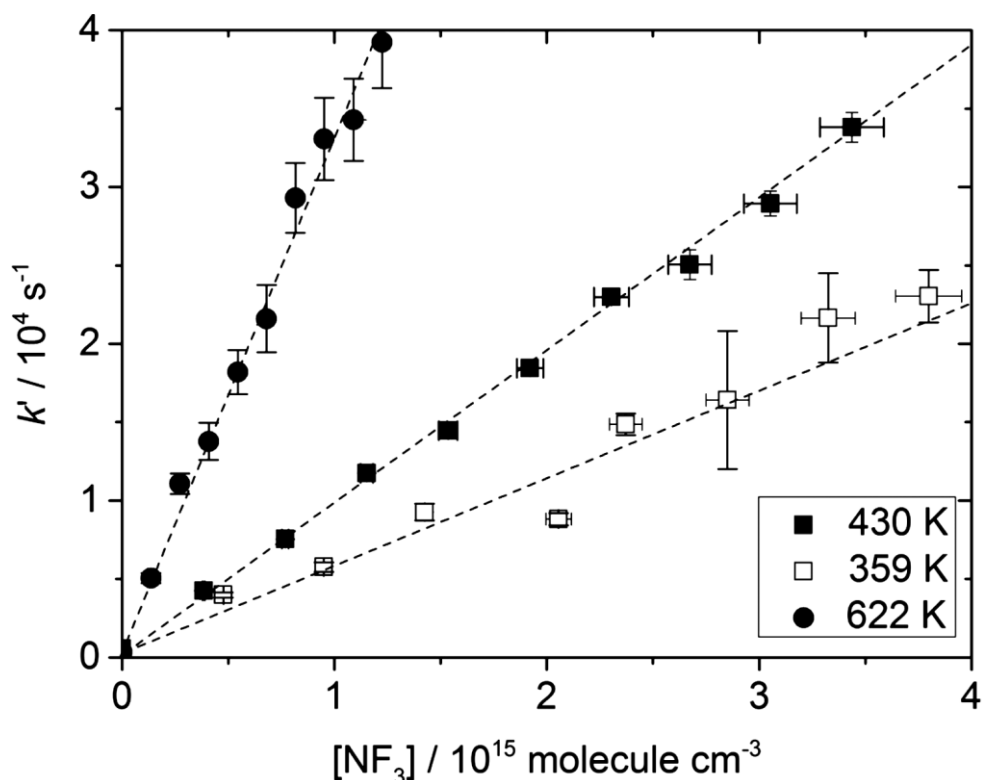
**Figure 3.2.** Bimolecular plots showing *k'* versus [NF₃] for the reaction between Na and NF₃ at 359 K (open squares), 430 K (filled squaress) and 622 K (filled circles). The solid lines are weighted linear regressions applied to the experimental data and a significantly larger intercept is observed on the 430 K data.

From E3.2, a plot of *k'* against [PFC] yields a line with slope *k* and intercept $k'_{\text{diff,M}} + k'_{\text{loss}}$. A typical example of these plots is shown in Figure 3.2. These bimolecular plots show results for R3.1 at three temperatures (359, 430 and 622 K) where error in *k* was propagated from the weighted linear regression of *k* and the determined uncertainty in [PFC].

### 3.3.1.2 Fast Flow Tube

Reactions R3.1 and R3.5 were also studied using the fast flow tube. This alternative methodology was used to test agreement between the two techniques. Due to the constraints of the apparatus measurements were only carried out over the range 197 – 296 K.

Each set of flow tube experiments was conducted by recording the Na LIF signal as a function of the concentration of the PFC at a fixed reaction time. As with the PLP – LIF experiments, loss of Na can be described by the pseudo first order rate coefficient, $k'$, as the concentrations of $SF_6$ and $NF_3$ were kept in excess of the Na concentration:

$$k't = -\ln\left(\frac{[\text{Na}]^t_{\text{PFC}}}{[\text{Na}]^t_0}\right) = -\ln\left(\frac{S^t_{\text{PFC}}}{S^t_0}\right)$$
(E3.3)

where $k'$ is the pseudo first order loss rate, $t$ is the reaction time, and $[\text{Na}]^t_{\text{PFC}}$ and $[\text{Na}]^t_0$ are respectively the Na concentrations with and without any PFC present at time $t$. $S^t_{\text{PFC}}$ and $S^t_0$ are the LIF signals proportional to these concentrations. Depletion of the sodium precursor over the duration of experiments results in the exponential decay of the Na LIF signal over time. In order to minimise the impact of this effect on uncertainty, every measurement of $S^t_{\text{PFC}}$ for a particular PFC concentration was carried out between two measurements of $S^t_0$, in such a way that that the value of $S^t_0$ corresponding to $S^t_{\text{PFC}}$ in equation E3.3 could be interpolated from the adjacent values.

To ensure the applicability of the above expression, a laminar flow profile within the flow tube was maintained. This was achieved by keeping velocity between 14 and 45 m s$^{-1}$ so that Reynold's number, Re, was kept within the laminar region (< 2300). Re is defined by:

$$\text{Re} = \frac{\rho v D_H}{\mu}$$
(E3.4)

where $\rho$ and $\mu$ are the gas density and dynamic viscosity (approximated here for nitrogen as 1.25 kg m$^{-3}$ and 1.7 x 10$^7$ kg m$^{-1}$s$^{-1}$ respectively). $D_H$ is the hydraulic diameter of the pipe and v is the velocity.

The reaction time $t$, is determined from the calculated flow velocity down the tube, over the distance between the reactant gas point of entry to the Na point of detection. As a result of laminar flow conditions (see Chapter 2 and Figure 3.3), a parabolic velocity flow profile exists within the flow tube and the calculated flow velocity is only achieved along the centre axis, while velocity at the walls is zero.

This effect can accurately be accounted for through application of the centroid correction coefficient (0.63) (15). An additional uncertainty in $t$ arises from the reactant mixing time, $t_{mix}$. This is defined as the amount of time required for the PFC to radially diffuse from its point of injection at the wall of the tube into the main bath flow. It can be estimated using the following expression for 3-dimensional diffusion:

$$t_{\text{mix}} = \frac{x^2}{6D} \tag{E3.5}$$

where $x$ is the radial distance of the flow tube; this value was taken to be 2.5 cm, equivalent to two – thirds of the tube diameter, in order to ensure complete mixing (16). D is the diffusion coefficient of the PFC in the bath gas $N_2$ (approximated here as the diffusion coefficient of $CO_2$ in $N_2$, 0.16 $cm^2\,s^{-1}$ at 1 bar) (5). Mixing time was derived as a percentage of $t$ across all measurements over the range of pressures and flows used and determined to be approximately 5% of $t$ on average. A corresponding correction factor of 0.95 was subsequently applied.
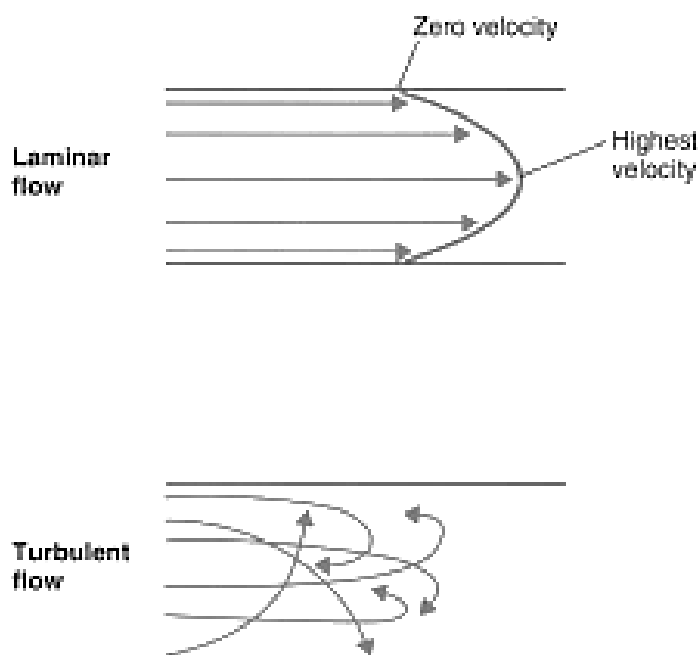


**Figure 3.3** Depiction of the differences between laminar and turbulent flows as applied to a flow tube (17).

Metal uptake on the flow tube walls is an extremely efficient process and therefore source of loss. Assuming an uptake coefficient on the walls close to unity, the loss rate is diffusion controlled and can be calculated using the following equation:

$$D_{Na-N_2} = k_{diff,Na} P \frac{r^2}{5.81} \qquad \text{(E3.6)}$$

where $P$ is the total pressure and $r$ is the flow tube radius. Unlike the pseudo first order rate

expression E3.2, the $k_{diff}$ term does not feature in E3.3 which has been derived by subtracting the integral of the Na loss rate in the absence of reactant from the Na loss rate in the presence of reactant. Thus, loss of Na due to diffusion and reaction with precursor is cancelled out (18), so that:

$$k' = k \text{ [PFC]} \qquad \text{(E3.7)}$$

Consequently, a plot of the observed quantity $\ln( S_{PFC}^t/S_0^t)$ versus [PFC] produces a straight line of slope $kt$, as illustrated in Figure 3.4. The values of $k$ at 297, 222 and 197 K are listed in Table 3.2.
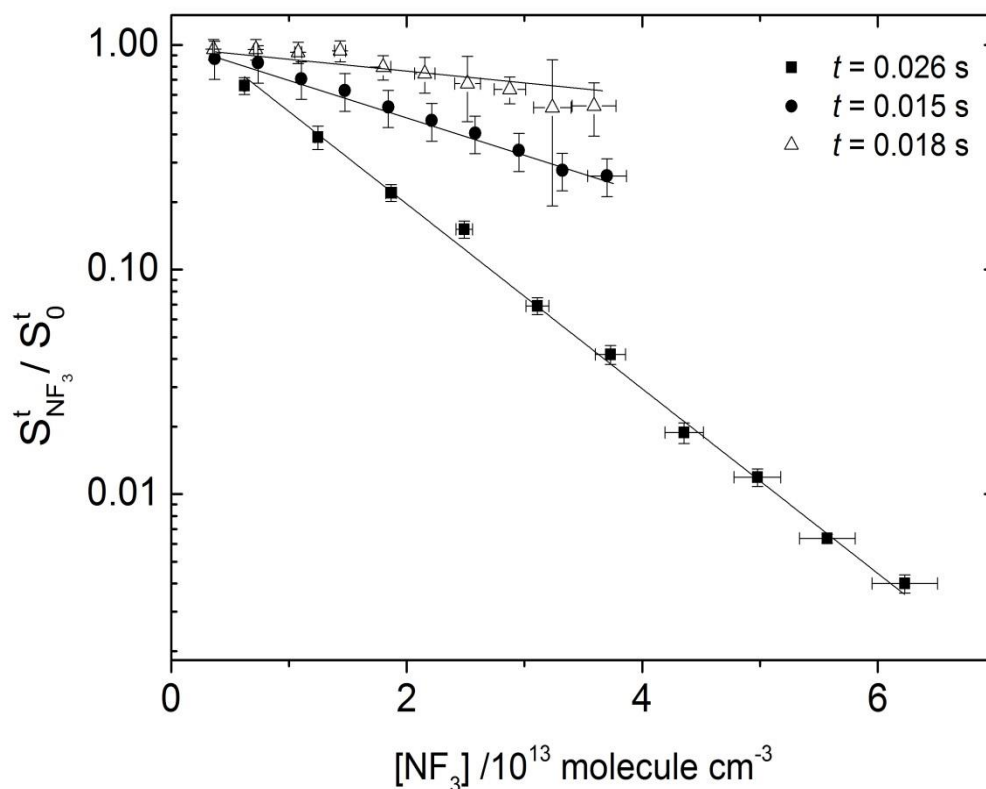
**Figure 3.4.** Plots of observed change in $S_{NF_3}^t/S_0^t$ with [NF$_3$] for the reaction of Na with NF$_3$ at the reaction times $t$ = 0.018 s (triangles), $t$ = 0.015 s (filled circles) and $t$ = 0.026 s (filled squares). $S_{NF_3}^t$ refers to the Na LIF signal in the presence of NF$_3$, and $S_0^t$ refers to the Na LIF signal in the absence of NF$_3$. The solid lines are weighted linear regressions to experimental data.

### 3.3.1.3 Comparison of Techniques

The temperature dependencies of reactions R3.1 – R3.11 were studied over the largest achievable temperature range. Measurements were primarily gathered using the PLP-LIF system which, unlike the fast flow tube has a self-contained furnace enabling rate coefficients to be measured over a substantial temperature range.

Measureable temperature limits are dictated by many factors, most of which are discussed in the previous chapter and include safety, coolant used, heat capacity of the apparatus and so forth. Further restrictive factors were encountered

throughout the duration of experiments. The reaction of K with $NF_3$ was found to decrease markedly at temperatures above about 650 K. This appeared to be due to the thermolysis of $NF_3$ on the hot reactor walls. This process, which produces $N_2$ and $F_2$, is well documented (17) and known to occur rapidly at temperatures > 600 K on metal/oxide surfaces. An observable but less pronounced effect was noted for the reaction with Na. We attribute this significant difference in the thermolysis efficiencies of $NF_3$ to the varying wall characteristics within the reactor. This can occur through deposition of the precursor onto the reactor walls, meaning that there may be significant variation of destruction efficiency depending on whether KI or NaI is coating the reactor walls. Thermolysis efficiency of $NF_3$ relative to a variety of metals has been studied previously, producing widely varying results (19).

For Mg and Fe + $NF_3$, the experimental temperature range was restricted to < 700 K because the MgAcAc and ferrocene precursors were found to rapidly decompose at higher temperatures. These reactions are both much slower than those with Na and K; since reliable rate coefficients smaller than ~$10^{-15}$ cm$^3$ molecule$^{-1}$ s$^{-1}$ could not be measured with the present technique, this constrained the measurements of $k_3$ and $k_4$ to temperatures above ~290 K.

For R3.1, R3.2, R3.4 – R3.6 and R3.8 – R3.11, the residence time within the reaction chamber was sustained between around 0.2 and 0.5 seconds. This proved to be an optimal timescale for maintaining a metal LIF signal. Loss of the metal precursor vapour by deposition to the reactor walls became too significant at longer times, determining 0.5 seconds to be the upper limit for residence time. However, for R3.3 and R3.7, residence times were significantly longer, ranging from 2.8 to 6.3 seconds.  This was because ferrocene possesses a vapour pressure significantly higher than the other precursors.

Second order kinetics for R3.1 and R3.2 were confirmed through the execution of pressure dependant studies between 268-348 K and 255 – 560 K for R3.1 and R3.2 respectively. The results obtained from this study are presented in Table 3.2 and demonstrate that there was no significant change in rate coefficient when the

reaction pressure was varied by up to a factor of three. All remaining reactions were consequently assumed not to be pressure dependant.

**Table 3.2** Experimental determination of rate coefficients for the reactions of $NF_3$ with Na as a function of pressure and temperature where quoted uncertainties are derived as a combination of error from the weighted linear regressions in kinetic plots and that calculated from concentration.

| P/ Torr | $k/ 10^{-12}$ cm$^3$ molecule$^{-1}$ s$^{-1}$ | | |
| --- | --- | --- | --- |
| | T/ K | 268 | 348 | 338 |
| 20 | 3.98 ± 0.58 | 6.28 ± 0.47 | 4.05 ± 0.60 |
| 25 | 4.05 ± 0.38 | 6.72 ± 0.29 | 4.23 ± 0.36 |

**Table 3.3** Experimental determination of rate coefficients for the reactions of $NF_3$ with K as a function of pressure and temperature where quoted uncertainties are derived as a combination of error from the weighted linear regressions in kinetic plots and that calculated from concentration.

| P/ Torr | $k/ 10^{-11}$ cm$^3$ molecule$^{-1}$ s$^{-1}$ | | |
| --- | --- | --- | --- |
| | T/ K | 255 | 420 | 560 |
| 5 | 0.46 ±0.07 | 2.34 ± 0.38 | 5.28 ± 0.72 |
| 15 | 0.48 ±0.06 | 2.08 ±0.25 | 4.74 ±0.60 |

### 3.3.2  Summary of Results: Reactions of Metals with Fluorinated Species

Reactions R3.1 and R3.5 were studied using both the PLP-LIF apparatus and the fast flow tube. The temperature dependence was explored with experiments carried out over a temperature range of 197 – 879 K. The measured rate coefficients are presented in Tables 3.4 – 3.14 as a function of temperature, where the given uncertainty encompasses the error of the weighted least-square linear fits to the kinetic plots (e.g. Figure 3.2) and the uncertainty derived from the concentrations of gas mixtures to a 95% confidence level.

**Table 3.4**  Experimental determination of the second order rate coefficient for the reactions of $NF_3$ with Na as a function of temperature, where quoted uncertainties are derived as a combination of systematic experimental error and from kinetic plots.

| $T$/ K | $k$ / $10^{-11}$ $cm^3$ molecule$^{-1}$ s$^{-1}$ |
|--------|--------------------------------------------------|
| 197 | $0.14 \pm 0.04$[a] |
| 214 | $0.12 \pm 0.01$ |
| 222 | $0.23 \pm 0.09$[a] |
| 248 | $0.27 \pm 0.02$ |
| 297 | $0.30 \pm 0.08$[a] |
| 325 | $0.37 \pm 0.03$ |
| 359 | $0.55 \pm 0.06$ |
| 430 | $0.95 \pm 0.08$ |
| 506 | $2.38 \pm 0.20$ |
| 622 | $3.38 \pm 0.30$ |

[a] Rate coefficients measured with the fast flow tube. All other measurements were obtained using the PLP-LIF technique.

**Table 3.5** Experimental determination of the second order rate coefficient for the reactions of $NF_3$ with K as a function of temperature, where quoted uncertainties are derived as a combination of systematic experimental error and from kinetic plots.

| $T/$ K | $k / 10^{-11}$ cm$^3$ molecule$^{-1}$ s$^{-1}$ |
|---|---|
| 210 | $0.22 \pm 0.03$ |
| 252 | $0.46 \pm 0.07$ |
| 285 | $0.64 \pm 0.10$ |
| 388 | $1.91 \pm 0.29$ |
| 421 | $2.43 \pm 0.38$ |
| 483 | $3.74 \pm 0.57$ |
| 528 | $5.03 \pm 0.77$ |
| 560 | $5.28 \pm 0.72$ |
| 626 | $7.25 \pm 0.12$ |

**Table 3.6** Experimental determination of the second order rate coefficient for the reactions of $NF_3$ with Fe as a function of temperature, where quoted uncertainties are derived as a combination of systematic experimental error and from kinetic plots.

| $T/$ K | $k / 10^{-14}$ $cm^3$ $molecule^{-1}$ $s^{-1}$ |
|--------|-----------------------------------------------|
| 298 | $0.36 \pm 0.05$ |
| 353 | $0.70 \pm 0.08$ |
| 412 | $1.46 \pm 0.15$ |
| 428 | $2.09 \pm 0.12$ |
| 453 | $3.37 \pm 0.87$ |
| 531 | $5.31 \pm 1.02$ |
| 592 | $16.1 \pm 1.2$ |

**Table 3.7** Experimental determination of the second order rate coefficient for the reactions of $NF_3$ with Mg as a function of temperature, where quoted uncertainties are derived as a combination of systematic experimental error and from kinetic plots.

| $T/$ K | $k/ 10^{-15}$ $cm^3$ $molecule^{-1}$ $s^{-1}$ |
|--------|-----------------------------------------------|
| 312 | $0.37 \pm 0.07$ |
| 349 | $1.3 \pm 0.2$ |
| 423 | $8.2 \pm 1.2$ |
| 562 | $87 \pm 14$ |
| 622 | $185 \pm 30$ |
| 693 | $332 \pm 51$ |

**Table 3.8** Experimental determination of the second order rate coefficient for the reactions of $SF_6$ with Na as a function of temperature, where quoted uncertainties are derived as a combination of systematic experimental error and from kinetic plots.

| $T/$ K | $k/10^{-12}$ cm$^3$ molecule$^{-1}$ s$^{-1}$ |
|:---:|:---:|
| 212 | $0.10 \pm 0.01$ |
| 248 | $0.40 \pm 0.04$ |
| 290 | $0.98 \pm 0.06$[a] |
| 327 | $1.86 \pm 0.15$ |
| 396 | $4.63 \pm 0.44$ |
| 418 | $4.53 \pm 0.34$ |
| 429 | $6.31 \pm 0.29$ |
| 539 | $15.81 \pm 1.27$ |
| 585 | $32.76 \pm 1.30$ |
| 637 | $59.72 \pm 8.18$ |
| 717 | $68.52 \pm 5.67$ |
| 771 | $32.76 \pm 1.30$ |
| 879 | $87.89 \pm 0.49$ |

**Table 3.9** Experimental determination of the second order rate coefficient for the reactions of $SF_6$ with K as a function of temperature, where quoted uncertainties are derived as a combination of systematic experimental error and from kinetic plots.

| $T$/ K | $k$ / $10^{-11}$ cm$^3$ molecule$^{-1}$ s$^{-1}$ |
|:---:|:---:|
| 207 | 1.21 ± 0.11 |
| 248 | 2.07 ± 0.22 |
| 320 | 3.16 ± 0.28 |
| 340 | 3.49 ± 0.32 |
| 388 | 7.13 ± 0.62 |
| 450 | 9.16 ± 0.78 |
| 486 | 10.96 ± 0.94 |
| 522 | 11.73 ± 0.10 |
| 566 | 15.49 ± 1.43 |
| 687 | 25.39 ± 2.15 |
| 817 | 28.39 ± 2.57 |

**Table 3.10** Experimental determination of the second order rate coefficient for the reactions of $SF_6$ with Fe as a function of temperature, where quoted uncertainties are derived as a combination of systematic experimental error and from kinetic plots.

| T/ K | $k / 10^{-15}$ cm$^3$ molecule$^{-1}$ s$^{-1}$ |
|------|------|
| 350 | 0.92 ± 0.30 |
| 396 | 2.18 ± 0.33 |
| 429 | 3.53 ± 0.38 |
| 461 | 4.06 ± 0.73 |
| 486 | 7.40 ± 1.12 |
| 583 | 21.31 ± 4.35 |

**Table 3.11** Experimental determination of the second order rate coefficient for the reactions of $SF_6$ with Mg as a function of temperature, where quoted uncertainties are derived as a combination of systematic experimental error and from kinetic plots.

| T/ K | $k / 10^{-14}$ cm$^3$ molecule$^{-1}$ s$^{-1}$ |
|------|------|
| 449 | 0.23 ± 0.09 |
| 568 | 1.11 ± 0.39 |
| 631 | 2.54 ± 0.65 |
| 738 | 9.38 ± 1.52 |
| 792 | 23.60 ± 4.26 |

**Table 3.12** Experimental determination of the second order rate coefficient for the reactions of $SF_5CF_3$ with Na as a function of temperature, where quoted uncertainties are derived as a combination of systematic experimental error and from kinetic plots.

| $T/$ K | $k/$ $10^{-12}$ cm$^3$ molecule$^{-1}$ s$^{-1}$ |
|--------|------------------------------------------------|
| 327 | 2.50 ± 0.07 |
| 373 | 4.40 ± 0.32 |
| 417 | 7.84 ± 0.86 |
| 588 | 30.08 ± 1.29 |
| 630 | 51.56 ± 8.31 |
| 714 | 67.93 ± 5.12 |

**Table 3.13** Experimental determination of the second order rate coefficient for the reactions of $CF_3CF_2Cl$ with Na as a function of temperature, where quoted uncertainties are derived as a combination of systematic experimental error and from kinetic plots.

| $T/$ K | $k/$ $10^{-13}$ cm$^3$ molecule$^{-1}$ s$^{-1}$ |
|--------|------------------------------------------------|
| 248 | 0.04 ± 0.01 |
| 342 | 0.41 ± 0.07 |
| 416 | 1.18 ± 0.11 |
| 477 | 2.88 ± 0.26 |
| 573 | 9.29 ± 0.82 |
| 685 | 22.77 ± 2.14 |
| 868 | 50.92 ± 6.90 |

**Table 3.14** Experimental determination of the second order rate coefficient for the reactions of $CF_3CF_2Cl$ with K as a function of temperature, where quoted uncertainties are derived as a combination of systematic experimental error and from kinetic plots.

| $T/$ K | $k/ 10^{-12} cm^3 molecule^{-1} s^{-1}$ |
|--------|------------------------------------------|
| 350 | $0.81 \pm 0.16$ |
| 372 | $1.00 \pm 0.20$ |
| 423 | $1.65 \pm 0.34$ |
| 468 | $3.15 \pm 0.34$ |
| 515 | $4.15 \pm 0.71$ |
| 586 | $7.08 \pm 1.24$ |
| 710 | $18.23 \pm 2.74$ |
| 851 | $19.60 \pm 2.21$ |

### 3.3.3 Temperature Dependence of the Reaction Rate Coefficients

With the exception of R3.5 and R3.6, the rate coefficients studied here have not been measured previously. However in this study of R3.1 good agreement is observed in our measurements between the FFT and PLP-LIF measurements between 190 and 300 K (Tables 3.4 and 3.8). It was not possible to obtain a room temperature measurement using the PLP-LIF apparatus. This was due to the high temperatures within the side arm housing the precursor.

The temperature dependencies of R3.1 – R3.4 are presented in the Arrhenius plots in Figure 3.5. R3.5 – R3.9 are presented in Figure 3.6 and R3.10 – R3.11 in Figure 3.7. For all eleven reactions standard Arrhenius behaviour is observed at temperatures < 500 K. At higher temperatures however, R3.1, R3.2, R3.5, R3.6 and R3.10 exhibit clear curvature. Their rate coefficients were therefore expressed as

the sum of two Arrhenius terms showing the high and low temperature dependence of each coefficient.

The experimental data of R3.3, R3.4, R3.7, R3.8, R3.9 and R3,11 were fitted with the standard single-term Arrhenius expression:

$k_{3.3}$(Mg + NF$_3$, 312 - 693 K) =

$$(9.2 \pm 0.5) \times 10^{-10} \exp(-(32.5 \pm 0.4)/RT) \text{ cm}^3\text{molecule}^{-1}\text{s}^{-1}$$

$k_{3.4}$(Fe + NF$_3$, 298 - 531 K) =

$$(7.8 \pm 0.5) \times 10^{-12} \exp(-(20.5 \pm 2.2)/RT) \text{ cm}^3\text{molecule}^{-1}\text{s}^{-1}$$

$k_{3.7}$(Fe + SF$_6$, 350 - 583 K) =

$$(1.90 \pm 1.01) \times 10^{-12} \exp(-(22.5 \pm 1.9)/RT) \text{ cm}^3\text{molecule}^{-1}\text{s}^{-1}$$

$k_{3.8}$(Mg + SF$_6$, 449 - 792 K) =

$$(1.15 \pm 1.10) \times 10^{-10} \exp(-(42.6 \pm 5.5)/RT) \text{ cm}^3\text{molecule}^{-1}\text{s}^{-1}$$

$k_{3.9}$(Na + SF$_5$CF$_3$, 327 - 875 K) =

$$(6.61 \pm 0.78) \times 10^{-10} \exp(-(15.2 \pm 0.4)/RT) \text{ cm}^3\text{molecule}^{-1}\text{s}^{-1}$$

$k_{3.11}$(K + C$_2$F$_5$Cl, 350 - 851 K) =

$$(1.86 \pm 0.40) \times 10^{-10} \exp(-(16.0 \pm 0.8)/RT) \text{ cm}^3\text{molecule}^{-1}\text{s}^{-1}$$

In order to model the non-Arrhenius behaviour observed at higher temperatures of R3.1, R3.2, R3.5, R3.6 and R3.10, an additional term was added to the standard Arrhenius expression giving k=A.exp(-B/T)+ C.exp(-D/T) and allowing the rate coefficient to be expressed in terms of its high and low temperature dependence. These four parameter Arrhenius expressions were obtained by fitting the low-temperature rate coefficients ($T$ < 500 K) to a single Arrhenius term, and then fitting the residual (i.e. high-temperature component) to a second Arrhenius term. The single Arrhenius term was assigned by systematically incorporating data points across the low temperature range and performing an iterative calculation to assign the residual, obtaining the second term. Values reported here are representative of

lower temperature terms which fall within the linear regime, allowing the high temperature term to converge to a  meaningful parameter within an acceptable level of uncertainty. This outcome is not achievable by applying the fit to the four parameters simultaneously, because the number of unknowns is then a significant fraction of the number of experimental points,  and so this method produces physically unreasonable pre-exponential factors with very large uncertainties. The separation of these terms yields some physical insight into the cause of the non-Arrhenius behaviour. This is discussed later in the chapter.

$$k_{3.1}(Na + NF_3, 197\text{-}622 \text{ K}) = (6.0 \pm 4.1) \times 10^{-10} \exp(-(18.6 \pm 3.8)/ RT) +$$

$$(2.3 \pm 1.4) \times 10^{-11} \exp(-(4.9 \pm 1.2)/ RT) \text{ cm}^3 \text{ molecule}^{-1} \text{ s}^{-1}$$

$$k_{3.2}(K + NF_3, 210\text{-}626 \text{ K}) = (16.0 \pm 5.4) \times 10^{-10} \exp(-(19.1 \pm 1.5)/ RT) +$$

$$(1.3 \pm 0.3) \times 10^{-11} \exp(-(7.2 \pm 0.5)/ RT) \text{ cm}^3 \text{ molecule}^{-1} \text{ s}^{-1}$$

$$k_{3.5}(Na + SF_6, 212\text{-}879 \text{ K}) = (19.0 \pm 17.2) \times 10^{-10} \exp(-(28.7 \pm 6.7)/ RT) +$$

$$(3.58 \pm 0.08) \times 10^{-10} \exp(-(14.3 \pm 0.5)/ RT) \text{ cm}^3 \text{ molecule}^{-1} \text{ s}^{-1}$$

$$k_{3.6}(K + SF_6, 207\text{-}817 \text{ K}) = (27.7 \pm 9.6) \times 10^{-10} \exp(-(16.8 \pm 1.7)/ RT) +$$

$$(1.79 \pm 0.20) \times 10^{-10} \exp(-(4.44 \pm 0.25)/ RT) \text{ cm}^3 \text{ molecule}^{-1} \text{ s}^{-1}$$

$$k_{3.10}(Na + C_2F_5Cl, 248\text{-}868 \text{ K}) = (5.92 \pm 3.45) \times 10^{-10} \exp(-(35.4 \pm 3.2)/ RT) +$$

$$(1.84 \pm 0.14) \times 10^{-11} \exp(-(17.4 \pm 0.3)/ RT) \text{ cm}^3 \text{ molecule}^{-1} \text{ s}^{-1}$$
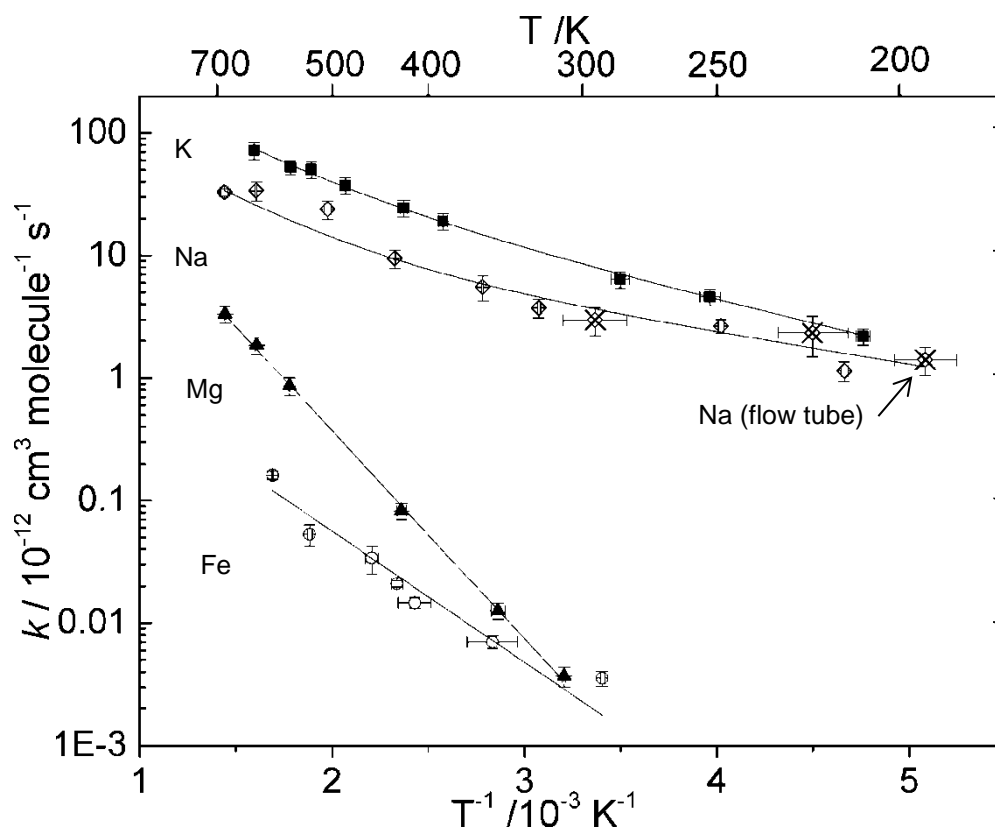
**Figure 3.5** Arrhenius plots for the reactions of $NF_3$ with Na (diamonds), K (filled squares), Mg (filled triangles) and Fe (circles) are shown. The measurements of R3.1(Na + $NF_3$) with the fast flow are indicated with a cross through the diamond. Uncertainty is shown as error in $k$ and the standard deviation in temperature throughout the experiment.
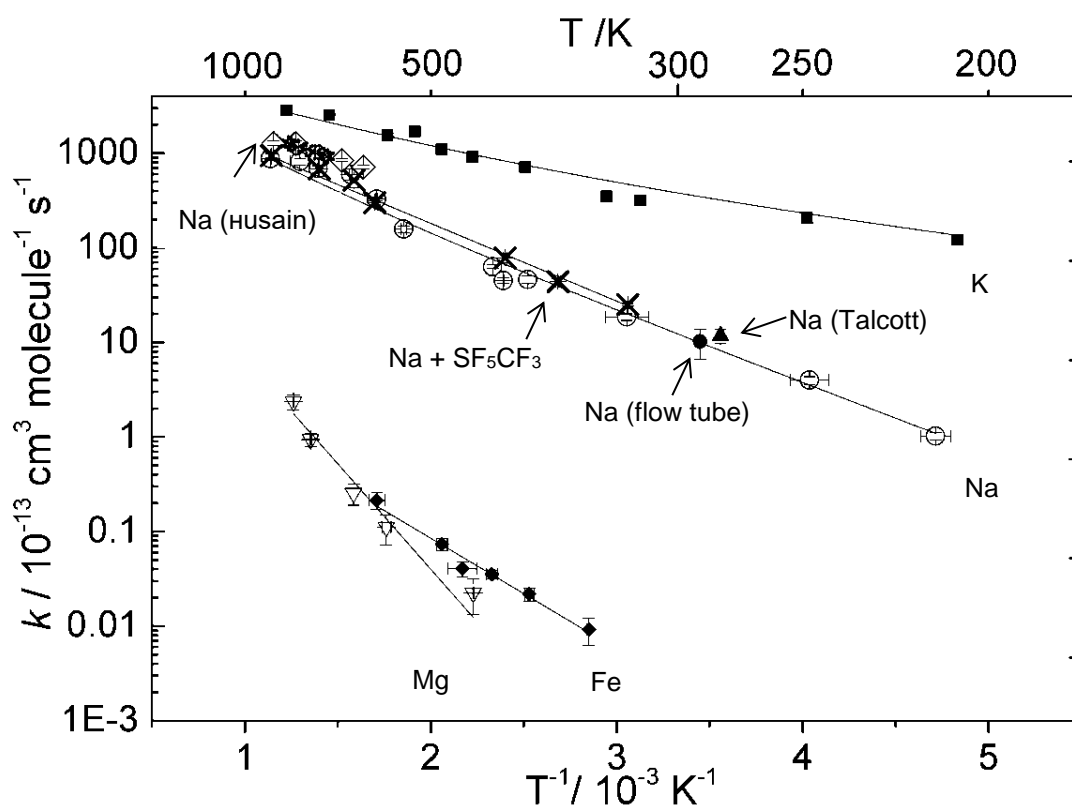
**Figure 3.6.** Arrhenius plots for the reactions of $SF_6$ with Na (circles), K (filled squares), Mg (upside down triangles) and Fe (filled diamonds) are shown. The measurements of R3.5(Na + $SF_6$) with the fast flow tube are indicated with a filled circle. Previous measurements of R3.5 obtained by Talcott *et al.* (6) and Husain *et al.* (7) are shown with filled triangles and open diamonds respectively. R3.9 (Na + $SF_5CF_3$) measurements are displayed with crosses. Uncertainty is shown as error in *k* and the standard deviation in temperature throughout the experiment.
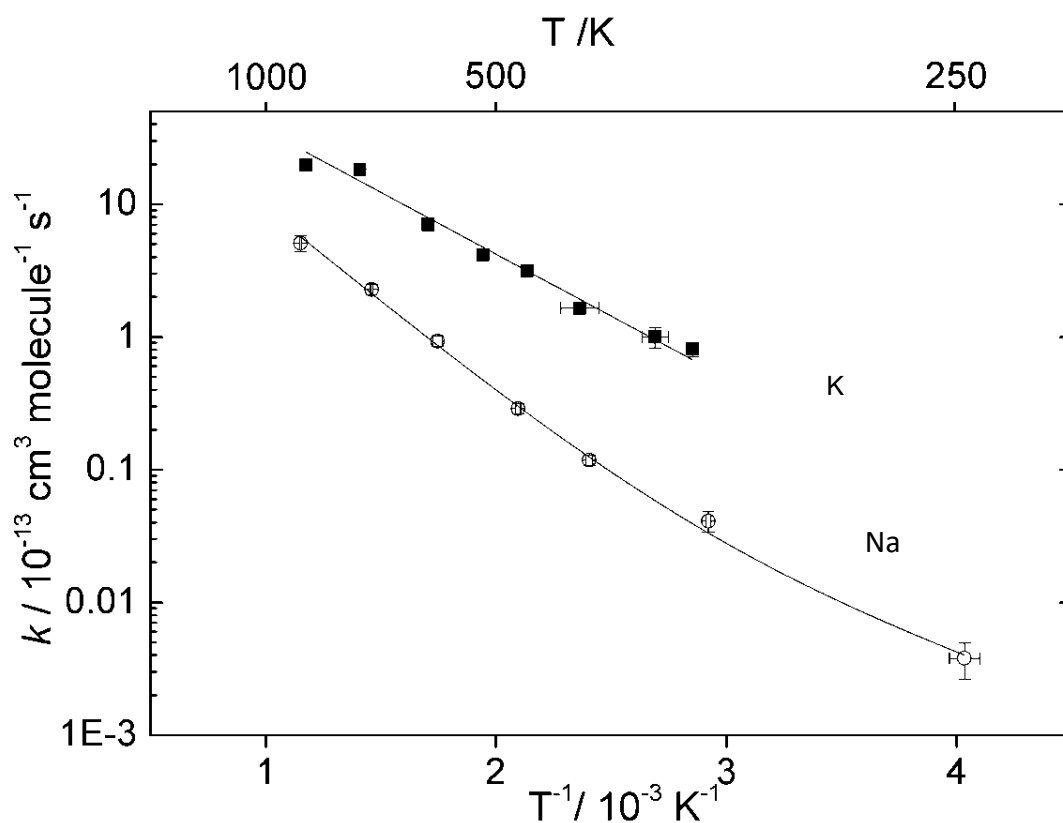
**Figure 3.7.** Arrhenius plots for the reactions of CFC-115 with Na (circles) and K (filled squares). Uncertainty is shown as error in *k* and the standard deviation in temperature throughout the experiment.

In the present study of R3.5 (Na + $SF_6$), a good agreement between the 290 K FFT and the PLP-LIF measurements were achieved (Table 3.8). R3.5 has been studied previously by Talcott *et al.* (20) in a flow tube study at 281 K, and by Husain and Marshall(7) in a flash photolysis/resonance absorption study over the temperature range 644 – 918 K. Figure 3.6 shows that our results are in very good agreement with both previous studies. R3.5 has also been studied in a diffusion flame, from which a rate constant of $k_1$(523 K) = 3.6 × $10^{-11}$ $cm^3$ molecule$^{-1}$ s$^{-1}$ was obtained (see Table 1 in Gislason and Kwei (21)), which is a factor of 2.3 larger than in the present study. Düren *et al.* (22) measured a reaction cross section $\sigma$ = 46 Å$^2$ at a collision velocity *v* = 3.1 × $10^5$ cm s$^{-1}$ (which corresponds to a kinetic temperature of 8670 K). Expressing the rate constant as the product $\sigma.v$ yields *k*(8670 K) ~ 1.4 × $10^{-9}$ $cm^3$

molecule$^{-1}$ s$^{-1}$, which is in surprisingly good agreement with a value of $1.6 \times 10^{-9}$ cm$^3$ molecule$^{-1}$ s$^{-1}$ extrapolated using the Arrhenius fit described above.

The reaction kinetics of R3.6 (K + SF$_6$) have also been studied previously by Husain *et al*. (8) over the temperature range 691 – 810 K. Figure 3.6 shows that although the activation energy at high temperature is similar to that from the present study, the rate constants are approximately 2.3 times smaller. The reason for this significant difference is unclear, particularly given the good agreement for R3.5 between the two techniques. The reaction cross section for R3.6 has also been measured in two molecular beam studies. Airey *et al*. (23) measured $\sigma$ = 60 Å$^2$ at a collision velocity $v$ = $6.8 \times 10^4$ cm s$^{-1}$, equivalent to $k_4$(677 K) ~ $4.1 \times 10^{-10}$ cm$^3$ molecule$^{-1}$ s$^{-1}$ which is a factor of 1.9 times larger than measured in the present study. Sloane *et al*. (24) obtained $\sigma$ = 55 Å$^2$ at a collision velocity $v$ = $6.9 \times 10^4$ cm s$^{-1}$, equivalent to $k_4$(687 K) ~ $3.8 \times 10^{-10}$ cm$^3$ molecule$^{-1}$ s$^{-1}$, which is a factor of 1.7 times larger than the present measurements. The agreement is therefore quite satisfactory. Sloane et al. showed in their beam-gas experiment that the reaction cross section increased by a factor of 1.5 when the SF$_6$ temperature was increased from 300 to 580 K, from which they concluded that excitation of the stretching modes of SF$_6$ enhanced its reactivity towards K. Riley and Herschbach (25) showed that the differential cross sections exhibit roughly symmetrical forward and backward scattering, indicating that the reaction proceeds via a collision complex which persists for at least several rotational periods.

Inspection of Figures 3.5 to 3.7 show that the rate coefficients for Na and K with each species decrease in the order NF$_3$ > SF$_6$ > CFC-115. Reactions with NF$_3$ proceed approximately 3 times faster than those with SF$_6$ and between ~ 2 and 10 times faster with K than Na overall. However, both metals react significantly faster with SF$_6$ than C$_2$F$_5$Cl, and the K reactions are ~5-120 times faster than the corresponding Na reactions at the same temperature. The rate constants for Na + SF$_6$ and Na + SF$_5$CF$_3$ are almost identical (Figure 3.6). Figures 3.5 and 3.6 show that Mg and Fe are comparatively unreactive compared to the Group 1 metal atoms.

**3.3.3.1        Electronic Structure Calculations and Potential Energy Surfaces**

Figures 3.5 to 3.7 also show that the rate coefficients for the metal atom + PFC reactions decrease in the order K > Na > Mg > Fe, which is the inverse order of the metal atom ionization potentials K (4.34 eV) < Na (5.14 eV) < Mg (7.64 eV) < Fe (7.90 eV). At first glance this might suggest that a classic electron transfer ("harpoon") mechanism governs these reactions. Furthermore, electronic structure calculations were unable to identify stable transition states for the reactions of Na with $SF_6$ or $NF_3$.

The harpoon mechanism applies to reactions where one species possesses a low ionisation potential and the other, a high electron affinity. When the species pass within a critical distance, an electron 'jump' occurs as the energy required for an electron transfer is balanced by the Coloumbic attraction which occurs between the resulting ions. Reactions proceeding via the harpoon mechanism usually possess rate coefficients which are much larger than predicted by collision theory. This is due to the reaction cross sections being greater than their geometrically calculated values.

To further explore the kinetics of R3.1 – R3.11, electronic structure calculations were performed as described earlier in the chapter, which indicate the reactions to be highly exothermic. Their collision frequencies were also then approximated according to the formula:

$$Z_{M,PFC} = \sigma_{M\,PFC}\sqrt{\frac{8\,k_B T}{\pi \mu}} \qquad (E3.8)$$

where $\sigma_{M\,PFC}$ is the collisional cross section of the two reactants, and $\mu$, their reduced mass. Taking a typical hard sphere value for $\sigma_{M\,PFC}$ of $\sim 1 \times 10^{-15}$ $cm^2$ yielded collision frequencies for the example reaction (R3.5) at 300 K in the region of $\sim 2 \times 10^{-10}$ $cm^3$ molecules$^{-1}$ s$^{-1}$, at least two orders of magnitude faster than the rate coefficients measured.

A detailed exploration into the significant relationship between the geometry and electron affinity of $NF_3$ has been published recently by Matsuura *et al.* (26) in a study of the reaction of $NF_3$ with metastable Kr atoms. The significant steric

constraint of R3.1 – R3.4 were then explored through the characterisation of the potential energy curves of $NF_3$ and $NF_3^-$ as a function of the $NF_2$-F distance (Figure 3.8). The potential energy surface of a reaction shows the potential energy as a function of the relative position of involved atoms. These curves were provided by J. M. C. Plane (Per. Comm., University of Leeds) to aid in interpreting the results and were calculated at the B3LYP/6-311+G(2d,p) level of theory as described earlier in Section 3.2.
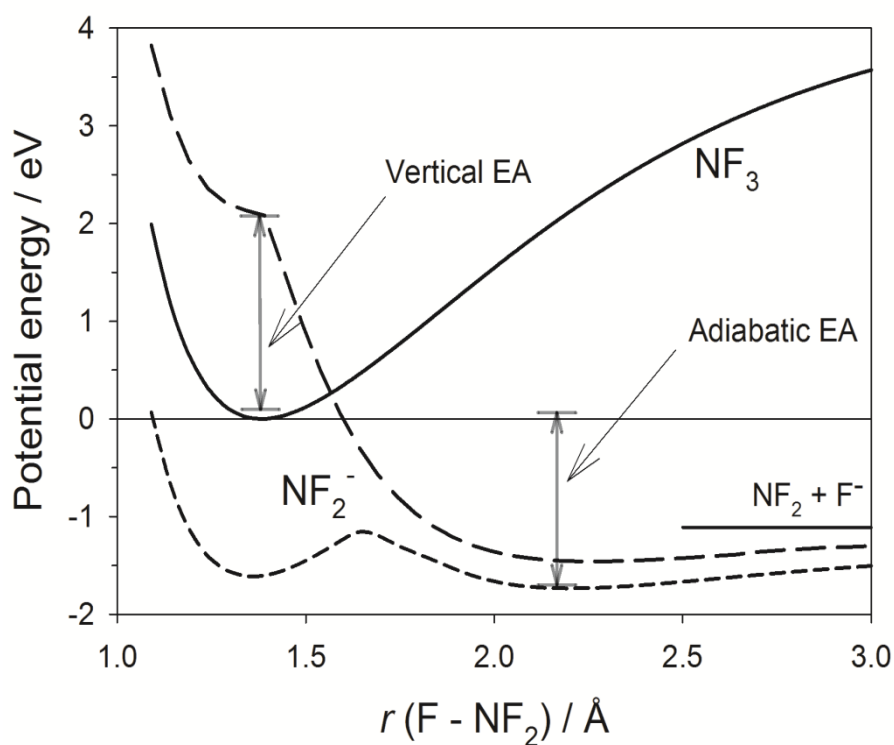


**Figure 3.8.** Potential energy curves for $NF_3$ and $NF_3^-$ as a function of $NF_2 - F$ distance, calculated at the B3LYP/6-311+g(2d)level of theory. The neutral $NF_2$ – F curve (solid line) and ionic $NF_2 - F^-$ curve (short dashed line) are relaxed scans along the reaction coordinate, i.e., the minimum energy paths of the respective potential energy surfaces. The points on the ionic $NF_2 - F^-$ curve (long dashed line) are calculated at the geometry of the neutral $NF_2 - F$ curve, thus providing the vertical electron affinity.

The curve for neutral $NF_2$-F (solid line) is a relaxed scan along the minimum path of the potential energy surface (PES). The ionic $NF_2$-F$^-$ curve (long dashed line) is calculated at the corresponding neutral geometry so that the vertical separation between these curves is the vertical electron affinity at each N-F separation. In contrast, the $NF_2$-F$^-$ curve (short dashed line) is a relaxed scan along the reaction co-ordinate, which shows that the adiabatic electron affinity (EA) is positive. The vertical EA is significantly negative, -2.1 eV at the equilibrium geometry of $NF_3$. This means that electron transfer is extremely unlikely to occur in this state, providing some explanation of why the measured rate coefficients are significantly slower than the calculated collision theories. However, as Figure 3.8 shows, EA does becomes favourable (i.e. positive) when the $NF_2$-F bond has stretched from its equilibrium length of 1.38 Å in neutral to $NF_3$, to more than 1.6 Å.

Figure 3.8 shows that the neutral and ionic curves cross about 0.2 eV above the minimum of neutral $NF_3$, so this amount of internal excitation should result in dissociative electron attachment leading to $NF_2$ + F$^-$.
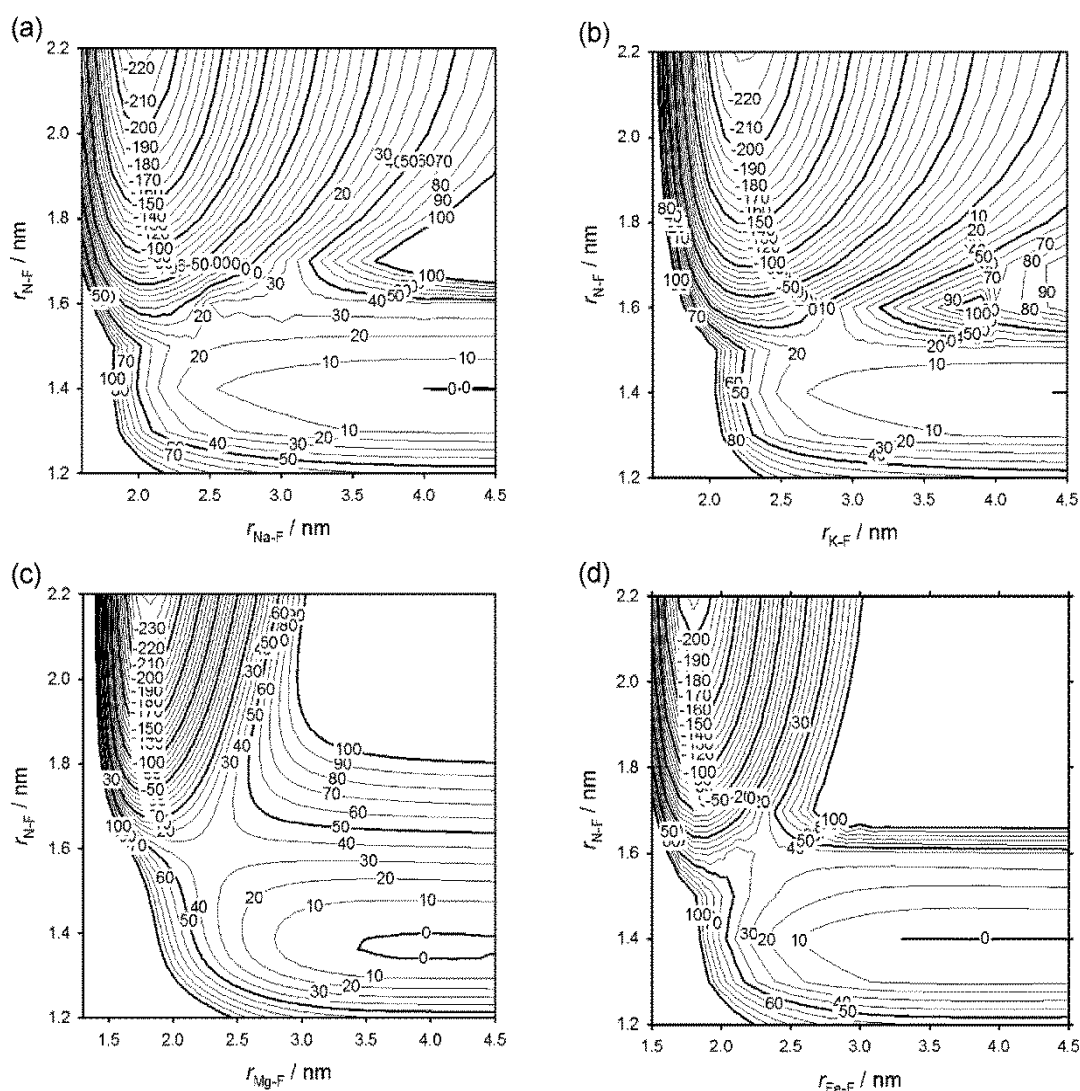
**Figure 3.9.** Potential energy surfaces for the reactions of Na, K, Mg, and Fe with NF₃, calculated at the MP2/ 6-311+g(2d) level of theory. The contour labels indicate the energy in kilojoules per mole. These surfaces are for the case where the metal atom attack is collinear with one of the N–F bonds. The scan is therefore along the N–F–M (M = metal atom) linear coordinate, where rN–F and rM–F are varied. Note that the geometry of the NF₂ moiety is frozen, which means that the surface does not represent the lowest possible energy path from reactants to products.

The surfaces above are representative of the reaction, they do not, however, present the lowest possible energy pathway from reactants to products. The scan is along the N-F-M (M = metal atom) linear co-ordinate, where $r_{N\text{-}F}$ and $r_{M\text{-}F}$ are varied, illustrating a mechanism where the metal atom attack is collinear with one of the N-

F bonds. Each of the potential energy surfaces presented here shows that at the start of the interaction the metal – F bond length is effectively infinite and the PFC – F bond is at its equilibrium length. Following a successful reaction, the metal – F bond is at its equilibrium length and the PFC – F bond length  becomes infinite.

The four PESs exhibit late barriers in their exit channels. The barriers increase in the order K (15 kJ mol$^{-1}$), Na (20 kJ mol$^{-1}$), Mg (35 kJ mol$^{-1}$) and Fe (36 kJ mol$^{-1}$), which is the same order in which the rate coefficients decrease (Figure 3.5).
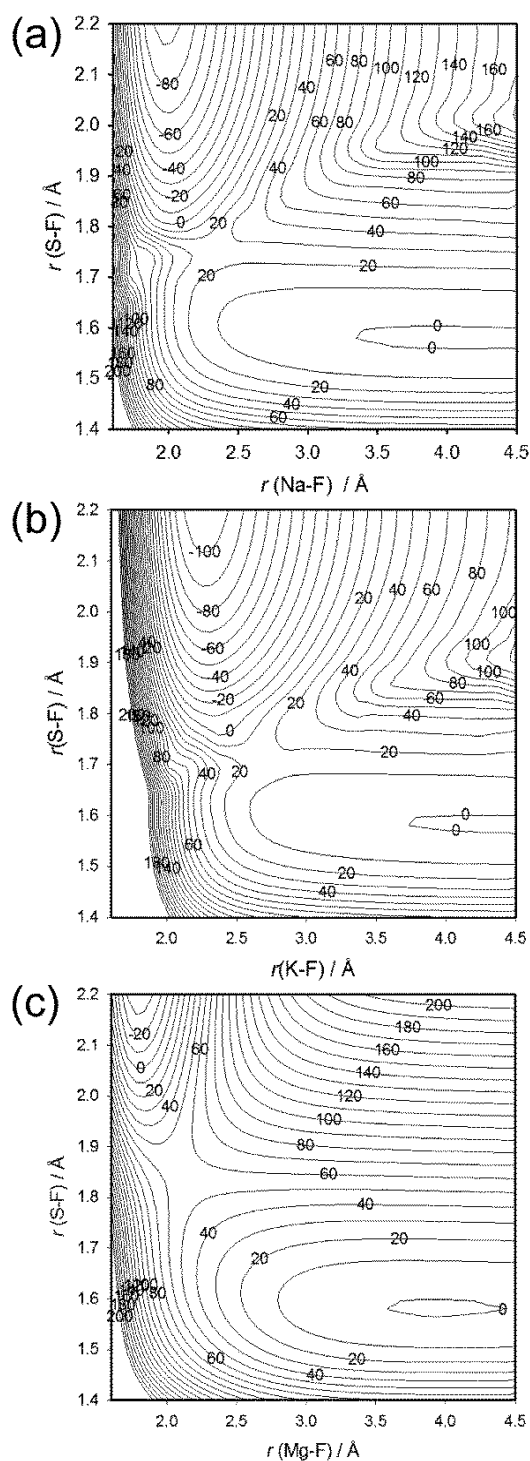
**Figure 3.10.** Potential energy surfaces for the reactions of Na, K, and Mg with $SF_6$ calculated at the MP2(FULL)/6-311+g(2d,p) level of theory. These surfaces are for the case where the metal atom attack is collinear with one of the S–F bonds. The scan is therefore along the S–F–M(metal atom) linear coordinate, where r(S–F) and r(M–F) are varied. Note that the geometry of the $SF_5$ moiety is frozen, which means that the surface does not represent the lowest possible energy path from reactants to products.

Figure 3.10 shows PESs for R3.5 -3.8. These surfaces illustrate the case where the metal atom attack is collinear with one of the S-F bonds. The scan is therefore along the S-F-M (M = metal atom) linear co-ordinate, where $r_{S-F}$ and $r_{M-F}$ are varied. Since the geometry of the $SF_5$ moiety is frozen in these scans, the surface does not represent the lowest possible energy path from reactants to products. However, the $SF_5$ geometry does not change significantly between $SF_5$-F and $SF_5$ + F, so that the energy of the frozen $SF_5$ geometry is only 12 kJ mol$^{-1}$ above that of the optimized geometry.

Reactions with late barriers tend to be activated by vibrational excitation in a reactant bond corresponding to the reaction co-ordinate (27). Inspection of the two Arrhenius terms in the expressions for $k_{3.1}$ and $k_{3.2}$ listed on page 99 shows that the difference between the activation energies in the two terms is (13.7 $\pm$ 5.0) kJ mol$^{-1}$ for $k_{3.1}$, and (11.9 $\pm$ 2.0) kJ mol$^{-1}$ for $k_{3.2}$. These differences correspond (within error) to one $\nu_3$ quantum (10.8 kJ mol$^{-1}$), suggesting the first term contains the probability of $\nu_3$ excitation. $\nu_3$ refers to the asymmetric stretch of $NF_3$, as shown in Figure 3.8, sufficient excitation of this $NF_2$-F stretching mode ($\nu_3$ = 907 cm$^{-1}$) (28) will make the electron affinity positive and allow the reaction to proceed via the longer range harpoon mechanism (15) and resulting in the large pre-exponential factors observed. Finally, the Boltzmann population of $NF_3$ ($\nu_3$>0) at 300 K is in the low region of around 1.3 %, increasing hugely at 700 K, to 15.5%

Similarly, the three PESs for R3.5, R3.6 and R3.8 exhibit late barriers in their exit channels, particularly Mg + $SF_6$ (Figure 3.9(c)). The barriers increase in the order K (13 kJ mol$^{-1}$), Na (22 kJ mol$^{-1}$) and Mg (51 kJ mol$^{-1}$), which is the same order in which the rate constants decrease (Figure 3.6). Reactions with late barriers tend to be activated by vibrational excitation in a reactant bond corresponding to the reaction co-ordinate(27). The Arrhenius expressions for $k_{3.5}$ and $k_{3.6}$ (see above) exhibit an increase in activation energy between the low and high temperature terms: the change in activation energy is (14.4 $\pm$ 7.2) and (12.4 $\pm$ 2.0) kJ mol$^{-1}$, respectively. These differences correspond (within error) to one quantum of the $\nu_3$ S-F stretching mode of $SF_6$ (940 cm$^{-1}$,(15) or 11.2 kJ mol$^{-1}$). This is consistent with the first term in each Arrhenius expression containing the probability of $\nu_3$ excitation: for example,

the Boltzmann population of $SF_6$ ($v_3 > 0$) increases from only 3.3 % at 300 K to 37.5 % at 700 K. The large pre-exponential factor of the first terms in both expressions is indicative of a long–range electron transfer.

## 3.4 Lyman-α Absorption Cross Sections

Lyman-α absorption cross sections for $NF_3$, $SF_6$ and CFC-115 were determined experimentally by T. Kovacs (Per. Comm., University of Leeds) using the method described in detail in the previous chapter. Briefly, a radiofrequency discharge was used to generate radiation which was optically filtered at 121.6 nm and transmitted through an absorption cell containing varying concentrations of the studied PFC. The corresponding change in signal intensity was recorded and averaged. The Lyman-α absorption cross section, σ, was then determined by applying the Beer-Lambert equation:

$$\ln\left(\frac{I_0}{I}\right) = \sigma(121.6 \text{ nm}) \, L \, [\text{PFC}] \tag{E3.9}$$

where $I_0$ and $I$ are respectively the light intensity transmitted through the absorption cell in the absence and presence of the PFC, and $L$ is the optical path length.
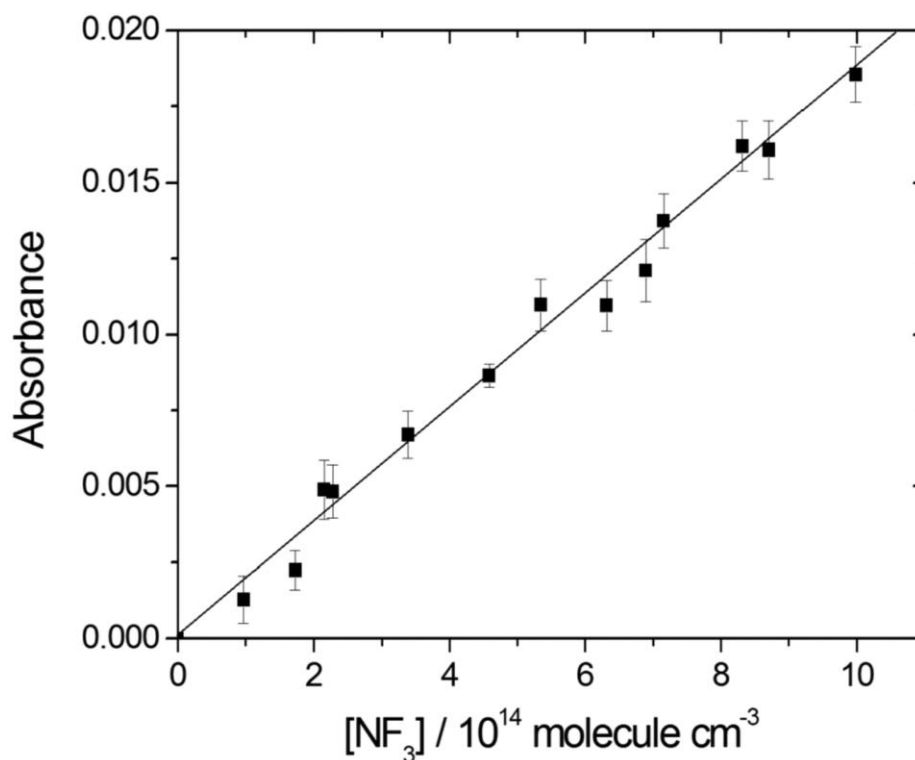
**Figure 3.11** Beer–Lambert plot of Lyman-α absorbance against $NF_3$ concentration where absorbance is determined as the natural log of the ratio of the measured signal, with and without $NF_3$ present.

Figure 3.11 shows an example of the experimentally obtained absorbance measurements as a function of $NF_3$ concentration. Absorbance measurements were recorded relative to a background signal, in the form, $\ln(I_0/I)$. The measured uncertainty is within the 95 % confidence level.

### 3.4.1 Summary of Results: Lyman-α Absorption Cross Sections

Discussion of Lyman- α absorption cross sections is provided in Chapter 4. In the case of $NF_3$ Figure 3.11 shows the average absorbance (defined here as $\ln(I_0/I)$) versus $[NF_3]$. Linear regression yields $\sigma(121.6 \text{ nm}) = (1.59 \pm 0.10) \times 10^{-18}$ $cm^2$ molecule$^{-1}$ at 300 K, where the stated uncertainty is at the 95% confidence level.

Similarly, the cross section of $SF_6$ was also measured yielding: $\sigma(SF_6, 121.6 \text{ nm}) = (1.37 \pm 0.12) \times 10^{-18} \text{ cm}^2$. Results obtained are in good agreement to previous literature results within error (9). Previous measurements of the $SF_6$ cross sections over the 116–180 nm and 121–125 nm ranges were reported by Pradayrol *et al.* (29) and Zetzsch (10), respectively.

Finally, the cross sections of CFC-115 were also measured giving:

$\sigma(\text{CFC-115}, 121.6 \text{ nm}) = (4.27 \pm 0.35) \times 10^{-18} \text{ cm}^2$. The UV cross sections for each PFC are shown in Chapter 4.

# List of References

1.      Totterdill, A., T. Kovacs, J.C.G. Martin, W.H. Feng and J.M.C. Plane. Mesospheric Removal of Very Long-Lived Greenhouse Gases $SF_6$ and CFC-115 by Metal Reactions, Lyman-alpha Photolysis, and Electron Attachment. *J. Phys. Chem. A*, 2015, **119**(10), pp.2016-2025.

2.      Totterdill, A., J.C.G. Martín, T. Kovács, W. Feng and J.M.C. Plane. Experimental Study of the Mesospheric Removal of $NF_3$ by Neutral Meteoric Metals and Lyman-$\alpha$ Radiation. *J. Phys. Chem.*, 2014, **118**(23), pp.4120-4129.

3.      Vondrak, T., J.M.C. Plane, S. Broadley and D. Janches. A Chemical Model of Meteoric Ablation *Atmos. Chem. Phys.*, 2008, **8**(7015–7032).

4.      NIST. *Computational Chemistry Comparison and Benchmark DataBase*. Available from: http://webbook.nist.gov/chemistry/. 2012.

5.      Lide, D.R. *Handbook of Physics and Chemistry.* Boca Raton, FL: CRC Press, 2006.

6.      Talcott, C.L., J.W. Ager and C.J. Howard. Gas Phase Studies of Na Diffusion in He and Ar and Kinetics of Na + $Cl_2$ and Na + $SF_6$. *J. Chem. Phys.*, 1986, **84**(11), pp.6161-6169.

7.      Husain, D. and P. Marshall. Determination of Absolute Rate Data for the Reaction of Atomic Sodium. *J. Chem. Soc., Faraday Trans.*, 1985, **81**(2), pp.613 - 624.

8.      Husain, D. and Y.H. Lee. Measurement of Absolute Rate Data for the Reaction of Atomic Potassium, $K(4^2S_{1/2})$, with $CF_3Cl$, $CF_2Cl_2$, $CFCl_3$, $CF_3Br$ and

SF$_6$ as a Function of Temperature by Time-Resolved Atomic Resonance Absorption Spectroscopy at [λ]= 404 nm [K($5^2$P$_J$) - K($4^2$S$_{1/2}$)]. *J. Chem. Soc. Faraday Trans. 2*, 1987, **83**(12), pp.2325-2337.

9.    Ravishankara, A.R., S. Solomon, A.A. Turnipseed and R.F. Warren. Atmospheric Lifetimes of Long-Lived Halogenated Species. *Science*, 1993, **259**, pp.194 - 199.

10.   Zetzsch, C. *UV Absorption Cross Sections of Sulfur Hexafluoride and Acetonitrile.* Ozone in the Atmosphere. Hampton: DEEPAK Publishing, 1989.

11.   Plane, J.M.C. *Pers. Comm.*, 28/05/2014. 2014.

12.   Frisch, M.J., G.W. Trucks, H.B. Schlegel, G.E. Scuseria, M.A. Robb, J.R. Cheeseman, G. Scalmani, V. Barone, B. Mennucci, G.A. Petersson, H. Nakatsuji, M. Caricato, X. Li, H.P. Hratchian, A.F. Izmaylov, J. Bloino, G. Zheng, J.L. Sonnenberg, M. Hada, M. Ehara, K. Toyota, R. Fukuda, J. Hasegawa, M. Ishida, T. Nakajima, Y. Honda, O. Kitao, H. Nakai, T. Vreven, J. J. A. Montgomery, J.E. Peralta, F. Ogliaro, M. Bearpark, J.J. Heyd, E. Brothers, K.N. Kudin, V.N. Staroverov, R. Kobayashi, J. Normand, K. Raghavachari, A. Rendell, J.C. Burant, S.S. Iyengar, J. Tomasi, M. Cossi, N. Rega, J.M. Millam, M. Klene, J.E. Knox, J.B. Cross, V. Bakken, C. Adamo, J. Jaramillo, R. Gomperts, R.E. Stratmann, O. Yazyev, A.J. Austin, R. Cammi, C. Pomelli, J.W. Ochterski, R.L. Martin, K. Morokuma, V.G. Zakrzewski, G.A. Voth, P. Salvador, J.J. Dannenberg, S. Dapprich, A.D. Daniels, O. Farkas, J.B. Foresman, J.V. Ortiz, J. Cioslowski and D.J. Fox. *Gaussian 09, Revision A.1.* Wallingford CT: Gaussian, Inc., 2009.

13. Plane, J.M.C. and R.J. Rollason. A Study of the Reactions of Fe and FeO with $NO_2$, and the Structure and Bond Energy of $FeO_2$. *Phys. chem. chem. phys.*, 1999, **1**, pp.1843 - 1849.

14. Alkemade, U. and K.H. Homann. Gas-phase Dimerization of Sodium Halides and Formation of Mixed Sodium/Phenyl Iodides. *Ber. Bunsenges. Phys. Chem.*, 1989, **93**(4), pp.434-439.

15. Howard, C.J. Kinetic Measurements Using Flow Tubes. *J. Phys. Chem.*, 1978, **83**(1), pp.3 - 9.

16. Engel, T. and P.J. Reid. *Physical Chemistry.* Pearson Benjamin Cummings, 2006.

17. Mangham, W. *Organization Of The Heart And Circulation* [online]. 2013. [Accessed 20/05/2016]. Available from: http://www.cram.com/flashcards/organization-of-the-heart-and-circulation-3369118.

18. Broadley, S.L., T. Vondrak and J.M.C. Plane. A Kinetic Study of the Reactions of $Ca^+$ Ions with $O_3$, $O_2$, $N_2$, $CO_2$ and $H_2O$. *Phys. chem. chem. phys.*, 2007, **9**(31), pp.4357-4369.

19. Elizabeth, V., M.K. LeClair, S.L. Suib, M.B. Cutlip, F.S. Galasso and S.J. Hardwick. Thermal Decomposition of $NF_3$ with Various Oxides. *Chem. Mat.*, 1996, **8**(6), pp.1217-1221.

20. Sorokin, V.I., N.P. Gritsan and A.I. Chichinin. Collisions of $O(^1D)$ with HF, $F_2$, $XeF_2$, $NF_3$, and $CF_4$: Deactivation and Reaction. *J. Chem. Phys.*, 1998, **108**(21), pp.8995-9003.

21. Gislason, E.A. and G.H. Kwei. Quenching of Glory Undulations in Scattering of Na Atoms from Polyhalide Molecules. *J. Chem. Phys.*, 1967, **46**, pp.2838-2840.

22. Düren, R., M. Färber, B. Heumann, M. Knepper, S. Mohr, C. Weiss, S.T.L. Hekkert, A.F. Linskens and J. Reuss. Differential Cross Sections for State Specific Reactive Scattering of Na + $SF_6 \rightarrow NaF + SF_5$. *J. Chem. Phys.*, 1996, **104**(10), pp.3620-3628.

23. Airey, J.R., E.F. Greene, G.P. Reck and J. Ross. Scattering of Potassium by a Series of Reactive and Nonreactive Compounds in Crossed Molecular Beams. *J. Chem. Phys.*, 1967, **46**, pp.3295-3305.

24. Sloane, T.M., S.Y. Tang and J. Ross. Dependence of Reactivity on Internal and Translational Energy in K + $SF_6$ , $CCl_4$, and $SnCl_4$. *J. Chem. Phys.*, 1972, **57**, pp.2745-2755.

25. Riley, S.J. and D.R. Herschbach. Molecular Beam Kinetics: Long-Lived Collision Complexes in Reactions of K, Rb, and Cs with $SnCl_4$ and $SF_6$. *J. Chem. Phys.*, 1973, **58**(1), pp.27-43.

26. Matsuura, Y. and H. Ohoyama. Collision-Induced Harpooning Observed in the Excimer Formation in the Orientated $NF_3$ + Orientated Kr* (Reaction). *J. Phys. Chem. A*, 2011, **115**, pp.4583 - 4591.

27. Smith, I.W.M. *Kinetics and Dynamics of Elementary Gas Reactions.* London: Butterworths, 1980.

28. Shimanouchi, T. Tables of Molecular Vibrational Frequencies. *Nat. Stand. Ref. Data Ser.*, 1972, **39**, p.16.

29.     Pradayrol, C., A.M. Casanovas, I. Deharo, J.P. Guelfucci and J. Casanovas.

Absorption Coeffcients of $SF_6$, $SF_4$, $SOF_2$, and $SO_2F_2$ in the Vacuum

Ultraviolet. *J. de Phys. III*, 1996, **6**(5), pp.603 - 612.

# Chapter 4: Calculation of the Global Warming Potentials of SF₆, NF₃ and CFC-115

Perfluorinated compounds (PFCs) such as those studied here potentially play a very significant role in global warming. The atmospheric concentrations of such species have rapidly increased in recent decades due to increased demand from the relatively modern processes for which they have been introduced. This has led to increased interest from the scientific community as many of these species have not been detected in the atmosphere prior to the advent of their related industries. This chapter aims to outline the process of calculating the global warming potentials of $SF_6$, $NF_3$ and CFC-115. This begins with some brief background on the derivation of their atmospheric lifetimes based on experimental results given in Chapter 3, to discussion of the infrared spectra obtained based on techniques outlined in Chapter 2 and how these cross sections are used to calculate radiative forcings which are used in conjunction with the atmospheric lifetimes to give GWPs. Results for these processes are given in Chapter 5.

## 4.1   Atmospheric Lifetimes

The rate-determining sinks for the PFCs in this study are thought to be photolysis, reaction with $O(^1D)$ and/or electron attachment in the mesosphere (1, 2). Bimolecular loss rate constants are reported for removal by $O(^1D)$ (3) and measured for mesospheric metals in Chapter 3. Other removal processes include photolysis and electron attachment.

### 4.1.1 Loss Rates

To assess the impact of our experimentally determined results on the lifetimes of the PFCs described in the atmosphere, the removal rates of each PFC through the reaction with metal atoms and by Lyman-α photolysis as measured in this study are compared with previous work on removal of these species by $O(^1D)$, electron attachment and photolysis at longer wavelengths.

#### 4.1.1.1 VUV Photolysis

A predominant focus of this study is species removal through photolysis by Lyman-α photons (121.6 nm) (4). However, In order to properly assess the role of photolysis in the atmosphere, the absorption cross sections over the VUV spectral range are required. As stated in the previous chapter, measurements of these cross sections for $SF_6$ have been reported over the $116 - 180$ nm and $121 - 125$ nm ranges by Pradarol *et al.* (5) and by Zetzch (6) respectively. The Lyman-α absorption cross sections for $SF_6$ were measured and found to be in generally good agreement with the more recent studies (1, 6). The Lyman-α absorption cross section of $SF_6$ from the present study is:

$$\sigma(\,SF_6, 121.6 \text{ nm}) = (1.37 \pm 0.12) \text{ x } 10^{-18} \text{ cm}^2$$

and previous measurements in chronological order are 2.74 x $10^{-18}$ cm$^2$ by Bastien *et al.* (7), (1.76 ± 0.13) x $10^{-18}$ cm$^2$ by Ravishankara *et al.* (1), 1.83 x $10^{-18}$ cm$^2$ by Pradarol *et al.* (5) and 1.20 x $10^{-18}$ cm$^2$ by Zetzch (6). The earliest measurement by Bastien *et al.* appears to be an outlier with the other values varying by about 50 %. Our value is reasonably close to the average of 1.5 x $10^{-18}$ cm$^2$.

Polynomial expressions were derived describing the cross sections as a function of wavelength from composite data sets containing the cross sections obtained in this research by Dr Tamás Kovács at 121.6 nm and the literature values described above at longer UV wavelengths. Figure 4.1 shows the resulting cross sections as a function of wavelength, together with the solar irradiance, which emphasises the importance of the Lyman-α line in the solar spectrum.
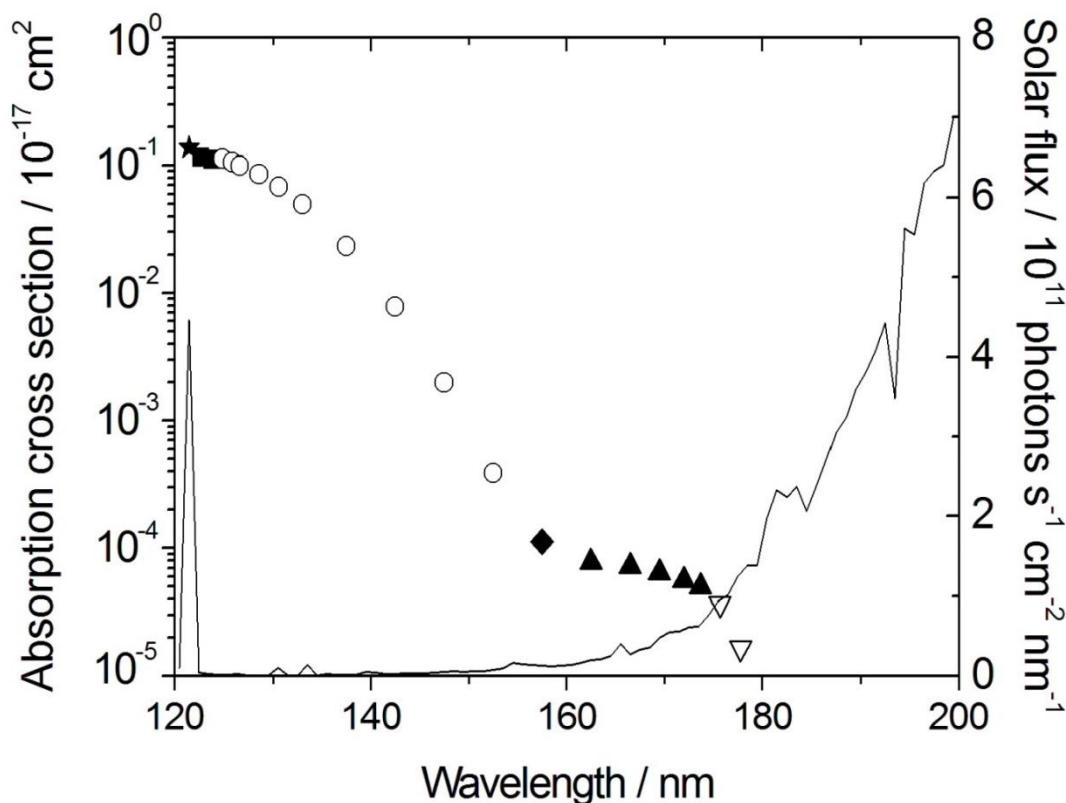
**Figure 4.1.** SF$_6$ absorption cross sections (left-hand ordinate): present study (121.6 nm, ★); fit to Zetzch *et al.* (6) (115 – 125 nm, ■); fits to Pradayrol *et al.* (5) (125 – 155 nm, ○; 155 – 160 nm, ◆; 160 – 175 nm, ▲; 175 – 180 nm, △, see text for further details). The solid line is the solar spectral irradiance (right-hand ordinate).

The solar photon flux as a function of wavelength (i.e. the actinic flux) is taken from a box model version of the three dimensional chemical transport model SLIMCAT (8, 9). The photolysis rate $J$(SF$_6$) is calculated using a scheme (10) which employs a four-dimensional look-up table as a function of pressure from the surface to $10^{-5}$ hPa, temperature, column ozone and zenith angle. This same method is used to calculate $J$(NF$_3$) and $J$(CFC-115).

Similarly, photolysis by Lyman-α photons (121.6 nm) is examined here as a major loss process for NF$_3$. This does not appear to have been studied previously. The experimental cross sections illustrated below in Figure 4.2 were therefore used

with the following linear interpolation between 121.6 and 126.6 nm where there is no experimental data:

$$\sigma(NF_3\ 121.6 - 126.6\ nm) = 5.22 \times 10^{-19}\lambda + 6.18\ 10^{-17}\ cm^2\ molecule^{-1}$$
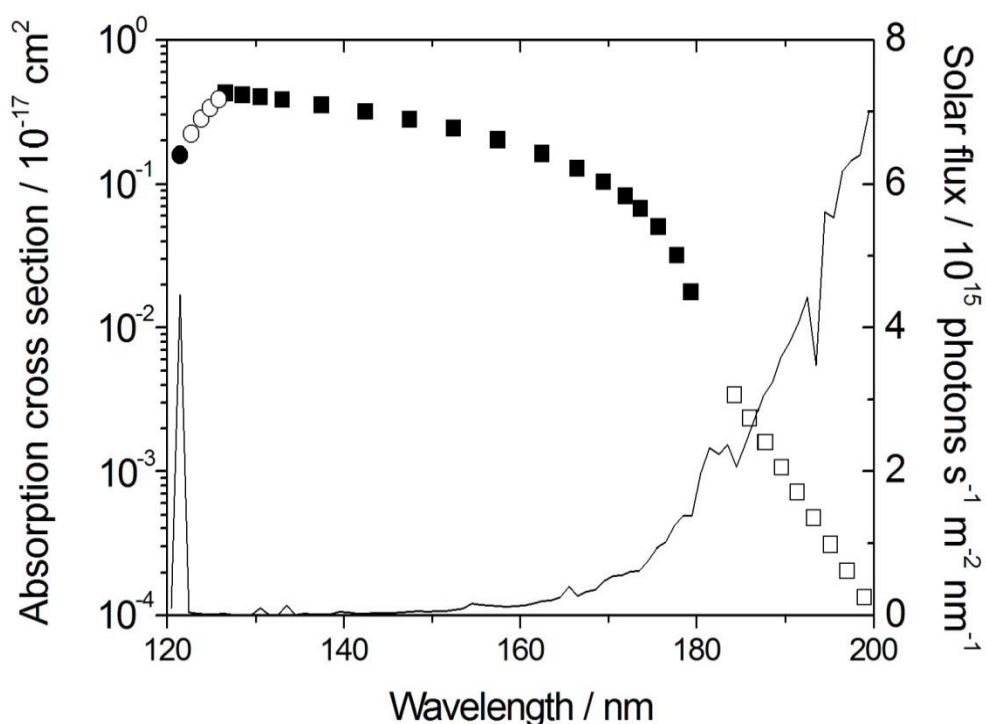


**Figure 4.2.** NF$_3$ absorption cross section (left-hand ordinate) between 121.6 and 200 nm: Lyman-α from the present study (●), extrapolation (○), La Paglia and Duncan (11) (■), and Papadimitriou *et al.* (12) (□). The solid line is the solar spectral irradiance (right-hand ordinate). Note the intense Lyman-α emission line at 121.6 nm.

The Lyman-α absorption cross sections for CFC-115 were measured and found to be in generally good agreement with the more recent studies (1, 6). The absorption cross section for CFC-115 from the present study is:

$$\sigma(CFC - 115, 121.6\ nm) = (4.27 \pm 0.35) \times 10^{-18} cm^2$$

This is significantly smaller than a very old measurement of 1.76 x 10$^{-17}$ cm$^2$ by Doucet *et al.* (13) but in excellent agreement with a value of (4.57 ± 0.37) x 10$^{-18}$

$cm^2$ measured by Ravishankara *et al.* (1). In order to assess the role of photolysis in the atmosphere, absorption cross sections over the VUV spectral range are required. The only reported measurements between 122 and 172 nm are by Doucet *et al.* (13). As noted above, their measurement at 121.6 nm is 4 times larger than the present study. In contrast, at 172 nm, Doucet *et al.* (13) are in good agreement with the recent JPL recommendation (14) (which extends to 230 nm). Since the cross sections between 122 and 170 nm (i.e. not including Lyman-α) do not make a significant contribution to the photodissociation rate of CFC-115 (Figure 4.3), therefore the Doucet *et al.* (13) results are used over this range without scaling them downward to match the Lyman-α measurements from the present study and that of Ravishankara *et al.* (1).
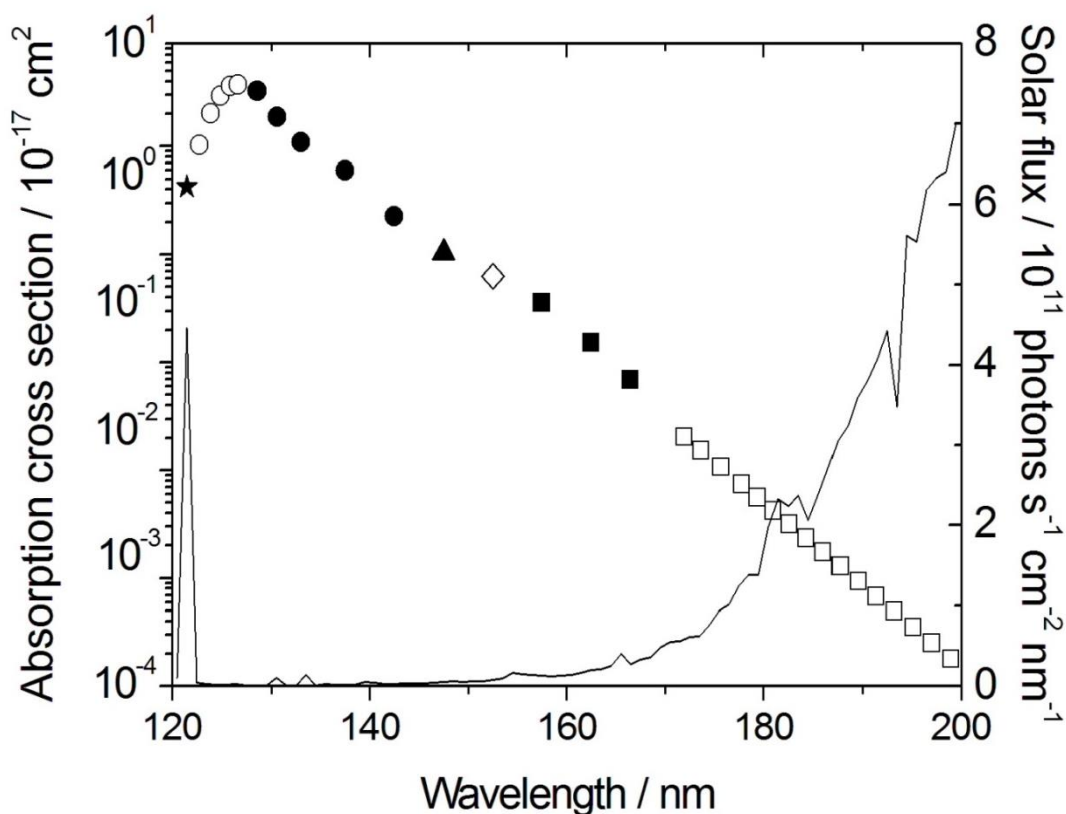
**Figure 4.3.** CFC-115 absorption cross section (left hand ordinate): present study
(121.6 nm, ★); fits to Doucet *et al.* (13) (121.6 – 127 nm), ○; 127 – 142 nm,

●; 146 – 172 nm, ▲, ◊ and ■); JPL recommendation (14) (172 – 230 nm, □
). The solid line is the solar spectral irradiance (right-hand ordinate).

VUV photolysis is the major loss process for CFC-115 above 60 km, but the removal
of this species by reaction with $O(^1D)$ dominates in the stratosphere and hence,
controls its lifetime.

### 4.1.1.2 Electron Attachment

Low energy electrons are in thermal equilibrium with the surrounding gas in the
upper mesosphere and lower thermosphere (15). Below 80 km electrons are
mostly attached to molecules in the form of negative ions, such as $HCO_3^-$ and $NO_3^-$.
Because the electron detachment energies from these ions are larger than the
electron affinity of $SF_6$, only direct attachment of free electrons will lead to the
potential destruction of $SF_6$ via two pathways: associative attachment to form the

$SF_6^-$ anion, which can then either undergo photodetachment or react with various compounds; and dissociative attachment to form $SF_5^- + F$ (16).

Both associative and dissociative electron attachment have been treated in detail in a series of papers by Troe *et al.* (17). The net associative rate coefficient, $k_{at}$, at an atmospheric density $[N_2 + O_2]$ and temperature $T$ is given by the following expression (17) which neglects radiative stabilisation (since this is only important at much lower pressures) and assumes that $O_2$ has a similar efficiency to $N_2$:

$$k_{at} = \frac{x}{1+x} F_c^{[1+ \log_{10}(\frac{x}{N})^2]^{-1}} \qquad \text{(E4.1)}$$

In this expression x is the ratio of the low to the high pressure limiting rate coefficients (i.e. $x = k_{at,0} / k_{at,\infty}$) where:

$$k_{at,0} = [N_2 + O_2] 2.5 \times 10^{-18} \exp\left(\frac{-T}{80\,K}\right) x \left[1 + 3.5 \times 10^{-22} \left(\frac{T}{K}\right)^7\right]$$

$$\text{cm}^3 \text{ molecule}^{-1} \text{ s}^{-1} \text{ (E4.2)}$$

And:

$$k_{at,\infty} = 2.2 \times 10^{-7} \left(\frac{T}{500\,K}\right)^{-0.35} \text{cm}^3 \text{ molecule}^{-1} \text{ s}^{-1} \qquad \text{(E4.3)}$$

The temperature dependence of the broadening factor $F_c$ is given by:

$$F_c = \exp\left(\frac{-T}{520\,K}\right) \qquad \text{(E4.4)}$$

and the parameter N is given by:

$$N = 0.75 - 1.27 \log_{10}(F_c) \qquad \text{(E4.5)}$$

Chemical removal of $SF_6^-$ can either recycle or remove $SF_6$. The removal reactions are:

$$SF_6^- + H \rightarrow products$$
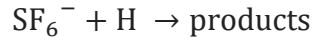
$$k_{R5.1} = 2.1 \times 10^{-10} cm^3 \ molecule^{-1} \ s^{-1} \qquad (R4.1)$$

$$SF_6^- + HCl \rightarrow products$$
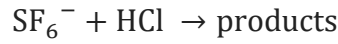
$$k_{R5.2} = 1.5 \times 10^{-9} cm^3 \ molecule^{-1} \ s^{-1} \ (16) \qquad (R4.2)$$

While the recycling channels are:

$$SF_6^- + O_3 \rightarrow SF_6 + O_3^-$$
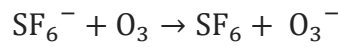
$$k_{R5.3} = 1.2 \times 10^{-9} cm^3 \ molecule^{-1} \ s^{-1} \ (16) \qquad (R4.3)$$

$$SF_6^- + O \rightarrow SF_6 + O^-$$
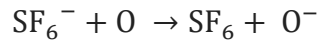
$$k_{R5.4} = 1.4 \times 10^{-10} \ cm^3 \ molecule^{-1} \ s^{-1} \ (16) \qquad (R4.4)$$

The photodetachment coefficient for $SF_6^-$ ($J_{PD}$) can be estimated by integrating the product of the electron photodetachment cross section and the extra-terrestrial solar irradiance from 280 to 700 nm (18), assuming a quantum yield of unity. The cross section was calculated by combining the recent theoretical spectrum of Eisfeld (19) with absolute experimental values reported by Bopp *et al.* (20) Christophorou and Olthoff (21) and Datskos *et al.* (22). This gives a midday value of 1.1 s$^{-1}$ at 85 km. Assuming that $SF_6^-$ is in steady state, the permanent removal rate of $SF_6$ by associative electron attachment becomes $k_{EA}$ [$SF_6$][e$^-$], where:

$$k_{EA} = k_{at} \frac{k_{4.1}[H] + k_{4.2}[HCl]}{J_{PD} + k_{4.1}[H] + k_{4.2}[HCl] + k_{4.3}[O_3] + k_{4.4}[O]} \qquad (E4.6)$$

Secondly, we consider the dissociative channel. At pressures above 10$^{-4}$ Torr, the branching ratio $\beta(P,T)$ for the dissociative thermal electron attachment channel for $SF_6$ is very small (~0.001) (2, 23, 24). Figure 4.4 reproduced from Troe *et al.* shows the more significant branching ratios and that at a pressure of 10$^{-2}$ Torr (corresponding to an altitude of ~80 km), the fraction that dissociates is less than

$10^{-4}$. The dissociative electron attachment removal rate as a function of temperature can be obtained by fitting an Arrhenius expression to the $10^{-2}$ Torr line in Figure 4.4, over the temperature range $200 - 320$ K where an Arrhenius plot is reasonably linear.
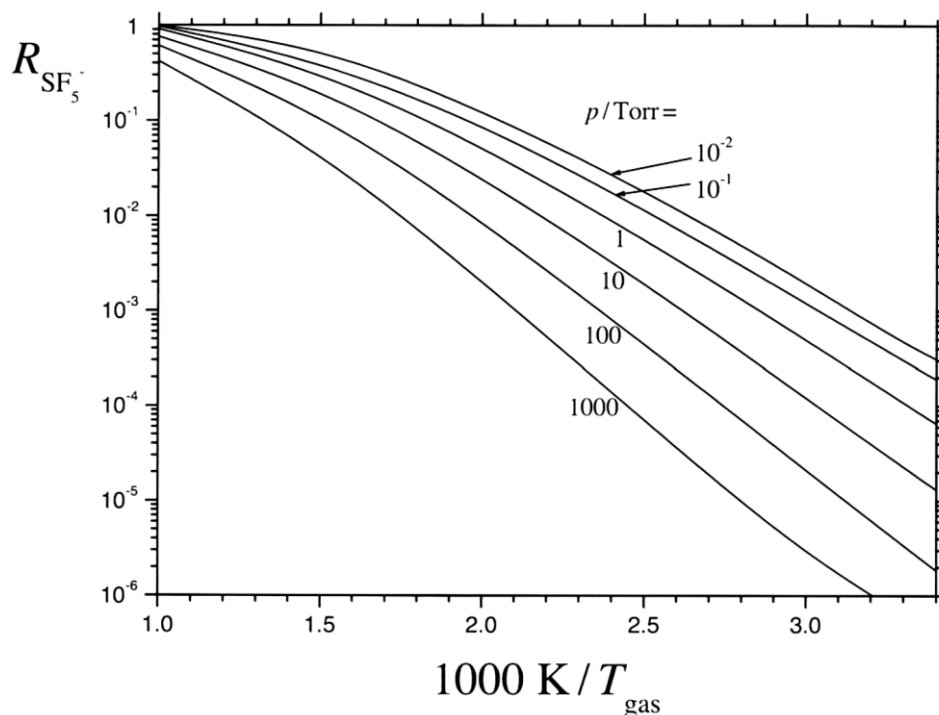


**Figure 4.4.** Reproduced from Troe *et al.* (25) shows the modelled temperature dependences of branching fractions $R$SF$_5$⁻ as a function of bath gas pressure, *P*.

This results in the following expression:

$$\beta(10^{-2}\text{ Torr, T}) = e^{\left(-\frac{4587}{T+7.74}\right)} \tag{E4.7}$$

The pressure-dependent results at 300 K from Troe *et al.* (25) can then be combined with the data point from Foster and Beauchamp (26) at 1.5 x $10^{-7}$ Torr to yield a pressure dependant expression for β at 300 K:

$$\log_{10}[\beta(P, 300 \text{ K})] =$$

$$-4.362 - 0.582 \log_{10}\left(\frac{P}{Torr}\right) - 0.0203 \left[\log_{10}\left(\frac{P}{Torr}\right)\right]^2 \qquad \text{(E4.8)}$$

Troe *et al.* (25) have shown that the pressure dependence of $\beta$ is very similar over a range of temperatures between 200 and 300 K. Therefore, E5.8 can be used to scale E5.7 by normalising to $\beta(10^{-2}$ Torr, 300 K) = 5.26 x $10^{-4}$, producing an expression for $\beta$ as a function of both $T$ and $P$:

$$\beta(P, T) = e^{\left(-\frac{4587}{T+7.74}\right)} \times 10^{4.362 - 0.582 \log_{10}\left(\frac{P}{torr}\right) - \frac{0.0203\left[\log_{10}\left(\frac{P}{torr}\right)\right]^2}{5.26 \text{ x } 10^{-4}}} \qquad \text{(E4.9)}$$

Finally,

$$\beta(P, T) = \frac{k_{\text{dis}}}{k_{\text{dis}} + k_{\text{at}}} \qquad \text{(E4.10)}$$

so that $k_{\text{dis}}$ can be calculated from $k_{\text{at}}$ (E4.1). Figure 4.5 illustrates the variation of $\beta$ with altitude and also shows the atmospheric temperature profile (a global average for January 2010, see below). $\beta$ is at a minimum around the tropopause, where the relatively low temperature and high pressure causes associative attachment to dominate. In contrast, at the high temperatures and low pressures of the lower thermosphere (above 115 km), dissociative attachment dominates and $\beta$ approaches unity. In the mesosphere between 50 and 100 km, $\beta$ is approximately constant because the effect of decreasing temperature is offset by the decreasing pressure.
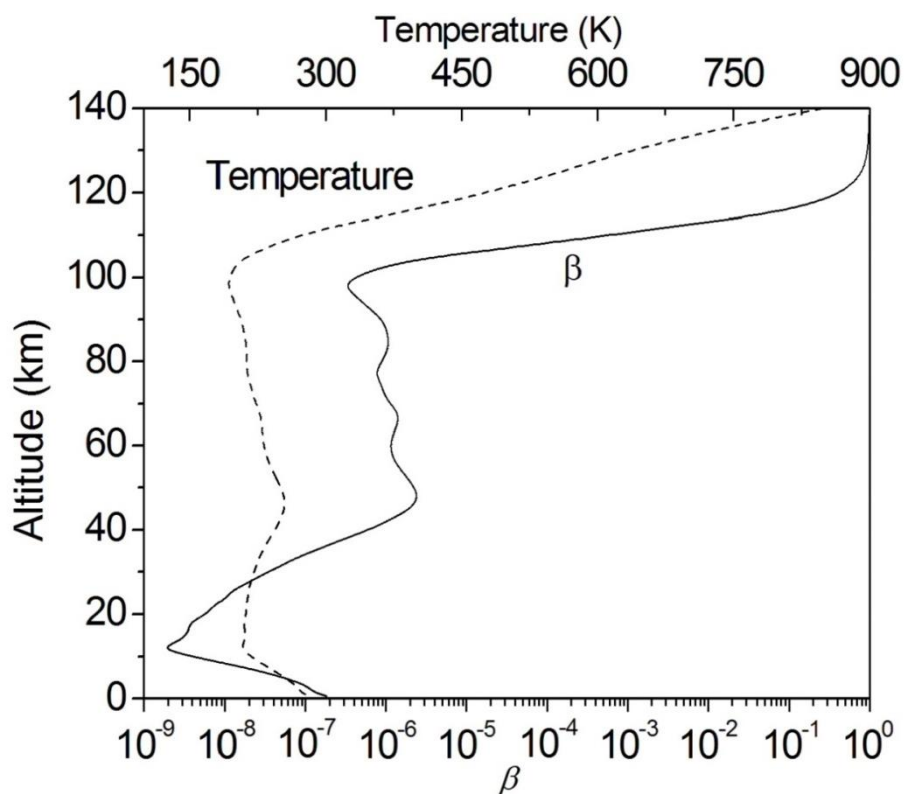
**Figure 4.5.** $SF_5^-$/ $SF_6^-$ branching ratio for thermal electron attachment to $SF_6$. The vertical profiles of electron density and temperature are global averages are obtained from the Whole Atmosphere Community Climate Model (WACCM).

Unlike $SF_6$, electron attachment of thermal electrons to $NF_3$ above 50 km should be a negligible process. This is due to the negative vertical electron affinity of $NF_3$, shown in Figure 4.6.
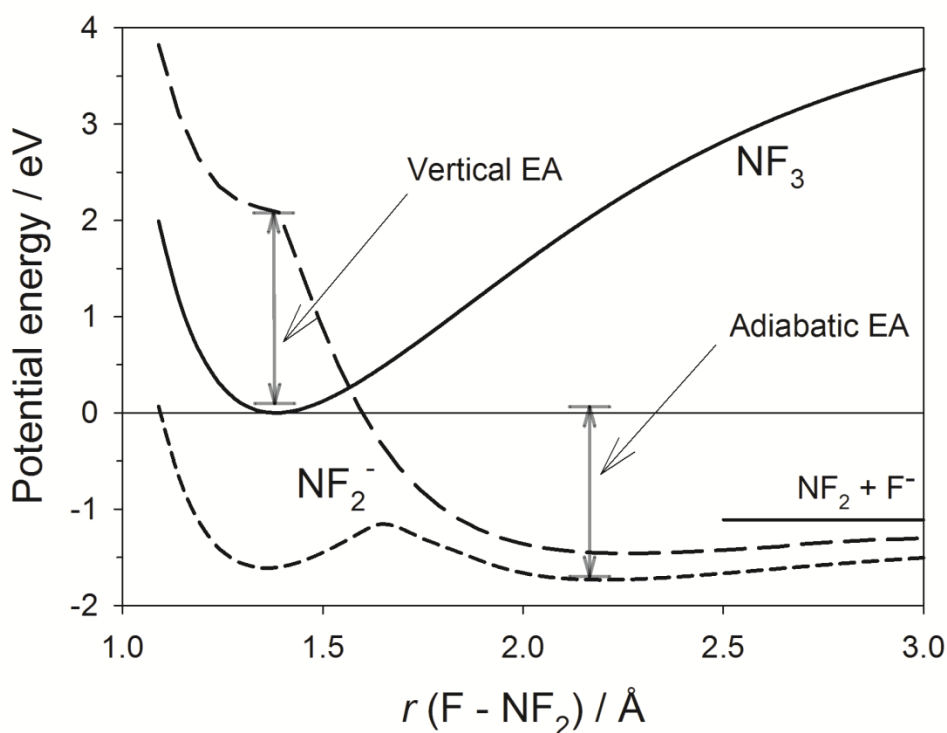
**Figure 4.6.** Potential energy curves for NF$_3$ and NF$_3^-$ as a function of NF$_2$ – F distance, calculated at the B3LYP/ 6-311 + g(2d) level by Prof. John Plane (27). The neutral NF$_2$ – F curve (solid line) and ionic NF$_2$ – F curve (short dashed line) are relaxed scans along the reaction coordinate, i.e. the minimum energy paths of the respective potential energy surfaces. The points on the ionic NF$_2$ – F curve (long dashed line) are calculated at the geometry of the neutral NF$_2$ – F curve, thus providing the vertical electron affinity.

Similarly, the vertical electron affinity of CFC-115 is -1.3 eV (calculated at the B3LYP/ 6-311+g(2d) level by J. M. C. Plane (27) using the method described in Chapter 2), so that thermal electron attachment to CFC-115, like NF$_3$, was found not to be significant. Because of this, loss rates of these species with respect to electron attachment were not explored further.

### 4.1.1.3 O($^1$D)

O($^1$D) profiles for all studies are taken from the Whole Atmosphere Community Climate Model (WACCM) (28). The rate constant for the reaction of O($^1$D) with $SF_6$ has an upper limit of $1.8 \times 10^{-14}$ cm$^3$ s$^{-1}$ (14), which is consistent with an endothermicity of 39 kJ mol$^{-1}$ (29). This low value suggests the reaction is likely to occur too slowly to be of atmospheric significance and is therefore not considered further.

For the reaction of $NF_3$ and O($^1$D), the reactive channels, rather than quenching, account for most of the loss by O($^1$D) with branching ratios between (0.83 ± 0.25) (30) and (0.99 ± 0.01) (31). Zhao *et al.* (31) observed a very weak negative temperature dependence ($5.68 \times 10^{-11}$ exp (5/ T) cm$^3$ molecule$^{-1}$ s$^{-1}$ ), whereas Dillon *et al.* (32) reported a temperature independent value of (2.0 ± 0.3) $\times 10^{-11}$ cm$^3$ molecule$^{-1}$ s$^{-1}$. When these two data sets are compared, there is little evidence of temperature dependence between 199 – 356 K. We therefore use here the result from Dillon *et al.* (32) and assume 100 % reactive loss of $NF_3$.

Removal of $NF_3$ by O($^1$D) is nearly as important as photolysis in the stratosphere where the concentration of O($^1$D) is relatively high because of the ozone layer.

The reaction of CFC-115 with O($^1$D) was also investigated as part of this study:

$$C_2F_5Cl + O(^1D) \ \rightarrow ClO + \ CF \tag{R4.5}$$

R4.5 is fast with an overall (i.e. quenching + reaction) rate constant of $k$(217 – 373 K) = $6.5 \times 10^{-11}$ exp (+30/T) cm$^3$ molecule$^{-1}$ s$^{-1}$ and a reactive yield of 0.72 (3). This reaction is important in the stratosphere where photolysis of $O_3$ leads to a relatively high concentrations of O($^1$D).

**4.1.1.4 Metal Reactions**

The Na profiles used in the modelling aspect of the study are extracted from a recent implementation of Na chemistry in WACCM (28), and the profile of atomic K was measured at the representative latitude of 54 °N (33).

Apart from the reactions of $SF_6$ with K and Na (although with apparent significant disagreement in the case of the $SF_6$ + Na reaction) (34-36), the rate coefficients of the other metal - PFC reactions do not appear to have been measured previously.

Na and K reactions are not competitive in the removal of $SF_6$. This is true even where metal atom concentrations peak (~ 90 km). At this altitude, associative electron attachment occurs at a rate three orders of magnitude faster than removal by Na or K. Removal of $SF_6$ by both metals occurs at a similar rate. We do not further consider the reactions of Mg and Fe with any PFC because their rate coefficients will be very slow at a typical temperature of 180 K in the upper mesosphere.

Although dominant in the stratosphere, $NF_3$ removal by $O(^1D)$ becomes less important in the mesosphere and is overtaken by Na removal above 80 km. The metals clearly play a secondary role in this model scenario. However, the Na and K reactions will be the only removal processes at high latitudes during winter when photolysis rates become very small (note the metal atom concentrations are highest in the winter mesosphere during polar night) (28). Whether this impacts on the overall atmospheric lifetime of $NF_3$ depends on the circulation of $NF_3$ from the tropical tropopause where it will enter the stratosphere, to the upper mesosphere (37). Nevertheless, at the low temperatures of the mesosphere, reactions with the metal atoms are not important routes for $NF_3$ removal.

Na reaction rates peak with the metal atom concentration at ~ 90 km but still are unable to compete with photolysis or $O(^1D)$ in the removal of CFC-115. At this altitude, removal by Na occurs at a rate ~ 3 orders of magnitude greater than removal by K.

**4.1.1.5 Total Loss**

The loss rates of $SF_6$ and CFC-115 as a function of altitude, due to the various processes discussed above, are illustrated in Figures 4.7 – 4.9.

In order to assess the impact of our new results on the atmospheric lifetimes of $SF_6$, the loss rates of the metal atom reactions and VUV photolysis were then compared with the loss rates due to associative and dissociative attachment of electrons to $SF_6$ (17, 25).
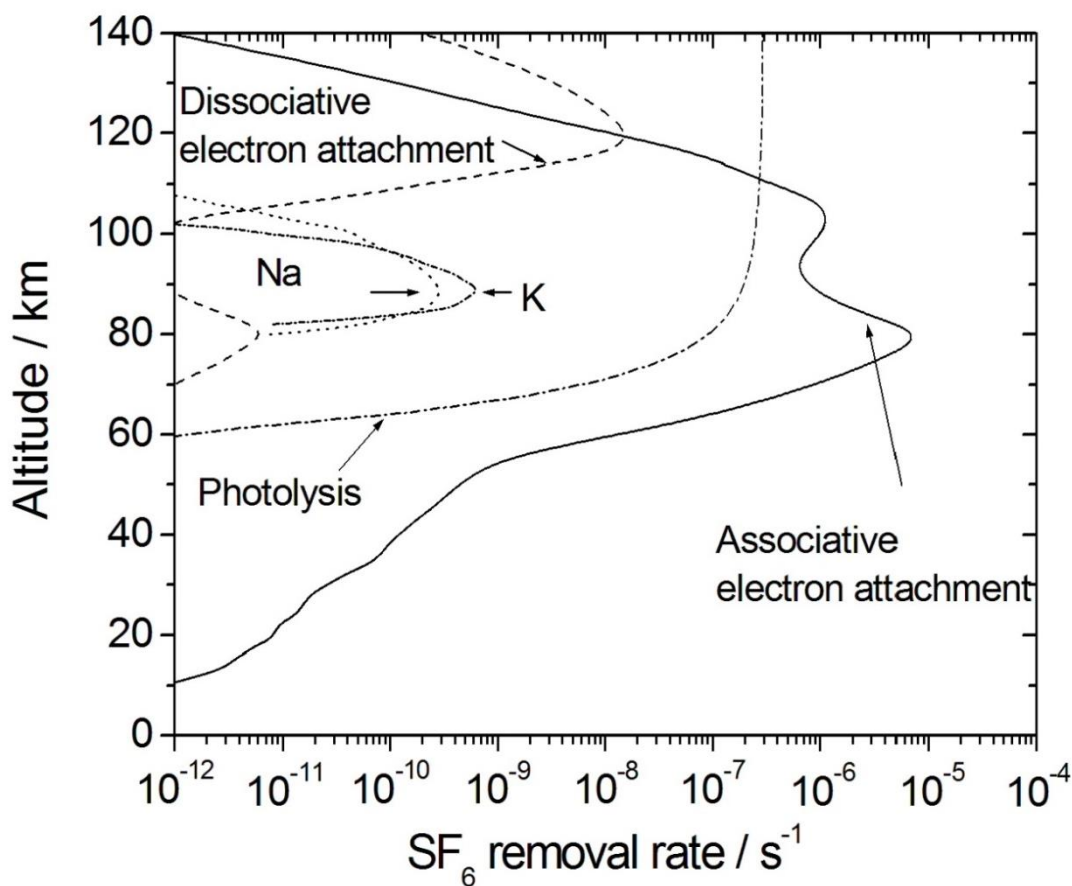


**Figure 4.7.** First-order removal rates of $SF_6$ by photolysis (dash-dot line), associative electron attachment (solid line), dissociative electron attachment (dashed line), reaction with Na (short dash – dot line) and reaction with K (dotted line).

Figure 4.7 shows that associative electron attachment is the dominant removal process for $SF_6$ throughout the atmosphere up to 100 km; at higher altitudes, photolysis dominates. Nevertheless, the absolute loss rate by electron attachment only becomes significant in the mesosphere where the removal rate exceeds $10^{-9}$ s$^{-1}$ (e folding lifetime < 30 years). Combining this slow rate of removal with the time taken to transport $SF_6$ above 60 km (~10 years) (2) explains the exceptionally long atmospheric lifetime of $SF_6$.

The $NF_3$ removal rates are plotted as a function of altitude in Figure 4.8 below, for the conditions of noon at 40 °N latitude in January (50 ° solar zenith angle). The photolysis rates for solar radiation over the complete spectral range, and for the Lyman-α line only, are both illustrated in Figure 4.8. This shows photolysis by Lyman-α is negligible below 50 km but becomes dominant above 66 km and contributes 75 % of the total photolysis rate in the upper mesosphere ( 80 – 90 km). Photolysis is the dominant removal process throughout the stratosphere and mesosphere.
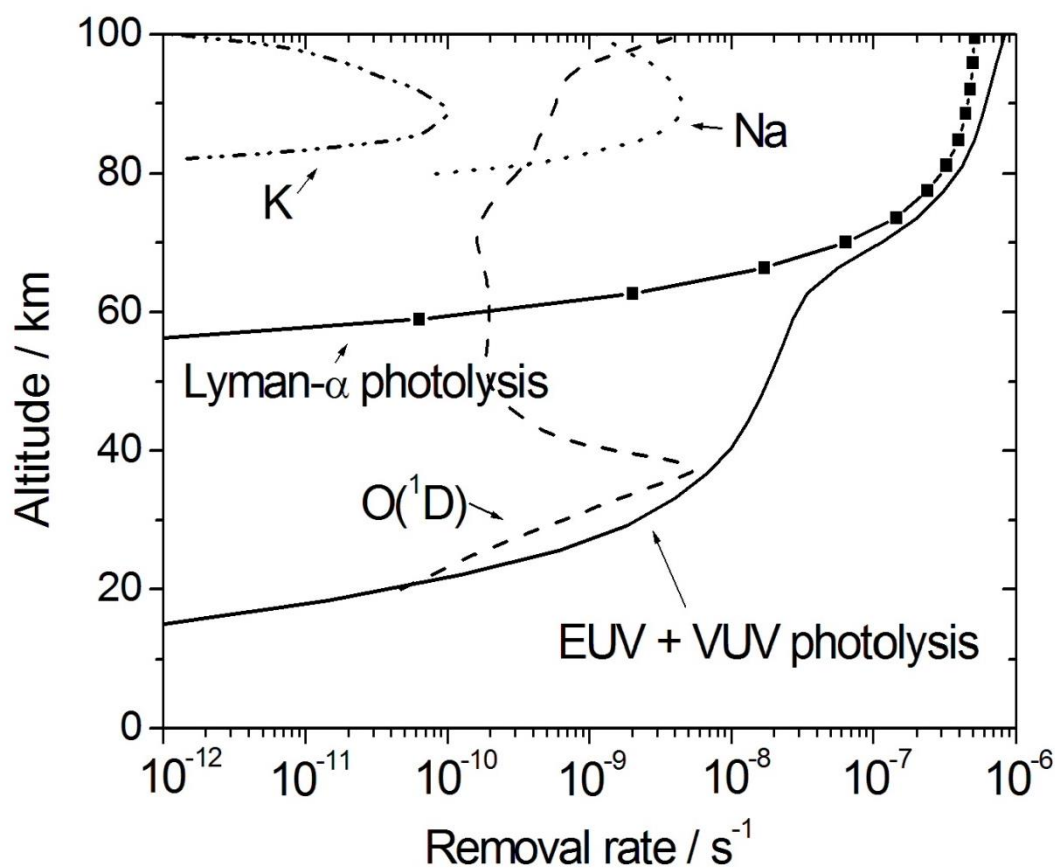
**Figure 4.8.** First-order removal rates of NF₃ by different processes (solid line, full spectral range; solid line with symbols, Lyman-α only; short dash-dot, reaction with O($^1$D); dashed line, reaction with Na; dashed-dotted line, reaction with K).

Finally, In order to assess the impacts of these new results on the atmospheric lifetimes of CFC-115, the loss rates of the metal atom reactions and VUV photolysis were then compared with the reaction of O($^1$D) atoms with CFC-115 (3). The loss rates of CFC-115 according to these processes are shown below in Figure 4.9.
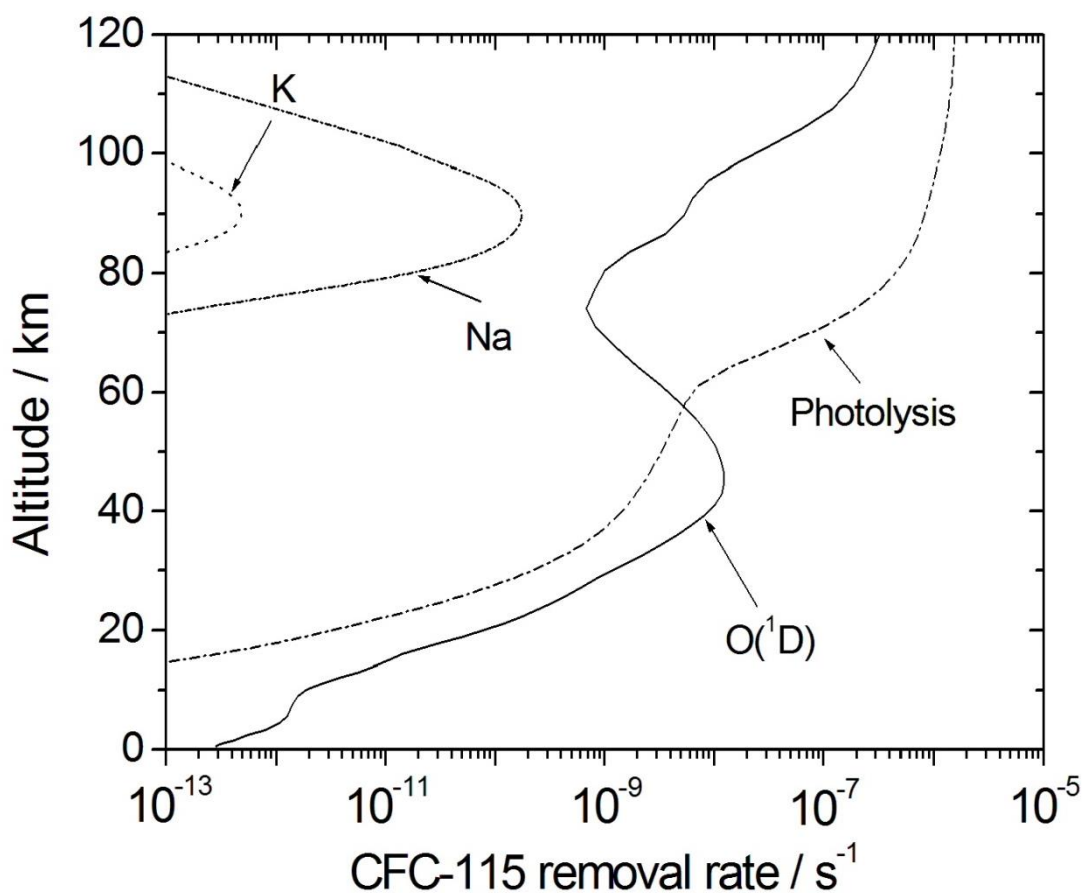
**Figure 4.9.** First order removal rates of CFC-115 by photolysis (dash – dot line) and reaction with O($^1$D) (solid line), Na (short dash – dot line) and K (dotted line).

Figure 4.9 shows that the reaction with O($^1$D) is the major removal process, up to 50 km. This process peaks in the upper stratosphere around 40 km; this is where there is a maximum in O($^1$D) because the O$_3$ concentration on the topside of the O$_3$ layer is still high enough for relatively rapid photochemical production of O($^1$D), but the total atmospheric density is low enough that electronic quenching of O($^1$D) is comparatively slow (15).

### 4.1.1.6 Additional Removal Processes

In the middle and upper mesosphere there are significant concentrations of O($^3$P) and H (15), so the reaction enthalpies and transition state energies for the

following reactions were calculated by J. M. C. Plane (27) using the accurate CBS-QB3 level of theory (38):

$$SF_6 + O(^3P, ^1D) \rightarrow FO + SF_5 \quad \Delta H_r(298\ K) = +228,\ 38\ \text{kJ mol}^{-1}\ (R4.6)$$

$$SF_6 + H \rightarrow HF + SF_5 \quad \Delta H_r(298\ K) = -125\ \text{kJ mol}^{-1}\ (R4.7)$$
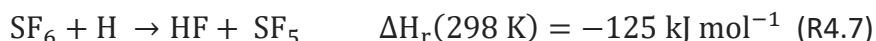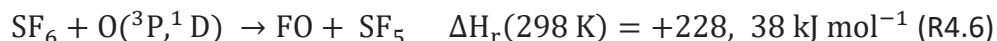
Although R4.7 is exothermic, it has a significant calculated transition state energy (including zero-point energy) of 103 kJ mol$^{-1}$, and so would not be important at atmospheric temperatures. R4.6 is too endothermic even for the reaction of SF$_6$ with O($^1$D), which is 190 kJ mol$^{-1}$ above the ground state, to be possible.

In the mesosphere above 80 km, NF$_3$ will encounter relatively high concentrations of O($^3$P) and H atoms (37). Although the reaction with H is thermodynamically favourable:

$$NF_3 + H \rightarrow HF + NF_2 \quad \Delta H_r(298\ K) = -326\ \text{kJ mol}^{-1}\ (R4.8)$$
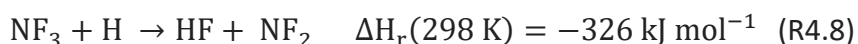
this reaction (29) has an energy barrier of 59 kJ mol$^{-1}$ at the CBS-QB3 level of theory and so will be too slow at mesospheric temperatures to affect the NF$_3$ lifetime. Similarly, the reaction (29):

$$NF_3 + O \rightarrow FO + NF_2 \quad \Delta H_r(298\ K) = 29\ \text{kJ mol}^{-1} \quad (R4.9)$$
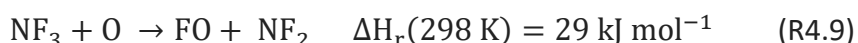
has a barrier of 148 kJ mol$^{-1}$ (CBS-QB3 level), and so can be discounted.

The Lyman-α absorption cross section of NF$_3$ was also measured, and this is revealed as the dominant removal process for the gas if it survives long enough to reach altitudes above 60 km.

WACCM was also used to provide vertical profiles of H, HCl, O$_3$, O($^1$D) and electron density. For illustrative purposes, we have taken the global averages of these parameters for January 2010.

Additionally, in the middle and upper mesosphere there are significant concentrations of O($^3$P) and H (15), so the reaction enthalpies and transition state energies for the following reactions were calculated by J. M. C. Plane (27) using the accurate CBS-QB3 level of theory (38):

$$C_2F_5Cl + O(^3P) \rightarrow ClO + C_2F_5 \quad \Delta H_r(298 \text{ K}) = +103 \text{ kJ mol}^{-1} \quad \text{(R4.10)}$$

$$C_2F_5Cl + H \rightarrow HCl + C_2F_5 \quad \Delta H_r(298 \text{ K}) = -67 \text{ kJ mol}^{-1} \quad \text{(R4.11)}$$
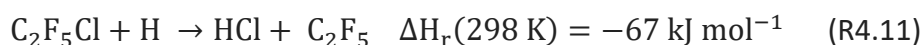
Although reaction R4.11 is exothermic, it has a significant calculated transition state energy (including zero-point energy) of 44 kJ mol$^{-1}$, and so would not be important at atmospheric temperatures.

### 4.1.2 Atmospheric Lifetime - Models and Methodology

Atmospheric lifetimes have been determined for each PFC by 3-D model simulation using the Whole Atmosphere Community Climate Model (WACCM) (39) where all work relating to lifetimes was conducted by Dr Tamás Kovács.

WACCM is a coupled chemistry-climate numerical model extending vertically from the ground up to the lower thermosphere (~140 km). Although a simple 1-D model may be relatively accurate for local concentrations, it would not be capable of simulating the large scale horizontal distribution of mesospheric species. These are affected by several mesospheric processes, including meteoric ablation.

Calculations were carried out on WACCM 4 which has 88 pressure levels from the surface to $5.96 \times 10^{-6}$ Pa and a horizontal resolution of $1.9° \times 2.5°$ (latitude × longitude). The model contains a detailed treatment of middle atmosphere chemistry including interactive treatments of Na and K. The SD (specified dynamic) version of the model was used as it allowed for comparison with observations.

The model does not include any negative ion reactions. In order to use a realistic electron concentration, the role of negative ions in the *D* region was considered through a scaling factor. This was introduced to convert the standard WACCM electron concentrations, which are calculated from charge balance with the five major positive *E* region ions (N$^+$, N$_2^+$, O$^+$, O$_2^+$ and NO$^+$), to more realistic electron concentrations. The latitude and altitude dependent scaling factors were then built into the SF$_6$ model and the model run used them *in situ*.

All possible loss channels were identified, including reactions with mesospheric metals (Na, K), $O(^1D)$ radicals, background electrons and UV photolysis. All the necessary concentrations (Na, K, electron, $O(^1D)$) needed to determine the loss rates were directly simulated in the WACCM runs and the WACCM simulation for each PFC included different tracers (including a passive tracer) for each loss process as well as a 'total reactive' tracer so that the importance of each sink could be quantified. The rate constants for the metal reactions were measured  under mesospheric conditions for the first time (Chapter 3), while the values for the reactions with $O(^1D)$ were adopted from Baasandorj *et al.* (3). Emission data for $NF_3$ and CFC-115 were input from mean surface concentrations of each species for averaged monthly concentrations across 2010. Emissions of $SF_6$ were included in the model from IPCC daily emission data up to 2010.

The model was run for the period of 18 years (January 1990 – December 2007) for $SF_6$, and for 13 years for CFC-115 and $NF_3$ in order to allow enough time for the lifetime to reach a steady state. The first five years in the $SF_6$ model run (1990-1994) were used to spin the model up.

## 4.2    Infrared Absorption Cross Sections

PFCs are very potent global warming agents, not only because of the very long lifetimes discussed above, but also because they absorb infrared radiation strongly between 800 and 1200 $cm^{-1}$. This region of the electromagnetic spectrum, known as the 'atmospheric window' occurs where atmospheric absorption from $H_2O$, $CO_2$ and $O_3$ is at a minimum. Furthermore, it overlaps with the peak in the terrestrial infrared spectrum (500 - 1500 $cm^{-1}$) making it a particularly important region (40).

Quantitative absorption spectra of $SF_6$ across the main band are available from the GEISA: Spectroscopic database (41) and the HITRAN 2012 Molecular Spectroscopic Database (42). Similarly, previous spectra of $NF_3$ have been measured by Robson *et. al* (43) and Molina *et. al* (44), and CFC-115 by McDaniel *et. al* (45).

There is some deviation across existing literature cross sections and few quantitative full spectra measurements are available. This work was consequently carried out in order to provide a more complete set of measurements and reduce uncertainty in published data.

### 4.2.1 Theory

Before experimental infrared cross sections were obtained, theoretical frequency calculations were performed to predict and understand the spectra of each species. These were calculated using the Gaussian suite of programs (46) described in Chapter 3.

Previous studies (47-49) indicate that it is possible to calculate infrared spectra using density functional theory (DFT) or *ab initio* methods with useful accuracy. Computed vibrational frequencies predict fundamental frequencies for molecules to which an empirical scaling factor (between 0.8 and 1) is commonly applied as a means of accounting for errors due to the approximate nature of the electronic structure calculation which are predominantly associated with calculations of force constants. Another consideration is anharmonicity effects which, when not accounted for, mean calculated frequencies can exceed observed frequencies by as much as 12%. For calculations of this nature it is assumed the potential energy surface is harmonic, however, the Morse potential (Figure 4.10) provides a much better description (11).
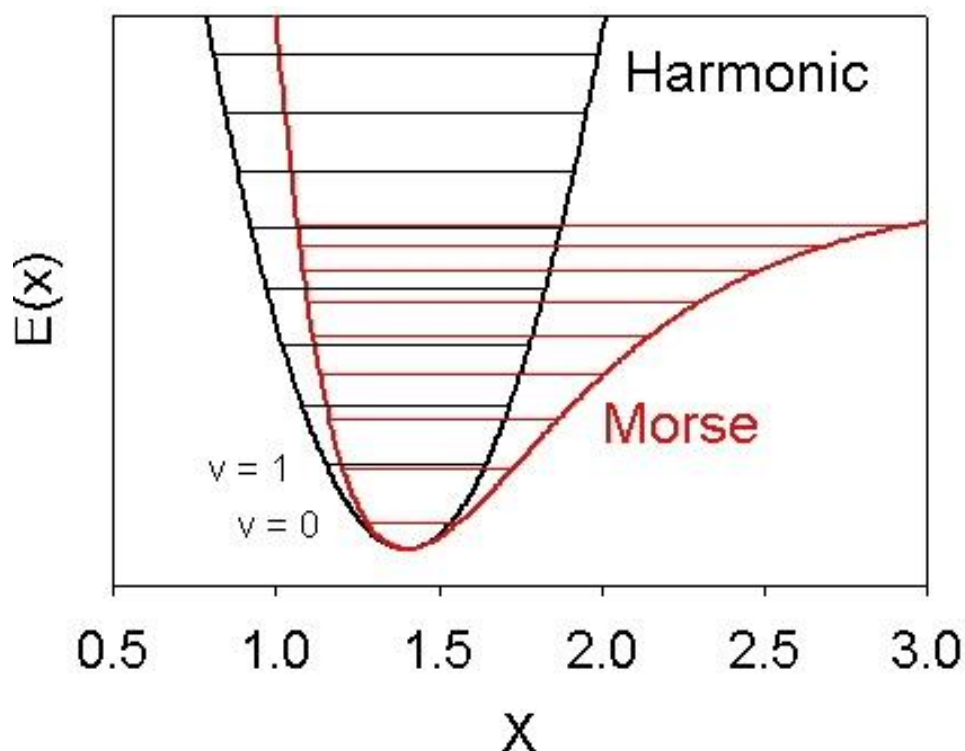
**Figure 4.10.** Comparison of the harmonic and Morse potentials where E is the potential energy and x is the equilibrium internuclear distance. Reproduced from Martin *et al.* (50).

The Morse potential can be described by:

$$E(x) = D(1 - e^{(-\beta(x-x_0))})^2 \tag{E4.8}$$

where D, β and $x_0$ are constants, E is the potential energy and x is the internuclear distance. The harmonic potential is described by:

$$E(x) = kx^2 \tag{E4.9}$$

where E(x) is the potential energy, *k* is the bond force constant and *x* the internuclear distance.

The harmonic potential is only ever used as an approximation. This is because it is unrealistic as a bond within a diatomic molecule obeying the harmonic potential cannot dissociate whereas the Morse potential allows for dissociation of the bond (50).

The vibrational frequency is predicted by calculating the second derivative of the potential energy surface with respect to the nuclear coordinates of the molecule. This is demonstrated as the curve minima shown on Figure 4.10 where for each well the minimum is the same and the effects of anharmonicity can be seen as smaller spacing between the vibrational energy levels.

The application of a scaling factor means that it can be assumed anharmonicity effects are accounted for. There have been many studies which attempt to ascertain the scaling factor for calculations at various theory level/ basis set combinations. The standard formula for calculating these is:

$$sf = \frac{\sum v_i w_i}{\sum w_i{}^2} \qquad \text{(E4.10)}$$

The largest source for computational values is the computational chemistry benchmark database (CCCBD) (50) containing data on over a million calculated vibrational frequencies with their experimentally determined values and scaling factors for given quantum chemistry models (50).

As stated, the Gaussian 09 software package was used to perform theoretical calculations where the choice of theory level and basis set are critical to obtaining accurate results. *Ab. initio* techniques such as Hartree-Fock (HF), DFT and Møller-Plesset 2 (MP2) are combined with different basis sets to obtain infrared wavenumbers and intensities with varying degrees of accuracy. Computational techniques have previously been to demonstrate that inclusion of electronic correlation is important to obtain accurate infrared intensities for small (< 6 atoms) molecules (51). Papasavva *et al.* studied CF using semi-empirical Austin-Model 1 (AM1) and Parameterised Model 3 (PM3) methods and HF and MP2 with a wide range of basis sets. The best agreement was obtained using the MP2/ 6-31G** level of theory where deviations were systematic and could be corrected using a scaling factor. Furthermore, theoretical intensities were generally consistent with experiments. In a similar study, Halls and Schlegel (52) found that DFT methods produced a good prediction of infrared wavenumbers and intensities for a selection of small molecules. A review by Bravo *et al.* (48) suggested that DFT methods could

be more accurate than both MP2 and HF in carrying out frequency calculations on small molecules than some higher theory levels when combined with a large basis set containing polarised functions. The successful deployment of the DFT- B3LYP/ 6-31G** theory level and basis set in obtaining accurate spectra was demonstrated even for larger molecules (48). It was also shown that increased basis set size and functions resulted in reduced scaling factors and consequently, increased accuracy (53, 54).

### 4.2.2  Infrared Absorption Cross Sections

Tables 4.1 – 4.3 present the experimentally determined infrared band frequencies for $SF_6$, $NF_3$ and CFC-115 respectively. These values are compared to previous studies and theoretically determined values.

**Table 4.1.** Comparison of experimentally determined infrared bands for $SF_6$ against their theoretically derived counterparts. Two theory levels are used, DFT B3LYP/6-311**G and MP2/6 – 31 G, in order to demonstrate the accuracy of DFT theory level with polarised basis set against the higher, MP2 theory level. Wavenumbers from Varanasi *et al.* (41) are also provided and the symmetry assignment of each band.

| Theoretical Frequency Following Application of Relevant Scaling Factor | | Experimental Wavenumber $(cm^{-1})$ | Band Assignment | |
| --- | --- | --- | --- | --- |
| DFT B3LYP 6-311**G[a] $(cm^{-1})$ | MP2 6 – 31G[b] $(cm^{-1})$ | | Literature wavenumber (41) $(cm^{-1})$ | Symmetry |
| 313 | 327 | - | 347 | 3 x $T_{2u}$ |
| 502 | 489 | - | 525 | 3 x $T_{2g}$ |
| 595 | 576 | 616 | 616 | 3 x $T_{1u}$ |
| 608 | 670 | - | 642 | 2 x $E_g$ |
| 745 | 756 | - | 774 | $A_{1g}$ |
| 919 | 998 | 947 | 948 | 3 x $T_{1u}$ |

[a] where scaling factor is equal to 0.9668

[b] where scaling factor is equal to 0.9568

For the above scenario, the scaled DFT B3LYP 6-311**G $SF_6$ spectrum is plotted against our experimentally determined result. The agreement between the two spectra over the main bands is presented below in Figure 4.11.

**Figure 4.11** Comparison of experimentally determined infrared spectra for $SF_6$ (black line) between 500 and 1200 $cm^{-1}$ against the theoretically derived equivalent (red line). The theoretical spectra was calculated using the DFT B3LYP/6-311**G level of theory.

**Table 4.2.** Comparison of experimentally determined infrared bands for $NF_3$ against their theoretically derived counterparts. Two theory levels are used, DFT B3LYP/6-311**G and MP2/6 – 31 G, in order to demonstrate the accuracy of DFT theory level with polarised basis set against the higher, MP2 theory level. Wavenumbers from Wilson *et al.* (55) are also provided and the symmetry assignment of each band. Scaling factors are taken from Irikura *et al.* (56).

| Theoretical Frequency Following Application of Relevant Scaling Factor | | Experimental Wavenumber (cm$^{-1}$) | Band Assignment | |
|---|---|---|---|---|
| DFT B3LYP 6-311**G[a] | MP2 6 – 31G[b] | | Literature wavenumber (cm$^{-1}$) | Symmetry |
| 471 | 381 | 490 | 492 | E |
| 626 | 519 | 647 | 647 | $A_1$ |
| 864 | 765 | 909 | 907 | E |
| 1011 | 828 | 1032 | 1032 | $A_1$ |

[a] where scaling factor is equal to 0.9668

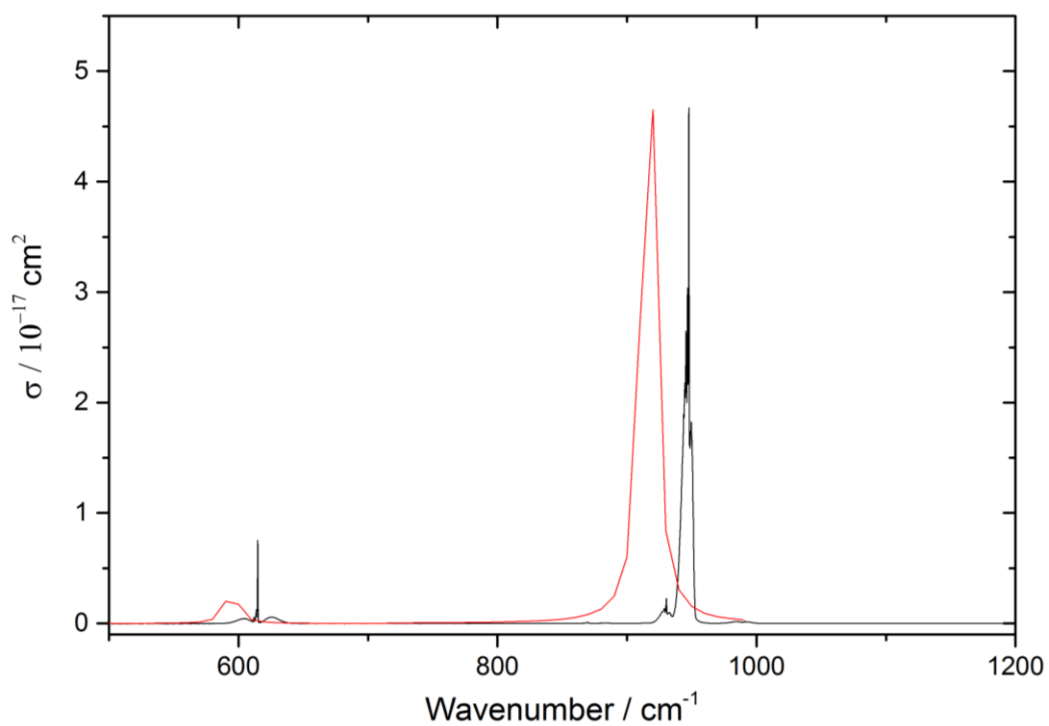[b] where scaling factor is equal to 0.9568

**Table 4.3.** Comparison of experimentally determined infrared bands for CFC-115 against their theoretically derived counterparts. Two theory levels are used, DFT/B3LYP 6-311**G and MP2/6 – 31 G, in order to demonstrate the accuracy of DFT theory level with polarised basis set against the higher, MP2 theory level. Wavenumbers from Wilson *et al.* (55) are also provided and the symmetry assignment of each band.

| Theoretical Frequency Following Application of Relevant Scaling Factor | | Experimental Wavenumber | Band Assignment | |
|---|---|---|---|---|
| DFT B3LYP 6-311G**G[a] | MP2 6 – 31G[b] | (cm$^{-1}$) | Literature wavenumber (cm$^{-1}$) | Symmetry |
| 56 | 65 | - | - | A'' |
| 175 | 171 | - | - | A' |
| 209 | 205 | - | - | A'' |
| 301 | 292 | - | - | A' |
| 319 | 301 | - | - | A'' |
| 328 | 330 | - | - | A' |
| 413 | 390 | - | - | A' |
| 432 | 399 | - | - | A'' |
| 529 | 484 | - | - | A' |
| 569 | 538 | - | - | A'' |
| 622 | 563 | 560 | 558 | A' |
| 728 | 664 | 648 | 644 | A' |
| 925 | 901 | 762 | 762 | A' |
| 1081 | 1040 | 983 | 978 | A' |
| 1140 | 1111 | 1132 | 1130 | A'' |
| 1177 | 1157 | 1184 | 1182 | A' |
| 1191 | 1167 | 1241 | 1242 | A'' |
| 1285 | 1274 | 1350 | 1346 | A' |

[a] where scaling factor is equal to 0.9668

[b] where scaling factor is equal to 0.9568

Tables 4.1 – 4.3 show our results have good agreement with previous measurements in terms of band frequency position. Furthermore, they support the proposition made by Bravo *et al.* (48) that a DFT level calculation combined with polarised basis sets provides better agreement with experimental results than calculations at the higher, MP2 level of theory.

The integrated infrared absorption cross-sections measured here are listed in Tables 4.4 – 4.6 and the full spectra shown in Figures 4.12 – 4.14. The integrated cross-sections for $SF_6$ from the GEISA: 2011 Spectroscopic Database (57) and the HITRAN 2012 Molecular Spectroscopic Database (42) are presented in Table 4.4 for comparison with the experimentally determined values from the present study. The spectrometer error is given as ± 1% for all experiments and uncertainty in the sample concentrations of $SF_6$ were calculated to be 0.7%. Spectral noise was averaged at ± 5 x $10^{-21}$ $cm^2$ molecule$^{-1}$ per 1 $cm^{-1}$ band. However at wavenumbers < 550 $cm^{-1}$, towards the edge of the mid infrared where opacity of the KBr filter was increased, this value was 1 x $10^{-20}$ $cm^2$ molecule$^{-1}$ per 1 $cm^{-1}$ band. The error from determining the scaling cross-section was 5 %. This results in an average overall spectral error of ± 5 %.
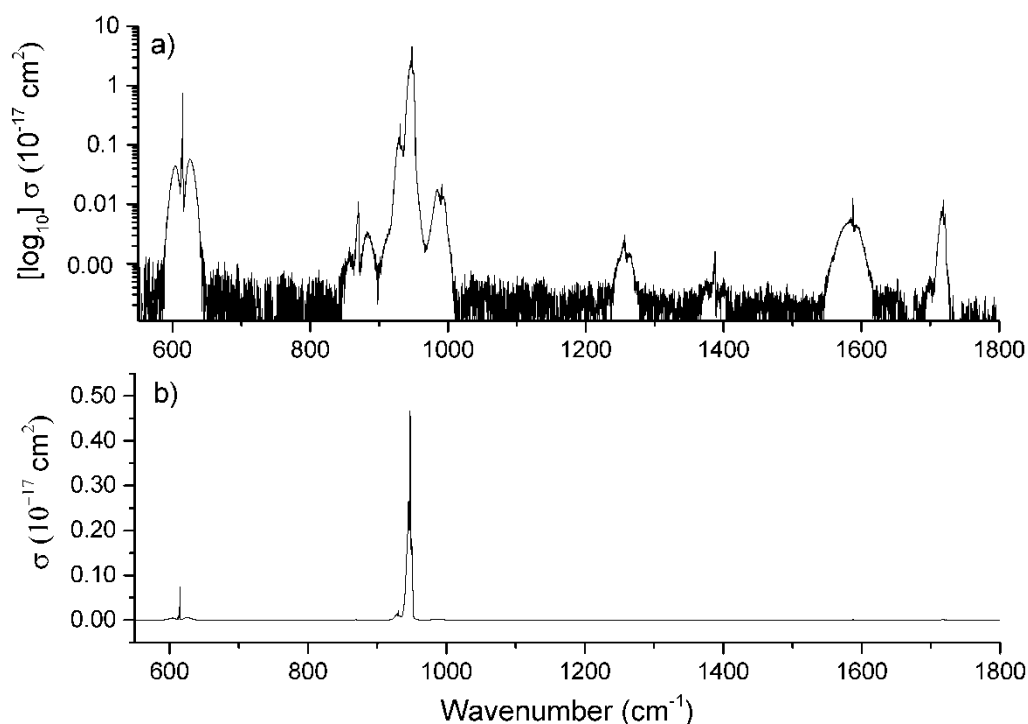
**Figure 4.12** Infrared absorption spectrum of SF$_6$ at ~295 K on (a) a logarithmic y axis and (b) a linear y axis. A logarithmic scale is used for panel a) in order to demonstrate the relative positions of the minor bands.

**Table 4.4.** Integrated absorption cross-sections for SF$_6$ measured in present work and compared with those obtained by Hurley (58), Varanasi (59) and HITRAN (42).

| Molecule | Band Limits, cm$^{-1}$ | Integrated Cross-section, 10$^{-16}$ cm$^2$ molec$^{-1}$ cm$^{-1}$ | Ratio of Integrated Cross-section in Present Work to Hurley | Ratio of Integrated Cross-section in Present Work to Varanasi | Ratio of Integrated Cross-section in Present Work to HITRAN |
|---|---|---|---|---|---|
| SF$_6$ | 925 - 955 | 2.02 | 1.07 | 1.01 | 0.99 |
| | 600 - 2000 | 2.40 | - | 1.09 | - |

The intensities of the main absorption band (925-955 cm$^{-1}$) of SF$_6$ measured in the present work and shown in Table 4.4, is 7 % greater than those reported Hurley (58), 1 % greater than Varanasi (59) and 1 % lower than those given in HITRAN (42). Comparison against Varanasi (59) between 650 and 2000 cm$^{-1}$ gives an agreement within 9 %. All differences reported are within the combined error of both experiments.

Table 4.5 lists the integrated cross-sections of the new set of spectra for NF$_3$ as shown in Figure 4.13. Similarly, Table 4.6 lists the integrated cross-sections for the new CFC-115 spectra displayed in Figure 4.14. In Tables 4.5 and 4.6 the relevant integrated cross-sections from literature are also given for comparison. Experimental and noise uncertainties were the same as for SF$_6$ and sample concentrations of NF$_3$ and CFC-115 were calculated to be ± 0.8 and 0.7%, respectively. Error in scaling cross section for NF$_3$ and CFC-115 were ± 5 and 6 % respectively (error in pressure dependence). This results in an average overall spectral error of ± 6 % in both cases.

**Figure 4.13.** Infrared absorption spectrum of NF₃ at ~295 K on (a) a logarithmic y axis and (b) a linear y axis. A logarithmic scale is used for panel a) in order to demonstrate the relative positions of the minor bands.
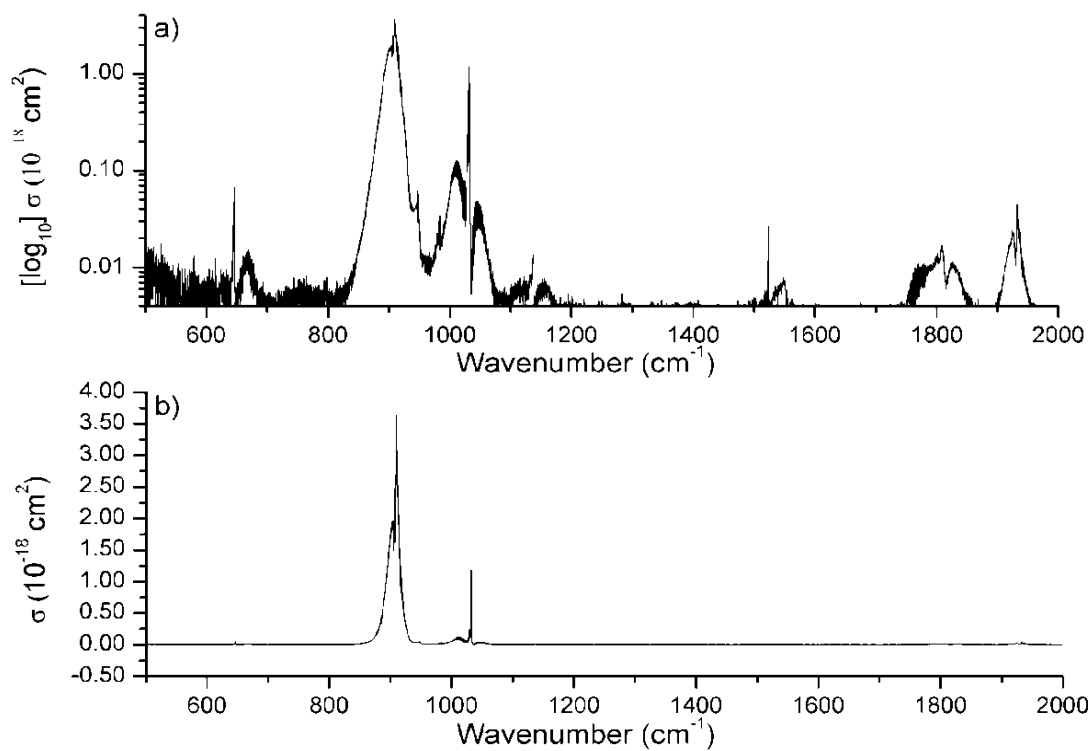
**Table 4.5.** Integrated absorption cross-sections for $NF_3$ measured in present work and compared with those obtained by Robson *et al.* (43) and Molina *et. al* (44).

| Molecule | Band Limits, $cm^{-1}$ | Integrated Cross-section, $10^{-18}$ $cm^2$ $molec^{-1}$ $cm^{-1}$ | Ratio of Integrated Cross-section in Present Work to Robson *et al.* | Ratio of Integrated Cross-section in Present Work to Molina *et al.* |
|---|---|---|---|---|
| | 600-700 | 0.41 | 0.94 | 0.83 |
| | 840-960 | 65.03 | 0.97 | 0.56 |
| | 970-1085 | 5.88 | 0.89 | 0.72 |
| | 1085-1200 | 0.10 | 1.52 | 1.46 |
| $NF_3$ | 1330-1440 | 0.08 | 0.23 | 0.21 |
| | 1460-1580 | 0.21 | 0.65 | 0.63 |
| | 1720-1870 | 0.71 | 1.03 | 0.92 |
| | 1890-1970 | 0.65 | 0.99 | 0.94 |
| | 600-1970 | 73.50 | 0.96 | 0.58 |

Panel b) of Figure 4.13 gives the spectrum in a logarithmic scale to show the positions of the minor and combination bands. The intensities of the two main absorptions bands (840-960 and 970-1085 $cm^{-1}$) of $NF_3$ measured in the present work and shown in Table 4.6, are 44 % and 28 % greater than those reported by Molina *et al.* (44). The integrated cross sections of the minor bands calculated by Molina *et al.* (44)display an average deviation of 32 % from our current results whereas the integrated cross-sections across the entire spectrum is 42 % greater than that of Molina *et al.* (44). All differences are greater than the combined error from both experiments and some explanation for this is provided by Robson *et al.*(43). In contrast, the intensities of the two main absorption bands are only 3 % and 11 % greater than those reported by Robson *et al.* with an average deviation of

29 % over the minor bands and merely 4 % across the entire spectrum. All differences excluding the minor bands in the region between 1085 and 1580 cm$^{-1}$ are comfortably within the combined error of both experiments.
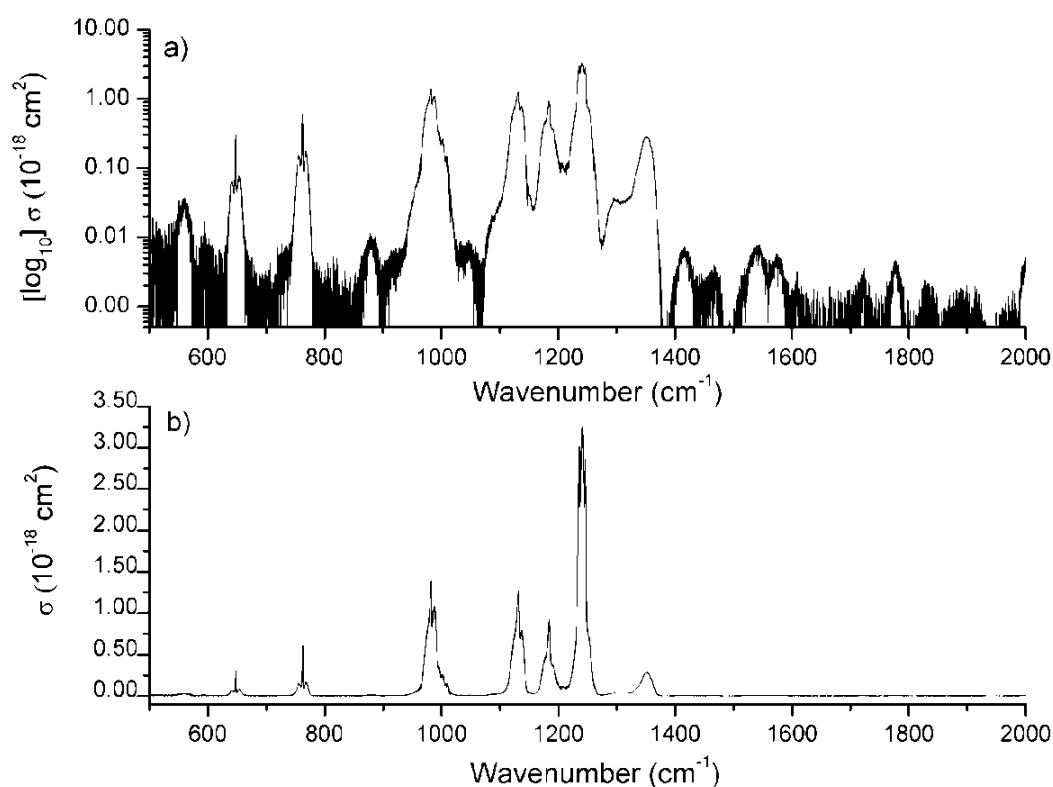


**Figure 4.14.** Infrared absorption spectrum of CFC-115 at ~295 K on (a) a logarithmic y axis and (b) a linear y axis. A logarithmic scale is used for panel a) in order to demonstrate the relative positions of the minor bands.

The intensity of the main absorption band for CFC-115 (1212-1265 cm$^{-1}$) as measured in the present work and shown in Table 4.6, is 94 % of that reported by McDaniel *et al.* (45). Three other main bands occurring at 946-1020, 1105-1150 and 1160-1212 cm$^{-1}$ show agreement with McDaniel *et al.* (45) of 90 %, 94 % and 95 % respectively. The small band occurring between 1326-1368 cm$^{-1}$ has an agreement of 97 %. These results are well within the combined error of both experiments.

**Table 4.6.** Integrated absorption cross-sections for CFC-115 measured in present work and compared with those obtained by McDaniel *et. al* (45).

| Molecule | Band Limits, $cm^{-1}$ | Integrated cross section, $10^{-17}$ $cm^2$ $molec^{-1}$ $cm^{-1}$ | Ratio of integrated cross section in Present Work to McDaniel *et. al* |
|---|---|---|---|
| | 946-1020 | 2.546 | 1.10 |
| | 1105-1150 | 2.015 | 1.06 |
| CFC-115 | 1160-1212 | 1.370 | 1.05 |
| | 1212-1265 | 5.381 | 1.06 |
| | 1326-1368 | 0.620 | 1.03 |

## 4.3 Radiative Forcings and Efficiencies

The infrared absorption cross-sections as obtained in the previous section were input into the Reference Forward Model (RFM) (60) and Library for Radiative Transfer (libRadtran) (61), two radiative transfer models used to obtain radiative forcings and efficiencies. Here, radiative forcing refers to the perturbation of the modern day concentration of the PFC against its pre-industrial concentration and is given in units of $Wm^{-2}$. Radiative efficiency refers to a perturbation of $0 - 1$ ppb and is given in units of $Wm^{-2}\,ppbv^{-1}$.

It is difficult to quantify surface temperature changes resulting from small perturbations due to climate variability and large uncertainties in climate feedback mechanisms (40). The historic effects of various drivers of climate change are typically specified and compared in terms of their radiative forcings, a measure of the perturbation to the Earth's energy budget. Various types of radiative forcing exist (62). The effective radiative forcing (ERF) measures the top of atmosphere energy budget changes following adjustments to the vertical temperature profile,

clouds and land-surface temperatures. The stratospherically adjusted radiative forcing (RF) is typically defined as 'the change in net (down minus up) irradiance (solar plus longwave; in $Wm^{-2}$) at the tropopause after allowing for stratospheric temperatures to readjust to radiative equilibrium, but with surface and tropospheric temperatures and state held fixed at the unperturbed values (63). The instantaneous radiative forcing (IRF) can be obtained by not applying the stratospheric adjustment. Although ERF estimates are more representative of temperature changes they are more uncertain as they rely on climate model estimates of cloud response (64). Further, climate model radiation codes do not typically represent minor GHGs, therefore it is not currently possible to estimate the ERF for the species considered here. We therefore estimate RF and IRF using the line-by-line Reference Forward Model (RFM). As the RFM only accounts for absorption, the extension to clouds and scattering processes was performed by a secondary radiative transfer model (libRadtran) using atmospheric optical depth profiles generated by the RFM.

From the absorption cross section spectrum the radiative efficiency can be approximated through the following equation developed by Pinnock *et al.* (40):

$$\text{RE} = \sum_{i=1}^{250} \ell \sigma_i(v_i) F_i(v_i) \qquad \text{(E4.11)}$$

where $\ell$ is the wavelength range over which measurements are taken; σ is the averaged absorption cross-section around the wavenumber, $v_i$, and $F_i(v_i)$ is adjusted cloudy sky radiative forcing per unit cross section ($cm^2$ molecule$^{-1}$ $cm^{-1}$)$^{-1}$ (40).

## 4.3.1 Models and Methodology

Radiative forcing calculations were made using the RFM (60). The RFM is a line-by-line radiative transfer model based on the previous GENLN2 model (65), and includes absorption cross sections for multiple background species extracted from the HITRAN database. Alongside providing upwelling and downwelling longwave fluxes for calculating clear-sky forcing, the RFM was used to generate optical depth

profiles at a resolution of 1cm$^{-1}$ for input into the DISORT radiative transfer solver (66) as implemented in the libRadtran (Library for Radiative Transfer) package (61). The clear-sky fluxes obtained from the RFM were validated against results from libRadtran for the cloudless, non-scattering case. Unlike the RFM, libRadtran includes scattering processes and provides a natural interface for including clouds, so the all-sky forcing is calculated in libRadtran.

Calculations to obtain the IRF and RF were performed using the flux form of the RFM at a spectral resolution of 0.1 cm$^{-1}$, determined by the resolution of the infrared spectra measured in this study. The radiative transfer calculation was performed on each spectral band between 550 – 2000 cm$^{-1}$ and irradiance flux integrated over wavelength to obtain the net irradiance at each level in the model atmosphere. For these calculations integration over the zenith angle was performed via a first moment double-Gauss procedure with 8 streams where the Planck function was set to vary linearly with optical depth. For the stratospheric adjustment, the stratosphere temperatures are adjusted using an iterative process based on heating rate changes that after 100 days have changed the stratospheric temperatures and returned them to radiative equilibrium as a result of the introduction of the PFC. For these PFCs, temperature change at the tropopause is of the order of ~ 1.5 x 10$^{-5}$ K for a perturbation of 1 x 10$^{-3}$ ppm (average tropospheric volume mixing ratio) and ~0.01 K for a perturbation of 1 ppb.

The model atmospheres were obtained from WACCM and consisted of vertical profiles at 66 levels from sea level up to 140 km. These consisted of temperature, pressure and mixing ratios of the major atmospheric constituents $CO_2$, $H_2O$, $CH_4$, $N_2O$, $O_3$ as well as the PFC trace species for evaluation. The mixing ratio was assumed to vary linearly between atmospheric levels. Zonal mean profiles were obtained from the 15th year of output by globally averaging over longitude.

A compilation of line data for background species was obtained from HITRAN 2012 (42) and absorption cross sections for the PFCs were taken from spectra carried out in this work. The temperature dependence of background species absorption is automatically interpolated from HITRAN data. However this was not considered for

the experimentally determined absorption cross-sections as the IRFs calculated using HITRAN cross-sections were in good agreement (5 – 10 %) with those from this study.

**4.3.1.1 Model Comparison**

Line-by-line calculations, where each local transition has its strength and linewidth adjusted for local conditions, and the contributions summed at each spectral grid point, are more accurate but computationally expensive. Results were used to calibrate experiments by obtaining IRF values from the RFM and repeating them in libRadtran.

The effect of seasonal and geographical variations on factors influencing radiative forcing means that multiple averaged local radiative forcings calculated across the location - time grid will give the best indication of global forcing. The instantaneous and adjusted radiative forcings and efficiencies were first calculated in the RFM for each month between -90° and 90° at a 9° resolution. This resolution is shown to be accurate to within 1% of a grid with 1.5° spacing in Section 4.3.2.1. From these results averaging three latitudes (representing the tropics and the mid and high latitudes) for each month yields a forcing value within 1 – 2 % of that obtained from the grid. When comparing this method to using a global annual mean profile Freckleton *et al.* (67) demonstrated this method to be more accurate by 5 – 10% than using the global annual mean profile. Explanations for this difference in accuracy will be discussed later in this chapter. The profiles representing the three latitudes for each month were used to calculate radiative forcings and efficiencies in libRadtran. This yielded an average agreement of approximately 97% for IRFs calculated using the RFM and libRadtran.

**4.3.1.2 Impact of Cloud**

Because clouds absorb across the same spectral region as PFCs, their presence will cause a reduction in radiative forcing. Consideration of cloud coverage is therefore

crucial to forcing calculations. The treatment of clouds involves determination of cloud band transmittance from user specified liquid water path, effective radius and cloud fraction at each altitude level. Up to three cloud layers were included with data obtained as monthly means from the International Satellite Cloud Climatology Project (ISCCP) D2 dataset averaged from between 1983 and 2008. This data was averaged to obtain the zonal mean coverage for a given latitudinal band. Results were calculated from different, weighted combinations of clear sky plus various configurations of cloud coverage using the independent pixel approximation (IPA) in libRadtran.

### 4.3.2  Analysis

Full results and final values for IRFs, RFs and their corresponding radiative efficiencies are presented in Chapter 5.  In the following section the impact of tropopause height and grid resolution is explored.

#### 4.3.2.1 Tropopause

The definition of radiative forcing incorporating the tropopause suggests a relationship between tropopause height and radiative forcing.  The tropopause is known as the boundary between the troposphere and the stratosphere but there are several ways we can determine where this is located. The most commonly used definitions are:

- The thermal tropopause, defined by WMO (68) as the lowest level at which the temperature lapse rate between this and all higher levels within 2 km falls below 2 K km$^{-1}$.
- The temperature minimum, the base of the stratospheric temperature inversion. However this definition is problematic as the temperature inversion can be caused through the efficacy with which ozone absorbs UV radiation.

- A proxy for the top of the convective level defined by Forster *et al*. (69) as the altitude at which a significant change in stability is observed below the thermal tropopause.

Forster *et al*. (69) identified the latter as the most appropriate for radiative forcing calculations at high horizontal resolution. However, the thermal tropopause (ThT) used in this study was found to be accurate to within 0.5% (67). At higher horizontal resolution this uncertainty is greater.

Temperature profile and thus tropopause height vary significantly spatially and are affected by profile averaging. This adds additional inaccuracies when using a global annual mean profile which does not account for variation in tropopause height. This effect was explored with respect to the instantaneous radiative forcing of $NF_3$. Figure 4.15 shows the latitudinal variation in tropopause when using the ThT, temperature minimum (TMT) and globally averaged tropopauses.

The globally averaged thermal tropopause was found to be 12.8 km. When this spatially varying thermal tropopause was applied to the forcing calculations it yielded an average instantaneous radiative forcing 10 % lower than that employing the ThT. The globally averaged TMT was found to be 14.9 km. When this was applied it resulted in an average instantaneous radiative forcing 5 % higher than the ThT.  where the spatially averaged TMT was used, forcings were found to be 3 % higher on average.
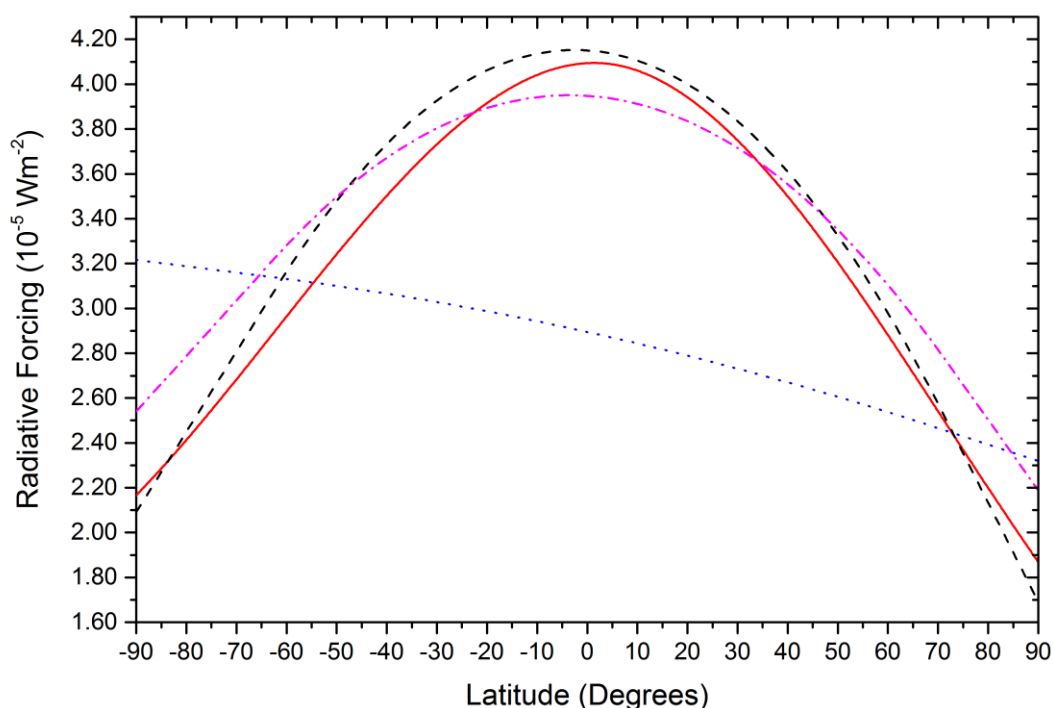
**Figure 4.15.** Variation of instantaneous radiative forcing for NF$_3$ (Wm$^{-2}$) with tropopause height for four profiles: thermal tropopause (red solid line), average thermal tropopause (black dashed line), temperature minimum tropopause (dash dot magenta line) and average temperature minimum tropopause (blue dotted line).

The global mean TMT gives a significant overestimation of radiative forcing from a high, non-representative tropopause of 14.9 km caused by temperature variations being smoothed out through averaging. Additionally, the averaging procedure affects the parameters such as water vapour and ozone profiles meaning that averaging monthly profiles over latitudes representing the topics and mid-latitudes (rather than globally) gives a better representation of these variables. Because both NF$_3$ and CFC-115 are well mixed in the stratosphere they are potentially less affected by tropopause height than species which decay strongly in the lower stratosphere (70). Consequently, the spatially averaged ThT was selected for subsequent calculations.

### 4.3.2.2 Seasonal – Latitudinal Variation

Figure 4.16 shows the difference in seasonal-latitudinal variation for the instantaneous clear sky radiative forcing for $SF_6$ on two different resolution grids. Panel a) shows this high resolution, 1.5° spaced grid and panel b) the lower, 9° resolution. Averaging radiative forcings over the lower resolution grid gives an average forcing within 1% of the higher resolution grid.

Many forcing calculations calculate their findings using a single global mean atmospheric profile for variables including cloud cover, ozone or water vapour concentration and temperature. Since atmospheric transmittance is strongly affected by the spatial variation of these factors, differences in global mean radiative forcing and radiative forcings calculated using a global mean profile may be significant. Similarly, our calculations are based on monthly averaged profiles, whereas other methods may use an annually averaged profile. When comparing this method to using a global annual mean profile, Freckleton *et al.* (67) demonstrated this method to be more accurate by 5 – 10 %. For $SF_6$, we compared instantaneous radiative forcing values determined using the lower resolution grid described above against a global- annually averaged profile and obtained a result 10 % lower than that of the average profile from Figure 4.16 a), in line with the finding of Freckleton *et al*. (67).
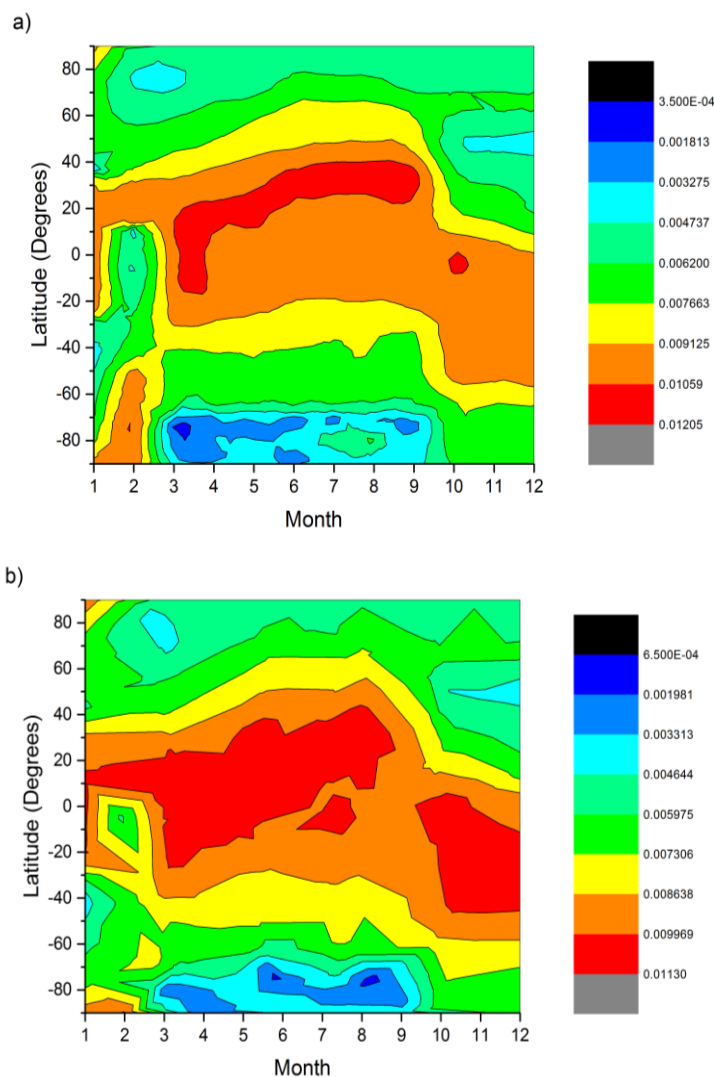
**Figure 4.16.** Contour plots for radiative forcing (Wm$^{-2}$) by latitude and month for a) high resolution (1.5°spacing) instantaneous radiative forcing of SF$_6$, b) low resolution (9° spacing) instantaneous radiative forcing of SF$_6$.

Figure  4.17 shows the large seasonal-latitudinal impact on variation in the instantaneous and adjusted radiative forcing of NF$_3$ and CFC-115 in clear skies. Variation in latitudinal forcings for a single month can be as large as a factor of 8; variation in monthly forcing for a single latitude is much smaller, approximately a factor of 2 on average. The lack of uniformity across this grid demonstrates the requirement for higher resolution calculations.
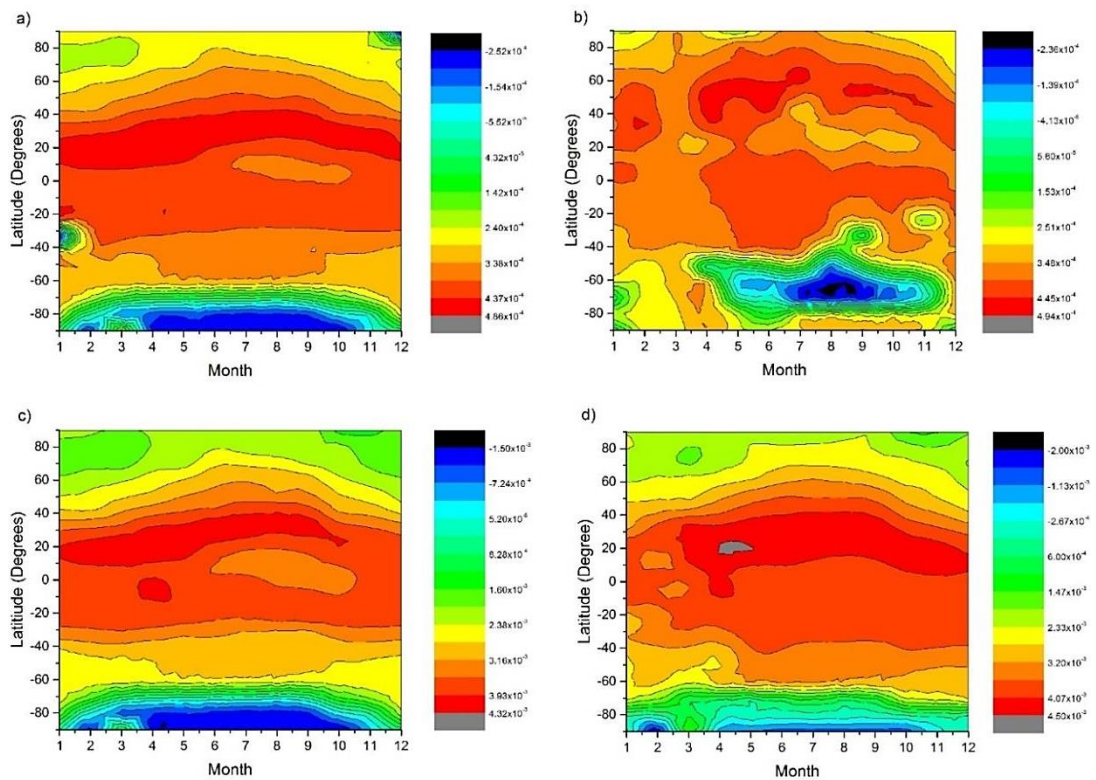
**Figure 4.17.** Contour plots for clear sky radiative forcing (Wm$^{-2}$) by latitude and month for a) instantaneous radiative forcing of NF$_3$, b) stratospheric adjusted radiative forcing of NF$_3$ c) instantaneous radiative forcing of CFC-115 and d) stratospheric adjusted radiative forcing of CFC-115.

The variation of radiative forcing and efficiency as a function of latitude is primarily due to local changes in the Planck function. This is the variation in the Earth's surface temperature with latitude and consequently, it's radiative heat loss. Equatorial latitudes receiving higher solar will radiate more terrestrial infrared radiation. A perturbation of any greenhouse gas in this region will subsequently have a higher probability of absorbing and re-emitting, an infrared photon, causing warming and resulting in a larger radiative forcing value.

Latitudinal variations in cloudiness and water density levels also contribute to variation in radiative forcings with further variation in the PFC VMRs and local temperatures and pressures also playing a role. Results averaged from across the

southern hemisphere were approximately 25 % lower than those averaged across the northern hemisphere where the majority of emissions occur (71).

The lowest radiative forcings for each month are observed at the South Pole with negative forcings occurring at the winter Antarctic polar vortex. The Antarctic polar vortex is a dynamical structure in which stratospheric air develops a cyclonic circulation around the pole. They typically form in the winter when warmer air cools and descends against the westerly wind circulation. The temperature within the vortex is so cold that it allows polar stratospheric clouds to form. These clouds contain ozone depleting substances and as a result, cause ozone depletion over the pole. A PFC molecule in the Antarctic polar vortex may therefore be more likely to absorb a shortwave photon, resulting in negative forcing.

## 4.4    Global Warming Potentials

The purpose of this work is to determine new, accurate values of global warming potentials (GWPs) for $SF_6$, $NF_3$ and CFC-115 based on their cloudy sky adjusted radiative efficiencies. GWP is defined by the expression:

$$\text{GWP} = \frac{\int_0^{TH} a_\chi[\chi(t)]dt}{\int_0^{TH} a_r[r(t)]dt} \qquad (E4.12)$$

where TH is the time horizon; $a_\chi$ is radiative forcing due to a unit increase in atmospheric abundance of the PFC ($Wm^{-2} ppbv^{-1}$); and $[\chi(t)]$ is its time-dependent decay in concentration following its instantaneous release at time t=0. The denominator contains the corresponding quantities for $CO_2$ as a reference gas (72). GWP is the most common metric used by the WMO and IPCC to compare the potency of a greenhouse gas relative to an equivalent emission of $CO_2$ over a set time period. GWP takes into account the species' lifetime. This means a species with a very high radiative forcing may still have a low GWP if it also possesses a short lifetime.

Note that GWP is only one of a range of possible metrics and is not necessarily representative of temperature changes or other climate impacts (62), and does not

account for factors such as changes in emission or the introduction of replacement species. Criticisms are discussed in greater detail by Myhre *et al.* (62).

GWP is not a measure of absolute global warming impact as it does not account for current or future emissions. All GWPs presented are calculated from direct forcings however, in order to account for indirect effects it would be necessary to include (potentially very long lived) atmospheric degradation products in this study. The concept is further flawed in that by definition, two sets of emissions that are equal in terms of their total GWP-weighted emissions will not be equivalent in terms of the temporal evolution of climate response (73). GWP can therefore only produce identical changes in terms of integrated temperature change following emissions impulses under a rigid set of assumptions. In order to address some of these issues, the Global Temperature Potential (GTP) was proposed as an alternative to GWP by comparing the global mean temperature change at the end of a given time horizon. The GTP gives equivalent climate response at a chosen time, while putting less emphasis on near-term climate fluctuations caused by emissions of short-lived species. However, with the lack of a defined, widely accepted time horizon for evaluating anthropogenic interference in the climate system, the GWP concept is still valid.

# List of References

1.      Ravishankara, A.R., S. Solomon, A.A. Turnipseed and R.F. Warren. Atmospheric Lifetimes of Long-Lived Halogenated Species. *Science*, 1993, **259**, pp.194 - 199.

2.      Reddmann, T., R. Ruhnke and W. Kouker. Three-dimensional Model Simulations of $SF_6$ with Mesospheric Chemistry. *J. Geophys. Res.*, 2001, **106**(D13), pp.14525-14537.

3.      Baasandorj, M., E.L. Fleming, C.H. Jackman and J.B. Burkholder. $O(^1D)$ Kinetic Study of Key Ozone Depleting Substances and Greenhouse Gases. *J. Chem. Phys. A.*, 2013, **117**, pp.2434-2445.

4.      Wayne, R.P. *Chemistry of Atmospheres* Third ed. Oxford: University Press, 2006.

5.      Pradayrol, C., A.M. Casanovas, I. Deharo, J.P. Guelfucci and J. Casanovas. Absorption Coeffcients of $SF_6$, $SF_4$, $SOF_2$, and $SO_2F_2$ in the Vacuum Ultraviolet. *J. de Phys. III*, 1996, **6**(5), pp.603 - 612.

6.      Zetzsch, C. *UV Absorption Cross Sections of Sulfur Hexafluoride and Acetonitrile.* Ozone in the Atmosphere. Hampton: DEEPAK Publishing, 1989.

7.      Bastien, F., P.A. Chatterton, E. Marode and J.L. Moruzzi. Photoabsorption Measurements in $SF_6$, $SF_6$ Mixtures and Some Fluorocarbon Gases. *J. Phys. D.*, 1985, **18**, pp.1327 - 1337.

8. Chipperfield., M.P. New Version of the TOMCAT/SLIMCAT Off-Line Chemical Transport Model: Intercomparison of Stratospheric Tracer Experiments. *Quart. J. Roy. Meteor. Soc.*, 2006, **132**, pp.1179-1203.

9. Feng, W., M.P. Chipperfield, S. Davies, B. Sen, G. Toon, J.F. Blavier, C.R. Webster, C.M. Volk, A. Ulanovsky, F. Ravegnani, P.v.d. Gathen, H. Jost, E.C. Richard and H. Claude. Three-dimensional Model Study of the Arctic Ozone Loss in 2002/2003 and Comparison with 1999/2000 and 2003/2004. *Atmos. Chem. Phys.*, 2005, **5**, pp.139-152.

10. Lary, D.J. and J.A. Pyle. Diffuse-radiation, Twilight, and Photochemistry .1. *J. Atmos. Chem.*, 1991, **13**(4), pp.373-392.

11. Paglia, S.R.L. and A.B.F. Duncan. Vacuum Ultraviolet Absorption Spectrum and Dipole Moment of Nitrogen Trifluoride. *J. Chem. Phys.*, 1961, **34**(3), pp.1003-1007.

12. Papadimitriou, V.C., M.R. McGillen, E.L. Fleming, C.H. Jackman and J.B. Burkholder. $NF_3$: UV Absorption Spectrum Temperature Dependence and the Atmospheric and Climate Forcing Implications. *Geophys. Res. Lett.*, 2013, **40**, pp.440 - 445.

13. Doucet, J., P. Sauvegeau and C. Sandorfy. Photoelectron and Far - Ultraviolet Absorption Spectra of Chlorofluoro Derivatives of Ethane. *J. Chem. Phys.*, 1975, **62**, pp.335 - 359.

14. Sander, S.P., J. Abbatt, J.R. Barker, J.B. Burkholder, R.R. Friedl, D.M. Golden, R.E. Huie, C.E. Kolb, M.J. Kurylo, G.K. Moortgat, V.L. Orkin and P.H. Wine. *Chemical Kinetics and Photochemical Data for Use in Atmospheric Studies;*

*Evaluation No. 17, JPL Publication 10 - 6.* Pasadena, CA: Jet Propulsion

Laboratory, 2011.

15.     Brasseur, G.P. and S. Solomon. *Aeronomy of the Middle Atmosphere.*

Atmospheric and Oceanographic Sciences Library.  Springer, 2005.

16.     Huey, L.G., D.R. Hanson and C.J. Howard. Reactions of $SF_6^-$ and $I^-$ with

Atmospheric Trace Gases. *J. Phys. Chem.*, 1995, **99**(14), pp.5001-5008.

17.     Troe, J., T.M. Miller and A.A. Viggiano. Low-energy Electron Attachment to

$SF_6$. I. Kinetic Modeling of Non - Dissociative Attachment. *J. Chem. Phys.*,

2007, **127**, p.244303.

18.     Gueymard, C.A. The Sun's Total and Spectral Irradiance for Solar Energy

Applications and Solar Radiation Models. *Sol. Energy*, 2004, **76**(4), pp.423-

453.

19.     Eisfeld, W. Highly Accurate Determination of the Electron Affinity of $SF_6$ and

Analysis of Structure and Photodetachment Spectrum of $SF_6$. *J. Chem. Phys.*,

2011, **134**, p.054303.

20.     Bopp, J.C., J.R. Roscioli, J. M. A, T.M. Miller, A.A. Viggiano, S.M. Villano, S.W.

Wren and W.C. Lineberger. Spectroscopic Characterization of the Isolated

$SF_6^-$ and $C_4F_8^-$ Anions: Observation of Very Long Harmonic Progressions in

Symmetric Deformation Modes upon Photodetachment. *J. Phys. Chem.*,

2007, **111**, pp.1214-1221.

21.     Christophorou, L.G. and J.K. Olthoff. Electron Interactions with $SF_6$. *J. Phys.*

*Chem. Ref. Data*, 2000, **29**, pp.267-330.

22.   Datskos, P.G., J.G. Carter and L.G. Christophorou. Photodetachment of $SF_6^-$. *Chem. Phys. Lett.*, 1995, **239**, pp.38-43.

23.   Fehsenfeld, F.C. Electron Attachment to $SF_6$. *J. Chem. Phys.*, 1970, **53**, p.2000.

24.   Miller, T.M., A.E.S. Miller, J.F. Paulson and X. Liu. Thermal Electron Attachment to $SF_4$ and $SF_6$. *J. Chem. Phys.*, 1994, **100**, p.8841.

25.   Troe, J., T.M. Miller and A.A. Viggiano. Low-energy Electron Attachment to $SF_6$. II. Temperature and Pressure Dependences of Dissociative Attachment. *J. Chem. Phys.*, 2007, **127**, p.244304.

26.   Foster, M.S. and J. Beauchamp. Electron Attachment to Sulphur Hexafluoride: Formation of Stable $SF_6$ at Low Pressure. *Chem. Phys. Lett.*, 1975, **31**, pp.482–485.

27.   Plane, J.M.C. *Pers. Comm.*, 28/05/2014. 2014.

28.   Marsh, D.R., D. Janches, W. Feng and J.M.C. Plane. A Global Model of Meteoric Sodium. *J. Geophys. Res.*, 2013, **118**(19), pp.11,442-11,452.

29.   Lide, D.R. *Handbook of Physics and Chemistry.* Boca Raton, FL: CRC Press, 2006.

30.   Sorokin, V.I., N.P. Gritsan and A.I. Chichinin. Collisions of $O(^1D)$ with HF, $F_2$, $XeF_2$, $NF_3$, and $CF_4$: Deactivation and Reaction. *J. Chem. Phys.*, 1998, **108**(21), pp.8995-9003.

31.   Zhao, Z., P.L. Laine, J.M. Nicovich and P.H. Wine. Reactive and Nonreactive Quenching of $O(^1D)$ by $SO^2F_2$, $NF_3$, and $SF_5CF_3$. *Proc. Nat. Acad. Sci.*, 2010.

32. Dillon, T.J., A. Horowitz and J.N. Crowley. Cross-Sections and Quantum Yields for the Atmospheric Photolysis of the Potent Greenhouse Gas Nitrogen Trifluoride. *Atmos. Environ.*, 2010, **44**, pp.1186 - 1191.

33. Eska, V., U.v. Zahn and J.M.C. Plane. The Terrestrial Potassium Layer (75-110 km) Between 71° S and 54° N: Observations and Modeling. *J. Geophys. Res.*, 1999, **104**(A8), pp.17173-17186.

34. Talcott, C.L., J.W. Ager and C.J. Howard. Gas Phase Studies of Na Diffusion in He and Ar and Kinetics of Na + Cl$_2$ and Na + SF$_6$. *J. Chem. Phys.*, 1986, **84** (11), pp.6161-6169.

35. Husain, D. and Y.H. Lee. Measurement of Absolute Rate Data for the Reaction of Atomic Potassium, K($4^2S_{1/2}$), with CF$_3$Cl, CF$_2$Cl$_2$, CFCl$_3$, CF$_3$Br and SF$_6$ as a Function of Temperature by Time-Resolved Atomic Resonance Absorption Spectroscopy at [$\lambda$]= 404 nm [K($5^2P_J$) - K($4^2S_{1/2}$)]. *J. Chem. Soc. Faraday Trans. 2*, 1987, **83**(12), pp.2325-2337.

36. Husain, D. and P. Marshall. Determination of Absolute Rate Data for the Reaction of Atomic Sodium. *J. Chem. Soc., Faraday Trans.*, 1985, **81**(2), pp.613 - 624.

37. Plane, J.M.C. Atmospheric Chemistry of Meteoric Metals. *Chem. Rev.*, 2003, **103**, pp.4963 - 4984.

38. Montgomery, J.A., M.J. Frisch, J.W. Ochterski and G.A. Petersson. A Complete Basis Set Model Chemistry. VI. Use of Density Functional Geometries and Frequencies. *J. Chem. Phys.*, 1999, **110**, pp.2822-2827.

39.    Garcia, R.R., D.R. Marsh, D.E. Kinnison, B.A. Boville and F. Sassi. Simulation

of Secular Trends in the Middle Atmosphere, 1950-2003. *J. Geophys. Res.*,

2007, **112**.

40.    Pinnock, S., M.D. Hurley, K.P. Shine, T.J. Wallington and T.J. Smyth.

Radiative Forcing of Climate by Hydrochlorofluorocarbons and

Hydrofluorocarbons. *J. Geophys. Res. - Atmos.*, 1995, **100**(D11), pp.23227-

23238.

41.    Varanasi, P. and M.D. Hurley. *SF6 Infrared Absorption Cross-Sections*.

[Accessed 03/03/2015]. Available from:

http://ether.ipsl.jussieu.fr/ether/pubipsl/GEISA/geisa_crossIR_frame_2011

_uk.jsp. 2011.

42.    Rothman, L.S., I.E. Gordon, Y. Babikov, A. Barbe, D.C. Benner, P.F. Bernath,

M. Birk, L. Bizzocchi, V. Boudon, L.R. Brown, A. Campargue, K. Chance, E.A.

Cohen, L.H. Coudert, V.M. Devi, B.J. Drouin, A. Faytl, J.M. Flaud, R.R.

Gamache, J.J. Harrison, J.M. Hartmann, C. Hill, J.T. Hodges, D. Jacquemart,

A. Jolly, J. Lamouroux, R.J.L. Roy, G. Li, D.A. Long, O.M. Lyulin, C.J. Mackie,

S.T. Massie, S. Mikhailenko, H.S.P. Müller, O.V. Naumenko, A.V. Nikitin, J.

Orphal, V. Perevalov, A. Perrin, E.R. Polovtseva, C. Richard, M.A.H. Smith, E.

Starikova, K. Sung, S. Tashkun, J. Tennyson, G.C. Toon, W.G. Tyuterev and G.

Wagner. The HITRAN 2012 Molecular Spectroscopic Database. *J. Quant.

Spectrosc. Radiat. Transfer*, 2012, (30), pp.4 - 50.

43.     Robson, J.L., L.K. Gohar, M.D. Hurley, K.P. Shine and T.J. Wallington. Revised IR Spectrum, Radiative Efficiency and Global Warming Potential of Nitrogen Trifluoride. *Geophys. Res. Lett.*, 2006, **33**(10), p.L10817.

44.     Molina, L.T., P.J. Wooldridge and M.J. Molina. Atmospheric Reactions and Ultraviolet and Infrared Absorptivities of Nitrogen Trifluoride. *Geophys. Res. Lett.*, 1995, **22**(14), pp.1873 - 1876.

45.     McDaniel, A.H., C.A. Cantrell, J.A. Davidson, R.E. Shetter and J.G. Calvert. The Temperature Dependent, Infrared Absorption Cross Sections for the Chlorofluorocarbons: CFC-11, CFC-12, CFC-13, CFC-14, CFC-22, CFC-113, CFC-114, and CFC-115. *J. Atmos. Chem.*, 1991, **12**(3), pp.211-227.

46.     Frisch, M.J., G.W. Trucks, H.B. Schlegel, G.E. Scuseria, M.A. Robb, J.R. Cheeseman, G. Scalmani, V. Barone, B. Mennucci, G.A. Petersson, H. Nakatsuji, M. Caricato, X. Li, H.P. Hratchian, A.F. Izmaylov, J. Bloino, G. Zheng, J.L. Sonnenberg, M. Hada, M. Ehara, K. Toyota, R. Fukuda, J. Hasegawa, M. Ishida, T. Nakajima, Y. Honda, O. Kitao, H. Nakai, T. Vreven, J. J. A. Montgomery, J.E. Peralta, F. Ogliaro, M. Bearpark, J.J. Heyd, E. Brothers, K.N. Kudin, V.N. Staroverov, R. Kobayashi, J. Normand, K. Raghavachari, A. Rendell, J.C. Burant, S.S. Iyengar, J. Tomasi, M. Cossi, N. Rega, J.M. Millam, M. Klene, J.E. Knox, J.B. Cross, V. Bakken, C. Adamo, J. Jaramillo, R. Gomperts, R.E. Stratmann, O. Yazyev, A.J. Austin, R. Cammi, C. Pomelli, J.W. Ochterski, R.L. Martin, K. Morokuma, V.G. Zakrzewski, G.A. Voth, P. Salvador, J.J. Dannenberg, S. Dapprich, A.D. Daniels, O. Farkas, J.B.

Foresman, J.V. Ortiz, J. Cioslowski and D.J. Fox. *Gaussian 09, Revision A.1.* Wallingford CT: Gaussian, Inc., 2009.

47.    Papasavva, S., S. Tai, K.H. Illinger and J.E. Kenny. Infrared Radiative Forcing of CFC Substitutes and their Atmospheric Reaction Products. *J. Geophys. Res.*, 1997, **102**(D12), pp.13643-13650.

48.    Bravo, I., A. Aranda, M.D. Hurley, G. Marston, D.R. Nutt, K.P. Shine, K. Smith and T.J. Wallington. Infrared Absorption Spectra, Radiative Efficiencies, and Global Warming Potentials of Perfluorocarbons: Comparison Between Experiment and Theory. *J. Geophys. Res.*, 2010, **115**(D24), pp.n/a-n/a.

49.    Bera, P.P., J.S. Francisco and T.J. Lee. Design Strategies to Minimize the Radiative Efficiency of Global Warming Molecules. *PNAS*, 2010, **107**(20), pp.9049-9054.

50.    Martin, J.C.G., M.A. Blitz and J.M.C. Plane. Kinetic Studies of Atmopsherically Relevant Silicon Chemistry Part I: Silicon Atom Reactions. *Phys. chem. chem. phys.*, 2008, **11**, pp.671 - 678.

51.    Papasavva, S., S. Tai, A. Esslinger, K.H. Illinger and J.E. Kenny. Ab Initio Calculations of Vibrational Frequencies and Infrared Intensities for Global Warming Potential of CFC Substitutes: $CF_3CH_2F$ (HFC-134a). *J. Phys. Chem.*, 1995, **99**(11), pp.3438-3443.

52.    Halls, M.D. and H.B. Schlegel. Comparison of the Performance of Local, Gradient-corrected, and Hybrid Density Functional Models in Predicting Infrared Intensities. *J. chem. phys*, 1998, **109**(24), pp.10587-10593.

53.   NIST. *Computational Chemistry Comparison and Benchmark DataBase*. Available from: http://webbook.nist.gov/chemistry/. 2012.

54.   Foresman, J.B. and A. Frisch. *Exploring Chemistry with Electronic Structure Methods.* 2 ed. Pittsburgh: Gaussian, 1996.

55.   Wilson, M.K. and S.R. Polo. The Infrared Spectra of $NF_3$ and $PF_3$. *J. Chem. Phys.*, 1952, **20**(11), pp.1716-1719.

56.   Irikura, K.K., R.D.J. III and R.N. Kacker. Uncertainties in Scaling Factors for ab Initio Vibrational Frequencies. *J. Phys. Chem.*, 2005, **109**(37 ), pp.8430-8437.

57.   GEISA. *GEISA : Spectroscopic Database*. [Accessed 10/2014]. Available from: http://www.pole-ether.fr/ether/pubipsl/GEISA/geisa_crossIR_frame_2011_uk.jsp. 2011.

58.   Hurley, M.D. *GEISA : 2011 Spectroscopic Database; $SF_6$ Infrared Absorption Cross-sections*. [Accessed 10/2014]. Available from: http://www.pole-ether.fr/ether/pubipsl/GEISA/geisa_crossIR_frame_2011_uk.jsp. 2003.

59.   Varanasi, P. *GEISA : 2011 Spectroscopic Database; $SF_6$ Infrared Absorption Cross-sections*. [Accessed 10/2014]. Available from: http://www.pole-ether.fr/ether/pubipsl/GEISA/geisa_crossIR_frame_2011_uk.jsp. 2001.

60.   Dudhia, A. *Reference Forward Model V4.30* [online]. 2013. [Accessed]. Available from: http://www.atm.ox.ac.uk/RFM/.

61.   *Library for Radiative Transfer* [CD-ROM]. 2005.

62.   Myhre, G., D. Shindell, F.-M. Bréon, W. Collins, J. Fuglestvedt, J. Huang, D. Koch, J.-F. Lamarque, D. Lee, B. Mendoza, T. Nakajima, A. Robock, G. Stephens, T. Takemura and H. Zhang. doi:10.1017/

CBO9781107415324.018. *Anthropogenic and Natural Radiative Forcing. In: Climate Change 2013: The Physical Science Basis.* Contribution of Working Group I to the Fifth Assessment Report of the Intergovernmental Panel on Climate Change, Cambridge, United Kingdom and New York, NY, USA, 2013.

63. Ramaswamy, V., M.L. Chanin, J. Angell, J. Barnett, D. Gaffen, M. Gelman, P. Keckhut, Y. Koshelkov, K. Labitzke, J.J.R. Lin, A. O'Neill, J. Nash, W. Randel, R. Rood, K. Shine, M. Shiotani and R. Swinbank. Stratospheric Temperature Trends: Observations and Model Simulations. *Rev. Geophys.*, 2001, **39**(1), pp.71-122.

64. Sherwood, S.C., S. Bony, O. Boucher, C. Bretherton, P.M. Forster, J.M. Gregory and B. Stevens. Adjustments in the Forcing-Feedback Framework for Understanding Climate Change. *Bull. Amer. Meteor. Soc.*, 2015, **96**, pp.217–228.

65. *GENLN2* [CD-ROM]. 1987.

66. *DISORT, a General-Purpose Fortran Program for Discrete-Ordinate-Method Radiative Transfer in Scattering and Emitting Layered Media: Documentation of Methodology* [CD-ROM]. 2000.

67. Freckleton, R.S., E.J. Highwood, K.P. Shine, O. Wild, K.S. Law and M.G. Sanderson. Greenhouse Gas Radiative forcing: Effects of Averaging and Inhomogeneities in Trace Gas Distribution. *Q. J. Roy. Meteor. Soc.*, 1998, **124**(550), pp.2099-2127.

68. WMO. *Scientific Assessment of Ozone Depletion: 2006, Global Ozone Research and Monitoring Project - Report No. 50*. Geneva, 2007.

69. Forster, P.M.F. and K.P. Shine. Radiative Forcing and Temperature Trends from Stratospheric Ozone Changes. *J. Geophys. Res.*, 1997, **102**(D9), pp.10841-10855.

70. Myhre, G., E.J. Highwood, K.P. Shine and F. Stordal. New Estimates of Radiative Forcing Due to Well Mixed Greenhouse Gases. *Geophys. Res. Lett.*, 1998, **25**(14), pp.2715-2718.

71. Prather, M.J. and J. Hsu. $NF_3$, the Greenhouse Gas Missing from Kyoto. *Geophys. Res. Lett.*, 2008, **35**(12).

72. Solomon, S., D. Qin, M. Manning, Z. Chen, M. Marquis, K.B. Averyt, M. Tignor and H.L. Miller. *Contribution of Working Group I to the Fourth Assessment Report of the Intergovernmental Panel on Climate Change.* Climate Change 2007: The Physical Science Basis. Cambridge: Cambridge University Press, 2007.

73. Fuglestvedt, J.S., T.K. Berntsen, O. Godal and T. Skodvin. Climate Implications of GWP-based Reductions in Greenhouse Gas Emissions. *Geophys. Res. Lett.*, 2000, **27**(3), pp.409-412.

# Chapter 5: Atmospheric Implications

The atmospheric implications of the kinetic studies described in Chapter 3 are explored in Chapter 4 and will be fully discussed in this Chapter. The ways in which these kinetics affect loss rates and consequently the atmospheric lifetimes of the species $SF_6$, $NF_3$ and CFC-115 will be also be discussed. New measurements of infrared absorption cross-section data collected in this study and their impact on radiative forcings calculations are also discussed here. These updated atmospheric lifetimes and radiative forcings are used to calculate new values for global warming potential. Both the results of this calculation and their implications are presented in the Chapter.

## 5.1    Atmospheric Lifetimes and Loss Rates

The definition of the atmospheric lifetime ($\tau$) of a greenhouse gas is discussed in detail in Chapter 1. Atmospheric lifetime refers to the approximate amount of time required for an (often anthropogenic) increment of the species to be removed from the atmosphere. This may occur either through conversion to another species or through some alternative sink. The amount of time required for removal of the species may depend on the rate at which it is injected into the atmosphere, as well as its reactivity (1). Furthermore, and particularly relevant to this study, atmospheric lifetime may also be considered in conjunction with atmospheric mixing. This is because species which are very long lived ($\tau \geq 400$ years) (2) will mix throughout the atmosphere, predominately being removed in the upper atmosphere.

The perfluorinated compounds (PFCs) explored in this study are $SF_6$, $NF_3$ and CFC-115. Each of these species has an atmospheric lifetime of more than 400 years and they are consequently mostly removed in the mesosphere. The value of $\tau$ for $SF_6$ as reported by the Intergovernmental Panel on Climate Change (IPCC) (1) and the World Meteorological Organisation (WMO) (3) is 3,200 years. This value was first

reported by Ravishankara *et al.* (4) who attributed a 0.24 fractional loss due to photolysis by Lyman-α radiation (λ = 121.6 nm) and the remainder from reaction with free electrons in the mesosphere. By using an assumed rate constant for total electron attachment of $k_{EA}=10^{-9}$ cm$^3$ s$^{-1}$ they derived a lower limit for τ of 580 years. Morris *et al.* (5) also investigated the effect of atmospheric electron attachment on the lifetime of SF$_6$. They assumed that the associative electron attachment forming the SF$_6^-$ anion would not regenerate the parent molecule and determined τ = 800 years as a lower limit.

The most recent published WMO value of τ for NF$_3$ is 569 years (3). This lifetime was derived through consideration of measured photolysis cross-sections across the UV at room temperature obtained by Molina *et al.* (6) (180 – 250 nm), Dillon *et al.* (7) (184 – 226 nm) and Papadimitriou *et al.* (8). Agreement across these spectra was within ~ 5% between the critical region (200 – 220 nm) and absorption cross-sections obtained by Papadimitriou *et al.* (8) were also measured at 212, 231, 253, 273 and 296 K allowing temperature dependence parameterisation. The reported fractional loss of NF$_3$ by photolysis is 0.70 – 0.75, with 0.29 being accounted for through reactive loss by O($^1$D) (9). The room temperature rate coefficient for O($^1$D) + NF$_3$ has been reported by Dillon *et al.* (10), Baasandorj *et al.* (11), Sorokin *et al.* (12) and Zhao *et al.* (13). Rate coefficients range between (1.20 ± 0.25) and (2.55 ± 0.38) x 10$^{-11}$ cm$^3$ molecule$^{-1}$ s$^{-1}$.

The two dominant loss processes for NF$_3$ described above are also the two dominant loss processes for CFC-115. CFC-115 has a most recent published atmospheric lifetime of 540 years (14). This was determined through consideration of new reaction rate data for CFC-115 + O($^1$D) measured by Baasandorj *et al.* (15). The fractional loss of CFC-115 through reaction with O($^1$D) is reported to be 0.63 with the remainder being accounted for by photolysis (9).

### 5.1.1  Loss Rates

The loss processes for each PFC are described in detail in Chapter 4.

In summation, apart from the reactions of $SF_6$ with K and Na, the kinetics of the other reactions of $SF_6$ as well as those of $NF_3$ and CFC-115 with metals do not appear to have been measured previously.

In Chapter 4 it is demonstrated that the Na and K reactions are not competitive in the removal of each PFC. This is true even where metal removal rates peak (~ 90 km).

For $SF_6$ where associative electron attachment occurs at a rate three orders of magnitude greater than removal by Na or K. Removal by both metals occurs at a similar rate. Electron attachment is the dominant removal process for $SF_6$ throughout the atmosphere up to 100 km; at higher altitudes, photolysis dominates.

$NF_3$ removal by $O(^1D)$ is dominant in the stratosphere but becomes less important in the mesosphere and is overtaken by removal by reaction with Na above 80 km. The Na and K reactions will be the only removal processes at high latitudes during winter when photolysis rates become very small (16). Whether this impacts on the overall atmospheric lifetime of $NF_3$ depends on the circulation of $NF_3$ from the tropical tropopause where it will enter the stratosphere, to the upper mesosphere (17).

The Lyman-α absorption cross-section of $NF_3$ was also measured, and this is revealed as the dominant removal process for the gas if it survives long enough to reach altitudes above 60 km.

Photolysis and reaction with $O(^1D)$ dominate in the removal of CFC-115. At approximately 90 km where metal atom concentrations peak, removal by Na occurs at a rate ~ 3 orders of magnitude greater than removal by K.

We do not further consider the reactions of Mg and Fe with any PFC because their rate coefficients will be very slow at a typical temperature of 180 K in the upper mesosphere.
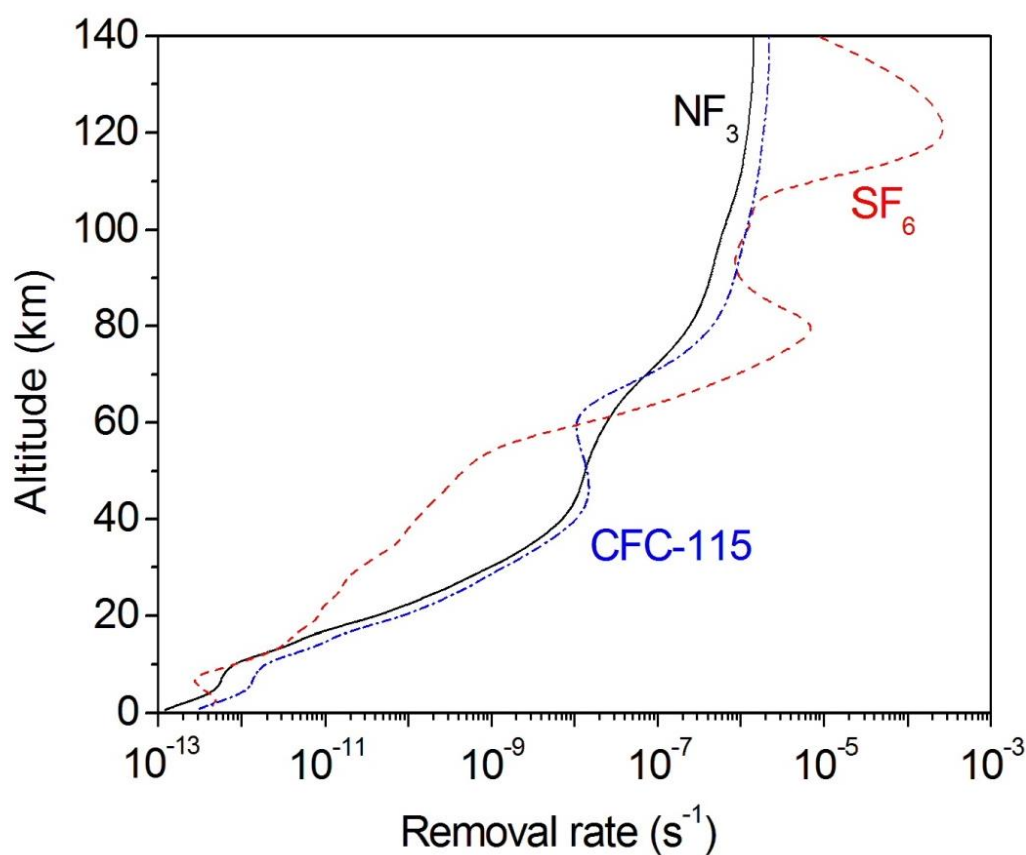
## 5.1.2 Atmospheric Lifetimes

Characterising the atmospheric lifetimes of the PFCs studied here is a crucial step in assessing their potential impact on global warming. These PFCs are potent greenhouse gases which possess large global warming potentials (GWPs) resulting from a combination of strong infrared absorptions in the atmospheric window and very long atmospheric lifetimes. A general circulation model is required to account for their transport into the upper stratosphere and mesosphere (18).

As we broadly define the atmospheric lifetime as the ratio of the total atmospheric burden to the total loss rate, the mixing ratios and the loss rates were calculated in each grid box of the model. The loss rates derived are the products of the rate constants and the reactant concentration – or in the case of photolysis, the $J$ photolysis rate.

Total loss rates were obtained from the sum of the individual loss rates due to photolysis, electron attachment, reactions with mesospheric metals and with $O(^1D)$. In the case of $SF_6$ it was determined that 95 % of its total loss rate was dominated by thermal electron attachment, with the remainder being accounted for by photolysis. In the case of $NF_3$, photolysis is the dominant removal process accounting for 60 % of loss with 40 % being removed through reaction with $O(^1D)$. Finally, in the case of CFC-115, it was determined that 67 % was removed through reaction with $O(^1D)$ and the remaining third by photolysis.

As discussed, in order to calculate the atmospheric lifetimes, the ratio of the atmospheric burden to the integrated loss rate, output was stored from the WACCM simulation. The total loss rates were obtained from the sum of the individual loss rates due to photolysis, reactions with mesospheric metals, electrons and with $O(^1D)$ (19, 20). The overall atmospheric lifetimes, and contributions from different processes, are summarised in Table 5.1. The total loss rates for each PFC in the atmosphere are plotted in Figure 5.1 which shows that in the stratosphere $NF_3$ and CFC-115 are removed by up to two orders of magnitude faster than the $SF_6$. This means that $SF_6$ is more stable in this region. However, in the mesosphere, due to destructive electron attachment, $SF_6$ is removed more

quickly than the two other components. The removal of $SF_6$ is dominated by electron attachment, while for CFC-115 and $NF_3$ removal is due to photolysis and reaction with $O(^1D)$. As discussed in Chapter 4, the electron attachment to $SF_6$ has a major role in the atmospheric removal. As a result of this both dissociative and non-dissociative attachments have been considered.



**Figure 5.1.**     Globally averaged altitude dependant atmospheric loss rates for $SF_6$, $NF_3$ and CFC-115 obtained from the 3D model simulations.

**Table 5.1.** Summary of contributions of the partial to the total atmospheric lifetimes determined in present study and previously reported in the literature (SPARC (9)) (in brackets), together with the determined net atmospheric lifetimes.

| Molecule | Contribution to Atmospheric Loss | | | | Total atmospheric lifetime / years |
| --- | --- | --- | --- | --- | --- |
| | Photolysis | Electron attachment | $O(^1D)$ | Metals | |
| SF$_6$ | 2.5 % | 97.5 % | 0 | 0 | 1221 |
| | (2.6 %) | (97.4 %) | 0 | | (2,100) |
| NF$_3$ | 59.6% | 0 | 40.4% | 0 | 594.0 |
| | (71.3%) | 0 | (28.7%) | | (569.2) |
| CFC-115 | 24.5% | 0 | 75.5% | 0 | 539.0 |
| | (37.4%) | 0 | (62.6%) | | (539.9) |

Figures 5.2 a), c) and e) present the globally averaged profiles of the different model SF$_6$, NF$_3$ and CFC-115 tracers, showing the impact of different loss processes. The largest mixing ratio profile is shown by the passive tracers as they are not subject to the removal processes. Note that the decay of the passive tracer mixing ratios above about 80 km is due to the very long timescale for the tracers to mix vertically in this region. The length of the model run (13 years) is not long enough to allow this, but it is long enough for the tracers to mix in the region where the dominant loss processes occur. This is verified by the fact that modelled lifetimes have reached a steady state by the end of year 13 (Figure 5.3).
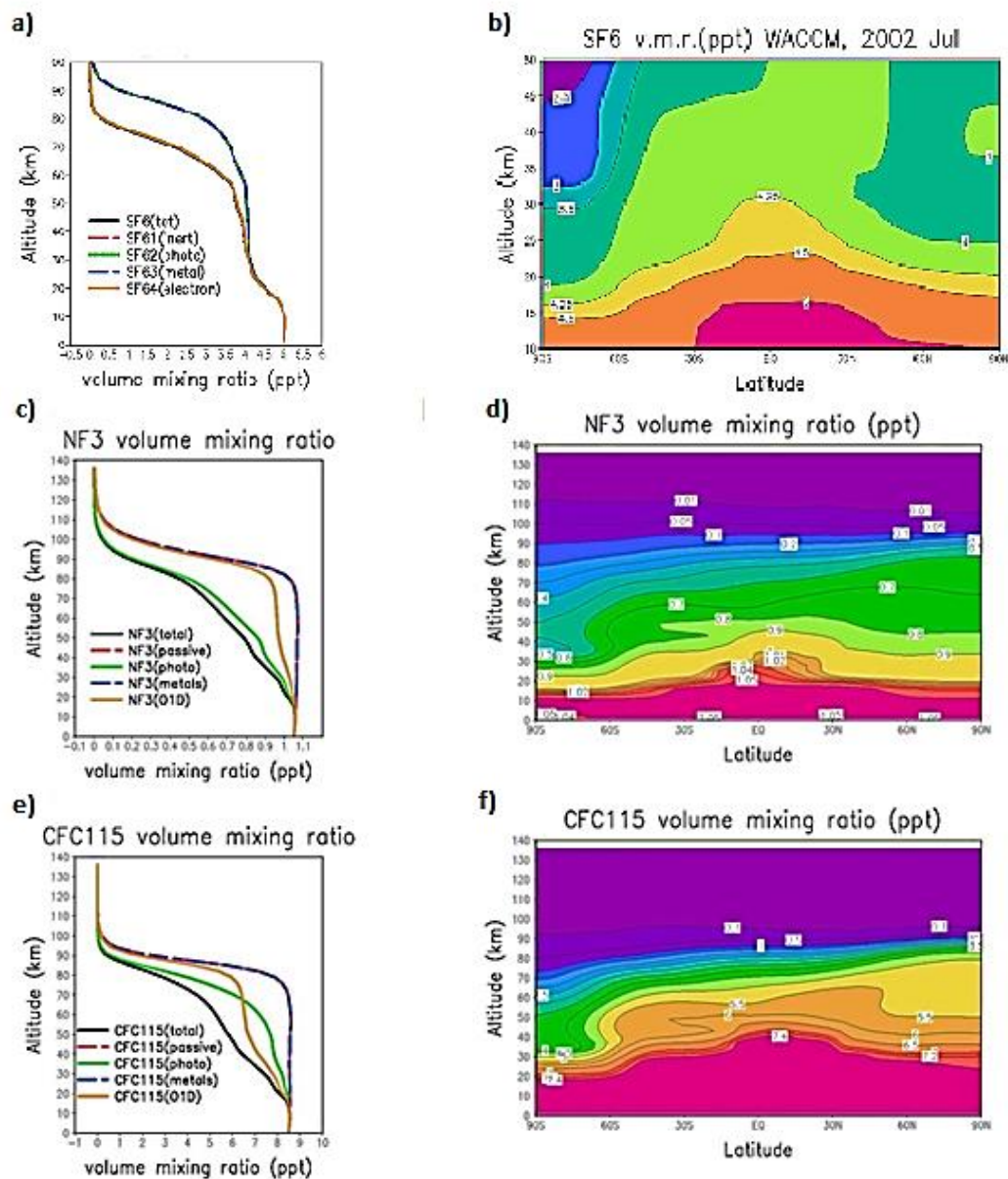
**Figure 5.2.** (a). Globally averaged SF$_6$ volume mixing ratio in January at the 13$^{th}$ year of the WACCM simulation that includes the profiles of the individual tracers (passive, photolysis, metal reaction and reaction with O($^1$D)). (d). Zonal mean NF$_3$ volume mixing ratio in January at the 13$^{th}$ year of the simulations. (c & e) As panel (c) but for NF$_3$ and CFC-115. (d & f) As panel (d) but for NF$_3$ and CFC-115.

Figure 5.2 a), c) and e) clearly show that the reactions with atmospheric metals do not contribute to the atmospheric removal of these gases (i.e. the metal loss tracers profiles are the same as the passive profiles) and hence their impact on the lifetimes is effectively zero (Table 5.1). In contrast, electron attachment (in the case

of $SF_6$) and photolysis and the reactions with atmospheric $O(^1D)$ (in the cases of $NF_3$ and CFC-115) are the dominant removal processes.

The model outputs were converted to zonal mean data and then the global atmospheric lifetimes were plotted as shown in Figure 5.3.
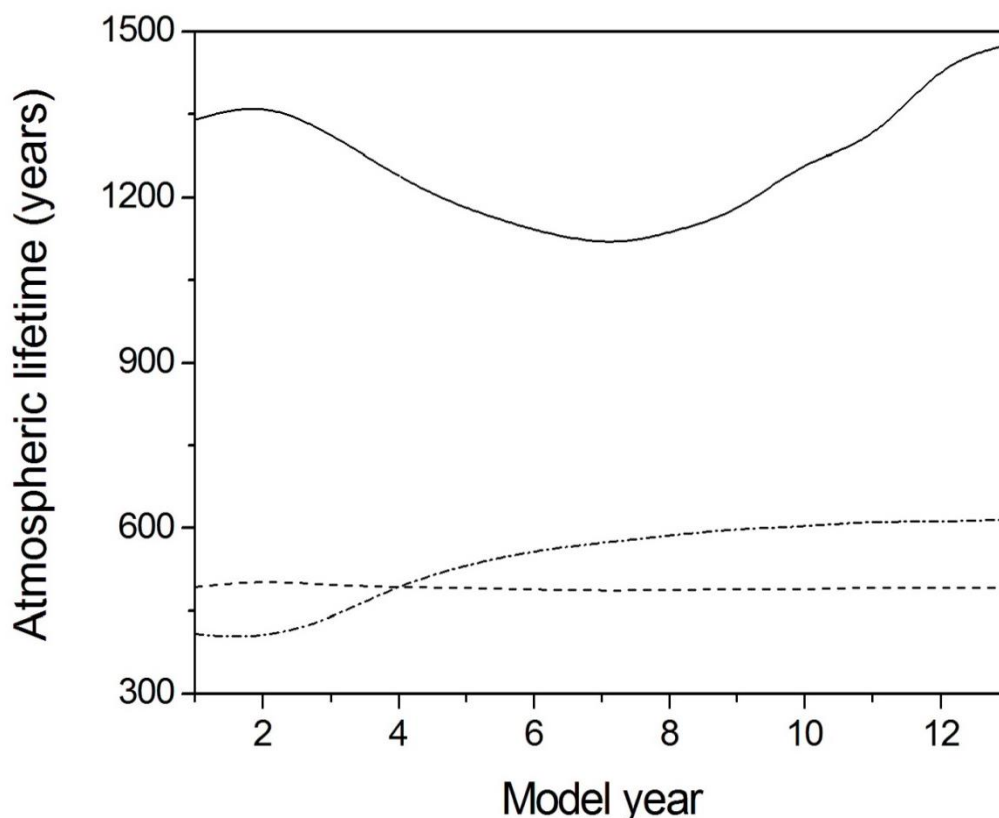


**Figure 5.3.** Annually averaged atmospheric lifetimes for $SF_6$ (solid line), $NF_3$ (dashed-dot line) and CFC-115 (dashed line) as a function of simulation time.

Estimates of the atmospheric lifetimes of each PFC have recently been reported by SPARC (2013). For $SF_6$ the reported value is 2,100 years based on 2-D model calculations, where 97.4 % removal was shown to be by electron attachment. Associative attachment leads to the regeneration of $SF_6$ and by considering this, $SF_6$ lifetime will slightly increase. The dissociative and associative electron attachment rate constants were calculated from literature data. Note that this is the first time that Troe's theory (21-23) has been applied to the MLT region. Its initial step is the

formation of $SF_6^-$ molecular anion which can either lose an electron through photodetachment or react with neutral compounds. The photodetachment rate from $SF_6^-$ ($J_{PD}$) is unknown but can be estimated from the $NO_2$ photodissociation rate as $J_{PD} = X\,J(NO_2)$, where the $X$ ratio can be determined from the wavelength dependent photodetachment $SF_6$ cross section and the WACCM value for $J(NO_2)$ at 85 km altitude ($5.3 \times 10^{-2}$ $s^{-1}$) (giving a value of 20.4). Since $NO_2$ also dissociates mainly in the near UV, this is a good approximation.

From the loss rates described, atmospheric lifetimes were determined according to the method outlined in Chapter 4. SPARC 2013 (24) provides a current lifetime for $SF_6$ of 3,200 years. However, our lifetime estimation of 1221 years is explained by the detailed treatment of associative and dissociative electron attachment. Negative ions have a significant effect on the lifetime: the value drops to 776 years when negative ions are not treated in WACCM but all electrons are free to react with $SF_6$. This lower limit is in accordance with Morris's recommendation (25) which also reports the value obtained for the highest reactivity.

Recent lifetime values of $NF_3$ and CFC-115 have been reported in SPARC 2013 (24) as 569 years and 540 years, respectively. The results from the present study are in good accord: $NF_3$: 594 years, CFC-115: 539 years. Previous JPL recommendations (26) suggested respective lifetimes of 1,588 years for $NF_3$ and 961 for CFC-115. However, that recommendation for $NF_3$ is based only on removal by $O(^1D)$. The results obtained in this study suggest that the removal by photolysis is an important loss channel meaning that its exclusion would certainly lead to an overestimation of the lifetime. For CFC-115 the recommendation assumed a smaller reaction yield for reaction with $O(^1D)$ versus quenching. Our values should also be more accurate due to our use of a 3-D model, while SPARC data is based on a 2-D model. In the present results the contributions from photolysis are lower than in the SPARC Report. 3-D atmospheric transport was studied in the model run by defining individual tracers for different loss processes, as well as the non-reactive tracer, which helped to identify the contributions of the different loss processes to the atmospheric lifetimes.

## 5.2 Radiative Forcings, Efficiencies and GWPs

The PFCs examined in this study are very potent global warming agents. This is not only because of their long lifetimes determined in the previous section, but also because they absorb infrared radiation strongly within the atmospheric window region and with the peak in the terrestrial infrared spectrum (27).

GWP is defined in the previous section as the metric used by the WMO and IPCC to compare the potency of a greenhouse gas relative to an equivalent emission of $CO_2$ over a set time period.

### 5.2.1 Results

#### 5.2.1.1 Infrared Absorption Cross-Sections

Infrared absorption cross-sections for each PFC were measured in this study and were input into radiative transfer models described in the previous chapter in order to obtain radiative forcings and efficiencies. Here, radiative efficiency refers to a perturbation of $0 - 1$ ppb. The relative positions of these spectra to the atmospheric window is shown below in Figure 5.4:
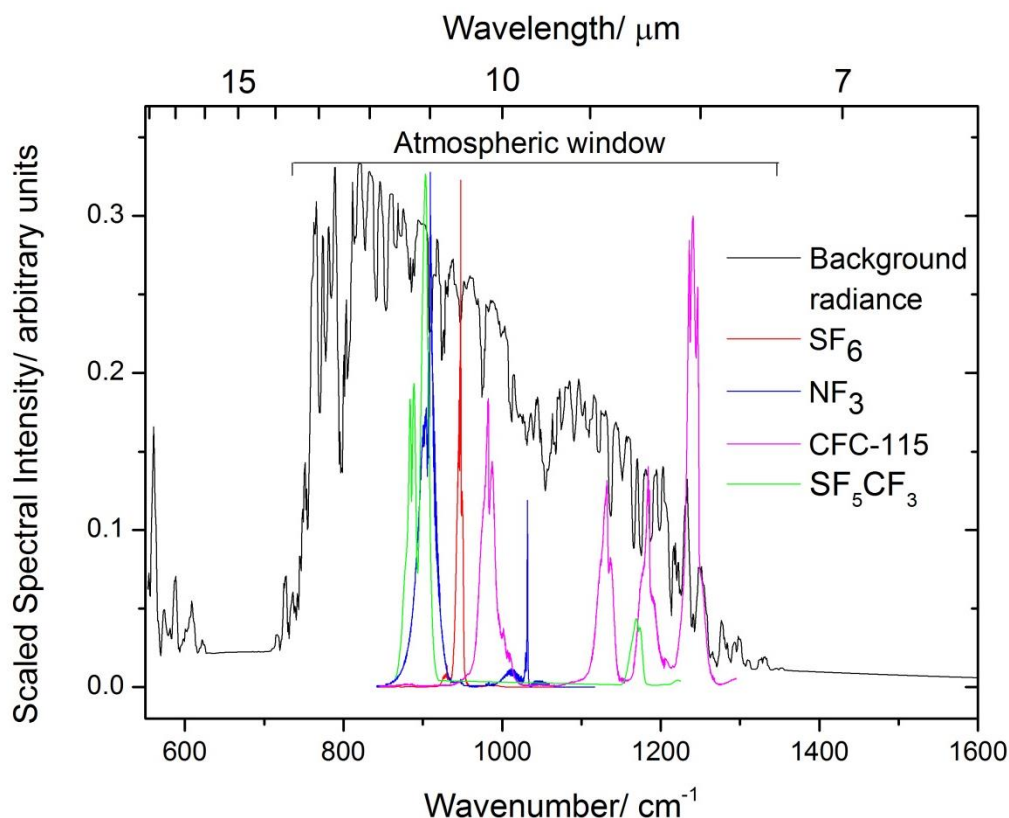
**Figure 5.4**. Infrared absorption cross-sections for $SF_6$, $NF_3$, CFC-115 and $SF_5CF_3$ obtained in this study relative to the atmospheric window.

The integrated infrared absorption cross-sections obtained in this study are described in detail in the previous chapter. They were generally found to be within the combined error of available quantitative literature studies. The intensities of the main absorptions band (925-955 cm$^{-1}$) of $SF_6$ measured in the present work are 7 % greater than those reported Hurley (28), 1 % greater than Varanasi (29) and 1 % lower than those given in HITRAN (30). Comparison against Varanasi (29) between 650 and 2000 cm$^{-1}$ gives an agreement within 9 %. The intensities of the two main absorptions bands (840-960 and 970-1085 cm$^{-1}$) of $NF_3$ measured in the present work are 3 % and 11 % greater than those reported by Robson *et al.* with an average deviation of 29 % over the minor bands and 4 % across the entire spectrum. Finally, the intensity of the main absorption band for CFC-115 (1212-1265 cm$^{-1}$) as measured in the present work is 94 % of that reported by McDaniel *et al.* Three other main bands occurring at 946-1020, 1105-1150 and 1160-1212

cm$^{-1}$ show agreement with McDaniel *et al.* of 90 %, 94 % and 95 % respectively. The small band occurring between 1326-1368 cm$^{-1}$ has an agreement of 97 %.

### 5.2.1.2 Radiative Forcings and Efficiencies

Our forcing calculations suggest that for each SF$_6$, NF$_3$ and CFC-115, the minor bands contribute < 5 % to the final value. This means that deviation between our experimentally determined spectra and those in literature may only result in a significant change to previously published radiative forcings / efficiencies where that deviation occurs over a major band.

The IRFs and RFs in clear and all sky conditions for SF$_6$, NF$_3$ and CFC-115 are given in Table 5.2 . The relative radiative efficiencies are given in Table 5.3.

**Table 5.2.** Instantaneous and stratospheric adjusted radiative forcings of SF$_6$, NF$_3$ and CFC-115 in clear and cloudy sky conditions.

| Molecule | Instantaneous | | Adjusted | |
|---|---|---|---|---|
| | Clear, $10^{-4}$ Wm$^{-2}$ | Cloudy, $10^{-4}$ Wm$^{-2}$ | Clear, $10^{-4}$ Wm$^{-2}$ | Cloudy, $10^{-4}$ Wm$^{-2}$ |
| SF$_6$ | 76.43 | 48.91 | 81.81 | 56.01 |
| NF$_3$ | 3.30 | 2.08 | 3.53 | 2.79 |
| CFC–115 | 27.70 | 18.09 | 29.77 | 19.05 |

**Table 5.3.** Instantaneous and stratospheric adjusted radiative efficiencies of $SF_6$, $NF_3$ and CFC-115 in clear and cloudy sky conditions.

| Molecule | Instantaneous | | Adjusted | |
|---|---|---|---|---|
| | Clear, $Wm^{-2} ppbv^{-1}$ | Cloudy, $Wm^{-2} ppbv^{-1}$ | Clear, $Wm^{-2} ppbv^{-1}$ | Cloudy, $Wm^{-2} ppbv^{-1}$ |
| $SF_6$ | 0.77 | 0.50 | 0.85 | 0.59 |
| $NF_3$ | 0.35 | 0.22 | 0.40 | 0.25 |
| CFC–115 | 0.32 | 0.20 | 0.35 | 0.21 |

Variation in the clear: cloudy sky radiative forcing ratios between the species can be explained by the variation in each species' VMR. For example, $SF_6$ has a longer lifetime and consequently a higher upper atmosphere concentration than CFC-115. This means that at higher altitudes less incoming solar radiation is reflected by clouds and is therefore able to be absorbed by a larger fraction of the molecule. This results in a larger fraction of the outwelling radiation is more likely to be reflected and no reabsorbed when compared to CFC-115.

For a selection of experiments carried out over a range of months and latitudes, the average contribution from the main bands of each species were compared against the calculations presented here, incorporating the full measured spectrum. In the case of $SF_6$, calculations performed over $580 - 640$ and $925 - 955$ cm$^{-1}$ were found to contribute almost 99 % to the instantaneous radiative forcing. $NF_3$ instantaneous radiative forcings calculated between $750 - 1200$ cm$^{-1}$ were found to contribute over 97 % to the total value. CFC-115 results calculated between $900 - 1400$ contributed 98 % of the final value.

Uncertainties in the modelled values of lifetimes and radiative forcings cannot be accurately determined as model uncertainties are not known and physical

measurements cannot be taken. Therefore, to get a sense of the accuracy of the values presented her, it is necessary to compare to other results.

The adjusted cloudy sky radiative efficiencies published by the Intergovernmental Panel on Climate Change and used to determine their values for GWPs are 0.52, 0.21 and 0.18 $Wm^{-2}$ $ppbv^{-1}$ for $SF_6$, $NF_3$ and CFC-115, respectively. These compare to adjusted cloudy sky radiative efficiencies of the same species as determined in this study of 0.59, 0.25 and 0.21 $Wm^{-2}$ $ppbv^{-1}$.

A review on radiative efficiencies and global warming potentials published by Hodnebrog *et al.* (31) provides a comprehensive list of all published values for these parameters for each species we investigate in this study. They establish the range of published radiative efficiencies for $SF_6$ to be 0.49 – 0.68 $Wm^{-2}$ $ppbv^{-1}$, with a mean value of 0.56 $Wm^{-2}$ $ppbv^{-1}$. This mean value for radiative efficiency is within 95 % of the value determined in this study (0.59 0.56 $Wm^{-2}$ $ppbv^{-1}$). The Hodnebrog review used the same HITRAN (30) and GEISA (28, 29) used in the previous chapter to compare infrared data (Section 4.2), and obtained radiative efficiencies in the range 0.54 – 0.59 $Wm^{-2}$ $ppbv^{-1}$. Radiative efficiencies obtained from the same data in this study range from 0.5 – 0.57 $Wm^{-2}$ $ppbv^{-1}$ when using the same conditions.

Hodnebrog *et al.* (31) quote the radiative efficiency of $NF_3$ used by the IPCC and published by Robson *et al.* (32) as the only complete value in the literature. Using their infrared cross-section data, the review found a value for radiative efficiency of 0.2 $Wm^{-2}$ $ppbv^{-1}$, within the quoted 5% uncertainty of the 0.21 $Wm^{-2}$ $ppbv^{-1}$ published by Robson *et al.* (32). This is within 85 % of the value determined in this study of 0.25 $Wm^{-2}$ $ppbv^{-1}$.

Finally, Hodnebrog *et al.* also quote the range of published radiative efficiencies for CFC-115 as 0.2 – 0.3 $Wm^{-2}$ $ppbv^{-1}$. The value of 0.18 $Wm^{-2}$ $ppbv^{-1}$ reported by the IPCC is outside this range as they quote the instantaneous radiative efficiency. The value of 0.21 $Wm^{-2}$ $ppbv^{-1}$ determined in this study however, is within the quoted range.

### 5.2.1.3 Global Warming Potentials

Table 5.4 gives the 20, 100 and 500 year GWPs based on cloudy sky adjusted radiative efficiencies of $SF_6$, $NF_3$ and CFC − 115 compared with IPCC AR5 values (33). Forcing efficiencies determined in this study are somewhat higher than in literature, leading us to expect a higher value for GWP. However, where atmospheric lifetimes are smaller than IPCC AR5 values, larger values of GWP have been determined. The radiative efficiency effect is most obvious for the case of a 20-year GWPs where, because the atmospheric lifetimes of $SF_6$, $NF_3$ and CFC-115 are 1221, 594 and 539 years respectively, the species do not have time to deplete sufficiently to impact GWP. The 500 year GWP differences are more indicative of the impact of the change in calculated lifetimes.

**Table 5.4.** Comparison of 20, 100 and 500-year global warming potentials for $SF_6$ $NF_3$ and CFC-115 from this work with IPCC values.

| | This Work | | | IPCC | | |
|---|---|---|---|---|---|---|
| Molecule | $GWP_{20}$ | $GWP_{100}$ | $GWP_{500}$ | $GWP_{20}$ | $GWP_{100}$ | $GWP_{500}$ |
| $SF_6$ | 18,900 | 22,800 | 27,400 | 16,300 [a] | 21,650 [a] | 32,600 [a] |
| $NF_3$ | 14,600 | 19,400 | 21,400 | 12,300 [b] | 17,200 [b] | 20,700 [b] |
| CFC-115 | 6,120 | 8,060 | 8,630 | 5,310 [c] | 7,370 [c] | 9,990 [c] |

[a] based on an atmospheric lifetime of 3,200 years

[b] based on an atmospheric lifetime of 740 years

[c] based on an atmospheric lifetime of 1,700 years.

The trade-off between these competing effects is demonstrated as an example for $SF_6$ in Figure 5.5 and the values presented in Table 5.4 above, where each species exhibits 20-year GWPs significantly larger than their IPCC determined values. This

difference decreases for the 100 year GWPs and more so for the 500 year GWP. In the case of CFC-115, where the atmospheric lifetime used to define the GWP is 1,700 years, over three times that of our value of 539 year, The 500 year GWP of 9,990 quoted in IPCC AR5 is actually greater than our value of 8,630. The effect is displayed in Figure 5.5 for $SF_6$ where despite the larger radiative forcing value at t=0, our considerably lower value for $\tau$ of 1221 year (versus that determined by Ravishankara *et al.* of 3,200 years) results in $d$RF over 500 years being more rapid than current values. This equates to a $GWP_{500}$ of 27,400 for experimental data, 15 % lower than the literature $GWP_{500}$ of 32,600. This is a more significant difference than the 5% determined for the $GWP_{100}$.
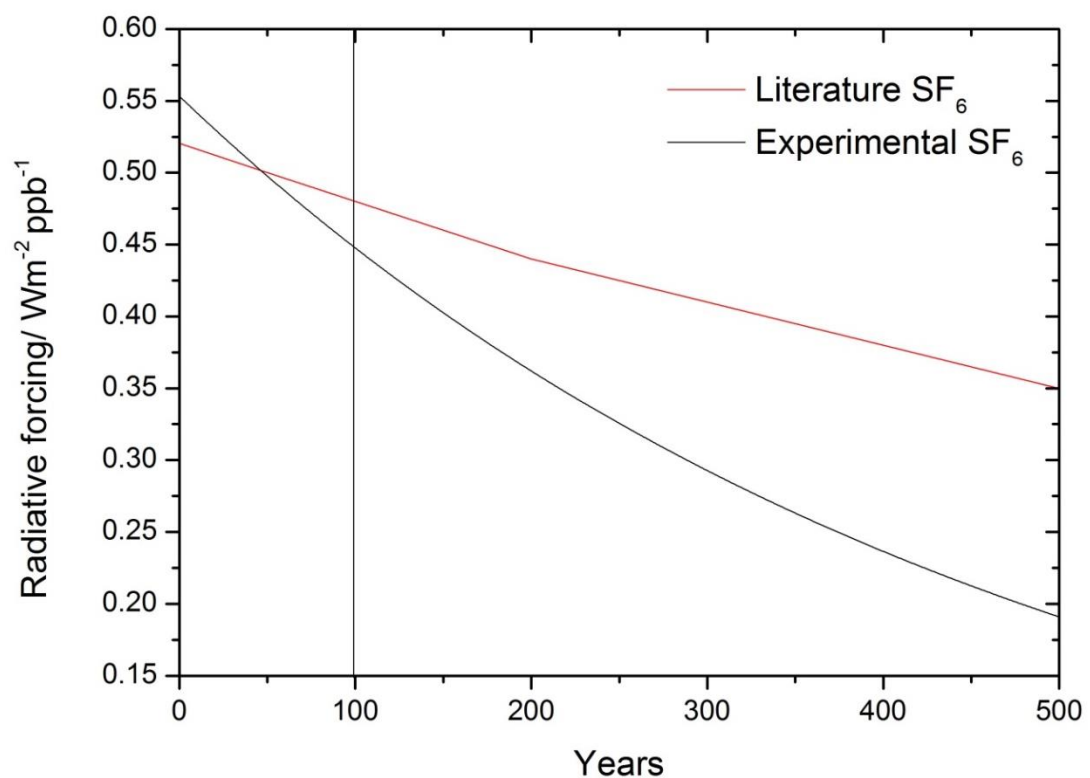


**Figure 5.5.** Simulation of change in $SF_6$ radiative forcing determined in this study over a 500 year period compared against literature radiative forcing decays using published and e-folding lifetimes.

The 100 year global warming potentials published by the Intergovernmental Panel on Climate Change (IPCC) for $SF_6$, $NF_3$ and CFC-115 are 21,650, 17200 and 7,370 respectively. The adjusted cloudy sky radiative efficiencies from which these values are derived are 0.52, 0.21 and 0.18 $Wm^{-2}$ $ppbv^{-1}$ for $SF_6$, $NF_3$ and CFC-115 respectively (1).

The cloudy sky adjusted radiative efficiency of $SF_6$ determined in this study is 0.59 $Wm^{-2}$ $ppbv^{-1}$. This value is 14 % higher than that used by the IPCC. A comparison between our experimentally determined infrared cross-sections for $SF_6$ and an identical set of experiments using infrared cross-section data from the HITRAN 2012 Molecular Spectroscopic Database (30) outlined in Chapter 4, determined an agreement in average instantaneous radiative efficiency of within 4 %. This suggests other factors play a role in determining the differences between the radiative efficiency determined in this study and that used by the IPCC. Variation between models is < 5 % and so the remaining difference arises from the vertical profiles calculated by WACCM. Similarly, our cloudy sky adjusted radiative efficiencies for $NF_3$ and CFC-115 are 0.25 and 0.21 $Wm^{-2}$ $ppbv^{-1}$; 16 and 14 % greater than their IPCC determined values respectively.

Our 20, 100 and 500 year global warming potentials for $SF_6$ are 18,900, 22,800 and 27,400. These numbers are 16 % greater, 5 % greater and 16 % smaller than their IPCC counterparts. Despite the larger radiative forcing value at t=0, our considerably lower value for τ of 1221 year (compared with that determined by Ravishankara *et al.* of 3,200 years) results in the greater rapidity of *d*RF over 500 years than indicated by current values. It also demonstrates that for these very long lived species, the 500 year GWP is a more suitable metric.

Similarly, the 20, 100 and 500 year global warming potentials for $NF_3$ are 14,600, 19,400 and 21,400. These numbers are 18 %, 13 % and 3 % greater than their IPCC counterparts, while the 20, 100 and 500 year GWPs for CFC-115 are 6,120, 8,060 and 8,630 making them 15 %, 9 % greater and 14 % smaller than the IPCC equivalents.

Our GWPs for each PFC suggest that in the case of very long lived species our revised values for radiative efficiency play a more significant role than our revised lifetimes in the global warming potential of each species over the first 100 years after their release. Our revised values of $\tau$ do not appear to play a significant role in this metric as 100 years is not a sufficient time period for significant atmospheric depletion of that species. Consequently, we determine that the 500 year GWP is a more appropriate metric for determining the long term impact of these agents. This is especially true in the case of $SF_6$ which has a revised lifetime of 1,221 years, versus $\tau$ for $NF_3$ and CFC-115 which are 594 and 539 years respectively.

# List of References

1.      Solomon, S., D. Qin, M. Manning, Z. Chen, M. Marquis, K.B. Averyt, M. Tignor and H.L. Miller. *Contribution of Working Group I to the Fourth Assessment Report of the Intergovernmental Panel on Climate Change.* Climate Change 2007: The Physical Science Basis. Cambridge: Cambridge University Press, 2007.

2.      Plane, J.M.C. The Chemistry of Meteoric Metals in the Earths Upper - Atmosphere. *Int. Rev. Phys. Chem.*, 1991, **10**(1), pp.55-106.

3.      Carpenter, L.J., S. Reimann, J.B. Burkholder, C. Clerbaux, B.D. Hall, R. Hossaini, J.C. Laube and S.A. Yvon-Lewis. *Ozone-Depleting Substances (ODSs) and Other Gases of Interest to the Montreal Protocol*. Chapter 1 in Scientific Assessment of Ozone Depletion: 2014, Global Ozone Research and Monitoring Project, Geneva, Switzerland: World Meteorological Organization, 2014.

4.      Ravishankara, A.R., S. Solomon, A.A. Turnipseed and R.F. Warren. Atmospheric Lifetimes of Long-Lived Halogenated Species. *Science*, 1993, **259**, pp.194 - 199.

5.      Morris, R.A., T.M. Miller, A.A. Viggiano, J.F. Paulson, S. Solomon and G. Reid. Effects of Electron and Ion Reactions on Atmospheric Lifetimes of Fully Fluorinated Compounds. *J. Geophys. Res.*, 1995, **100**, pp.1287-1294.

6.      Molina, L.T., P.J. Wooldridge and M.J. Molina. Atmospheric Reactions and Ultraviolet and Infrared Absorptivities of Nitrogen Trifluoride. *Geophys. Res. Lett.*, 1995, **22**(14), pp.1873 - 1876.

7. Dillon, T.J., A. Horowitz and J.N. Crowley. Cross-Sections and Quantum Yields for the Atmospheric Photolysis of the Potent Greenhouse Gas Nitrogen Trifluoride. *Atmos. Environ.*, 2010, **44**, pp.1186 - 1191.

8. Papadimitriou, V.C., M.R. McGillen, E.L. Fleming, C.H. Jackman and J.B. Burkholder. $NF_3$: UV Absorption Spectrum Temperature Dependence and the Atmospheric and Climate Forcing Implications. *Geophys. Res. Lett.*, 2013, **40**(2), pp.440-445.

9. Ko, M.K.W., P.A. Newman, S. Reimann and S.E. Strahan. WCRP-15/2013. *Lifetimes of Stratospheric Ozone-Depleting Substances, Their Replacements, and Related Species*. SPARC Report, 2013.

10. Dillon, T.J., L. Vereecken, A. Horowitz, V. Khamaganov, J.N. Crowley and J. Lelieveld. Removal of the Potent Greenhouse Gas $NF_3$ by Reactions with the Atmospheric Oxidants $O(^1D)$, OH and $O_3$. *Phys. chem. chem. phys.*, 2011, **13**, pp.18600-18608.

11. Baasandorj, M., B.D. Hall and J.B. Burkholder. Rate Coefficients for the Reaction of $O(^1D)$ with the Atmospherically Long-lived Greenhouse Gases $NF_3$, $SF_3CF_3$, $CHF_3$, $C_2F_6$, $c$-$C_3F_8$, n-C5 *Atmos. Chem. Phys.*, 2012, **12**, pp.11753-11764.

12. Sorokin, V.I., N.P. Gritsan and A.I. Chichinin. Collisions of $O(^1D)$ with HF, $F_2$, $XeF_2$, $NF_3$, and $CF_4$: Deactivation and Reaction. *J. Chem. Phys.*, 1998, **108**(21), pp.8995-9003.

13. Zhao, Z., P.L. Laine, J.M. Nicovich and P.H. Wine. Reactive and Nonreactive Quenching of $O(^1D)$, $SO^2F_2$, $NF_3$, and $SF_5CF_3$. *Proc. Nat. Acad. Sci.*, 2010.

14. WMO. *Scientific Assessment of Ozone Depletion: 2006, Global Ozone Research and Monitoring Project - Report No. 50*. Geneva, 2007.

15. Baasandorj, M., E.L. Fleming, C.H. Jackman and J.B. Burkholder. $O(^1D)$ Kinetic Study of Key Ozone Depleting Substances and Greenhouse Gases. *J. Phys. Chem.*, 2013, **117**, pp.2434-2445.

16. Marsh, D.R., D. Janches, W. Feng and J.M.C. Plane. A Global Model of Meteoric Sodium. *J. Geophys. Res.*, 2013, **118**, pp.11,442–11,452.

17. Plane, J.M.C. Atmospheric Chemistry of Meteoric Metals. *Chem. Rev.*, 2003, **103**, pp.4963 - 4984.

18. Reddmann, T., R. Ruhnke and W. Kouker. Three-dimensional Model Simulations of $SF_6$ with Mesospheric Chemistry. *J. Geophys. Res.*, 2001, **106**(D13), pp.14525-14537.

19. Totterdill, A., T. Kovacs, J.C.G. Martin, W.H. Feng and J.M.C. Plane. Mesospheric Removal of Very Long-Lived Greenhouse Gases $SF_6$ and CFC-115 by Metal Reactions, Lyman-alpha Photolysis, and Electron Attachment. *J. Phys. Chem. A*, 2015, **119**(10), pp.2016-2025.

20. Totterdill, A., J.C.G. Martín, T. Kovács, W. Feng and J.M.C. Plane. Experimental Study of the Mesospheric Removal of $NF_3$ by Neutral Meteoric Metals and Lyman-$\alpha$ Radiation. *J. Phys. Chem. A.*, 2014.

21. Troe, J., T.M. Miller and A.A. Viggiano. Low-energy Electron Attachment to $SF_6$. I. Kinetic Modeling of Non - Dissociative Attachment. *J. Chem. Phys.*, 2007, **127**, p.244303.

22. ---. Low-energy Electron Attachment to $SF_6$. II. Temperature and Pressure Dependences of Dissociative Attachment. *J. Chem. Phys.*, 2007, **127**, p.244304.

23. Viggiano, A.A., T.M. Miller, J.F. Friedman and J. Troe. Low-energy Electron Attachment to $SF_6$. III. From Thermal Detachment to the Electron Affinity of $SF_6$. *J. Chem. Phys.*, 2007, **127**, p.244305.

24. SPARC-Report. WCRP-15/2013. *Lifetimes of Stratospheric Ozone-Depleting Substances, Their Replacements, and Related Species*. SPARC Report, 2013.

25. Morris, R.A., Miller, T.M., Viggiano, A.A., Paulson, J.F., Solomon, S., Reid, G. Effects of electron and ion reactions on atmospheric lifetimes of fully fluorinated compounds. *J. Geophys. Res.*, 1995, **100**, pp.1287-1294.

26.     GREAT BRITAIN. *JPL Publication No. 10-6*. 2010.

27.     Pinnock, S., M.D. Hurley, K.P. Shine, T.J. Wallington and T.J. Smyth. Radiative Forcing of Climate by Hydrochlorofluorocarbons and Hydrofluorocarbons. *J. Geophys. Res. - Atmos.*, 1995, **100**(D11), pp.23227-23238.

28.     Hurley, M.D. *GEISA : 2011 Spectroscopic Database; SF$_6$ Infrared Absorption Cross-sections*. [Accessed 10/2014]. Available from: http://www.pole-ether.fr/ether/pubipsl/GEISA/geisa_crossIR_frame_2011_uk.jsp. 2003.

29.     Varanasi, P. *GEISA : 2011 Spectroscopic Database; SF$_6$ Infrared Absorption Cross-sections*. [Accessed 10/2014]. Available from: http://www.pole-ether.fr/ether/pubipsl/GEISA/geisa_crossIR_frame_2011_uk.jsp. 2001.

30.     Rothman, L.S., I.E. Gordon, Y. Babikov, A. Barbe, D.C. Benner, P.F. Bernath, M. Birk, L. Bizzocchi, V. Boudon, L.R. Brown, A. Campargue, K. Chance, E.A. Cohen, L.H. Coudert, V.M. Devi, B.J. Drouin, A. Faytl, J.M. Flaud, R.R. Gamache, J.J. Harrison, J.M. Hartmann, C. Hill, J.T. Hodges, D. Jacquemart, A. Jolly, J. Lamouroux, R.J.L. Roy, G. Li, D.A. Long, O.M. Lyulin, C.J. Mackie, S.T. Massie, S. Mikhailenko, H.S.P. Müller, O.V. Naumenko, A.V. Nikitin, J. Orphal, V. Perevalov, A. Perrin, E.R. Polovtseva, C. Richard, M.A.H. Smith, E. Starikova, K. Sung, S. Tashkun, J. Tennyson, G.C. Toon, W.G. Tyuterev and G. Wagner. The HITRAN 2012 Molecular Spectroscopic Database. *J. Quant. Spectrosc. Radiat. Transfer*, 2012, (30), pp.4 - 50.

31.     Hodnebrog, Ø., M. Etminan, J.S. Fuglestvedt, G. Marston, G. Myhre, C.J. Nielsen, K.P. Shine and T.J. Wallington. Global Warming Potentials and Radiative Efficiencies of Halocarbons and Related Compounds: A Comprehensive Review. *Rev. Geophys.*, 2013, **51**(2), pp.300-378.

32.     Robson, J.L., L.K. Gohar, M.D. Hurley, K.P. Shine and T.J. Wallington. Revised IR Spectrum, Radiative Efficiency and Global Warming Potential of Nitrogen Trifluoride. *Geophys. Res. Lett.*, 2006, **33**(10), p.L10817.

33.    IPCC. *Climate Change 2013: The Physical Science Basis. Contribution of Working Group I to the Fifth Assessment Report of the Intergovernmental Panel on Climate Change.* Cambridge, United Kingdom and New York, NY, USA: Cambridge University Press, 2013.

# Chapter 6: Conclusions

This study has explored the impact of a number of processes which may be responsibe for the removal of the long-lived greenhouse gases $SF_6$, $NF_3$ and CFC-115. The reactions of these PFCs with Na, K, Mg and Fe atoms, which occur in the mesosphere as a result ofmeteoric ablation, were studied over a range of temperatures. Despite the reactions of the meteoric metals with these of these PFCs being very exothermic, the reactions have substanital barriers on their respective potential energieswhich cause the reactions to be much slower than their collision frequencies (particularly the reactions of Mg and Fe). They were also found to be too slow at the temperatures of the upper mesosphere (< 230 K) to contribute significantly to the removal of the PFCs.

In the case of the $NF_3$ reactions, this appears to arise from the negative vertical electron affinity of $NF_3$. Vibrational excitation along the F2N−F coordinate leads to a positive electron affinity, which may cause the observed non-Arrhenius behavior in the Na and K reactions at higher temperatures, and is consistent with the late barriers on the potential energy surfaces.

Similarly, theoretical caluations with $SF_6$ have indicated that the Na and K reactions may be activated by vibrational excitation of the F-$SF_6$ (v3) asymmetric stretching mode. A limited set of measurements on Na + $SF_5CF_3$ have indicated that $SF_5CF_3$ behaves much like $SF_6$.

The Lyman-α absorption cross sections for each PFC were also measured and found to be in generally good agreement with the more recent previous studies. Although VUV photolysis of $SF_6$ is the major loss process above 105 km, below this height associative electron attachment dominates and so this is the process which controls the atmospheric lifetime of this PFC.

In the case of $NF_3$ photolysis turned out to be the dominant removal process for the gas if it survives long enough to reach altitudes above 60 km. In the case of CFC-115, VUV photolysis is the major loss process above 60 km, but the removal of

this species by reaction with O($^1$D) dominates in the stratosphere and hence controls its lifetime.

We have also presented updated values for the atmospheric lifetimes and infrared absorption cross-sections as well radiative forcing efficiencies of SF$_6$, NF$_3$ and CFC-115 taking into account stratospheric adjustment and cloudy skies to within a 10 – 15 % uncertainty. These values have then been used to obtain updated values for the 20, 100 and 500 year GWPs of both species. A discussion of sensitivity analysis for forcing calculations relating to tropopause definition and grid resolution has also been provided.

Our model results show that omitting stratospheric adjustment can result in an under estimation of around 10 – 15 % and omitting cloud can result in an overestimation of between 30 – 40 %. These differences are in line previous studies by Pinnock *et al.* (27) who found an overestimation of between ~25 – 50 % over several RF and IRF calculations for a range of hydrohalocarbons. Our results also show a strong variation of greenhouse gas forcings with season and latitude, varying as much as several orders of magnitude.

Our infrared cross sections are in good agreement with previous measurements. The resulting radiative forcings and efficiencies are in reasonable agreement although somewhat larger than those reported previously.

Atmospheric lifetimes have been determined for each PFC by 3D model simulation using the Whole Atmosphere Community Climate Model (WACCM) It was found that each gas has an exceptionally long atmospheric lifetime: SF$_6$: 1221, NF$_3$: 594 years, CFC-115: 539 years. These results are very similar to the ones reported by SPARC Reports but the contribution from the loss via photolysis seems to be less significant in the present case. These lifetimes were used in conjunction with the above in order to determine updated global warming potentials (over a 500 year period) for SF$_6$, NF$_3$ and CFC-115 of 27,400, 21,400 and 8,630 respectively.